Morariu, Razvan (2021) *Accurate characterisation of Resonant Tunnelling Diodes for high-frequency applications*. PhD thesis.

http://theses.gla.ac.uk/81966/

Copyright and moral rights for this work are retained by the author

A copy can be downloaded for personal non-commercial research or study, without prior permission or charge

This work cannot be reproduced or quoted extensively from without first obtaining permission in writing from the author

The content must not be changed in any way or sold commercially in any format or medium without the formal permission of the author

When referring to this work, full bibliographic details including the author, title, awarding institution and date of the thesis must be given

Enlighten: Theses
https://theses.gla.ac.uk/
research-enlighten@glasgow.ac.uk

Accurate Characterisation of Resonant Tunnelling Diodes for High-Frequency Applications

Răzvan Morariu

School of Engineering

University of Glasgow

A thesis submitted in fulfilment of the requirements for the degree of

Doctor of Philosophy

January 2021

© Răzvan Morariu, 2021

University of Glasgow

School of Engineering

Statement of Originality to Accompany Thesis Submission

Name: Răzvan Morariu

Registration Number:

I certify that the thesis presented here for examination for a PhD degree of the University of Glasgow is solely my own work other than where I have clearly indicated that it is the work of others (in which case the extent of any work carried out jointly by me and any other person is clearly identified in it) and that the thesis has not been edited by a third party beyond what is permitted by the University's PGR Code of Practice.

The copyright of this thesis rests with the author. No quotation from it is permitted without full acknowledgement.

I declare that the thesis does not include work forming part of a thesis presented successfully for another degree.

I declare that this thesis has been produced in accordance with the University of Glasgow's Code of Good Practice in Research.

I acknowledge that if any issues are raised regarding good research practice based on review of the thesis, the examination may be postponed pending the outcome of any investigation of the issues.

Signature: ……………………………………………………….

Date: …………………………29.01.2021……………………….

Acknowledgements

I would like to express my deepest gratitude to my supervisor, Prof. Edward Wasige for giving me the opportunity to pursue this research topic. His expertise in the field, together with the continuous support and guidance offered have proven invaluable to me throughout this project.

I would like to thank my colleagues Dr. Andrei Cornescu, Dr. Afesomeh Ofiare, Dr. Jue Wang, and Dr. Abdullah Al-Khalidi for sharing their support and knowledge with regards to design, fabrication and measurements of resonant tunnelling diodes, which helped me towards completing my research. Special thanks to Prof. José Figueiredo, from University of Lisbon for the discussions regarding this subject and help with device simulations.

I would also like to extend my gratitude to the James Watt Nanofabrication Centre (JWNC) staff for their help in device fabrication and to the Engineering and Physical Sciences Research Council (EPSRC) for the financial support offered for my studentship.

Finally, and most of all, I would like to express my thanks to my parents Silviu and Violeta Morariu and to Anca Amariei for their unconditional support and encouragement throughout these past years.

Abstract

Recent scientific advancements regarding the generation and detection of terahertz (THz) radiation have led to a rapid increase in research interest in this frequency band in the context of its numerous potential applications including high-speed wireless communications, biomedical diagnostics, security screening and material science. Various proposed solutions have been investigated in the effort to bridge this relatively unexplored region of the electromagnetic spectrum, and thus exploit its untapped potential. Among them, the resonant tunnelling diode (RTD) has been demonstrated as the fastest electronic device with its room temperature operation extending into the THz range. The RTD exhibits a negative differential resistance (NDR) region in its *I-V* characteristics, with this feature being key to its capabilities.

Even though the unique capabilities of RTD devices have been experimentally proven in the realisation of compact NDR oscillators and detectors, with fundamental frequencies of about 2 THz, and high-sensitivity detectors up to 0.83 THz, the reliable design procedures and methodologies of RTD-based circuits are yet to be fully developed. In this regard, significant effort has been devoted primarily to the accurate theoretical description of the high-frequency behaviour of RTDs, using various small-signal equivalent circuit models. However, many of these models have had either limited or no experimental validation, and so a robust and reliable RTD device model is desirable. The aim of this thesis is to describe a systematic approach regarding the design, fabrication and characterisation of RTD devices, providing a universal methodology to accurately determine their radio-frequency (RF) behaviour, and so this way enable a consistent integrated circuit design procedure for high-frequency circuits.

A significant challenge in the modelling of RTD devices is represented by the presence of parasitic bias oscillations within the NDR region. This has been identified as one of the main restricting factors with regards to the accurate high-frequency characterisation of this operating region. The common approach to overcoming this

limitation is through a stabilising technique comprising of an external shunt-resistor network. This has been successfully demonstrated to suppress bias oscillations in RTD-based circuits which require operation within the NDR region. However, the introduction of the additional circuit component associated with this method increases the complexity of the de-embedding procedure of the extrinsic parasitic elements, rendering the overall device characterisation generally difficult at high-frequencies.

In this work, a novel on-wafer bond-pad and shunt resistor network de-embedding technique was developed in order to facilitate the characterisation of RTDs throughout the complete bias range, without limitation to device sizing or frequency, under a stable operating regime. The procedure was demonstrated to accurately determine the circuit high-frequency behaviour of the RTD device from S-parameter measurements up to 110 GHz. The universal nature of this procedure allows it to be easily adapted to accommodate higher complexity stabilising networks configuration or different bond-pad geometries. Furthermore, the de-embedding method has also enabled the development of a novel quasi-analytical procedure for high accuracy extraction of the device equivalent circuit parameters, which is expected to provide a strong experimental foundation for the further establishment of a universal RTD RF model.

The applicability of the developed high-frequency model, which can be easily scaled for various device sizes, together with the measured RTD *I-V* characteristics was further demonstrated in the development of a non-linear model, which was integrated in a commercial simulator, the Advanced Design Systems (ADS) software from Keysight Technologies. From an application perspective, the model was used in the design of an RTD as a square-law detector for high-frequency data transmission systems. The simulated detector performance was validated experimentally using an RTD-based transmitter in the W-band (75 – 110 GHz) up to 4 Gbps (error free transmission: BER $< 10^{-10}$ in a waveguide connection), and in the Ka-band (26.5 – 50 GHz) up to 2.4 Gbps (error free transmission in a wireless data link), which demonstrated the accuracy of the developed RTD modelling approach.

Lastly, a sensitivity analysis of the RTD-based detector within the Ka-band showed a superior RTD performance over commercially available solutions, with a peak (corrected) detector responsivity of 13.48 kV/W, which is a factor of >6 better compared to commercially available Schottky barrier diode (SBD) detectors.

Publications

[1] **R. Morariu**, J. Wang, A. C. Cornescu, A. Al-Khalidi, A. Ofiare, J. M. L. Figueiredo, and E. Wasige, "Accurate small-signal equivalent circuit modelling of resonant tunneling diodes to 110 GHz," *IEEE Transactions on Microwave Theory and Techniques*, vol. 67, no. 11, pp. 4332-4340, 2019.

[2] **R. Morariu**, A. C. Cornescu, and E. Wasige, "Wireless Ka-band data link using resonant tunneling diodes," *25th Workshop on Compound Semiconductor Devices and Integrated Circuits (WOCSDICE)*, 2021. (Accepted)

[3] A. C. Cornescu, **R. Morariu**, A. Ofiare, A. Al-Khalidi, J. Wang, J. M. L. Figueiredo, and E. Wasige, "High-efficiency bias stabilization for resonant tunneling diode oscillators," *IEEE Transactions on Microwave Theory and Techniques*, vol. 67, no. 8, pp. 3449-3454, 2019.

[4] J. Wang, A. Al-Khalidi, **R. Morariu**, I. A. Ofiare, L. Wang, and E. Wasige, "15 Gbps wireless link using W-band resonant tunnelling diode transmitter," in *2018 48th European Microwave Conference (EuMC): IEEE*, pp. 1405-1408, 2018.

[5] J. Wang, A. Al-Khalidi, L. Wang, **R. Morariu**, A. Ofiare, and E. Wasige, "15-Gb/s 50-cm wireless link using a high-power compact III–V 84-GHz transmitter," *IEEE Transactions on Microwave Theory and Techniques*, vol. 66, no. 11, pp. 4698-4705, 2018.

[6] A. Cornescu, J. Wang, A. Al-Khalidi, **R. Morariu**, and E. Wasige, "IV characteristics of a stabilized resonant tunnelling diode," in *Compound Semiconductor Week (CSW), Berlin, Germany*, 14 - 18 May 2017, 2017.

[7] A. Al-Khalidi, K. H. Alharbi, J. Wang, **R. Morariu**, L. Wang, A. Khalid, J. M. Figueiredo, and E. Wasige, "Resonant tunneling diode terahertz sources with up to 1 mW output power in the J-band," *IEEE Transactions on Terahertz Science and Technology*, vol. 10, no. 2, pp. 150-157, 2019.

[8] J. Wang, A. Al-Khalidi, A. Cornescu, **R. Morariu**, A. Ofiare, and E. Wasige, "Design, fabrication and characterisation of RTD terahertz oscillators," in *2019 European Microwave Conference in Central Europe (EuMCE): IEEE*, pp. 261-264, 2019.

[9] J. Wang, A. Al-Khalidi, C. Zhang, A. Cornescu, **R. Morariu**, and E. Wasige, "Resonant tunneling diode oscillator source for terahertz applications," in *Oxford Circuits and Systems Conference (OXCAS 2017), Oxford, UK*, 19 Sep 2017, 2017.

[10] C. Paoloni, R. Basu, L. R. Billa, J. M. Rao, R. Letizia, Q. Ni, E. Wasige, A. Al-Khalidi, J. Wang, and **R. Morariu**, "Long-range millimetre wave wireless links enabled by travelling wave tubes and resonant tunnelling diodes," *IET Microwaves, Antennas & Propagation*, vol. 14, no. 15, pp. 2110-2114, 2020.

Table of Contents

List of figures xi

List of tables xxi

List of symbols, acronyms and constants xxii

Chapter 1. Terahertz wave technology 1

1.1 Introduction 1

1.2 THz technology applications 4

1.3 THz sources and detectors 9

1.3.1 THz Sources 9

1.3.2 THz detectors 12

1.4 Thesis overview 14

1.4.1 Thesis aims and objectives 14

1.4.2 Achievements and contributions to the field 15

1.4.3 Thesis organisation 16

1.5 References 18

Chapter 2. The resonant tunnelling diode 34

2.1 Theoretical background 34

2.2 RTD design concept and operating principle 37

2.3 RTD materials 42

2.4 RTD equivalent circuit models for high-frequency applications 44

2.5 Summary 53

2.6 References 54

Chapter 3. RTD MMIC technology and fabrication processes 64

3.1 Introduction 64

3.2 RTD layer structure and fabrication process overview 64

3.3 Fabrication processes 68

3.3.1 Sample preparation and cleaning 68

3.3.2 Lithography 68

3.3.3 Metal deposition and lift-off process 72
3.3.4 Dielectric deposition 74
3.3.5 Etching and via opening process 75
3.4 Summary and discussion 79
3.5 References 80
Chapter 4. Components for RTD circuits 83
4.1 Introduction 83
4.2 Design of passive components 83
4.2.1 Coplanar waveguide (CPW) 83
4.2.2 Metal-insulator-metal (MIM) capacitor 87
4.2.3 Thin-film resistors 89
4.3 Characterisation of passive components 90
4.3.1 Coplanar waveguide 91
4.3.2 MIM capacitors 93
4.3.3 Thin-film resistors 95
4.4 PIN diodes for high-speed applications 96
4.5 Summary and discussion 100
4.6 References 101
Chapter 5. RTD device modelling 104
5.1 Introduction 104
5.2 RTD DC characteristics and bias instabilities 105
5.3 RTD high-frequency characterisation 111
5.3.1 Bond-pad and shunt resistor de-embedding 112
5.3.2 Small-signal equivalent circuit parameter extraction procedure 118
5.3.3 Modelling of RTD intrinsic parameters 127
5.4 Summary and discussion 133
5.5 References 134
Chapter 6. RTD-based detector 141
6.1 Introduction 141

6.2 RTD detector basics 141

6.2.1 Square-law demodulation 144

6.2.2 Synchronous demodulation 148

6.3 RTD detector realisation and simulation 150

6.3.1 Detector design and modelling 150

6.3.2 Detector simulations 155

6.4 W-band measurements 159

6.5 Detector sensitivity measurements 164

6.6 Summary and discussions 168

6.7 References 169

Chapter 7. Conclusion and future work 175

7.1 Conclusion 175

7.2 Future work 177

7.2.1 RTD-based detector 177

7.2.2 High data-rate wireless links 177

7.3 References 181

Appendix A. Fabrication process 183

Appendix B. TLM measurements 187

Appendix C. RTD detector - simulation setup 192

Appendix D. RTD wireless transmission link 195

List of figures

Figure 1.1 The electromagnetic spectrum. 1

Figure 1.2 Atmospheric attenuation up to 1 THz for standard (red – relative humidity 50%) and dry (black – relative humidity 0%) conditions. Source:[11]. 2

Figure 1.3 THz images revealing on-body concealed firearm at 0.35 THz (left) and 0.85 THz (right). Source: [57]. 5

Figure 1.4 THz image of tooth sample displayed as power absorption spectra taken at different frequencies (0.14, 0.23 and 0.35 THz). Red arrows indicate cavity affected areas. Source: [63]. 6

Figure 1.5 Evolution of data rate capability for wireline, nomadic and wireless technology. Source: [37]. 7

Figure 1.6 Potential implementation of THz technology in backhaul and fronthaul architectures for optical fibre network extension. Source: [73]. 8

Figure 2.1 Particle wavefunction propagating through a potential barrier. 35

Figure 2.2 GaAlAs/GaAs superlattice with the corresponding conduction band energy profile along the x direction. 36

Figure 2.3 Resonant tunnelling through a double barrier quantum-well structure with associated confined state wavefunctions at two discrete energy levels. 36

Figure 2.4 Typical RTD layer structure. 37

Figure 2.5 Potential profile of an RTD for different bias conditions. (a) At equilibrium ($V_b = 0$). (b) Start of resonant current flow ($V_b > 0$) – 1st PDR region. (c) Peak current ($V_b = V_p$) at the alignment between the first resonant level (E_1) and the conduction band edge. (d) Decrease in resonant current ($V_p < V_b < V_v$) due to misalignment between E_1 and the conduction band edge – NDR region. (e) Valley current ($V_b = V_v$), after which the current will begin to increase again with bias, primarily due to

thermionic emissions, giving rise to a 2nd PDR region. (f) Corresponding device DC I-V characteristics. 39

Figure 2.6 Simplified conduction band profile of an RTD employing thick spacer layers adjacent to each barrier, under applied bias. Adapted from [7]. 42

Figure 2.7 RTD equivalent circuit model comprised of the parallel combination of device differential conductance (G_n) and self-capacitance (C_n). R_s denotes the series contact and access resistance. 45

Figure 2.8 RTD equivalent circuit model, in which the quantum-well inductance (L_{qw}) appears in series with the differential conductance (G_n) and in parallel with the device capacitance (C_n). R_s denotes the series contact and access resistance. 47

Figure 2.9 RTD equivalent circuit model, where the device capacitance is given by the parallel combination of the static capacitance (C_{dep}), determined by the depletion region and the bias dependent capacitance ($\tau_{rtd}G_n$), due to the electron delay time. . 49

Figure 2.10 Unified RTD equivalent circuit model, where C_0 and C_{qw} denote the geometric and quantum-well capacitance, respectively. 50

Figure 3.1 Diagram of RTD fabrication process: (a) Top contact metal deposition. (b) Etch to bottom contact layer. (c) Bottom contact metal deposition. (d) Etch to substrate. (e) Passivation layer deposition and via opening. (f). Bond-pad metal deposition.... 66

Figure 3.2 Micrograph of realised RTD device. 67

Figure 3.3 Typical photoresist spin coating cycle. Adapted from:[12]. 70

Figure 3.4 Characteristic spin speed curves for S1800 series photoresist. Source:[13]. 71

Figure 3.5 Photolithography process flow: (a) photoresist spin coating, (b) exposure using designed photomask under UV radiation, and (c) resist development 72

Figure 3.6 RTD metal contact fabrication steps: (a) spin coating S1805, (b) exposure and pattern development, (c) metal deposition, and (d) lift-off. 73

Figure 3.7 RTD bond-pad fabrication steps: (a) spin coating LOR-10A followed by S1805, (b) exposure and pattern development, showing the characteristic obtained undercut, (c) metal deposition, and (d) bi-layer lift-off process. 74

Figure 3.8 Illustration of the wet etching process used to define the InGaAs RTD mesa, using the metal contact as an etching mask (a). The isotropic nature of the process causes a large undercut profile of the mesa (b).. 76

Figure 3.9 SEM image of a realised RTD top a mesa displaying the undercut profile due to the isotropic nature of the wet etching process. 77

Figure 3.10 SEM image of the realised via in the polyimide passivation layer, which surrounds the RTD mesa and aid the connection between the top metal contact and bond-pads. 78

Figure 4.1 Diagram of a standard coplanar waveguide (CPW) transmission line structure. The key design parameters include the thicknesses of the substrate (h) and conductor (t), the conductor length (l), the conductor spacings (s) and the widths of the ground planes (g) and signal line (w).. 84

Figure 4.2 Inductor realised as a CPW in shorted configuration. Adapted from: [9]. 86

Figure 4.3 Top (a) and cross-sectional (b) view of a standard MIM capacitor layout used to load the shorted CPW, with an effective area defined by w and l, and a dielectric thickness d. 88

Figure 4.4 Top (a) and side view (b) of the thin-film NiCr shunt resistor network, for which w, l, and t are the width, length and thickness of the NiCr layer, respectively. 89

Figure 4.5 SEM image of a Finite Ground CPW transmission line test structure designed with a characteristic impedance $Z_0 = 50\ \Omega$. 91

Figure 4.6 Measured Port-1 and Port-2 reflection coefficients (S_{11} and S_{22}) of the CPW test structure presented on a Smith chart.. 92

Figure 4.7 Measured transmission coefficients (S_{12} and S_{21}) of the CPW test structure. 92

Figure 4.8 SEM image of a fabricated CPW test structure, shorted by a parallel capacitor. The inset shows the Si_3N_4 dielectric layer sandwiched between two metal layers to realise the MIM capacitor. 93

Figure 4.9 Equivalent circuit model of a shorted CPW by a MIM capacitor. 94

Figure 4.10 Measured and simulated reflection and transmission coefficients S_{11} and S_{21} of a shorted CPW by a MIM capacitor. 94

Figure 4.11 Micrograph of a fabricated resistor network test structure. 95

Figure 4.12 Measured Z_{11} parameter of a shunt resistor network test structure. 95

Figure 4.13 Illustration of a standard PIN diode. 96

Figure 4.14 Equivalent circuit of a PIN diode in forward bias operation (a), where R_s denotes the series variable resistance, and in reverse bias operation (b), where R_p is the large parallel resistance and C is the device capacitance. L denotes in both states the series parasitic inductance, independent of biasing condition. 97

Figure 4.15 Measured I-V (red) and R-V (black) characteristics of a fabricated $10 \times 10\ \mu m^2$ PIN diode. 99

Figure 4.16 Measured (solid line) and simulated (dotted line) real and imaginary part of device input impedance in the off-state at 0 V. 99

Figure 5.1 Measured I-V characteristics of a $10 \times 10\ \mu m^2$ RTD device, exhibiting a plateau-like distortion within the NDR region, due to the presence of low-frequency parasitic oscillations. 105

Figure 5.2 Stabilization circuit schematic of an RTD using a shunt-resistor (R_b), for low-frequency bias oscillation. A simplified RTD model consisting of the device negative differential conductance ($-G_n$) and self-capacitance (C_n) is considered, where L_p represents the parasitic inductance. 106

Figure 5.3 Micrograph of realised RTD with a 20 Ω stabilizing resistor network. 108

Figure 5.4 Comparison between the measured I-V characteristics of an un-stabilised (red) and stabilised (black) $10 \times 10\ \mu m^2$ RTD device. 108

Figure 5.5 Diagram of on-wafer RTD measurement setup. The B1500A provides the device bias voltage and also acquires the current measurement, while the spectrum analyser is used to measure the parasitic oscillations. 109

Figure 5.6 Measured low-frequency bias oscillations spectrum, in the NDR region for a stabilised (black) and un-stabilised (red) RTD.. 110

Figure 5.7 Measured stabilised device I-V characteristics using a forward and reverse voltage sweep. 110

Figure 5.8 Micrographs of an open (left) and short (right) RTD dummy pad test structures. Source:[41]. 113

Figure 5.9 RTD biased through a shunt resistor R_b, which is modelled as a 2-port network together with the bond-pad parasitic elements (L_p and C_p). 114

Figure 5.10 Micrograph of the auxiliary test structure – bond-pad and shunt resistor network. The red circles indicate the placement of standard ground-signal-ground (GSG) high-frequency probes for the 2-port measurement. 116

Figure 5.11 S-parameters stabilised (black trace) and unstabilised (red trace) RTD device biased at 2.9 V in the positive differential resistance (PDR) region – around the peak-current, showing magnitude (solid line) and phase (dashed line). 117

Figure 5.12 S-parameters of the pads and shunt resistor test structure used for de-embedding the stabilised device.. 118

Figure 5.13 S-parameters stabilised (black trace) and unstabilised (red trace) RTD device biased at 2.9 V in the positive differential resistance (PDR) region, showing magnitude (solid line) and phase (dashed line) after the de-embedding procedure. 118

Figure 5.14 RTD parallel inductance model used in the device high-frequency characterisation. R_s is the contact and access resistance, G_n the device conductance, C_n the device self-capacitance and L_{qw} the quantum-well inductance......................... 119

Figure 5.15 Real part of Z-parameters in the PDR region at 1V (blue curve) and in the NDR region at 3.1V (red curve). The high frequency regions used for Rs estimation are presented in the inset graph.. 120

Figure 5.16 Imaginary part of Y-parameters with de-embedded R_s – linear region shown in inset used to estimate C_n: in the PDR region C_n= 93 fF (a) and in the NDR region C_n= 110 fF (b). 121

Figure 5.17 Real part of Z-parameters with de-embedded R_s and C_n – linear region shown in inset used to estimate R_n: in the PDR region R_n= 284 Ω (a) and in the NDR region R_n= 136 Ω (b).................... 122

Figure 5.18 Imaginary part of Z-parameters with de-embedded R_s and C_n – linear region shown in inset used to estimate L_{qw}: in the PDR L_{qw} = 0.37 nH (a) and in the NDR region L_{qw} = -0.48 nH, where C_n is further adjusted to 94 fF to achieve linearity (b). 123

Figure 5.19 De-embedded real and imaginary measured (line) and fitted (circles) Z-parameters of a stabilised RTD at 1V in the first PDR region. 124

Figure 5.20 De-embedded real and imaginary measured (line) and fitted (circles) Z-parameters of a stabilised RTD at 3.1V in the NDR region. 125

Figure 5.21 De-embedded real and imaginary measured (line) and fitted (circles) Z-parameters of a stabilised RTD at 5V in the second PDR region. 125

Figure 5.22 Extracted RTD contact resistance R_s showing a variation of approximately 1.3 Ω over a bias range of 4V. 128

Figure 5.23 Differential device conductance Gn computed from the intrinsic I-V characteristics (black trace) and extracted (red dots). 129

Figure 5.24 RTD Device capacitance C_n simulated (black trace) and extracted (red dots). 130

Figure 5.25 Simulated transmission probability for the measured RTD layer structure. 131

Figure 5.26 Quantum-well inductance Lqw simulated (black trace) and extracted (red dots). 132

Figure 5.27 Electron dwell time τ_{dwell} computed (black dashed line) and extracted (red dots). 132

Figure 6.1 Typical RTD I-V characteristics showing the two high non-linearity regions. 142

Figure 6.2 Rectified response of an applied THz pulse by the device non-linear I-V characteristics (Fig. 6.1) for region (a). Adapted from [9]. 143

Figure 6.3 Typical TB-RTD I-V characteristics. 144

Figure 6.4 Frequency spectrum of a standard AM signal, showing the centre carrier frequency ω_c and the sidebands of the baseband signal of frequency ω_m. 144

Figure 6.5 Measured I-V characteristics of a fabricated device. Inset graph shows the non-linearity region approximated by a 5th order Taylor series expansion. 146

Figure 6.6 Amplitude modulated signals with different modulating index m. 147

Figure 6.7 Block diagram of standard coherent detector circuit. 148

Figure 6.8 Coherent detection by injection locking mechanism. Adapted from:[22]. 149

Figure 6.9 Modelled I-V characteristics under stable operating regime (black). Computed differential conductance G_n (red). 151

Figure 6.10 Modelled device capacitance C_n (black) and quantum-well inductance L_{qw} (red). 151

Figure 6.11 Shunt-diode detector circuit. 152

Figure 6.12 Micrograph of fabricated RTD detector. 153

Figure 6.13 Equivalent circuit model of the RTD detector. 154

Figure 6.14 Comparison between measured (black trace) and simulated (blue trace) real (a) and imaginary (b) Z_{11} of the RTD detector circuit. The result of the final optimisation process is shown as the red trace. 155

Figure 6.15 RTD large signal model used for software implementation, where the device I-V characteristics are represented as a voltage dependent current source. . 156

Figure 6.16 Schematic of complete RTD detector circuit...................................... 156

Figure 6.17 Simulated detector operation for a standard AM input signal (a), showing the rectified RTD response (b) and demodulated signal (c). 157

Figure 6.18 ADS generated OOK modulation of a 90 GHz carrier signal (shown in inset graph) by a 1 Gbps pseudo-random bit sequence... 158

Figure 6.19 Simulated 1 Gbps eye diagram at 90 GHz. Eye amplitude of 1.62 mV and a SNR of 27.1 dB 158

Figure 6.20 Simulated 12 Gbps eye diagram at 90 GHz. Eye amplitude of 0.87mV and a SNR of 16.1 dB. Eye contour at BER of 10^{-12}shown in purple outline. 159

Figure 6.21 Pictures of the packaged RTD oscillator integrated in a WR-10 rectangular waveguide, used as a Tx sub-system in data transmission experiment.................... 160

Figure 6.22 Block diagram of experimental setup, using a packaged RTD source. 160

Figure 6.23 Simulated detector output signal amplitude for various input signal power at 84 GHz. Saturation behaviour observed above -10 dBm.................................... 161

Figure 6.24 Simulated 1.5 Gbps eye diagram at 84 GHz. Eye amplitude of 94.64 mV and a SNR of 25.35 dB. 162

Figure 6.25 Measured eye-diagram of demodulated 1.5 Gbps signal. Eye amplitude of 83.94 mV and SNR of 21.3 dB. 163

Figure 6.26 Measured eye-diagram of demodulated 4 Gbps signal. Eye amplitude of 72.63 mV and SNR of 14.16 dB. 163

Figure 6.27 Measured S-parameters of fabricated detector circuit, with the RTD biased around the peak current region at 2.95V.. 164

Figure 6.28 RF spectrum of a 6 MHz central frequency AM wave, showing the 0.5 MHz original baseband signal.. 165

Figure 6.29 Block diagram of Ka-band sensitivity measurement setup, using a modulated continuous wave signal generator. 165

Figure 6.30 Measured (black) and corrected (red) detector responsivity as a function of carrier frequency for a 50 Ω load. 166

Figure 7.1 Epi-layer structure of RTD and PIN diode. 179

Figure 7.2 Circuit topology of a vector modulator using directional couplers enabled by PIN diode controls 179

Figure B.1 Diagram of a standard TLM test structure (cross-section view) and the corresponding 4-probe resistance measurement setup. The metallic contacts are fabricated with various separation distances (l_1, l_2, l_3, etc.) 187

Figure B.2 Illustration of measured total resistance R_t as a function of contact separation distance. The equivalent total contact resistance ($2 \times R_c$) and transfer length ($2 \times l_T$) can be obtained at the intersection of y-axis and x-axis, respectively......... 188

Figure B.3 SEM image of two fabricated TLM test structures, used to characterise the contact resistance of the RTD top and bottom metal contacts. 189

Figure B.4 Measured total resistance R_t as for the top and bottom metallisation layer as a function of contact separation distance. 189

Figure C.1 ADS schematic of implemented RTD model (left) and component (right). 192

Figure C.2 Measured (black) and fitted (red) RTD device I-V characteristics........ 194

Figure C.3 ADS schematic of the detector setup. 194

Figure D.1 Block diagram of wireless data transmission setup, using an on-wafer RTD source. 195

Figure D.2 Picture of wireless data transmission setup. 196

Figure D.3 Measured eye-diagram of demodulated 2 Gbps signal. Eye amplitude of 3.6 mV and SNR of 19.22 dB. 197

Figure D.4 Measured eye-diagram of demodulated 6 Gbps signal. No clear eye opening was identified. 197

Figure D.5 Measured BER vs data rate. Error free transmission up to 2.4 GHz. 197

List of tables

Table 3.1 RTD Epitaxial layer structure 65

Table 4.1 PIN diode epitaxial layer structure.. 98

Table 5.1 Summary of extracted parameters.. 126

Table 5.2 Computed goodness-of-fit between measurement and simulation 127

Table 5.3 Summary of material parameters 129

Table 6.1 Summary of material parameters. 150

Table 6.2 Summary of extracted parameters.. 154

Table 6.3. Summary of Ka-band detector performances. 167

Table 7.1 Summary of modulator operation 180

Table B.1 Summary of extracted parameters from TLM measurements. 190

Table C.1 Summary of fitting coefficients.. 193

List of symbols, acronyms and constants

Acronyms

- 2DEG Two-dimensional electron gas
- AC Alternative current
- ADS Advanced design system
- AM amplitude modulation
- BER Bit-error rate
- BWO Backward wave oscillators
- CAD Computer aided software
- CMOS Complementary metal-oxide semiconductor
- CPS Coplanar stripline
- CPW Coplanar waveguide
- DBQW Double-barrier quantum well
- DC Direct current
- EBL Electron-beam lithography
- EBPVD Electron-beam physical vapour deposition
- FEL Free-electron laser
- FET Field effect transistors
- FIR Far-infrared
- FOM Figure of merit
- Gbps Gigabits per second
- GSG Ground-signal-ground
- HBT Heterojunction bipolar transistor
- HEB Hot-electron bolometer
- HEMT High-electron-mobility transistor
- ICP-CVD Inductively coupled plasma chemical vapour deposition
- IF Intermediate frequency
- IMPATT Impact ionization avalanche transit-time
- IoT Internet-of-Things
- IP Internet protocol

- IR Infrared
- M2M Machine-to-machine
- MBE Molecular beam epitaxy
- MIM Metal-insulator-metal
- MMIC Monolithic microwave/mmWave integrated circuit
- mmWave Millimetre-wave
- NDR Negative differential resistance
- NEP Noise equivalent power
- NFC Near-field communications
- NLO Non-linear optics
- NSD Noise spectral density
- OOK On-off keying
- PCA Photoconductive antenna
- PDR Positive differential resistance
- PIN Positive intrinsic negative
- PLL Phase-locked loop
- PRBS Pseudo-random bit sequence
- QAM Quadrature amplitude modulation
- QCL Quantum cascade laser
- RF Radio frequency
- RSS Received signal strength
- RTD Resonant tunnelling diode
- SBD Schottky barrier diode
- SEM Scanning electron microscope
- SI Semi-insulating
- SNR Signal-to-noise ratio
- SOLT Short-open-load-thru
- S-parameter Scattering parameter
- TBQW Triple-barrier quantum well
- TDS Time-domain spectroscopy
- THz Terahertz
- TLM Transmission line model

- TUNNETT Tunnelling transit-time
- UTC-PD Uni-travelling-carrier photodiode
- UV Ultraviolet
- VNA Vector network analyser
- WLAN Wireless local area network
- WPAN Wireless personal area networks

Constants

- c_0 $= 3 \times 10^8$ m/s Speed of light in free space
- μ_0 $= 4\pi \times 10^{-7}$ H/m Vacuum permeability
- ε_0 $= 8.85 \times 10^{-12}$ F/ m Vacuum permittivity
- h $= 4.136 \times 10^{-15}$ eVs Planck's constant
- ħ $= 6.582 \times 10^{-15}$ eVs Reduced Planck's constant
- e $= 1.6 \times 10^{-19}$ C Electron charge
- m_0 $= 9.11 \times 10^{-31}$ kg Electron rest mass

Chemical symbols

- $(CH_3)_2CO$ Acetone
- Al Aluminium
- AlAs Aluminium arsenide
- AlGaAs Aluminium gallium arsenide
- AlSb Aluminium antimonide
- Au Gold
- C_3H_8O Isopropyl alcohol
- C_6H_5Cl Chlorobenzene
- C_7H_8 Toluene
- CF_4 Tetrafluoromethane
- CH_3OH Methanol
- CH_4 Methane
- CO_2 Carbon dioxide
- Ga Gallium
- GaAs Gallium arsenide

- GaN Gallium nitride
- GaSe Gallium selenide
- Ge Germanium
- H_2O_2 Hydrogen peroxide
- H_2S Hydrogen sulphide
- H_3PO_4 Orthophosphoric acid
- HCl Hydrochloric acid
- HCN Hydrogen cyanide
- HeNe Helium-neon
- InAs Indium Arsenide
- InGaAs Indium gallium arsenide
- InP Indium phosphide
- InSb Indium antimonide
- Mo Molybdenum
- N_2 Nitrogen
- NbN Niobium nitride
- NH_3 Ammonia
- NiCr Nickel-chromium
- Pd Palladium
- Si Silicon
- Si_3N_4 Silicon Nitride
- SiGe Silicon germanium
- SiO_2 Silicon dioxide
- Ti Titanium
- ZnTe Zinc telluride

Symbols

- m^* Electron effective mass
- T(E) Transmission coefficient
- E_C Conduction band energy
- E_F Fermi level
- I_p Peak current

- I_v Valley current
- V_p Peak voltage
- V_v Valley voltage
- PVCR Peak-to-valley current ratio
- G_n Device differential conductance
- C_n Device capacitance
- L_{qw} Device quantum well inductance
- τ_{dwell} Electron dwell time
- Z_0 Characteristic impedance
- δ Skin depth
- β Phase constant
- R_s Device contact resistance

Chapter 1. Terahertz wave technology

1.1 Introduction

The terahertz (THz) frequency range is generally regarded as the region in the electromagnetic spectrum that encapsulates frequencies from 300 GHz up to 3 THz, with a corresponding wavelength (λ) between 1 mm and 100 µm [1]. Due its spectral position, as seen in Fig. 1.1, between the millimetre-wave (mmWave) band (30 GHz – 300 GHz) and the infrared (IR) photonics band (3 THz – 430 THz), until recently, it was commonly referred to as sub-millimetre [2][3] or far-infrared (FIR) radiation [4][5], depending on the methodological perspective [6] (modal or bulk – wave or photon).

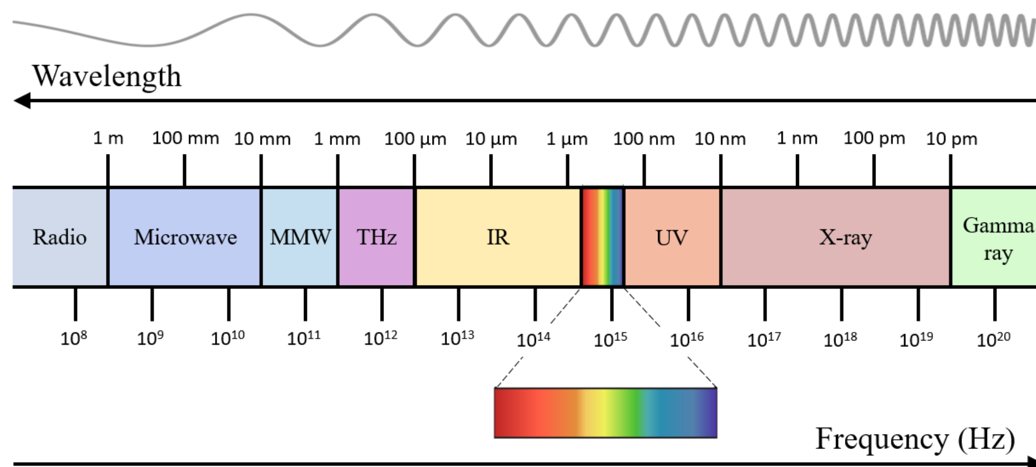

Figure 1.1 The electromagnetic spectrum.

From a historical perspective, the presence of this uncharted region in the frequency spectrum, between traditional electronics and optical sources, was first specifically acknowledged in the mid-1920s [7].

Despite its designation as part of the highest official radio bands [8] (band 12: 300 GHz to 3 THz) by the International Telecommunication Union (ITU) in 1947, the development of successful applications within this spectral span was hindered by the Earth's relatively high atmospheric absorption. This is primarily due to the levels of rotational and vibrational transitions of water vapours, which overlap almost entirely with the THz domain [9], as shown in Fig. 1.2.

Over the next decades, this factor mainly limited exploration of this frequency range to the astrophysics and cosmology community, which made use of the scarce available transmission 'windows', while conducting experiments in the higher atmosphere [10].

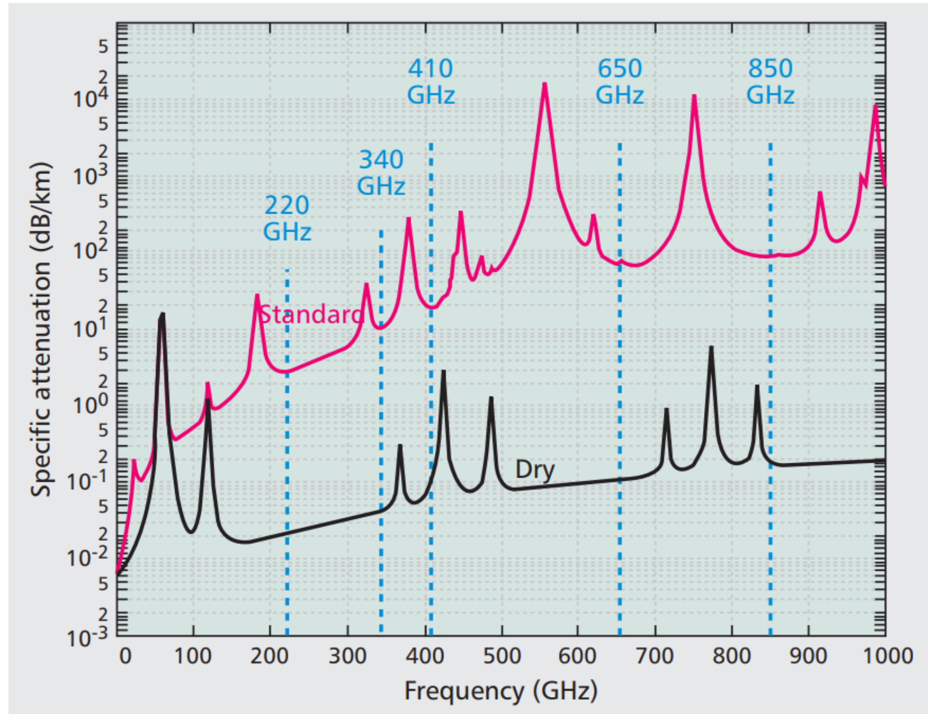

Figure 1.2 Atmospheric attenuation up to 1 THz for standard (red – relative humidity 50%) and dry (black – relative humidity 0%) conditions. Source:[11].

Although originally considered a relatively niche field, and frequently referred to as the 'terahertz gap' due to the limited technological development of reliable sources, with adequate power levels, and high sensitivity detectors, the unique properties of terahertz radiation started to draw a rising interest in the prospect of its potential applications. Its corresponding quantum energy level falls between 1.24 meV and 12.4 meV, which is considered non-ionizing (insufficient to displace an electron from an atom or molecule [12]) and thus harmless to biological tissue. However, it is capable to penetrate through various non-metallic materials such as plastic [13], fabric [14], wood [15], and paper [16], while reflected by conducting materials (metals and highly doped semiconductors). This property, in combination with the good spatial resolution achievable within this frequency range, enabled the prospect of developing novel high-resolution imaging techniques [17], with superior performance in comparison with the well-established X-ray and microwave systems. Furthermore, despite their poor suitability for applications involving long-range communication (i.e. radio and

television broadcasting), and detection (i.e. radar) systems, due to the above-mentioned environmental factors, the short wavelengths of millimetre and terahertz radiation offers high capability of handling transmission (over short ranges) of large amounts of data at a time [11].

Despite numerous notable advancements regarding the development of sources such as electrical discharge-pumped THz gas laser [18], optically excited gas laser [19], carcinotrons or backward wave oscillators (BWO [20]) and detectors (i.e. n-InSb electron bolometer [21], Ge bolometer [22], tunable far-infrared detector [23]), the most important milestone in the field of THz radiation was marked by the invention of the femtosecond laser in the late 1980s [24]. This led to the development of time-domain spectroscopy (THz-TDS), culminating with the successful demonstration in 1995 of the first THz imaging system [25], and has enabled a broader exploration of this technology in other related fields such as medical diagnostics [26], defence [27], pharmaceutics [28], genetics [29], security screening [30], and quality inspection [31].

With the beginning of the 21st century, THz technology witnessed another exponential growth in research activity, marked by the first successful demonstration of wireless THz transmissions systems [32]. This was achieved at frequencies of over 100 GHz and up to 1 THz using pulse and intensity-modulated lasers in combination with photoconductors and photodiodes for both impulse and continuous wave generation [33-35]. In the following years, record data rates of over 10 Gbps have been reached with the establishment of the first commercially available wireless-links. This has been proven to operate over an effective distance of 5 km [36], and received 18 GHz bandwidth allocation (116 GHz ~ 134 GHz) in Japan by the Ministry of Internal Affairs and Communications (MIC) for broadcasting purposes in 2014. Considering the continuous demand for increased data rates in recent years, in order to match the rapid ongoing developments in mobile and computer networks, a new milestone of 100 Gbps is expected to be achieved within the present decade [37], by exploring the unallocated frequency bands between 275 GHz and 3 THz.

Current research is now focussed on developing suitable semiconductor-based THz sources and detectors which are compact and cost-effective solutions in order to bring this technology to the consumer marketplace.

1.2 THz technology applications

As previously mentioned, the unique properties of THz radiation have been exploited in a vast number of scientific and industrial fields, involving space exploration, high data rate wireless communications, molecular analysis and high-resolution imaging and sensing. The aim of this section is to present a brief summary of some of the established emerging applications.

THz time-domain spectroscopy is considered one the most relevant direct applications of this type of radiation, due to its frequency correspondence to the resonance levels in different molecules [38]. This technique relies on generation and detection of short sub-picosecond pulses (typically <0.1 ps), where the amplitude and phase of the reflected signal, at a measured sample interface, provides information in relation to both its intramolecular and intermolecular interactions [39]. This type of chemical composition analysis, in combination with density functional theory (DFT) [40], can be performed to study various substances and compounds [41], and is adequate for detection of illicit substances such as drugs [42] or explosives [43]. Similar techniques can be applied for characterisation of several organic material by probing the low frequency collective vibrational modes of biomolecules.

From a more industrial perspective, THz spectroscopy has been used for characterisation and inspection of numerous materials and processes [44] such as behavioural observations of polymer properties (i.e. plastics [45], composite materials [46], foams [47] and adhesives [48]); multi-layer thickness measurements of paint and coatings [49]; fault inspection of integrated circuits (ICs) [50] and semiconductor carrier and mobility concentration measurements [51] in electronics; petrochemical quality assessment (i.e. fuels [52] and oils [53]); quality control of pharmaceuticals products [54]; and also food inspection [55].

Furthermore, THz waves have the distinct property of penetrating most common physical barriers, such as packaging and clothing items, with minimal attenuation, and when combined with their selective reflection and absorption levels can be implemented in non-destructive security imaging systems, for the purpose of revealing concealed items. In comparison to traditional systems, adopted at densely populated security checkpoints by customs and border control, which rely on pulse induction

systems for on-body metal detection or X-ray technology for baggage inspection, due to its non-invasive nature, THz imaging provides a universal solution for both people and package screening. Additionally, such systems have the superior ability to also identify non-metallic weapons and explosives (i.e. ceramic, plastic, polymer) [56]. Fig. 1.3 shows two images of an on-body hidden firearm, acquired using a THz camera at different frequencies (0.35 THz – left and 0.85 THz – right).

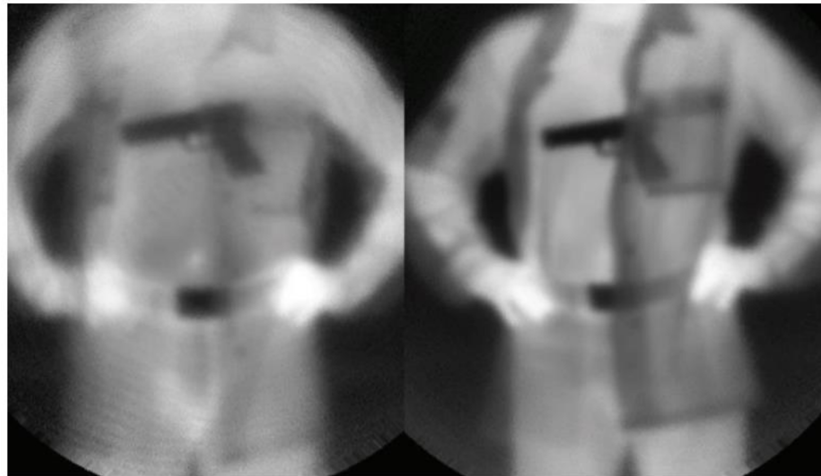

Figure 1.3 THz images revealing on-body concealed firearm at 0.35 THz (left) and 0.85 THz (right). Source: [57].

The demonstrated capabilities of THz radiation systems to generate two-dimensional (2D) images, in addition to its non-ionizing energy levels have opened new possibilities for this technology to be highly explored in the medical field, for various disease diagnostics [58], including cancer [59]. Currently, medical imaging techniques are limited to X-ray computed tomography (CT), which poses serious health risks due to its ionizing levels, magnetic resonance imaging (MRI), which require expensive and complex cryogenic cooling for superconductors, and ultrasonography, which most often cannot achieve the required resolution for comprehensive diagnosis. Due to high level of absorption of THz waves by polar molecules, such as water, which is the main constituent of biological tissue, THz radiation represents a promising solution for contrast imaging techniques. Using this property, cancerous tumours, which have a higher water concentration than healthy tissues, can thus be distinguished and identified based on the variation in energy absorption [60]. To date, multiple in vivo analysis of breast, lung, colon and oesophageal cancer tumours [61], and also extent and depth measurement of basal cell carcinomas (skin cancer) [26] have been

performed using THz reflectance mode imaging techniques. In addition to soft tissue density characterisation, similar systems have been used in the context of dental healthcare, for detection of tooth cavities [62], by variation in refractive index measurement, as shown in Fig. 1.4.

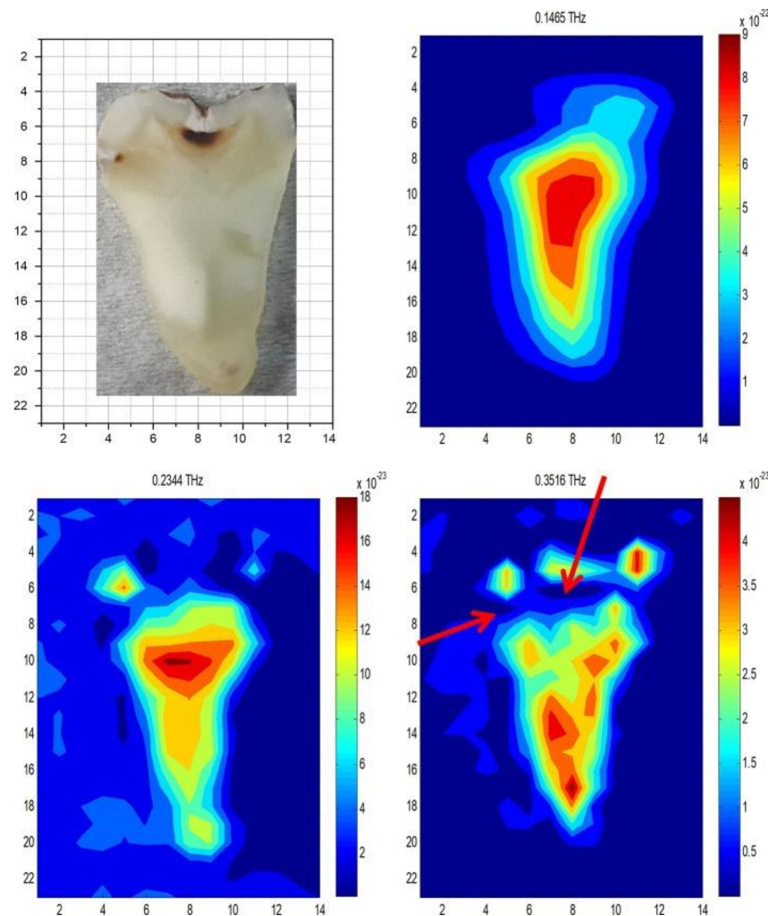

Figure 1.4 THz image of tooth sample displayed as power absorption spectra taken at different frequencies (0.14, 0.23 and 0.35 THz). Red arrows indicate cavity affected areas. Source: [63].

Recently, exploration of reflective imaging techniques, involving THz radiation have been extended to even more 'exotic' research fields, such as history and archaeology, for non-destructive evaluation of century-old artwork [64].

Another major field of application of THz technology is represented by wireless data communications. Following Edholm's law, which has modelled the exponential increase in telecommunication data rates for over half a century (Fig. 1.5), wireless communication systems will match and even surpass wireline technology (ethernet) around 2030, by effectively doubling their bandwidth every 18 months [65].

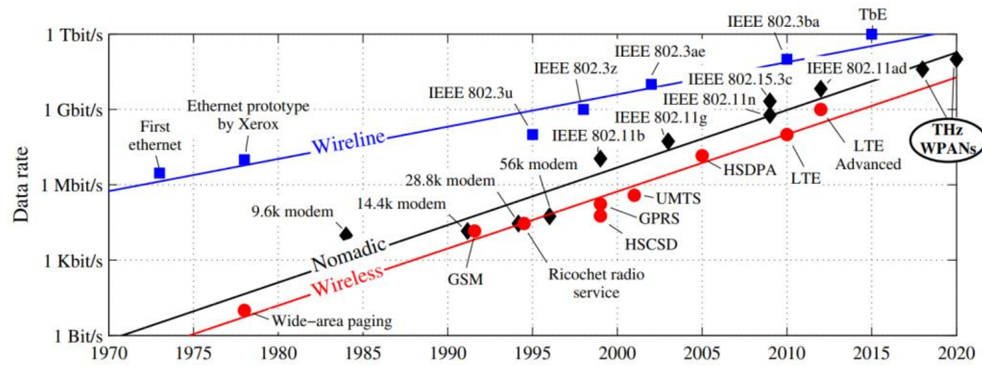

Figure 1.5 Evolution of data rate capability for wireline, nomadic and wireless technology. Source: [37].

This continuously growing effort to achieve and provide data rates upwards of tens of gigabit per second (Gbps) is fuelled by the unceasing market demand, predominantly in the modern multimedia sector, in which currently researched techniques for video and data compression are unable to provide a unique solution to the strain imposed on the current wireless infrastructure [66].

An annual report conducted by Cisco in 2020 [67] predicts that around 66% of the global population will have access to internet services and around 70% to mobile connectivity by 2023, with the consumer segment accounting for almost 75% of the global devices and connections. Furthermore, the estimated number of devices connected to internet protocol (IP) networks will reach approximately 29 billion, of which the share of mobile devices would be more than half. This includes the fastest projected growing category Machine-to-Machine (M2M) connections (i.e. home automation, connected car systems, etc.), also referred to as the Internet-of-Things (IoT) [68].

Since the introduction of the ground-breaking smartphone concept by Apple in 2007, at the unveiling of the first generation of iPhones, the mobile data traffic has witnessed an unprecedented boost, reaching a combined uplink and downlink monthly figure of 41 exabytes (10^{18} bytes) in 2020 and is expected to almost double by 2022 [67].

Currently, in order to sustain the required IP traffic, mobile communication channels, based on mmWave frequencies have been proposed in the Ka-band around 28 GHz and 38 GHz, in the V-band at around 60 GHz and in the E-band between 71-76 GHz and 81-86 GHz, as part of the ongoing establishment of the emerging 5G technology

[69], with a maximum globally allocated continuous bandwidth of 7 GHz. This however constitutes a major bottleneck in terms of channel capacity, and delivering a targeted speed of 100 Gbps would require unrealistic transmission efficiencies of 14 bit/s/Hz [37]. In order to tackle this problem, unallocated frequency bands in the THz range are currently explored by various research groups as potential targets for the next ultra-high bandwidth beyond-5G or even six generation (6G) technologies [70-72], with potential data rates above 10 Gb/s.

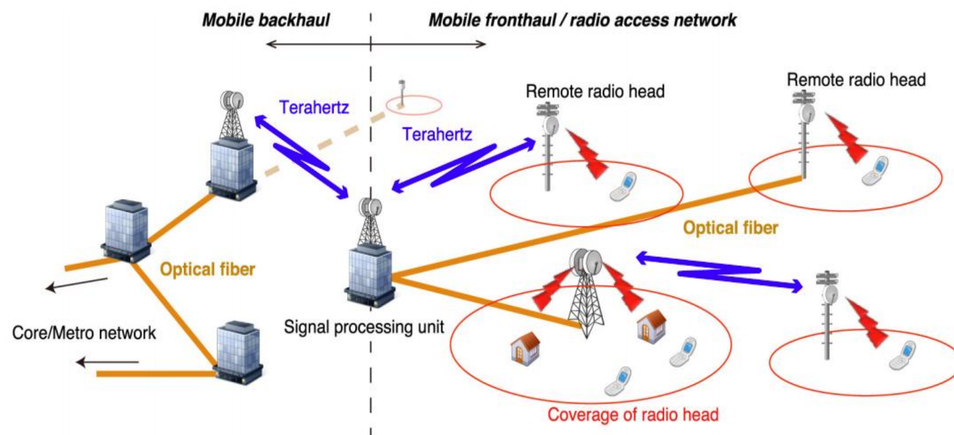

Figure 1.6 Potential implementation of THz technology in backhaul and fronthaul architectures for optical fibre network extension. Source: [73].

The primary outdoor applications for THz communications are mobile backhaul (connection to and between mobile base stations) and fronthaul (connection between cell tower remote radio heads and baseband units) infrastructures, which would serve as optical fibre extensions of the backbone networks by switchable point-to-point or point to multipoint connections [74], as shown in Fig. 1.6. For this purpose, high gain directive antennas/antenna arrays with automatic error correction capabilities (i.e. beam steering [75]) need to be considered in order to compensate for potential events (i.e. wind, animal interaction, seismic activity, etc), that could cause misalignment.

Other prospective outdoor macro scale applications for THz wireless systems include small and ultra-dense cell technology [76], based on short-range wireless base station for additional mobile coverage; traffic communication networks for autonomous vehicles [77]; space applications involving inter-satellite communication [78]; and even military grade communication systems between aircrafts [79]. The most suitable range of applications for this particular technology is represented however by short

range (<10 m) indoor communication systems. Among these, wireless local area networks (WLAN), wireless personal area networks (WPAN), kiosk downloading and near-field communications (NFCs) would highly benefit from the potential ultra-high speed connectivity offered between multiple users and access points and also inter-device communications (i.e. smartphones, cameras, projectors, displays, etc.) [37].

With the increasing necessity for distributed storage and recent advancements in cloud computing, server stacks interconnects in data centres have become another important target application for THz wireless links [80]. At this end of the network backbone, the integration of THz technology would be able to replace the need for extended lengths of category 6 ethernet cables [81], which highly restrict adequate airflow, while also requiring high maintenance costs. Such wireless implementation would thus provide an efficient solution for space requirements, offering a new degree of flexibility, while and also promoting superior cooling performance [82].

Clearly, there is rising interest in THz technology from a wide variety of scientific fields and industry applications due to the unique properties of THz radiation and therefore the advantages that THz systems can offer. However, the lack of efficient, compact, high-power sources and high-sensitivity detectors has often hindered successful development and deployment of the technology solutions beyond controlled lab environments [83].

1.3 THz sources and detectors

1.3.1 THz Sources

From the THz emission techniques perspective, the majority of available sources can be generally classified as either electronic or photonic based technologies [84]. On the photonics side, far infrared (FIR) gas lasers have been considered the oldest source of coherent THz emission [85][86]. As a more recent alternative to FIR technology, quantum cascade lasers (QCLs) have become an established method for generation of THz radiation [87], with the lowest frequency reported in continuous-wave operational mode at 1.2 THz with around 0.12 mW of output power [88]. However, the required environmental temperature to achieve this value is very low, around 10 K, and thus complex cryogenic cooling systems are typically needed.

Furthermore, THz emission mechanisms have also been demonstrated in bulk semiconductor lasers with highly doped p-type/n-type junctions, such as electrically excited Ge lasers, or optically excited Si lasers [89]. The drawbacks related to the operation of these sources arise from the very specific emission conditions (i.e. temperature, electric and magnetic fields, etc.), which limits their usability outside controlled lab environments. Similarly, optical excitation mechanisms, typically from femtosecond lasers sources, have been used in combination with photoconductive antennas (PCAs) for the generation of short THz pulses [90].

Several other approaches of generating THz radiation have been investigated using photonic sources in combination with various optical-to-THz conversion methods. As such, one of the most generally employed methods in high-speed communication systems is photomixing, also known as heterodyne frequency down-conversion [91][92]. Generally, for this purpose, solid-state photomixers such as, uni-traveling-carrier photodiodes (UTC-PDs) [93], GaAs-Schottky diodes [94] and even PCAs [95] have been used, however their reported output powers are typically in the μW range [96], with low conversion efficiency between high-frequency light and THz waves.

In a similar system configuration, differential frequency generation (DFG) of continuous wave THz radiation can be achieved by mixing two optical near-IR lasers beams in nonlinear optical (NLO) crystals [97-99]. The presented optical-to-THz conversion techniques [100] typically represent an unattractive solution for most applications due to their complex and cumbersome system architectures highly limiting their wide range implementation.

At the lower end of the THz frequency spectrum, high-power free-electron based sources, such as free-electron lasers (FELs), vacuum-tube sources and extended-interaction klystrons have been demonstrated to produce both continuous-wave and pulsed-mode THz radiation [101] with output powers up to tens of W [92]. This performance, however, can be achieved at the cost of bulky and complex systems, requiring high vacuum and magnetic field conditions and also water-cooling, due to the high operating voltages [102].

In contrast to vacuum devices, solid-state electronic sources have been intensively researched in the context of THz range radiation generation at room temperatures. The

main intrinsic limitations of these devices to operate within the entire THz spectrum is associated with the very short carrier transit time requirement through semiconductor junctions [85]. In order to overcome this performance limitation, the most commonly employed method for increasing the operational frequencies of solid-state emitters is by implementing them in frequency multiplier circuits [103]. Typically, this implies the use of non-linear device chain circuits, which can up-convert the microwave frequencies of provided RF signals by harmonic generation [104]. The main drawback of this technique is represented by the fact that in order to achieve THz range operation, several cascaded frequency multiplier stages are required, which leads to very poor DC-to-RF conversion efficiencies (~0.001% [105]), due to associated power losses. The average output powers of such circuits are in μW range and require complex amplification stages for frequencies above 2 THz [106].

However, based on continuous advancements in the field of semiconductor material and monolithic microwave integrated circuit (MMIC) technology, the reported fundamental operating frequencies of solid-state sources have seen a steady increase over the past years [92]. As such, three-terminal devices (i.e. transistors) have witnessed significant improvement in terms of their maximum cut-off frequencies, derived from increased electron mobility, together with reduced gate length and contact resistance [107]. Operating frequencies above 1 THz at room temperatures have recently been reported for indium phosphide (InP) based heterojunction bipolar transistors (HBTs) [108] and high-electron-mobility transistors (HEMTs) [109].

Furthermore, oscillators based on two terminal devices, which have been considered relevant sources for microwave and mm-wave technologies in the past, are being investigated for their potential to extend their operational frequencies well into the THz range [110]. These systems exploit the capability of particular non-linear devices (i.e. diodes) to exhibit negative differential resistance (NDR) regions in their current-voltage (*I*-*V*) characteristics, which when integrated in a resonant circuit are capable of generating sustained oscillations [111]. Commonly employed two-terminal NDR devices for this purpose include Gunn diodes (10 mW up to 0.4 THz [112]), impact ionization avalanche transit-time (IMPATT) diodes (300 mW at 140 GHz [113], tunnelling transit-time (TUNNETT) diodes (up to 0.7 THz [114]) and resonant tunnelling diodes (RTDs).

Among two-terminal solid-state THz sources, RTDs have demonstrated the highest fundamental oscillation frequency at room temperature operation [115]. These devices rely on the quantum mechanical tunnelling transport mechanism through successive barriers, by alignment of discrete energy levels between the adjacent semiconductor layers, under specific bias conditions [116]. NDR can be achieved with further increase in bias, for which the resonant condition is no longer satisfied. Since this device is the main focus of this thesis, a more in-depth description of the operation principle of RTDs is presented in Chapter 2.

1.3.2 THz detectors

From the perspective of coherent THz radiation detection, two main methodologies are generally adopted. The first relies on down-converting the received signal to significantly lower intermediate frequencies (IF), for which well-established signal processing and amplification techniques can be employed. This is known as heterodyne detection [117], and typically involves the use of an active device for mixing the received signal frequency with a locally generated reference frequency. Usually for this purpose, complex circuitry is required in the form of beam splitters or diplexers to couple the two signals, together with expensive low-noise amplifier and filter stages, in order to compensate for the noise component introduced by the mixer element [118].

Conversely, THz sensing can be achieved in a direct detection approach, relying on a quantifiable physical response of the employed device in relation to the imposed signal. Generally, direct detection is preferred in the context of applications that require higher sensitivity such as imaging, while heterodyne detection is capable of offering higher spectral resolution [119][120], also being characterised by the fact that it preserves information regarding the frequency and phase of the incoming THz signal (i.e. coherent detection). However, the choice of detector topology design for specific applications is primarily made from the employed device perspective. As such, the most generally described classification of THz detectors, in relation to the device technology, is based on their detection mechanism [121].

An important category, predominantly employed in direct detection schemes, is represented by thermal detectors, in which the implemented device exhibits a material

temperature variation, when subjected to THz radiation, further translated into a generated electrical response based on various thermal phenomena. The most common thermal detectors include bolometers [122], Golay cells [123], pyroelectric detectors [124] and thermopiles [125]. Out of these, microscale niobium nitride hot electron bolometers (NbN HEBs) have been demonstrated to operate in direct detection schemes, with responsivities around 100 A/W at 0.65 THz [126], however the reported operating temperature is around 4 K.

The second relevant class of detectors can be defined based on the device coherent electron movement variation, or individual electron excitation by incident photons, as a result of THz radiation absorption [127]. Plasmonic detectors, which are based on collective motion of carriers can typically be implemented as HEMTs [128] and field effect transistors (FETs) [129], for which GaN THz FET detectors (TeraFETs) have been demonstrated to operate at high temperatures (473 K) up to 0.14 THz, with respectable sensitivities of 15 kV/W [130]. However, the main limitation of these detectors is represented by their relatively small spectral range [131].

In highly doped extrinsic semiconductors, (i.e. Ge:Ga, Ge:Be, Si:Ga, Si:In), absorbed photons are capable of exciting carriers from impurity-bound states and generate a highly specific wavelength response due to a variation in electron energy distribution [132]. Ge:Ga based photoconductor are considered among the most sensitive detectors at the higher frequency end of the THz spectrum [133], due to the small material energy band-gap at room temperature (0.67 eV for Ge), however they require cooling at liquid helium temperatures.

Photon-electron interaction mechanisms have also been exploited for THz radiation sensing in the context two-terminal junction devices, in which charged particles acquire sufficient energy to overcome potential barriers, thus providing a rectification effect for the incoming field. This rectification principle has been demonstrated for various p-n junction photodiodes, however for this purpose Schottky barrier diodes (SBDs) are most commonly employed [127]. SBDs are capable of offering a superior high-frequency performance in comparison to generic p-n diodes, due to their faster switching times and low shot noise, when operated under zero bias conditions at room temperature. GaAs based SBD detectors have become the wide commercially available packaged solution for direct THz detection, with responsivities ranging from

1000 V/W to 400 V/W between 0.1 THz and 0.9 THz [134], whereas Si based SBD cell arrays have been intensively researched due to their compatibility with most CMOS processes and technologies [135]. Several factors, however, need to be considered for the operation of these detectors at frequencies above 1 THz, primarily the presence of various parasitic effects, which renders the design procedure highly complex and costly [136]. Furthermore present non-linearity in their *I*-*V* characteristics enables SBDs to be also implemented as mixers in heterodyne detection [137][138], demonstrated up to 25 THz [139].

More recently, based on the same electron excitation principle, high-sensitivity RTD based detectors have been demonstrated up to 0.83 THz for direct detection and also 0.78 THz, when implemented as oscillators in a heterodyne detection scheme, using an injection-locking phenomena [140]. A more comprehensive performance analysis of different RTD detector topologies (coherent and direct detection schemes), in comparison with more conventional solutions, particularly zero bias SBD detectors is presented in Chapter 6.

1.4 Thesis overview

1.4.1 Thesis aims and objectives

Due to the distinct capabilities of RTDs, mentioned in the previous section in relation to their ability to source and detect THz radiation, numerous studies have been focused on understanding their complex high-frequency behaviour. Generally, this has been attempted through the aid of either theoretical (physics based) small-signal equivalent circuit models or empirical models, derived based on data trends acquired from measurements. However, due to the fact that typically there has been limited agreement between the two methodologies, more precisely limited frequency validation of the developed models, or a low degree of experimental repeatability, a systematic approach for RTD characterisation is yet to be developed.

The aim of this thesis was to design, fabricate and characterise RTDs, in order to investigate the development and experimental validation of accurate high-frequency equivalent circuit models, for the purpose of assessing the performance of these devices as THz sources and detectors.

1.4.2 Achievements and contributions to the field

The main achievement described in this thesis is the development of a universal on-wafer pad and stabilising network de-embedding technique to accurately determine the device small-signal behaviour of an RTD device throughout its entire bias range. In comparison to more traditional de-embedding methods, such as the cascade method, or the short and open dummy pad test structure technique, previously used in RTD characterisation studies, the theoretical basis of the proposed approach does not suffer from frequency limitations due to idealised models of the pad parasitics (which are valid in a limited spectral span). Furthermore, based on its capability to accommodate different biasing circuitry (i.e. different bond-pad and stabilising network configurations), the described procedure is applicable to external stabilised devices. As such, the de-embedding method is not restricted by device sizing, which is known to play a key role in the RTD stability.

The performance of the proposed methodology was assessed in the characterisation of an externally stabilised (by a shunt resistor network), large active area RTD (100 μm^2), through S-parameter measurements up to 110 GHz, which is to date, the highest reported frequency range of a study of this nature [141]. Based on the acquired measurements, an accurate device large-signal model, enabled by a novel proposed quasi-analytical equivalent circuit parameter extraction methodology was created.

Furthermore, the relatively large measurement span enabled the investigation of the RTD device behaviour throughout the complete bias range using a physics based equivalent circuit model [142], which confirmed the theoretical prediction regarding the frequency independent nature of the intrinsic parameters. These findings play a key role in the validation and establishment of a universal equivalent RTD model and confirms its expected usability in predicting the device behaviour in THz range.

Finally, the developed device non-linear model, based on the presented characterisation study was validated in the context of designing, simulating and realising a high sensitivity RTD-based detector, operating in the 26.5 GHz – 84 GHz frequency range, which demonstrates the applicability of the systematic characterisation approach.

1.4.3 Thesis organisation

The thesis is structured as follows: Chapter 1 presents an introduction to THz radiation technology and its research evolution, in relation to its potential scientific and industrial applications. A review of various generation and detection techniques is given from the perspective of employed devices.

In Chapter 2 the fundamental operating principles of RTDs are presented, together with the general device epitaxial structure and common employed material systems. A review of the evolution and state of the art RTD high-frequency equivalent circuit models is discussed.

Chapter 3 introduces the main fabrication process involved in the realization of RTD devices and circuits in MMIC technology. The various stage processing techniques including photolithography, dry/wet etching, metallization, lift-off and via opening through polyimide are presented.

Chapter 4 presents the realisation (design and fabrication) and characterisation of various components required for the realisation of RTD integrated circuits, such as coplanar-waveguide (CPW) transmission lines, metal-insulator-metal (MIM) capacitors, and thin-film resistors. An InP-based PIN diode epitaxial structure, suitable for monolithic integration with the RTD structure is proposed and investigated for potential high-frequency switching applications.

Chapter 5 discusses the associated RTD parasitic oscillations and their impact on the DC *I-V* characteristics, together with common device stabilisation methods. A novel, on-wafer de-embedding technique is presented for accurate high-frequency device characterisation and demonstrated using S-parameter measurements up to 110 GHz. Furthermore, based on the de-embedded data, a novel quasi-analytical extraction procedure for the device small-signal equivalent circuit parameters is proposed and validated using experimental and theoretical determined parameters.

In Chapter 6, the detection capabilities of an RTD operating in the square-law regime are investigated. An RTD large-signal model is developed based on the device DC and high-frequency behaviour and is used in the design of an RTD detector operating in a direct detection scheme. The detector simulations are validated experimentally using

an RTD-based transmitter in a data transfer experiment in the W-band (with waveguide connections) and in the Ka-band (wireless data-link over 15 cm), with achieved error-free transmission bit-rates (BER $<10^{-10}$) of 4 Gbps and 2.4 Gbps respectively for an on-off keying (OOK) modulation scheme. Lastly, from a sensitivity analysis in the Ka-band, a comparison of the responsivity between the realised RTD detector (peak corrected responsivity of 13.38 kV/W) and commercially available SBD detectors is shown.

Finally, the conclusions and future work are covered in Chapter 7.

1.5 References

[1] A. Rostami, H. Rasooli, and H. Baghban, "An overview of the technological and scientific achievements of the terahertz," in *Terahertz Technology: Fundamentals and Applications*. Berlin, Heidelberg: Springer Berlin Heidelberg, pp. 1-89, 2011.

[2] P. L. Richards, "Bolometers for infrared and millimeter waves," *Journal of Applied Physics,* vol. 76, no. 1, pp. 1-24, 1994.

[3] J. Chamberlain, "Where optics meets electronics: recent progress in decreasing the terahertz gap: one contribution of 16 to a discussion meeting 'The terahertz gap: the generation of far-infrared radiation and its applications'," *Philosophical Transactions of The Royal Society B: Biological Sciences,* vol. 362, pp. 199-213, 2004.

[4] G. Chattopadhyay, "Sensor technology at submillimeter wavelengths for space applications," 2007.

[5] J.-M. Lamarre, F.-X. Désert, and T. Kirchner, "Background limited infrared and submillimeter instruments," *Space Science Reviews,* vol. 74, no. 1-2, pp. 27-36, 1995.

[6] P. H. Siegel, "Terahertz technology," *IEEE Transactions on Microwave Theory and Techniques,* vol. 50, no. 3, pp. 910-928, 2002.

[7] E. F. Nichols and J. D. Tear, "Joining the infra-red and electric wave spectra," *The Astrophysical Journal,* vol. 61, p. 17, 1925.

[8] P. H. Siegel, "Terahertz technology in biology and medicine," *IEEE Transactions on Microwave Theory and Techniques,* vol. 52, no. 10, pp. 2438-2447, 2004.

[9] J. C. Quintanilla, "Water, vibrational and rotational transitions," in *Encyclopedia of Astrobiology*. Berlin, Heidelberg: Springer Berlin Heidelberg, pp. 2647-2650, 2015.

[10] E. Bründermann, H.-W. Hübers, and M. F. Kimmitt, "Introduction," in *Terahertz Techniques*. Berlin, Heidelberg: Springer Berlin Heidelberg, pp. 1-22, 2012.

[11] P. Smulders, "The road to 100 Gb/s wireless and beyond: basic issues and key directions," *IEEE Communications Magazine,* vol. 51, no. 12, pp. 86-91, 2013.

[12] P. Sowa, J. Rutkowska-Talipska, U. Sulkowska, K. Rutkowski, and R. Rutkowski, "Ionizing and non-ionizing electromagnetic radiation in modern medicine," *Polish Annals of Medicine,* vol. 19, pp. 134–138, 2012.

[13] G. Pastorelli, T. Trafela, P. F. Taday, A. Portieri, D. Lowe, K. Fukunaga, and M. Strlič, "Characterisation of historic plastics using terahertz time-domain spectroscopy and pulsed imaging," *Analytical and Bioanalytical Chemistry,* vol. 403, no. 5, pp. 1405-1414, 2012.

[14] J. Bjarnason, T. Chan, A. Lee, M. Celis, and E. Brown, "Millimeter-wave, terahertz, and mid-infrared transmissionthrough common clothing," *Applied Physics Letters,* vol. 85, no. 4, pp. 519-521, 2004.

[15] P. Zolliker, M. Rüggeberg, L. Valzania, and E. Hack, "Extracting wood properties from structured THz spectra: birefringence and water content," *IEEE Transactions on Terahertz Science and Technology,* vol. 7, no. 6, pp. 722-731, 2017.

[16] M. Peccianti, R. Fastampa, A. M. Conte, O. Pulci, C. Violante, J. Łojewska, M. Clerici, R. Morandotti, and M. Missori, "Terahertz absorption by cellulose: Application to ancient paper artifacts," *Physical Review Applied,* vol. 7, no. 6, p. 064019, 2017.

[17] W. L. Chan, J. Deibel, and D. M. Mittleman, "Imaging with terahertz radiation," *Reports on Progress in Physics,* vol. 70, no. 8, p. 1325, 2007.

[18] A. Crocker, H. Gebbie, M. Kimmitt, and L. Mathias, "Stimulated emission in the far infra-red," *Nature,* vol. 201, no. 4916, pp. 250-251, 1964.

[19] T. Chang and T. Bridges, "Laser action at 452, 496, and 541 μm in optically pumped CH_3F," *Optics Communications,* vol. 1, no. 9, pp. 423-426, 1970.

[20] P. Guenard, O. Doehler, B. Epsztein, and R. Warnecke, "New UHF tubes with wide electronic tuning. range," *CR Acad. Sci.(Paris),* vol. 235, p. 235, 1952.

[21] E. Putley, "Impurity photoconductivity in n-type InSb," *Journal of Physics and Chemistry of Solids,* vol. 22, pp. 241-247, 1961.

[22] F. J. Low, "Low-temperature germanium bolometer," *JOSA,* vol. 51, no. 11, pp. 1300-1304, 1961.

[23] M. Brown and M. Kimmitt, "Far-infrared resonant photoconductivity in indium antimonide," *Infrared Physics,* vol. 5, no. 2, pp. 93-97, 1965.

[24] D. Grischkowsky, S. Keiding, M. Van Exter, and C. Fattinger, "Far-infrared time-domain spectroscopy with terahertz beams of dielectrics and semiconductors," *JOSA B,* vol. 7, no. 10, pp. 2006-2015, 1990.

[25] B. B. Hu and M. C. Nuss, "Imaging with terahertz waves," *Opt. Lett.,* vol. 20, no. 16, pp. 1716-1718, 1995.

[26] R. M. Woodward, V. P. Wallace, R. J. Pye, B. E. Cole, D. D. Arnone, E. H. Linfield, and M. Pepper, "Terahertz pulse imaging of ex vivo basal cell carcinoma," *Journal of Investigative Dermatology,* vol. 120, no. 1, pp. 72-78, 2003.

[27] H.-B. Liu, H. Zhong, N. Karpowicz, Y. Chen, and X.-C. Zhang, "Terahertz spectroscopy and imaging for defense and security applications," *Proceedings of the IEEE,* vol. 95, no. 8, pp. 1514-1527, 2007.

[28] K. Ajito, "Terahertz spectroscopy for pharmaceutical and biomedical applications," *IEEE Transactions on Terahertz Science and Technology,* vol. 5, no. 6, pp. 1140-1145, 2015.

[29] M. Tsurkan, N. Balbekin, E. Sobakinskaya, A. Panin, and V. Vaks, "Terahertz spectroscopy of DNA," *Optics and Spectroscopy,* vol. 114, no. 6, pp. 894-898, 2013.

[30] G. E. Tsydynzhapov, P. A. Gusikhin, V. M. Muravev, I. V. Andreev, and I. V. Kukushkin, "New terahertz security body scanner," in *2018 43rd International Conference on Infrared, Millimeter, and Terahertz Waves (IRMMW-THz)*: IEEE, pp. 1-1, 2018.

[31] J. A. Zeitler and Y.-C. Shen, "Industrial applications of terahertz imaging," in *Terahertz Spectroscopy and Imaging*: Springer, pp. 451-489, 2012.

[32] T. Nagatsuma, G. Ducournau, and C. C. Renaud, "Advances in terahertz communications accelerated by photonics," *Nature Photonics,* vol. 10, no. 6, pp. 371-379, 2016.

[33] T. Kleine-Ostmann, K. Pierz, G. Hein, P. Dawson, and M. Koch, "Audio signal transmission over THz communication channel using semiconductor modulator," *Electronics Letters,* vol. 40, no. 2, pp. 124-126, 2004.

[34] T. Liu, G.-R. Lin, Y.-C. Chang, and C. Pan, "Wireless audio and burst communication link with directly modulated THz photoconductive antenna," *Optics Express,* vol. 13 25, pp. 10416-23, 2005.

[35] T. Nagatsuma, A. Hirata, Y. Royter, M. Shinagawa, T. Furuta, T. Ishibashi, and H. Ito, "A 120-GHz integrated photonic transmitter," in *International Topical Meeting on Microwave Photonics MWP 2000 (Cat. No.00EX430)*, pp. 225-228, 11-13 Sept. 2000, 2000.

[36] A. Hirata, T. Kosugi, H. Takahashi, J. Takeuchi, H. Togo, M. Yaita, N. Kukutsu, K. Aihara, K. Murata, Y. Sato, T. Nagatsuma, and Y. Kado, "120-GHz-Band Wireless Link Technologies for Outdoor 10-Gbit/s Data Transmission," *IEEE Transactions on Microwave Theory and Techniques,* vol. 60, no. 3, pp. 881-895, 2012.

[37] T. Kürner and S. Priebe, "Towards THz communications - status in research, standardization and regulation," *Journal of Infrared, Millimeter, and Terahertz Waves,* vol. 35, no. 1, pp. 53-62, 2014.

[38] S. L. Dexheimer, *Terahertz spectroscopy: principles and applications*. CRC press, 2017.

[39] J.-F. Roux, F. Garet, and J.-L. Coutaz, "Principles and applications of THz time domain spectroscopy," in *Physics and Applications of Terahertz Radiation*. Dordrecht: Springer Netherlands, pp. 203-231, 2014.

[40] R. M. Dreizler and E. K. Gross, *Density functional theory: an approach to the quantum many-body problem*. Springer Science & Business Media, 2012.

[41] Y. Chen, H. Liu, Y. Deng, D. Schauki, M. J. Fitch, R. Osiander, C. Dodson, J. B. Spicer, M. Shur, and X.-C. Zhang, "THz spectroscopic investigation of 2, 4-dinitrotoluene," *Chemical Physics Letters,* vol. 400, no. 4-6, pp. 357-361, 2004.

[42] T. He and J. L. Shen, "Applications of terahertz spectroscopy in illicit drugs detection," *Guang Pu Xue Yu Guang Pu Fen Xi,* vol. 33, no. 9, pp. 2348-53, 2013.

[43] W. Liu, J. Li, and W. Yang, "Detection and identification of explosives and illicit drugs by terahertz spectroscopy technology," in *2010 IEEE International Geoscience and Remote Sensing Symposium*, pp. 3576-3579, 25-30 July 2010, 2010.

[44] M. Naftaly, N. Vieweg, and A. Deninger, "Industrial applications of terahertz sensing: State of play," *Sensors,* vol. 19, no. 19, p. 4203, 2019.

[45] S. Wietzke, C. Jördens, N. Krumbholz, B. Baudrit, M. Bastian, and M. Koch, "Terahertz imaging: a new non-destructive technique for the quality control of plastic weld joints," *Journal of the European Optical Society-Rapid Publications,* vol. 2, 2007.

[46] S. Wietzke, C. Jansen, F. Rutz, D. Mittleman, and M. Koch, "Determination of additive content in polymeric compounds with terahertz time-domain spectroscopy," *Polymer Testing,* vol. 26, no. 5, pp. 614-618, 2007.

[47] M. Werner, C. Kolb, G. Schober, and S. Kremling, "Charakterisierung von polymerschäumen mittels zeitaufgelöster terahertz-spektroskopie," *DGZFP-Jahrestagung: Berlin, Germany,* 2017.

[48] E. Stübling, L. Gomell, S. Sommer, A. Winkel, M. Kahlmeyer, S. Böhm, and M. Koch, "THz properties of adhesives," *Journal of Infrared, Millimeter, and Terahertz Waves,* vol. 39, no. 6, pp. 586-593, 2018.

[49] T. Yasui, T. Yasuda, K.-i. Sawanaka, and T. Araki, "Terahertz paintmeter for noncontact monitoring of thickness and drying progress in paint film," *Applied Optics,* vol. 44, no. 32, pp. 6849-6856, 2005.

[50] M. Nagel, A. Michalski, and H. Kurz, "Contact-free fault location and imaging with on-chip terahertz time-domain reflectometry," *Optics Express,* vol. 19, no. 13, pp. 12509-12514, 2011.

[51] G. Sharma, L. Razzari, F. H. Su, F. Blanchard, A. Ayesheshim, T. L. Cocker, L. Titova, H. C. Bandulet, T. Ozaki, j. c. Kieffer, R. Morandotti, M. Reid, and F. Hegmann, "Time-resolved terahertz spectroscopy of free carrier nonlinear dynamics in semiconductors," *Photonics Journal, IEEE,* vol. 2, pp. 578-592, 2010.

[52] E. Arik, H. Altan, and O. Esenturk, "Dielectric properties of diesel and gasoline by terahertz spectroscopy," *Journal of Infrared, Millimeter, and Terahertz Waves,* vol. 35, no. 9, pp. 759-769, 2014.

[53] S. Gorenflo, U. Tauer, I. Hinkov, A. Lambrecht, R. Buchner, and H. Helm, "Dielectric properties of oil–water complexes using terahertz transmission spectroscopy," *Chemical Physics Letters,* vol. 421, no. 4-6, pp. 494-498, 2006.

[54] V. A. Trofimov and S. A. Varentsova, "High effective time-dependent THz spectroscopy method for the detection and identification of substances with inhomogeneous surface," *PloS One,* vol. 13, no. 8, p. e0201297, 2018.

[55] S. H. Baek, H. B. Lim, and H. S. Chun, "Detection of melamine in foods using terahertz time-domain spectroscopy," *Journal of Agricultural and Food Chemistry,* vol. 62, no. 24, pp. 5403-5407, 2014.

[56] D. Zimdars, J. White, G. Stuk, G. Sucha, G. Fichter, and S. Williamson, "Time domain terahertz imaging of threats in luggage and personnel," *International*

Journal of High Speed Electronics and Systems, vol. 17, no. 02, pp. 271-281, 2007.

[57] R. Knipper, A. Brahm, E. Heinz, T. May, G. Notni, H. Meyer, A. Tünnermann, and J. Popp, "THz absorption in fabric and its impact on body scanning for security application," *IEEE Transactions on Terahertz Science and Technology,* vol. 5, no. 6, pp. 999-1004, 2015.

[58] J.-H. Son, S. J. Oh, and H. Cheon, "Potential clinical applications of terahertz radiation," *Journal of Applied Physics,* vol. 125, no. 19, p. 190901, 2019.

[59] O. M. Koriech, "Breast cancer and early detection," *J Family Community Med,* vol. 3, no. 1, pp. 7-9, 1996.

[60] A. Postnikov, K. Moldosanov, N. Kairyev, and V. Lelevkin, "A device to inspect a skin cancer tumour in the terahertz range, transferring the image into the infrared," in *EPJ Web of Conferences*, vol. 195: EDP Sciences, p. 10010, 2018.

[61] M. Danciu, T. Alexa-Stratulat, C. Stefanescu, G. Dodi, B. I. Tamba, C. T. Mihai, G. D. Stanciu, A. Luca, I. A. Spiridon, L. B. Ungureanu, V. Ianole, I. Ciortescu, C. Mihai, G. Stefanescu, I. Chirilă, R. Ciobanu, and V. L. Drug, "Terahertz spectroscopy and imaging: a cutting-edge method for diagnosing digestive cancers," (in eng), *Materials (Basel),* vol. 12, no. 9, p. 1519, 2019.

[62] C. Longbottom, D. A. Crawley, B. E. Cole, D. D. Arnone, V. P. Wallace, and M. Pepper, "Potential uses of terahertz pulse imaging in dentistry: caries and erosion detection," in *Lasers in Dentistry VIII*, vol. 4610: International Society for Optics and Photonics, pp. 109-112, 2002.

[63] K. Kamburoğlu, B. Karagöz, H. Altan, and D. Özen, "An ex vivo comparative study of occlusal and proximal caries using terahertz and X-ray imaging," *Dentomaxillofac Radiol,* vol. 48, no. 2, pp. 20180250-20180250, 2019.

[64] C. L. Koch-Dandolo, T. Filtenborg, K. Fukunaga, J. Skou-Hansen, and P. U. Jepsen, "Reflection terahertz time-domain imaging for analysis of an 18th

century neoclassical easel painting," *Applied Optics,* vol. 54, no. 16, pp. 5123-5129, 2015.

[65] S. Cherry, "Edholm's law of bandwidth," *IEEE Spectrum,* vol. 41, no. 7, pp. 58-60, 2004.

[66] F. De Rango, M. Tropea, and P. Fazio, "Multimedia traffic over wireless and satellite networks," in *Digital Video*: IntechOpen, 2010.

[67] Cisco. "Cisco annual internet report (2018–2023) white paper." https://www.cisco.com/c/en/us/solutions/collateral/executive-perspectives/annual-internet-report/white-paper-c11-741490.html (accessed 08.09.2020).

[68] L. Atzori, A. Iera, and G. Morabito, "The internet of things: A survey," *Computer Networks,* vol. 54, no. 15, pp. 2787-2805, 2010.

[69] Y. Niu, Y. Li, D. Jin, L. Su, and A. V. Vasilakos, "A survey of millimeter wave communications (mmWave) for 5G: opportunities and challenges," *Wireless Networks,* vol. 21, no. 8, pp. 2657-2676, 2015.

[70] T. S. Rappaport, Y. Xing, O. Kanhere, S. Ju, A. Madanayake, S. Mandal, A. Alkhateeb, and G. C. Trichopoulos, "Wireless communications and applications above 100 GHz: Opportunities and challenges for 6G and beyond," *IEEE Access,* vol. 7, pp. 78729-78757, 2019.

[71] Z. Zhang, Y. Xiao, Z. Ma, M. Xiao, Z. Ding, X. Lei, G. K. Karagiannidis, and P. Fan, "6G wireless networks: Vision, requirements, architecture, and key technologies," *IEEE Vehicular Technology Magazine,* vol. 14, no. 3, pp. 28-41, 2019.

[72] P. Yang, Y. Xiao, M. Xiao, and S. Li, "6G wireless communications: Vision and potential techniques," *IEEE Network,* vol. 33, no. 4, pp. 70-75, 2019.

[73] A. Kanno, P. Dat, N. Sekine, I. Hosako, T. Kawanishi, Y. Yoshida, and K. Kitayama, "High-speed coherent transmission using advanced photonics in terahertz bands," *IEICE Trans. Electron.,* vol. 98-C, pp. 1071-1080, 2015.

[74] J. Bartelt, P. Rost, D. Wubben, J. Lessmann, B. Melis, and G. Fettweis, "Fronthaul and backhaul requirements of flexibly centralized radio access networks," *IEEE Wireless Communications,* vol. 22, no. 5, pp. 105-111, 2015.

[75] L. Kuger, A. Ichkov, P. Mähönen, and L. Simić, "Urban outdoor measurement study of phased antenna array impact on millimeter-wave link opportunities and beam misalignment," *arXiv preprint arXiv:1909.12024,* 2019.

[76] A. S. Cacciapuoti, R. Subramanian, K. R. Chowdhury, and M. Caleffi, "Software-defined network controlled switching between millimeter wave and terahertz small cells," *arXiv preprint arXiv:1702.02775,* 2017.

[77] C. Zhang, K. Ota, J. Jia, and M. Dong, "Breaking the blockage for big data transmission: Gigabit road communication in autonomous vehicles," *IEEE Communications Magazine,* vol. 56, no. 6, pp. 152-157, 2018.

[78] S.-W. Dong, Z.-b. Zhu, and Y. Wang, "Advances of terahertz research and terahertz satellite communications," in *2011 International Conference on Electronics, Communications and Control (ICECC)*: IEEE, pp. 4122-4125, 2011.

[79] S. Ergun and S. Sonmez, "Terahertz technology for military applications," *Journal of Management and Information Science,* vol. 3, no. 1, pp. 13-16, 2015.

[80] B. Peng and T. Kürner, "A stochastic channel model for future wireless THz data centers," in *2015 International Symposium on Wireless Communication Systems (ISWCS)*, pp. 741-745, 25-28 Aug. 2015, 2015.

[81] M. F. Bari, R. Boutaba, R. Esteves, L. Z. Granville, M. Podlesny, M. G. Rabbani, Q. Zhang, and M. F. Zhani, "Data center network virtualization: A survey," *IEEE communications surveys & tutorials,* vol. 15, no. 2, pp. 909-928, 2012.

[82] K. Wu, J. Xiao, and L. M. Ni, "Rethinking the architecture design of data center networks," *Frontiers of Computer Science,* vol. 6, no. 5, pp. 596-603, 2012.

[83] H.-J. Song and T. Nagatsuma, *Handbook of terahertz technologies: devices and applications*. CRC press, 2015.

[84] R. A. Lewis, "A review of terahertz sources," *Journal of Physics D: Applied Physics,* vol. 47, no. 37, p. 374001, 2014.

[85] G. P. Gallerano and S. Biedron, "Overview of terahertz radiation sources," in *Proceedings of the 2004 FEL Conference*, vol. 1, pp. 216-221, 2004.

[86] S. Hooker and C. Webb, *Laser Physics*. OUP Oxford, 2010.

[87] B. S. Williams, "Terahertz quantum-cascade lasers," *Nature Photonics,* vol. 1, no. 9, pp. 517-525, 2007.

[88] C. Walther, M. Fischer, G. Scalari, R. Terazzi, N. Hoyler, and J. Faist, "Quantum cascade lasers operating from 1.2 to 1.6 THz," *Applied Physics Letters,* vol. 91, no. 13, p. 131122, 2007.

[89] H. W. Hübers, S. G. Pavlov, and V. N. Shastin, "Terahertz lasers based on germanium and silicon," *Semiconductor Science and Technology,* vol. 20, no. 7, pp. S211-S221, 2005.

[90] B. Salem, D. Morris, V. Aimez, J. Beerens, J. Beauvais, and D. Houde, "Pulsed photoconductive antenna terahertz sources made on ion-implanted GaAs substrates," *Journal of Physics: Condensed Matter,* vol. 17, no. 46, pp. 7327-7333, 2005.

[91] R. Safian, G. Ghazi, and N. Mohammadian, "Review of photomixing continuous-wave terahertz systems and current application trends in terahertz domain," *Optical Engineering,* vol. 58, no. 11, p. 110901, 2019.

[92] I. Stavros, "Terahertz sources," in *Microwave Photonics: Devices and Applications*: IEEE, pp. 111-129, 2004.

[93] C. C. Renaud, M. Natrella, C. Graham, J. Seddon, F. V. Dijk, and A. J. Seeds, "Antenna integrated THz uni-traveling carrier photodiodes," *IEEE Journal of Selected Topics in Quantum Electronics,* vol. 24, no. 2, pp. 1-11, 2018.

[94] T. Crowe, R. Mattauch, H. P. Roser, W. L. Bishop, W. Peatman, and X. L. Liu, "GaAs schottky diodes for THz mixing applications," *Proceedings of the IEEE,* vol. 80, pp. 1827-1841, 1992.

[95] E. F. Plinski, "Terahertz photomixer," *Bulletin of the Polish Academy of Sciences, Technical Sciences,* vol. 58, p. 463, 2010.

[96] M. R. Stone, M. Naftaly, R. E. Miles, I. C. Mayorga, A. Malcoci, and M. Mikulics, "Generation of continuous-wave terahertz radiation using a two-mode titanium sapphire laser containing an intracavity Fabry–Perot etalon," *Journal of Applied Physics,* vol. 97, no. 10, p. 103108, 2005.

[97] M. Tang, H. Minamide, Y. Wang, T. Notake, S. Ohno, and H. Ito, "Tunable terahertz-wave generation from DAST crystal pumped by a monolithic dual-wavelength fiber laser," *Optics Express,* vol. 19, no. 2, pp. 779-786, 2011.

[98] K. Suto, T. Sasaki, T. Tanabe, K. Saito, J.-i. Nishizawa, and M. Ito, "GaP THz wave generator and THz spectrometer using Cr:Forsterite lasers," *Review of Scientific Instruments,* vol. 76, no. 12, p. 123109, 2005.

[99] T. Taniuchi, S. Okada, and H. Nakanishi, "Widely tunable terahertz-wave generation in an organic crystal and its spectroscopic application," *Journal of Applied Physics,* vol. 95, no. 11, pp. 5984-5988, 2004.

[100] H. Song, K. Ajito, Y. Muramoto, A. Wakatsuki, T. Nagatsuma, and N. Kukutsu, "Uni-travelling-carrier photodiode module generating 300 GHz power greater than 1 mW," *IEEE Microwave and Wireless Components Letters,* vol. 22, no. 7, pp. 363-365, 2012.

[101] N. Pala and A. N. Abbas, "Terahertz technology for nano applications," in *Encyclopedia of Nanotechnology*, B. Bhushan Ed. Dordrecht: Springer Netherlands, pp. 4070-4085, 2016.

[102] D. Dragoman and M. Dragoman, "Terahertz fields and applications," *Progress in Quantum Electronics,* vol. 28, no. 1, pp. 1-66, 2004.

[103] R. Miles, P. Harrison, and D. Lippens, *Terahertz sources and systems*. Springer Science & Business Media, 2001.

[104] J. Stake, T. Bryllert, T. A. Emadi, and J. Vukusic, "Terahertz generation by multiplication," Dordrecht: Springer Netherlands, in Terahertz Frequency Detection and Identification of Materials and Objects, pp. 17-30, 2007.

[105] F. Maiwald, S. Martin, J. Bruston, A. Maestrini, T. Crawford, and P. H. Siegel, "2.7 THz waveguide tripler using monolithic membrane diodes," in *2001 IEEE MTT-S International Microwave Sympsoium Digest (Cat. No.01CH37157)*, vol. 3, pp. 1637-1640 vol.3, 20-24 May 2001, 2001.

[106] A. Maestrini, I. Mehdi, J. V. Siles, J. S. Ward, R. Lin, B. Thomas, C. Lee, J. Gill, G. Chattopadhyay, and E. Schlecht, "Design and characterization of a room temperature all-solid-state electronic source tunable from 2.48 to 2.75 THz," *IEEE Transactions on Terahertz Science and Technology,* vol. 2, no. 2, pp. 177-185, 2012.

[107] R. Mohapatra and P. Dutta, "Improvement of transconductance and cut-off frequency in $In_{0.1}Ga_{0.9}N$ back-barrier-based double-channel $Al_{0.3}Ga_{0.7}N$ / GaN high etor by enhancing the drain source contact length ratio," *Pramana,* vol. 94, no. 1, p. 5, 2020.

[108] J. C. Rode, H.-W. Chiang, P. Choudhary, V. Jain, B. J. Thibeault, W. J. Mitchell, M. J. Rodwell, M. Urteaga, D. Loubychev, and A. Snyder, "Indium phosphide heterobipolar transistor technology beyond 1-THz bandwidth," *IEEE Transactions on Electron Devices,* vol. 62, no. 9, pp. 2779-2785, 2015.

[109] X. Mei, W. Yoshida, M. Lange, J. Lee, J. Zhou, P.-H. Liu, K. Leong, A. Zamora, J. Padilla, and S. Sarkozy, "First demonstration of amplification at 1 THz using 25-nm InP high electron mobility transistor process," *IEEE Electron Device Letters,* vol. 36, no. 4, pp. 327-329, 2015.

[110] G. I. Haddad, J. R. East, and H. Eisele, "Two-terminal active devices for terahertz sources," *International Journal of High Speed Electronics and Systems,* vol. 13, no. 02, pp. 395-427, 2003.

[111] V. Antti and A. Lehto, *Radio engineering for wireless communication and sensor applications*. Artech house, 2003.

[112] A. S. Hajo, O. Yilmazoglu, A. Dadgar, F. Küppers, and T. Kusserow, "Reliable GaN-based THz Gunn diodes with side-contact and field-plate technologies," *IEEE Access,* vol. 8, pp. 84116-84122, 2020.

[113] M. Wollitzer, J. Buechler, F. Schaffler, and J.-F. Luy, "D-band Si-IMPATT diodes with 300 mW CW output power at 140 GHz," *Electronics Letters,* vol. 32, no. 2, pp. 122-123, 1996.

[114] J. Nishizawa, P. Płotka, T. Kurabayashi, and H. Makabe, "706-GHz GaAs CW fundamental-mode TUNNETT diodes fabricated with molecular layer epitaxy," *Physica Status Solidi C,* vol. 5, no. 9, pp. 2802-2804, 2008.

[115] H. Mizuta and T. Tanoue, *The physics and applications of resonant tunnelling diodes*. Cambridge university press, 2006.

[116] J. P. Sun, G. I. Haddad, P. Mazumder, and J. N. Schulman, "Resonant tunneling diodes: Models and properties," *Proceedings of the IEEE,* vol. 86, no. 4, pp. 641-660, 1998.

[117] J. Darmo, D. Dietze, M. Martl, and K. Unterrainer, "Nonorthodox heterodyne electro-optic detection for terahertz optical systems," *Applied Physics Letters,* vol. 98, no. 16, p. 161112, 2011.

[118] T. W. Crowe, R. J. Mattauch, H. Roser, W. L. Bishop, W. C. Peatman, and X. Liu, "GaAs schottky diodes for THz mixing applications," *Proceedings of the IEEE,* vol. 80, no. 11, pp. 1827-1841, 1992.

[119] J. Zmuidzinas and P. L. Richards, "Superconducting detectors and mixers for millimeter and submillimeter astrophysics," *Proceedings of the IEEE,* vol. 92, no. 10, pp. 1597-1616, 2004.

[120] G. Chattopadhyay, "Future of heterodyne receivers at submillimeter wavelengths," in *2005 Joint 30th International Conference on Infrared and*

Millimeter Waves and 13th International Conference on Terahertz Electronics, vol. 2: IEEE, pp. 461-462, 2005.

[121] A. Rogalski, "Terahertz detectors," *Encyclopedia of Modern Optics,* p. 418, 2018.

[122] S. Cherednichenko, A. Hammar, S. Bevilacqua, V. Drakinskiy, J. Stake, and A. Kalabukhov, "A room temperature bolometer for terahertz coherent and incoherent detection," *IEEE Transactions on Terahertz Science and Technology,* vol. 1, no. 2, pp. 395-402, 2011.

[123] L. Fernandes, P. Kaufmann, R. Marcon, A. Kudaka, A. Marun, R. Godoy, E. Bortolucci, M. B. Zakia, and J. Diniz, "Photometry of THz radiation using Golay cell detector," in *2011 XXXth URSI General Assembly and Scientific Symposium*: IEEE, pp. 1-4, 2011.

[124] H. Zhong, N. Karpowicz, J. Xu, Y. Deng, W. Ussery, M. Shur, and X.-C. Zhang, "Detection of space shuttle insulation foam defects by using a 0.2 THz Gunn diode oscillator and pyroelectric detector," in *Frontiers in Optics*: Optical Society of America, p. FTuG28, 2004.

[125] F. Voltolina, A. Tredicucci, and P. H. Bolivar, "Low cost thermopile detectors for THz imaging and sensing," in *2008 33rd International Conference on Infrared, Millimeter and Terahertz Waves*: IEEE, pp. 1-2, 2008.

[126] R. Su, Y. Zhang, X. Tu, X. Jia, L. Kang, W. Xu, J. Chen, and P. Wu, "Terahertz direct detectors based on superconducting hot electron bolometers with different biasing methods," *IEEE Transactions on Applied Superconductivity,* vol. PP, pp. 1-1, 2019.

[127] R. A. Lewis, "A review of terahertz detectors," *Journal of Physics D: Applied Physics,* vol. 52, no. 43, p. 433001, 2019.

[128] Y. M. Meziani, M. Hanabe, A. Koizumi, T. Otsuji, and E. Sano, "Self oscillation of the plasma waves in a dual grating gates HEMT device," in *2007 IEEE 19th International Conference on Indium Phosphide & Related Materials*, pp. 534-537, 14-18 May 2007, 2007.

[129] Y. Pan, P. Zhang, Y. Chen, H. Wang, K. Wang, Z. Wang, Z. Lu, H. Gong, Z. Duan, and Y. Gong, "The interaction between two-dimensional electron gas and terahertz plasma wave in HEMT-like structure," in *2019 44th International Conference on Infrared, Millimeter, and Terahertz Waves (IRMMW-THz)*, pp. 1-2, 1-6 Sept. 2019, 2019.

[130] H. Hou, Z. Liu, J. Teng, T. Palacios, and S.-J. Chua, "A sub-terahertz broadband detector based on a GaN high-electron-mobility transistor with nanoantennas," *Applied Physics Express,* vol. 10, no. 1, p. 014101, 2016.

[131] D. Voß, W. Zouaghi, M. Jamshidifar, S. Boppel, C. McDonnell, J. R. P. Bain, N. Hempler, G. P. A. Malcolm, G. T. Maker, M. Bauer, A. Lisauskas, A. Rämer, S. A. Shevchenko, W. Heinrich, V. Krozer, and H. G. Roskos, "Imaging and spectroscopic sensing with low-repetition-rate terahertz pulses and GaN TeraFET detectors," *Journal of Infrared, Millimeter, and Terahertz Waves,* vol. 39, no. 3, pp. 262-272, 2018.

[132] H. Levinstein, "Extrinsic detectors," *Applied Optics,* vol. 4, no. 6, pp. 639-647, 1965.

[133] A. Rogalski and F. Sizov, "Terahertz detectors and focal plane arrays," *Opto-Electronics Review,* vol. 19, no. 3, pp. 346-404, 2011.

[134] J. L. Hesler and T. W. Crowe, "NEP and responsivity of THz zero-bias Schottky diode detectors," in *2007 Joint 32nd International Conference on Infrared and Millimeter Waves and the 15th International Conference on Terahertz Electronics*, pp. 844-845, 2-9 Sept. 2007, 2007.

[135] D. Y. Kim and K. O. K, "Reduction of NEP variations for terahertz detectors using Schottky barrier diodes in CMOS," *Electronics Letters,* vol. 53, no. 11, pp. 732-734, 2017.

[136] M. Sakhno, O. Golenkov, and F. Sizov, "Uncooled detector challenges: Millimeter-wave and terahertz long channel field effect transistor and Schottky barrier diode detectors," *Journal of Applied Physics,* vol. 114, pp. 164503-164503, 2013.

[137] D. Pardo, H. Wang, B. Alderman, B. Ellison, P. Huggard, J. Grajal, and H. Sanghera, *InGaAs Schottky technology for THz mixers*. 2017.

[138] W. Wang, Q. Li, N. An, X. Tong, and J. Zeng, "Fabrication and characterization of 8.87 THz schottky barrier mixer diodes for mixer," *AIP Conference Proceedings,* vol. 1955, no. 1, p. 040177, 2018.

[139] V. Bozhkov, "Semiconductor detectors, mixers, and frequency multipliers for the terahertz band," *Radiophysics and Quantum Electronics,* vol. 46, 2003.

[140] Y. Takida, S. Suzuki, M. Asada, and H. Minamide, "Sensitive terahertz-wave detector responses originated by negative differential conductance of resonant-tunneling-diode oscillator," *Applied Physics Letters,* vol. 117, no. 2, p. 021107, 2020.

[141] R. Morariu, J. Wang, A. C. Cornescu, A. Al-Khalidi, A. Ofiare, J. M. L. Figueiredo, and E. Wasige, "Accurate small-signal equivalent circuit modeling of resonant tunneling diodes to 110 GHz," *IEEE Transactions on Microwave Theory and Techniques,* vol. 67, no. 11, pp. 4332-4340, 2019.

[142] Q. Liu, A. Seabaugh, P. Chahal, and F. J. Morris, "Unified AC model for the resonant tunneling diode," *IEEE Transactions on Electron Devices,* vol. 51, no. 5, pp. 653-657, 2004.

Chapter 2. The resonant tunnelling diode

2.1 Theoretical background

From the perspective of classical physics, a particle propagating towards a barrier with a higher potential (U_0) than its kinetic energy ($E < U_0$), will not be able to overcome it, and will thus be reflected at its interface. However, based on the quantum mechanical concept described in 1924 by L. de Broglie, particles when in motion exhibit wave-like properties [1], and thus their behaviour can be described by the time-independent Schrodinger's equation, which for this simple system can be expressed as:

$$-\frac{\hbar^2}{2m^*}\frac{\partial^2}{\partial x^2}\psi(x) + (U_0 - E)\psi(x) = 0 \tag{2.1}$$

where m^* is the electron effective mass, $\hbar$ is the reduced Planck's constant, U_0 is the barrier potential, and $\psi(x)$ represents the particle wavefunction, for which the probability ($P(x)$) of the particle to occur at distance x can be computed as:

$$P(x) = |\psi(x)|^2 \tag{2.2}$$

By satisfying the energy conservation principle, together with the fact that $\psi(x)$ and its derivatives are considered continuous at the barrier boundary, the electron wavefunction is not entirely reflected by the potential barrier, and a fraction penetrates into the 'forbidden' region, where it starts decaying exponentially (Fig. 2.1). For a given barrier width l ($l < \infty$), the function will never reach zero inside the 'forbidden' region, and thus a particle that is initially observed on one side of the barrier, has a finite probability to be found on the opposite side. This quantum mechanical effect is known as tunnelling, and its probability is inversely proportional to the difference between the barrier's potential and particle's energy, and also to the width of the barrier. The particle tunnelling probability, or transmission coefficient $T(E)$, as a function of associated kinetic energy [2], can be approximated by:

$$T(E) = 16\frac{E}{U_0}\left(1 - \frac{E}{U_0}\right)e^{\frac{-2l\sqrt{2m^*(U_0-E)}}{\hbar}}, \qquad for\ T(E) < 1 \tag{2.3}$$

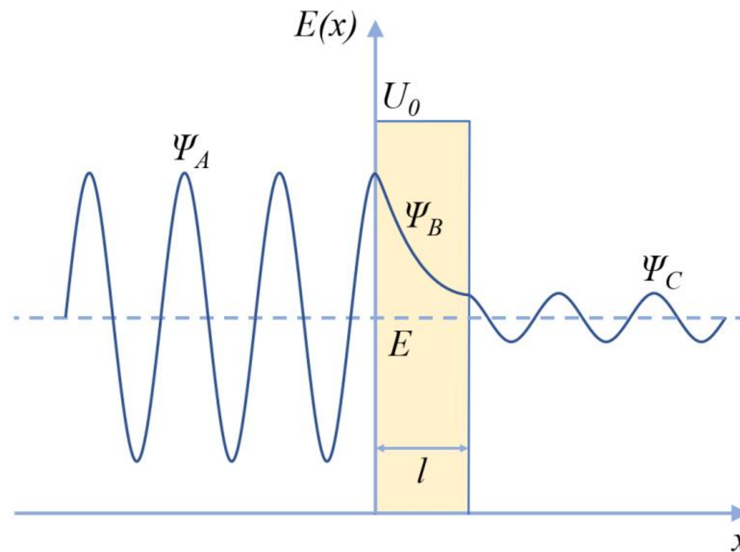

Figure 2.1 Particle wavefunction propagating through a potential barrier.

The general principle of electrons tunnelling in solids, where the potential barriers were created using high doping disparities in p-n junction Ge diodes, was theoretically introduced by L. Esaki in 1958 (Nobel prize laureate in 1973), in order to explain the transport mechanism [3] for the devices he co-invented a year earlier (Esaki tunnel diodes) [4]. Under specific bias conditions in such devices, electrons from the conduction band in the n-doped material are able, with sufficient energy, to tunnel through the barrier to the valence band in the p-doped material (inter-band tunnelling), on the opposite side of the junction [5].

In 1973, Tsu and Esaki reported a variation of this quantum mechanical phenomenon, in the form of resonant tunnelling (intra-band tunnelling), in finite GaAs/AlGaAs and GaAs/AlAs super-lattice heterostructures [6], in which alternating semiconductor materials, with different energy band-gaps are able to create periodic potential barriers (Fig. 2.2).

The concept of electron tunnelling through successive barriers, based on illustration in Fig. 2.3, at a first glance would indicate a decrease in transmission probability, due to the associated decay of the wavefunction amplitude in each individual barrier. However, if the barrier separation is comparable to that of the de Broglie thermal wavelength of the particle (typically <10 nm), a quantum-well (QW) is formed, where the allowed energy states of the carriers (i.e. electrons or holes) become discrete resonant states [7], confining their motion to two dimensions (Fig. 2.3).

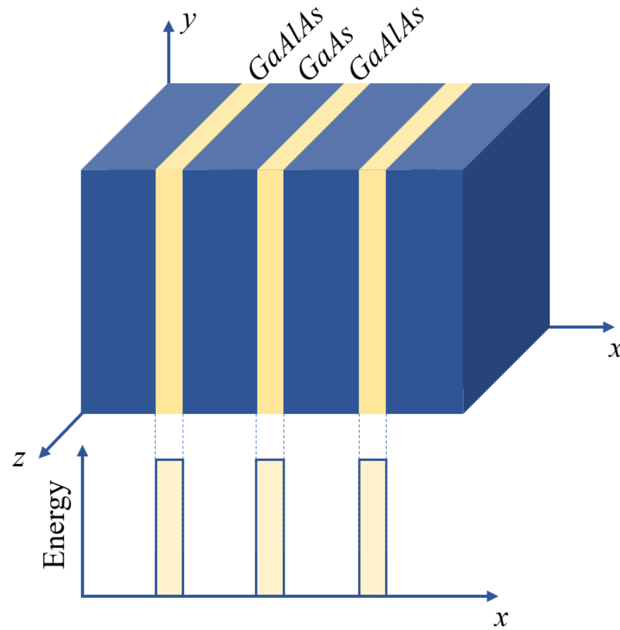

Figure 2.2 GaAlAs/GaAs superlattice with the corresponding conduction band energy profile along the x direction.

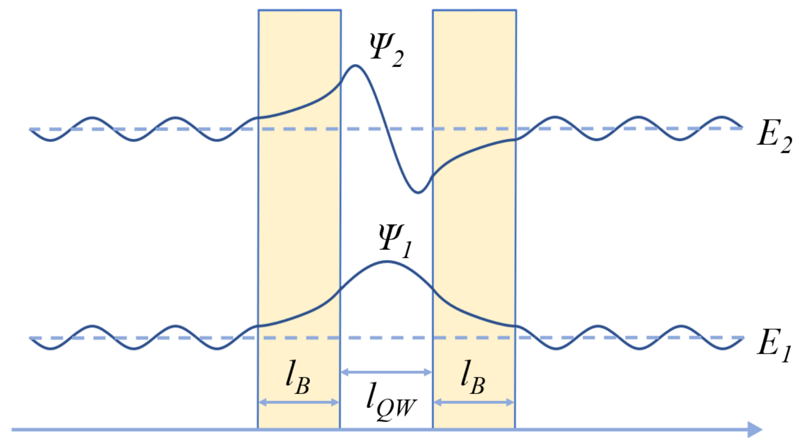

Figure 2.3 Resonant tunnelling through a double barrier quantum-well structure with associated confined state wavefunctions at two discrete energy levels.

The transmission coefficient $T(E)$ for incident wavefunctions, with matching energies to the quasibound states in the QW becomes close to unity for a perfectly symmetrical structure, and thus particles with these specific associated energy levels will tunnel through the structure without being reflected [8].

The experimental demonstration of this phenomenon was first reported in 1974 by Chang, Tsu and Esaki for a double barrier GaAs/GaAlAs heterostructure device [9], currently known as resonant tunnelling diode (RTD). This constituted a major

breakthrough in this field as also being the first demonstration of a semiconductor heterojunction to achieve negative differential resistance (NDR) in its current-voltage characteristics at 77 K [9]. The successful validation of the novel high-speed quantum mechanical process has led in the following years to extensive research involving resonant tunnelling devices employing double-barrier (DBQW), triple-barrier quantum well (TBQW) [10] heterostructures, and also multiple coupled quantum well systems [11], primarily in the underlying development of the QCL.

The high-frequency operation of RTDs was investigated by Sollner in 1983 [12], while comparing the current response as a function of applied bias voltage at DC and 2.5 THz respectively, for a GaAs/AlGaAs DBQW hetero-junction. The demonstrated high-speed switching capability, together with the first reported room temperature operation of such devices (within the same publication NDR was achieved at 230 K), opened a new perspective regarding their employability as electronic sources and detectors within the THz range.

2.2 RTD design concept and operating principle

The RTD is unipolar two-terminal device, primarily constructed in a vertical charge transport configuration, on a semi-insulating substrate as shown in Fig. 2.4.

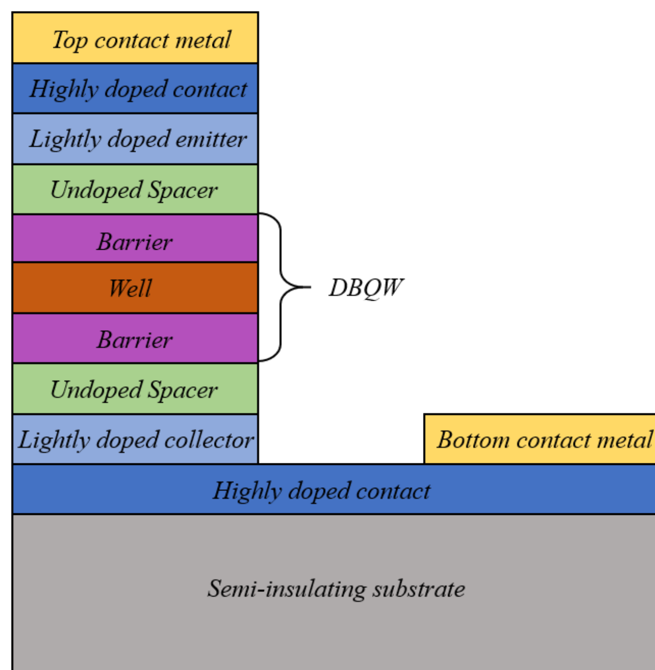

Figure 2.4 Typical RTD layer structure.

The core region within its structure, as previously described, is the DBQW structure, composed of an un-doped narrow band-gap material (QW) sandwiched between two thin wide band-gap layers (barriers). Adjacent to this structure, two un-doped spacer layers are employed, followed by a lightly-doped (n-type) emitter and collector region, in order to source and respectively collect the electrons that tunnel through the QW. The main purpose of the spacer layer included in the design is to avoid any unwanted dopants diffusing into the barriers (from the emitter/collector region) during the wafer material growth. The device is completed by two highly-doped contact layers, on which metal pads are deposited.

The resonant tunnelling mechanism through the DBQW structure in relation to the exhibited DC I-V characteristics of the device [13] can be illustrated using the simplified conduction band potential profile as shown in Fig. 2.5, under different bias (V_b) conditions. In this two-dimensional representation E_C^e, E_C^c, E_F^e, E_F^c denote the emitter and collector conduction band edges and quasi-Fermi levels respectively, while E_1 and E_2 indicate the first and second discrete resonant energy states in the QW.

When no voltage is applied across the region (Fig. 2.5 (a)), the Fermi levels on both sides of the structure are aligned below the first energy level E_1 in the well, and the device is considered in a “steady state”, due to thermal equilibrium. The presence of a small applied bias will shift the conduction band profile downwards (Fig. 2.5 (b)), and as soon as the first resonant state is lowered so that $E_1 = E_F^e$, electrons with sufficient acquired kinetic energy will be able to tunnel from the emitter towards the collector. Neglecting any contribution from thermionic emission components (for $E_1 > E_F^e$), a resonant current begins to flow, marking the onset of the first positive differential resistance (PDR) region. The current flow will continue to increase as E_1 is brought further below E_F^e, reaching a peak value (denoted I_p) when $E_1 = E_C^e$ (Fig. 2.5 (c)), for which the transmission coefficient is unity in the case of a symmetric structure.

Increasing the bias beyond the peak voltage point (V_p) will result in a misalignment between E_1 and E_C^e (Fig. 2.5 (d)), which in turn is translated to a rapid decrease in resonant current, displaying thus an NDR region in the I-V curve. The current will reach a minimum point (I_v), corresponding to the valley voltage (V_v), after which, further increase in applied bias causes a second tunnelling process (when $E_2 = E_F^e$) (Fig. 2.5 (e)). However, at this point the second barrier is shifted below E_F^e, and due to

the high applied field, the rapid increase in current (second PDR region) is primarily due to the thermionic emission of electrons over the first barrier [14].

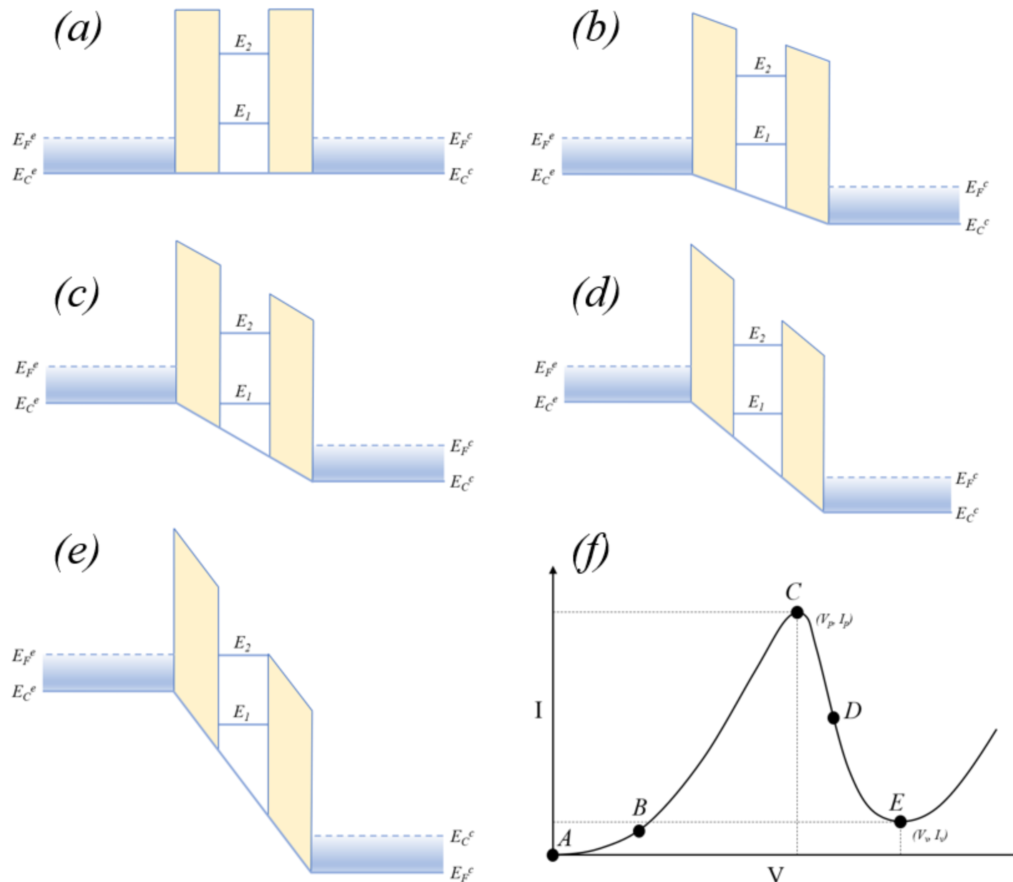

Figure 2.5 Potential profile of an RTD for different bias conditions. (a) At equilibrium (V_b = 0). (b) Start of resonant current flow (V_b > 0) – 1st PDR region. (c) Peak current ($V_b = V_p$) at the alignment between the first resonant level (E_1) and the conduction band edge. (d) Decrease in resonant current ($V_p < V_b < V_v$) due to misalignment between E_1 and the conduction band edge – NDR region. (e) Valley current ($V_b = V_v$), after which the current will begin to increase again with bias, primarily due to thermionic emissions, giving rise to a 2nd PDR region. (f) Corresponding device DC I-V characteristics.

The typical idealised representation of the complete RTD non-linear *I-V* characteristics (resembling a distinct '*N*'-like shape) is presented in Fig. 2.5 (f), from which various parameters can be extracted, in order to assess the device performance and suitability for the intended application. As such, from the perspective of its implementation as a

high-frequency source, the key investigated aspects are related to the NDR region. Among the important quantitative parameters that define this region are the peak-to-valley current ratio ($PVCR = I_p/I_v$) and the peak-to-valley current and voltage difference ($\Delta I = I_p - I_v$ and $\Delta V = V_v - V_p$), which can aid in the estimation of the absolute negative device conductance [15], together with the maximum output power delivered to a load [16]. For this purpose, the typical device *I-V* characteristics within the NDR region (defined between point *C* and *E* in Fig. 2.5 (f)) can be approximated using a cubic polynomial [17]:

$$I(V) = -aV + bV^3 \tag{2.4}$$

In order to derive the values of the device coefficients *a* and *b* using this analysis, the origin of the *I-V* curve is set at the middle of the NDR region (point *D* in Fig. 2.5 (f)). At the peak ($V = V_p$) and valley ($V = V_v$) points in the *I-V* curve the first derivative of the function is zero:

$$\frac{dI(V)}{dV} = -a + 3bV^2 = 0 \tag{2.5}$$

From Eqn. 2.5 the values of the peak and valley bias voltages can be expressed as:

$$\begin{aligned} V_p &= -\sqrt{\frac{a}{3b}} \\ V_v &= \sqrt{\frac{a}{3b}} \end{aligned} \tag{2.6}$$

Similarly, the peak-to-valley current and voltage difference can be derived in terms of the constant device coefficients:

$$\Delta V = V_v - V_p = 2\sqrt{\frac{a}{3b}} \tag{2.7}$$

$$\begin{aligned} \Delta I &= I_p - I_v = -aV_p + bV_p^3 + aV_v - bV_v^3 \\ &= a(V_v - V_p) - b(V_v^3 - V_p^3) = \frac{4a}{3}\sqrt{\frac{a}{3b}} \end{aligned} \tag{2.8}$$

By combining Eqn. 2.7 and Eqn. 2.8, the coefficients *a* and *b* can be expressed in terms of the peak-to-valley current and voltage difference as:

$$a = \frac{3\Delta I}{2\Delta V}$$
$$b = \frac{2\Delta I}{\Delta V^3} \tag{2.9}$$

The device conductance will reach its absolute maximum value at the center of the NDR region ($V = 0$), which can thus be approximated to:

$$|G_{device}| = |-a + 3bV^2| = \frac{3\Delta I}{2\Delta V}, \qquad for\ V = 0 \tag{2.10}$$

Following a similar analysis, the maximum RTD output power delivered to a load can be thus derived as:

$$P_{max} = \frac{G_{device}^2}{6b} = \frac{3}{16}\Delta I\Delta V \tag{2.11}$$

Furthermore, from a detector circuit standpoint, the most attractive device characteristic is represented by the high non-linearity exhibited in particular around the peak current region and at the onset of the resonant tunnelling current. The impact of the *I-V* curvature component in relation to the performance of the RTD, when employed in a direct detection scheme, is further discussed in Chapter 6.

The described device figures of merit (FOM) can be enhanced in a direct approach by varying the thickness of its structural semiconductor material layers. In addition to the barrier's thickness, which can exponentially impact the device peak current density (J_p), by altering the transmission probability $T(E)$, as previously discussed, the width of the QW contributes directly to the RTD DC behaviour by determining the level of quantised energy states as:

$$E_n = \left(\frac{\hbar^2 \pi^2}{2m_e^* w_{qw}^2}\right) n^2, \qquad for\ n = 1,2,3, \ldots \tag{2.12}$$

where m_e^* is the electron effective mass in the well and w_{qw} is the layer width. Thus, for a reduced QW size, the ground resonant state appears at a higher energy level, resulting in a shift in V_p to a higher bias point [18]. At the same time the PVCR will increase as a result of the reduced current leakage through the second resonant state, due to the higher separation between the E_1 and E_2 energy levels [19].

Furthermore, the introduction of a thick un-doped spacer layer will result in the formation of a pseudo-triangular well on the emitter side and a wide depletion region between the second barrier and the collector layer [7], when bias is applied across the device (Fig. 2.6).

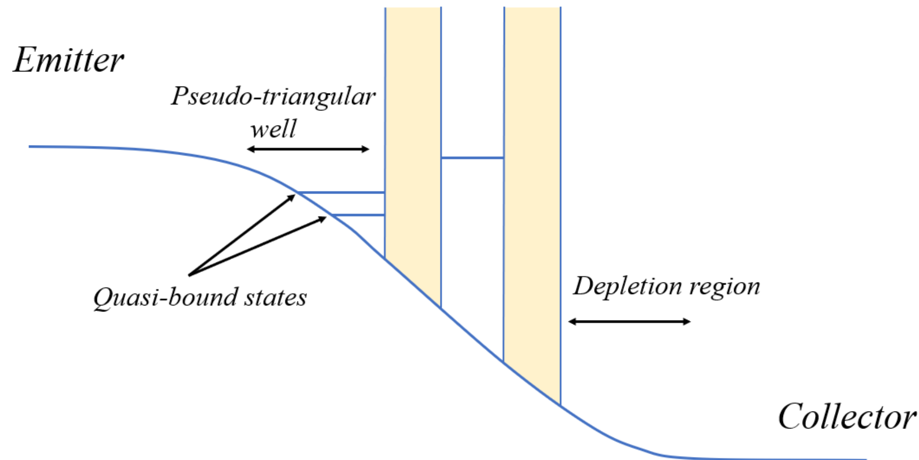

Figure 2.6 Simplified conduction band profile of an RTD employing thick spacer layers adjacent to each barrier, under applied bias. Adapted from [7].

Within the newly formed secondary well, a 2DEG system is formed by electrons localised in the quasibound states, leading to a $2D-2D$ resonant tunnelling mechanism [20]. This transport mechanism is based on the alignment of the discrete energy levels in the emitter with the resonant states in the primary QW, which is in a sense more limited than the $3D-2D$ resonant tunnelling. This effectively translates to a narrower transmission coefficient around the specific energy levels, improving thus the device PVCR at the cost of a reduced peak current density.

The effect of the narrower $T(E)$ can also be seen on the overall shape of the device *I-V* curve, creating a sharper transition between the positive and negative differential resistance regions. Other potential effects that are correlated with the width of the spacer layers, such as potential charge build-ups will be further discussed in Chapter 5, in the context of the employed layer structures within this thesis.

2.3 RTD materials

Various III-V compound semiconductor material systems have been investigated in the context of the specific heterojunctions realization, out of which the most relevant

are gallium arsenide (GaAs/AlAs, GaAs/AlGaAs and InAs/AlSb) and indium phosphide (InGaAs/AlAs) based. RTDs based on such material systems are typically characterised by high peak current densities and PVCRs due to their small electron effective mass (m^*) and large conduction band offset which offers high carrier mobility while providing a reduced valley current, by minimizing the thermionic emission component [21].

The first demonstration of the resonant tunnelling principle used GaAs in combination with AlGaAs [22] and AlAs [23] DBQW structures, grown on GaAs semi-insulating substrate [24]. These devices, however, have been proven to have the lowest performance among the above-mentioned material systems, due to their high m^* [25]. Nonetheless, fundamental oscillations of GaAs/AlAs RTDs up to 420 GHz have been reported at room temperature operation [23]. Several techniques have been attempted in order to improve the PVCR (from around 1.5) such as altering the barrier material mole fraction x ($Al_xGa_{1-x}As$) [26], or the introduction of an additional $Al_{0.2}Ga_{0.8}As$ monolayer, acting as 'chair' barrier on the emitter side, with which a PVCR value of 6.3 was achieved [27].

In contrast, InAs/AlSb [28] systems are able to provide superior peak current densities due to the fact that the effective mass in InAs is approximately three times smaller than in GaAs. This is also the result of the larger offered conduction band offset (~ 1 eV), which gives rise to more resonant levels [29] in the QW, while also improving the associated attenuation of carriers tunnelling through the AlSb barrier [30]. Furthermore, a lower device series resistance can be achieved due to almost ideal ohmic contact formation between the metal and InAs material [31]. However, such material systems are prone to impact ionisation due to the low energy bandgap of InAs, which in the presence of strong electric fields can lead to avalanche breakdown processes, thus placing a major limitation in terms higher power operation [32]. High-frequency oscillations of 712 GHz have been reported in InAs/AlSb RTDs with a low output power of 0.3 μW [33].

Although historically InGaAs alloys have been characterised by complex growth processes, due to the lack of lattice matched substrates in comparison to GaAs, the introduction of the pseudomorphic $In_{0.53}Ga_{0.47}As$/AlAs [34] has made InP based material systems the most widely employed choice for RTDs operating as high-power

THz sources and detectors. To date, the highest operating frequency [35] (1.98 THz) and output power (1 mW at 260 GHz) of an RTD oscillator have been achieved using InGaAs/AlAs heterostructures [36], being also the primary layer structure investigated throughout this thesis. Novel variations of this structure have been proposed in order to improve the performance of the device, by maximising the energy level difference between the adjacent resonant states in the QW. Methods such as the introduction of an additional InAs subwell [37] or the later indium-rich QW ($In_{0.9}Ga_{0.1}As$) [35] have yielded devices with PVCRs of 50 and current densities of 2.4×10^3 kA/cm^2, respectively. The high PVCR value, which translates to an increased slope of the device conductance, has been demonstrated experimentally to minimise the effective device switching time by providing superior current rise and fall times between the on- and off-resonant states [38], thus making this material system a primary target for high-speed applications [39].

The most important limitations of group III-V RTDs are represented by their high processing costs and incompatibility with most Si based CMOS technologies, which has not allowed their wide deployment in the mainstream application market. As an alternative, Si/SiGe heterostructures [40] have also been considered, however their performance has been proven inferior to III-V material systems, due to the limited conduction and valence band discontinuities between Si and SiGe alloys [41]. Resonant tunnelling of both electrons (reported $J_p = 282$ kA/cm^2 at room temperature) [42] and holes (reported PVCR = 9 at 4.2 K) [43] have been demonstrated through Si/SiGe heterostructures, however their performance degrades abruptly with increased device active area and operating temperature respectively, due to the poor thermal conductivity of the structure. The determined thermal conductivity of the fabricated *n*-$Si_{0.8}Ge_{0.2}$ structure was reported at 5.1 W/(m-K), in comparison to that of bulk Si, which is 140 W/(m-K) [44]. Such devices have been investigated primarily in the context of high-speed memory [45] and digital logic [46] applications.

2.4 RTD equivalent circuit models for high-frequency applications

Extensive research has been devoted to the prediction of the DC current-voltage characteristic of RTDs through self-consistent theoretical models [47][48] and

quantum transport numerical simulations [49][50], or even quasi-empirical approaches [51-53], compatible with simulation environments, in which long computation times are not particularly suitable [54]. However, due to the spectral band in which most targeted system applications are required to operate, in addition to the basic *I-V* characteristics, the high-frequency behaviour representation of the device, through the aid of accurate small-signal equivalent circuit models is of paramount importance for the successful realisation of RTD based circuits.

The first attempt to describe the radio frequency (RF) behaviour of RTDs, based on equivalent circuit models has been presented in [55]. The generical device model, for which the device polarity is neglected (i.e. device can be operated in both forward and reverse bias), comprises of a parallel combination of the device differential conductance (G_n) and the RTD self-capacitance (C_n), in series with the contact and access resistance (R_s), as shown in Fig. 2.7.

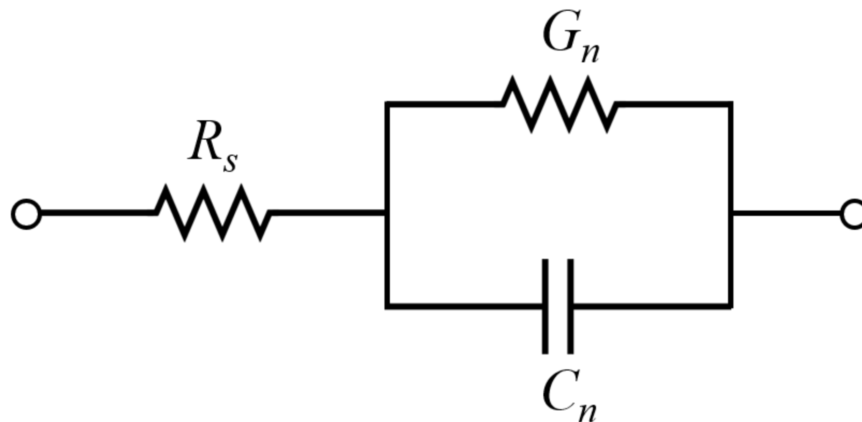

Figure 2.7 RTD equivalent circuit model comprised of the parallel combination of device differential conductance (G_n) and self-capacitance (C_n). R_s denotes the series contact and access resistance.

The device conductance can be directly determined from the first derivative of the *I-V* curve, with a bias dependent negative value within the NDR region:

$$G_n = \frac{\Delta I}{\Delta V} \tag{2.13}$$

The RTD self-capacitance, in this model, is attributed to the static capacitance that arises from the formation of the depletion region on the collector side, which confined

by the highly doped emitter and collector layers can be viewed as a standard parallel plate capacitor. The device capacitance can thus be estimated solely by the geometric static capacitance (*C_0*) as [56]:

$$C_n = C_0 = \frac{A}{\frac{l_{qw}}{\epsilon_w} + \frac{2l_b}{\epsilon_b} + \frac{l_d}{\epsilon_d}} \tag{2.14}$$

where l_{qw}, l_b, l_d, are the bias-dependent widths of the quantum-well, barrier and depletion region respectively, ε_w, ε_b, ε_d, are the corresponding material dielectric constants, and *A* is the RTD active area.

A validation of the proposed model is presented in the same publication using high-frequency measurements up to 12 GHz, for three similar GaAs/AlGaAs RTD structures. An interesting resonance behaviour was first observed beyond 3 GHz, which was simply attributed to an extrinsic series inductive element introduced by the measurement cables (series inductance model). As stipulated by the original assumption, the device capacitance was determined as bias independent within the limited voltage span of the measured impedance. However, the discrepancies between the fitted and experimentally acquired data, together with the variation of the extracted inductive element between the three RTD structures suggested a more complex device behaviour, difficult to characterise at low frequencies.

A different explanation for the displayed resonance was proposed in [57], which attributes the device inductive behaviour to an intrinsic phenomenon, particularly the charging and discharging effect of the quantum-well. The time constant required for this mechanism to take place was determined to be dominated by the electron dwell time (τ_{dwell}), which is defined as the electron quasibound-state lifetime in quantum-well [58] (i.e. the total time required for an electron to tunnel through the DBQW structure). This quantity, which plays an important role in the high-speed operation RTDs, can be estimated by:

$$\tau_{dwell} = \frac{\hbar}{\Delta E_n} \tag{2.15}$$

where ΔE_n is the energy full-width of the transmission probability function through the resonant state. This novel concept has given rise to an improved proposed device

model, in which the time delay, associated with the electron transport mechanism through the RTD structure, is represented by a quantum-well inductance (L_{qw}), in series with the differential conductance (parallel inductance model), as shown in Fig. 2.8.

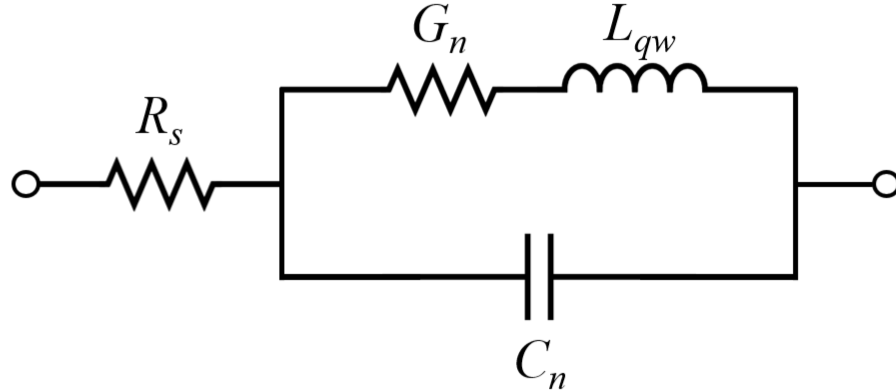

Figure 2.8 RTD equivalent circuit model, in which the quantum-well inductance (L_{qw}) appears in series with the differential conductance (G_n) and in parallel with the device capacitance (C_n). R_s denotes the series contact and access resistance.

Furthermore, the quantum-well inductance has been determined to have a bias dependency (i.e. determined by the net electron flow through the structure), and thus can be estimated based on the differential conductance by Eqn. 2.16, derived in [23]:

$$L_{qw} = \frac{\tau_{dwell}}{G_n} \tag{2.16}$$

Since its introduction, the described device parallel inductance model has become an important design resource for RTD circuits, particularly in their implementation as negative differential resistance oscillators [59] in THz sources. The fundamental concept of such circuits relies on the principle of a standard *LC* resonator comprised of the device capacitance (C_n) together with an external inductive element (L), typically realised through a transmission line [60], or in more compact designs an integrated antenna which acts as both a resonator as well as radiator [61].

The fundamental oscillation frequency of the circuit can be predicted using Eqn. 2.17, for which the device quantum well inductance (L_{qw}) is neglected.

$$f_{osc} \approx \frac{1}{2\pi\sqrt{LC_n}} \tag{2.17}$$

Large discrepancies have been reported between measured fundamental oscillations frequencies and theoretical predictions, based on the above presented estimation, and have generally been attributed to device extrinsic parasitic components [62]. However, such reported inconsistencies, in combination with large experimentally determined oscillator frequency variabilities (i.e. voltage-controlled oscillation [63][64]) indicate a complex bias dependent capacitive component of the RTD, which cannot be correlated to the small changes in geometric capacitance with applied bias voltage (i.e. due to variations in active depletion region thickness (Eqn. 2.14)).

A bias dependent capacitance variation of an RTD was initially presented in [65], as part of an impedance measurement experiment of a GaAs/AlGaAs device up to 18 GHz. The extracted device equivalent circuit, based on a simple fitting method of the series inductance model showed a distinctive capacitance peak in the NDR region, which was assumed related to the change in charge distribution, as a result of carrier tunnelling effects and transit times through the RTD structures [66].

Originally presented as a capacitance anomaly, the distinct behaviour (i.e. peak capacitance value within the NDR) has become widely acknowledged within the scientific community, as evidenced in multiple RTD studies [67-69], however, the underlying nature of this phenomenon has been highly disputed.

One theoretical approach to model this effect is presented in [66], where the geometric capacitance is determined solely by the depletion layers (C_{dep}), whereas the bias dependent capacitive element is considered as a result of the electron transit time through both the DBQW structure and depletion region. The carrier transit time through these regions (τ_{rtd}) is given as:

$$\tau_{rtd} = \tau_{dwell} + \frac{\tau_{dep}}{2} \tag{2.18}$$

where τ_{dep} is the transit time across the depletion region. This theorised effect has been translated into an alternative of the parallel inductance model, as shown in Fig. 2.9, with the introduction of an additional bias dependent capacitance component (given by $\tau_{rtd}G_n$). The total device capacitance C_n within this model, is thus given as the parallel combination of the depletion geometric capacitance (C_{dep}), and the bias dependent capacitance ($\tau_{rtd}G_n$), due to the electron delay time. The quantum-well

inductance has been intentionally omitted from the equivalent circuit, as it is estimated that the associated time delay that determines this value, can thus be incorporated by the capacitive component [70]. This model, however, has not yet been validated experimentally through high-frequency impedance measurements within the RTD NDR region. Typically, most RTD RF studies that adopt this device equivalent circuit (particularly the underlying mechanism of the charge variation), often compute the bias dependent capacitance from oscillator performance [71], numerical computations [72], or even empirical models based on Gaussian bell curves [73].

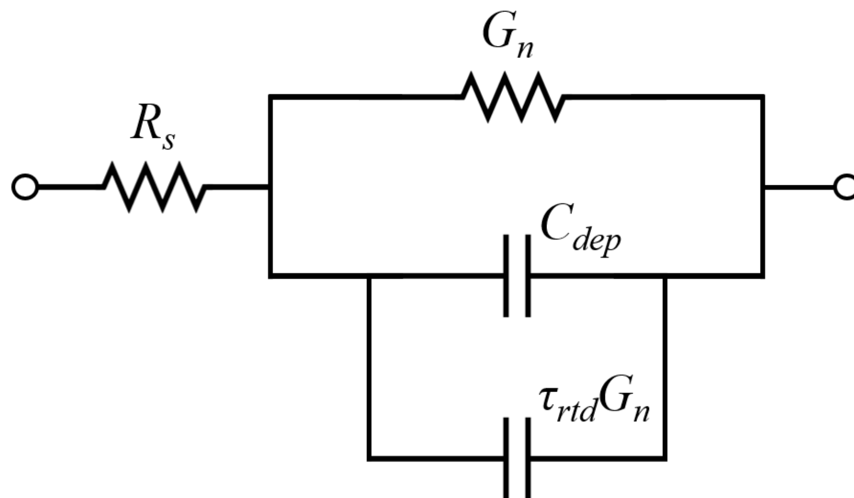

Figure 2.9 RTD equivalent circuit model, where the device capacitance is given by the parallel combination of the static capacitance (C_{dep}), determined by the depletion region and the bias dependent capacitance ($\tau_{rtd}G_n$), due to the electron delay time.

A different derivation of the bias dependent capacitance was proposed in [74], where the variation in charge distribution is governed predominantly by the much shorter electron tunnel time from the quantum-well to the collector (τ_c). Within this derivation however, the above described mechanism is considered restricted to the NDR region, assumed additionally to the depletion capacitance (C_{dep}), which solely determines the complete device capacitance in the two PDR regions. Furthermore, the quantum-well inductance is completely neglected in the device RF behaviour.

Based on the mentioned shortcomings of the described RTD high-frequency equivalent circuit representations, a unified model has been proposed in [75] (Fig. 2.10), incorporating the parallel-inductance model, and a voltage dependent quantum-well capacitance component (C_{qw}). The basis of the charge variation, described in this

model, that determines C_{qw} is represented by the change in the quantum-well – collector current density (ΔJ_c) as a function of electron escape rate through the second barrier ($\nu_c = 1/\tau_c$) expressed as:

$$\Delta J_c = \Delta \nu_c \Delta Q_{qw} \cong \nu_c \Delta Q_{qw} \quad (2.19)$$

where ΔQ_{qw} is the variation of stored charge in the quantum well, and the tunnelling current resulting from electron travelling from the collector back into the quantum-well is considered insignificant. Also, it is assumed that the escape rate is constant for a small variation in applied voltage.

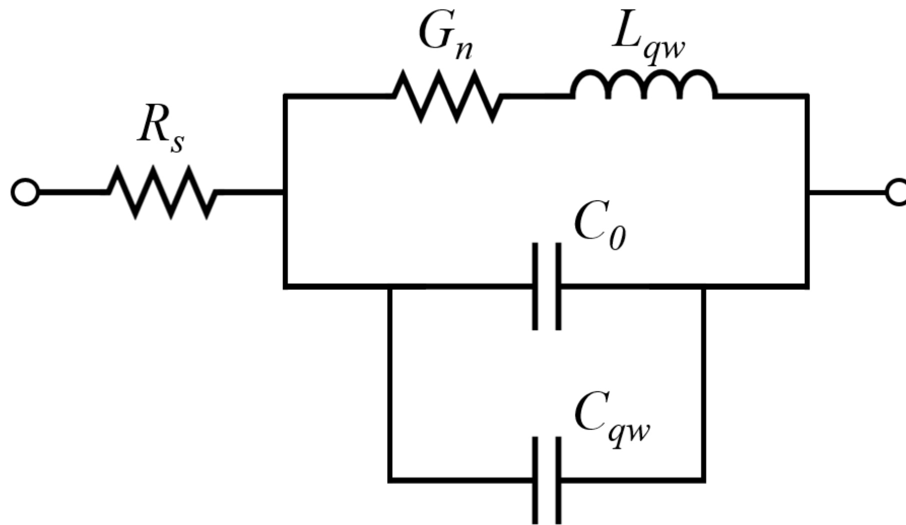

Figure 2.10 Unified RTD equivalent circuit model, where C_0 and C_{qw} denote the geometric and quantum-well capacitance, respectively.

By further considering the device differential conductance (G_n) being completely dependent on J_c (i.e. ignoring the very low contribution of the quantum-well – emitter current density J_e), it is given by:

$$G_n = A\frac{\Delta J_c}{\Delta V} \quad (2.20)$$

Combining Eqn. 2.19 and 2.20, and assuming that the charge variation in the quantum-well induces an equal positive charge variation in the collector (ΔQ_c):

$$\Delta Q_c = -\Delta Q_{qw} = -\frac{G_n}{A\nu_c}\Delta V \quad (2.21)$$

The derived charge variation in the collector, as a function of device differential conductance, results in a quantum-well capacitance as:

$$C_{qw} = A\frac{\Delta Q_c}{\Delta V} = -\frac{G_n}{\nu_c} \tag{2.22}$$

As the obtained formula for the quantum-well capacitance is identical to the one proposed in [74], the derivation, in the above presented form, demonstrates its existence throughout the entire bias range, which together with the geometric capacitance C_0, estimated by Eqn. 2.14, defines the complete RTD self-capacitance. In a similar fashion, the formula for the quantum-well inductance, proposed in [23] is derived, for which the electron dwell time is approximated by the electron escape rates through the emitter and collector barriers (i.e. ν_e and ν_c):

$$\tau_{dwell} = \frac{1}{\nu_e} + \frac{1}{\nu_c} \tag{2.23}$$

The validity of the unified RF model has been demonstrated with the aid of high-frequency impedance measurements in [76] and [77], in the entire device bias range of InGaAs/AlAs RTDs, however, within a relatively narrow frequency range (up to 20 GHz and 30 GHz, respectively). In both publications, the extracted RTD self-capacitance, as a function of applied bias voltage, displayed the expected behaviour, with a peak value occurring within the NDR region. The performance of the characterised devices was not further investigated from an application perspective.

The analysis and extraction of the derived quantum-well inductance, included in this model represents an important device quality factor, beyond its integration as a simple fitting parameter, as described in the series inductance model. Although, this quantity is not generally referenced in the design process of RTD circuits (e.g. estimating the fundamental oscillation frequency of sources), it was demonstrated relevant in the prediction of the RTD maximum operation frequency (f_{max}) due to conductance roll-off (i.e. NDR degradation) [78]. Thus, for an RTD operating within its NDR region, at a frequency that approaches the electron lifetime (i.e. $f_{max} \approx 1/(2\pi\tau_{rtd})$) the real part of the circuit admittance tends towards zero, as the imaginary part becomes predominantly inductive [79].

Most reported high-frequency sources have been designed to oscillate well below their cut-off frequencies, primarily due to epi-structure optimizations, that would enable low electron resonant-state lifetimes (i.e. $f_{osc} \ll 1/(2\pi\tau_{rtd})$). More recently, targeted studies have demonstrated the operation of individual devices and oscillators beyond the imposed limitation [80]. The presented behaviour has been theoretically attributed to the fact that the RTD response time, governed by the time constant associated to the charge-relaxation processes (τ_{rel}), can be considerably shorter or longer in comparison to the quasibound resonant-state lifetime (τ_{dwell}) [81], as a result of the Coulomb interactions between electrons, which were not considered in the original derivation. By a more complex derivation, τ_{rel} can be estimated as:

$$\tau_{rel} = \frac{1+\beta}{\nu_e} + \frac{1}{\nu_c} \tag{2.24}$$

where the factor β describes the mechanism of Coulomb acceleration of the charge relaxation and is typically in the range of 2 – 10 for InGaAs or GaAs devices [78]. The bias dependent change in the diode response time in comparison with electron lifetime was experimentally demonstrated for a specific wide barrier InGaAs/AlAs RTD using high-frequency impedance measurements up to 12 GHz [82]. The presented results showed that the above-mentioned factors highly impact the charge-relaxation time constant of the device, with a large variation between the positive ($\tau_{rel} \ll \tau_{dwell}$) and negative ($\tau_{rel} \gg \tau_{dwell}$) differential resistance regions.

Furthermore, it was suggested that the space-charge effects will also generate a displacement-current mechanism, which impacts the net current flow through the DBQW structure. The described complex behaviour can be modelled by adapting the existing RTD equivalent circuit, shown in Fig. 2.1, to include an additional parallel high-frequency channel with no associated delays (i.e. instantaneous current flow), in order to potentially explain the device operation capability beyond the described maximum cut-off frequency f_{max} [82].

Although the presented device RF model is considered to date, the most complex theoretical high-frequency representation of the RTD, due to its relatively limited validation (i.e. narrow frequency span and targeted device epi-structure) its applicability has yet to be fully demonstrated in the design process of RTD-based circuits.

2.5 Summary

This chapter provides an overview of the fundamental quantum mechanical charge transport mechanism in double-barrier quantum-well heterostructures, primarily from the perspective of the basic operation principles of resonant tunnelling diodes, together with the device general design concepts and common adopted material systems.

Furthermore, a review of the state of the art RTD equivalent circuit models, used to describe the device RF behaviour is presented, illustrating the key device bias dependent elements, such as the self-capacitance and quantum-well inductance, and their imposing performance limitations for high-frequency applications.

The accuracy of the small-signal equivalent circuit models will be further discussed in Chapter 5, in the context of a realised device high-frequency characterisation, together with the associated challenges in extracting the discussed specific circuit elements and their theoretical representation. Due to the predominantly experimental characterisation approach adopted in this work, the RF parallel inductance circuit (Fig. 2.8) has been considered as a starting point for device high-frequency modelling.

2.6 References

[1] G. Lochak and R. Dutheil, "Wave mechanics and relativity," in *Wave-particle duality*, F. Selleri Ed. Boston, MA: Springer US, pp. 157-167, 1992.

[2] H. D. Young, R. A. Freedman, T. Sandin, and A. L. Ford, *University Physics*. Addison-Wesley New York, 1996.

[3] L. Esaki, "New phenomenon in narrow germanium p-n junctions," *Physical Review,* vol. 109, no. 2, pp. 603-604, 1958.

[4] L. Esaki, "Discovery of the tunnel diode," *IEEE Transactions on Electron Devices,* vol. 23, no. 7, pp. 644-647, 1976.

[5] R. Yang, M. Sweeny, D. Day, and J. M. Xu, "Interband tunneling in heterostructure tunnel diodes," *Electron Devices, IEEE Transactions on,* vol. 38, pp. 442-446, 1991.

[6] R. Tsu and L. Esaki, "Tunneling in a finite superlattice," *Applied Physics Letters,* vol. 22, no. 11, pp. 562-564, 1973.

[7] H. Mizuta and T. Tanoue, *The physics and applications of resonant tunnelling diodes*. Cambridge university press, 2006.

[8] V. S. Olkhovsky, E. Recami, and A. K. Zaichenko, "Resonant and non-resonant tunneling through a double barrier," *EPL (Europhysics Letters),* vol. 70, no. 6, p. 712, 2005.

[9] L. L. Chang, L. Esaki, and R. Tsu, "Resonant tunneling in semiconductor double barriers," *Applied Physics Letters,* vol. 24, no. 12, pp. 593-595, 1974.

[10] T. Nakagawa, H. Imamoto, T. Kojima, and K. Ohta, "Observation of resonant tunneling in AlGaAs/GaAs triple barrier diodes," *Applied Physics Letters,* vol. 49, no. 2, pp. 73-75, 1986.

[11] K. Ohtani, K. Fujita, and H. Ohno, "InAs quantum cascade lasers based on coupled quantum well structures," *Japanese Journal of Applied Physics,* vol. 44, no. 4B, pp. 2572-2574, 2005.

[12] T. C. L. G. Sollner, W. D. Goodhue, P. E. Tannenwald, C. D. Parker, and D. D. Peck, "Resonant tunneling through quantum wells at frequencies up to 2.5 THz," *Applied Physics Letters,* vol. 43, no. 6, pp. 588-590, 1983.

[13] J. Ling, "Resonant tunneling diodes: Theory of operation and applications," *University of Rochester, Rochester, NY,* vol. 14627, 1999.

[14] P. Roblin and H. Rohdin, *High-speed heterostructure devices: from device concepts to circuit modeling*. Cambridge university press, 2002.

[15] L. Wang, "Reliable design of tunnel diode and resonant tunnelling diode based microwave sources," Phd Thesis PhD Thesis, University of Glasgow, 2012.

[16] C. Kim and A. Brandli, "High-frequency high-power operation of tunnel diodes," *IRE Transactions on Circuit Theory,* vol. 8, no. 4, pp. 416-425, 1961.

[17] M. Asada, S. Suzuki, and N. Kishimoto, "Resonant tunneling diodes for sub-terahertz and terahertz oscillators," *Japanese Journal of Applied Physics,* vol. 47, no. 6, pp. 4375-4384, 2008.

[18] R. Montecillo, R. Otadoy, M. Lee, F. Buot, and M. Nacar, "The dependence of the characteristics of THz current oscillations on the quantum-well width in resonant tunneling diode," in *AIP Conference Proceedings*, vol. 1871, no. 1: AIP Publishing LLC, p. 030002, 2017.

[19] S. G. Muttlak, O. S. Abdulwahid, J. Sexton, M. J. Kelly, and M. Missous, "InGaAs/AlAs resonant tunneling diodes for THz applications: an experimental investigation," *IEEE Journal of the Electron Devices Society,* vol. 6, pp. 254-262, 2018.

[20] H. L. Berkowitz and R. A. Lux, "Hysteresis predicted in I–V curve of heterojunction resonant tunneling diodes simulated by a self-consistent

quantum method," *Journal of Vacuum Science & Technology B: Microelectronics Processing and Phenomena,* vol. 5, no. 4, pp. 967-970, 1987.

[21] K. Jacobs, B. Stevens, R. Baba, O. Wada, T. Mukai, and R. Hogg, "Valley current characterization of high current density resonant tunnelling diodes for terahertz-wave applications," *AIP Advances,* vol. 7, no. 10, p. 105316, 2017.

[22] T. Shewchuk, P. Chapin, P. Coleman, W. Kopp, R. Fischer, and H. Morkoc, "Resonant tunneling oscillations in a GaAs-$Al_xGa_{1-x}As$ heterostructure at room temperature," *Applied Physics Letters,* vol. 46, no. 5, pp. 508-510, 1985.

[23] E. Brown, T. Sollner, C. Parker, W. Goodhue, and C. Chen, "Oscillations up to 420 GHz in GaAs/AlAs resonant tunneling diodes," *Applied Physics Letters,* vol. 55, no. 17, pp. 1777-1779, 1989.

[24] S. S. Li, "High-speed III–V semiconductor devices," in *Semiconductor Physical Electronics*: Springer, pp. 455-502, 1993.

[25] E. Brown, "High-speed resonant-tunneling diodes," in *VLSI Electronics Microstructure Science*, vol. 24: Elsevier, pp. 305-350, 1994.

[26] A. J. Hill and P. H. Ladbrooke, "Dependence of conduction-band discontinuity on aluminium mole fraction in GaAs/AlGaAs heterojunctions," *Electronics Letters,* vol. 22, no. 4, pp. 218-219, 1986.

[27] V. K. Reddy, A. J. Tsao, and D. P. Neikirk, "High peak-to-valley current ratio AlGaAs/AlAs/GaAs double barrier resonant tunnelling diodes," *Electronics Letters,* vol. 26, no. 21, pp. 1742-1744, 1990.

[28] D. H. Chow, J. N. Schulman, E. ÖZbay, and D. M. Bloom, "High speed InAs/AlSb and $In_{0.53}Ga_{0.47}As$/AlAs resonant tunneling diodes," *MRS Proceedings,* vol. 281, p. 269, 1992, Art no. 269..

[29] M. Omar, *Semiconductor heterojunctions and nanostructures*. McGraw-Hill Education, 2005, pp. -1.

[30] J. Söderström, E. Yu, M. Jackson, Y. Rajakarunanayake, and T. McGill, "Two-band modeling of narrow band gap and interband tunneling devices," *Journal of Applied Physics,* vol. 68, no. 3, pp. 1372-1375, 1990.

[31] C. A. Mead and W. G. Spitzer, "Fermi level position at metal-semiconductor interfaces," *Physical Review,* vol. 134, no. 3A, pp. A713-A716, 1964.

[32] J. Singh, *Semiconductor optoelectronics: physics and technology*. McGraw-Hill, 1995.

[33] E. Brown, J. Söderström, C. Parker, L. Mahoney, K. Molvar, and T. McGill, "Oscillations up to 712 GHz in InAs/AlSb resonant-tunneling diodes," *Applied Physics Letters,* vol. 58, no. 20, pp. 2291-2293, 1991.

[34] T. Inata, S. Muto, Y. Nakata, S. Sasa, T. Fujii, and S. Hiyamizu, "A pseudomorphic $In_{0.53}Ga_{0.47}As$/AlAs resonant tunneling barrier with a peak-to-valley current ratio of 14 at room temperature," *Japanese Journal of Applied Physics,* vol. 26, no. 8A, p. L1332, 1987.

[35] R. Izumi, S. Suzuki, and M. Asada, "1.98 THz resonant-tunneling-diode oscillator with reduced conduction loss by thick antenna electrode," in *2017 42nd International Conference on Infrared, Millimeter, and Terahertz Waves (IRMMW-THz)*, pp. 1-2, 27 Aug.-1 Sept. 2017, 2017.

[36] A. Al-Khalidi, K. H. Alharbi, J. Wang, R. Morariu, L. Wang, A. Khalid, J. M. Figueiredo, and E. Wasige, "Resonant tunneling diode terahertz sources with up to 1 mW output power in the J-band," *IEEE Transactions on Terahertz Science and Technology,* vol. 10, no. 2, pp. 150-157, 2019.

[37] J. H. Smet, T. P. E. Broekaert, and C. G. Fonstad, "Peak-to-valley current ratios as high as 50:1 at room temperature in pseudomorphic $In_{0.53}Ga_{0.47}As$/AlAs/InAs resonant tunneling diodes," *Journal of Applied Physics,* vol. 71, no. 5, pp. 2475-2477, 1992.

[38] W. Zhang, T. A. Growden, D. F. Storm, D. J. Meyer, P. R. Berger, and E. R. Brown, "Investigation of switching time in GaN/AlN resonant tunneling diodes

by experiments and P-SPICE models," *IEEE Transactions on Electron Devices,* vol. 67, no. 1, pp. 75-79, 2020.

[39] C. S. Y. Leung, M. Wintreert-Fouquet, and D. J. Skellern, "Switching time measurements of GaAs/AlAs and InGaAs/AlAs resonant tunnelling diodes," in *1998 Conference on Optoelectronic and Microelectronic Materials and Devices*, pp. 144-146, 14-16 Dec. 1998, 1998.

[40] K. Ismail, B. Meyerson, and P. Wang, "Electron resonant tunneling in Si/SiGe double barrier diodes," *Applied physics letters,* vol. 59, no. 8, pp. 973-975, 1991.

[41] J. D. Cressler, *Silicon heterostructure devices*. CRC Press, 2018.

[42] D. Paul, P. See, I. Zozoulenko, K.-F. Berggren, B. Holländer, S. Mantl, N. Griffin, B. Coonan, G. Redmond, and G. Crean, "n-type Si/SiGe resonant tunnelling diodes," *Materials Science and Engineering: B,* vol. 89, no. 1-3, pp. 26-29, 2002.

[43] S. Tsujino, N. Usami, A. Weber, G. Mussler, V. Shushunova, D. Grützmacher, Y. Azuma, and K. Nakajima, "SiGe double barrier resonant tunneling diodes on bulk SiGe substrates with high peak-to-valley current ratio," *Applied Physics Letters,* vol. 91, no. 3, p. 032104, 2007.

[44] J. P. Dismukes, L. Ekstrom, E. F. Steigmeier, I. Kudman, and D. S. Beers, "Thermal and electrical properties of heavily doped Ge-Si alloys up to 1300°K," *Journal of Applied Physics,* vol. 35, no. 10, pp. 2899-2907, 1964.

[45] G. Ternent and D. J. Paul, "Si/SiGe tunneling static random access memories," *ECS Transactions,* vol. 50, no. 9, p. 987, 2013.

[46] J. Núñez, M. J. Avedillo, and J. M. Quintana, "Evaluation of RTD-CMOS logic gates," in *2010 13th Euromicro Conference on Digital System Design: Architectures, Methods and Tools*: IEEE, pp. 621-627, 2010.

[47] J. N. Schulman, H. J. D. L. Santos, and D. H. Chow, "Physics-based RTD current-voltage equation," *IEEE Electron Device Letters,* vol. 17, no. 5, pp. 220-222, 1996.

[48] J. Wang and E. Wasige, "Self-consistent analysis of the IV characteristics of resonant tunnelling diodes," *International Journal of Terahertz Science and Technology,* vol. 5, no. 4, pp. 153-162, 2012.

[49] D. Querlioz, P. Dollfus, V.-N. Do, and A. Bournel, "An improved Wigner Monte-Carlo technique for the self-consistent simulation of RTDs," *Journal of Computational Electronics,* vol. 5, no. 4, pp. 443-446, 2006.

[50] Z. Peiji, C. Hong Liang, D. L. Woolard, K. L. Jensen, and F. A. Buot, "Equivalent circuit parameters of resonant tunneling diodes extracted from self-consistent Wigner-Poisson simulation," *IEEE Transactions on Electron Devices,* vol. 48, no. 4, pp. 614-627, 2001.

[51] E. Brown, O. McMahon, L. Mahoney, and K. Molvar, "SPICE model of the resonant-tunnelling diode," *Electronics Letters,* vol. 32, no. 10, pp. 938-940, 1996.

[52] G. Ternent and D. J. Paul, "SPICE modeling of the scaling of resonant tunneling diodes and the effects of sidewall leakage," *IEEE Transactions on Electron Devices,* vol. 59, no. 12, pp. 3555-3560, 2012.

[53] S. Diebold, M. Fujita, and T. Nagatsuma, "Asymmetrical conductance model to analyze resonant tunneling diode terahertz oscillators," in *2017 IEEE MTT-S International Microwave Symposium (IMS)*: IEEE, pp. 1795-1797, 2017.

[54] A. Sellai, H. Al-Hadhrami, S. H. Al-Harthi, and M. Henini, "Pspice resonant tunneling diode models and application circuits," *International Journal of Electronics,* vol. 92, no. 3, pp. 131-142, 2005.

[55] J. Gering, D. Crim, D. G. Morgan, P. Coleman, W. Kopp, and H. Morkoc, "A small-signal equivalent-circuit model for GaAs-$Al_xGa_{1-x}As$ resonant tunneling heterostructures at microwave frequencies," *Journal of Applied Physics,* vol. 61, no. 1, pp. 271-276, 1987.

[56] Y. Hu and S. Stapleton, "Capacitance of a resonant tunneling diode," *Japanese Journal of Applied Physics,* vol. 31, no. 1R, p. 23, 1992.

[57] E. R. Brown, C. D. Parker, and T. C. L. G. Sollner, "Effect of quasibound-state lifetime on the oscillation power of resonant tunneling diodes," *Applied Physics Letters,* vol. 54, no. 10, pp. 934-936, 1989.

[58] N. Harada and S. Kuroda, "Lifetime of resonant state in a resonant tunneling system," *Japanese Journal of Applied Physics,* vol. 25, no. 11A, p. L871, 1986.

[59] W. F. Chow, "Principles of tunnel diode circuits," 1964.

[60] J. Wang, A. Al-Khalidi, L. Wang, R. Morariu, A. Ofiare, and E. Wasige, "15-Gb/s 50-cm wireless link using a high-power compact III–V 84-GHz transmitter," *IEEE Transactions on Microwave Theory and Techniques,* vol. 66, no. 11, pp. 4698-4705, 2018.

[61] M. Shiraishi, S. Suzuki, A. Teranishi, M. Asada, H. Sugiyama, and H. Yokoyama, "Fundamental oscillation up to 915GHz in InGaAs/AlAs resonant tunneling diodes integrated with slot antennas," in *2009 34th International Conference on Infrared, Millimeter, and Terahertz Waves*, pp. 1-2, 21-25 Sept. 2009, 2009.

[62] R. Izumi, T. Sato, S. Suzuki, and M. Asada, "Resonant-tunneling-diode terahertz oscillator with a cylindrical cavity for high-frequency oscillation," *AIP Advances,* vol. 9, no. 8, p. 085020, 2019.

[63] N. Orihashi, S. Hattori, S. Suzuki, and M. Asada, "Voltage-controlled sub-terahertz oscillation of resonant tunnelling diode integrated with slot antenna," *Electronics Letters,* vol. 41, no. 15, pp. 872-874, 2005.

[64] M. Asada, N. Orihashi, and S. Suzuki, "Voltage-controlled harmonic oscillation at about 1 THz in resonant tunneling diodes integrated with slot antennas," *Japanese Journal of Applied Physics,* vol. 46, no. 5R, p. 2904, 2007.

[65] T. Wei, S. Stapleton, and E. Berolo, "Equivalent circuit and capacitance of double barrier resonant tunneling diode," *Journal of Applied Physics,* vol. 73, no. 2, pp. 829-834, 1993.

[66] M. Asada, N. Orihashi, and S. Suzuki, "Experiment and theoretical analysis of voltage-controlled sub-THz oscillation of resonant tunneling diodes," *IEICE Transactions,* vol. 89-C, pp. 965-971, 2006.

[67] N. Shimizu, T. Waho, and T. Ishibashi, "Capacitance anomaly in the negative differential resistance region of resonant tunneling diodes," *Japanese Journal of Applied Physics,* vol. 36, no. 3B, p. L330, 1997.

[68] A. T. Kamgaing, B. Muenstermann, R. Geitmann, O. Benner, K. Blekker, W. Prost, and F. Tegude, "High performance submicron RTD design for mm-wave oscillator applications," in *IPRM 2011-23rd International Conference on Indium Phosphide and Related Materials*, pp. 1-4, 2011.

[69] A. Matiss, A. Poloczek, W. Brockerhoff, W. Prost, and F.-J. Tegude, "Large-signal analysis and AC modelling of sub micron resonant tunnelling diodes," in *2007 European Microwave Integrated Circuit Conference*: IEEE, pp. 207-210, 2007.

[70] M. Asada, S. Suzuki, and N. Kishimoto, "Resonant tunneling diodes for sub-terahertz and terahertz oscillators," *Japanese Journal of Applied Physics,* vol. 47, no. 6R, p. 4375, 2008.

[71] H. Kanaya, R. Sogabe, T. Maekawa, S. Suzuki, and M. Asada, "Fundamental oscillation up to 1.42 THz in resonant tunneling diodes by optimized collector spacer thickness," *Journal of Infrared, Millimeter, and Terahertz Waves,* vol. 35, no. 5, pp. 425-431, 2014.

[72] S. F. Nafea and A. A. S. Dessouki, "An accurate large-signal SPICE model for resonant tunneling diode," in *2010 International Conference on Microelectronics*, pp. 507-510, 19-22 Dec. 2010, 2010.

[73] S. Diebold, S. Nakai, K. Nishio, J. Kim, K. Tsuruda, T. Mukai, M. Fujita, and T. Nagatsuma, "Modeling and Simulation of Terahertz Resonant Tunneling

Diode-Based Circuits," *IEEE Transactions on Terahertz Science and Technology,* vol. 6, no. 5, pp. 716-723, 2016.

[74] R. Lake and J. Yang, "A physics based model for the RTD quantum capacitance," *IEEE Transactions on Electron Devices,* vol. 50, no. 3, pp. 785-789, 2003.

[75] Q. Liu, "Tunnel diode/transistor integrated circuits," PhD Thesis, University Of Notre Dame, 2006.

[76] M. Long, H. Ying-Long, Z. Yang, W. Liang-Chen, Y. Fu-Hua, and Z. Yi-Ping, "A small signal equivalent circuit model for resonant tunnelling diode," *Chinese Physics Letters,* vol. 23, no. 8, p. 2292, 2006.

[77] Q. Liu, A. Seabaugh, P. Chahal, and F. J. Morris, "Unified AC model for the resonant tunneling diode," *IEEE Transactions on Electron Devices,* vol. 51, no. 5, pp. 653-657, 2004.

[78] M. Feiginov, "Frequency limitations of resonant-tunnelling diodes in sub-THz and THz oscillators and detectors," *Journal of Infrared, Millimeter, and Terahertz Waves,* vol. 40, no. 4, pp. 365-394, 2019.

[79] W. R. Frensley, "Wigner-function model of a resonant-tunneling semiconductor device," *Physical Review B,* vol. 36, no. 3, pp. 1570-1580, 1987.

[80] M. Feiginov, C. Sydlo, O. Cojocari, and P. Meissner, "Operation of resonant-tunnelling oscillators beyond tunnel lifetime limit," *EPL (Europhysics Letters),* vol. 94, no. 4, p. 48007, 2011.

[81] M. N. Feiginov, "Does the quasibound-state lifetime restrict the high-frequency operation of resonant-tunnelling diodes?," *Nanotechnology,* vol. 11, no. 4, p. 359, 2000.

[82] M. Feiginov and D. R. Chowdhury, "Experimental demonstration of resonant-tunneling-diode operation beyond quasibound-state-lifetime limit," in *Journal*

of Physics: Conference Series, vol. 193, no. 1: IOP Publishing, p. 012016, 2009.

Chapter 3. RTD MMIC technology and fabrication processes

3.1 Introduction

This chapter describes the main fabrication processes involved in the realisation of micron-scale RTD devices and monolithic integrated circuits. The generic fabrication flow of the devices will be discussed, with a detailed description of the specific device layer structure, followed by an in-depth explanation of the individual fabrication techniques. The basic processes that have been adopted in this thesis include optical lithography, metal and dielectric deposition, wet/dry etching and lift-off methods, suitable to be conducted entirely in the James Watt Nanofabrication Centre (JWNC) at the University of Glasgow.

3.2 RTD layer structure and fabrication process overview

The RTD wafer used in this work, for high-frequency device characterisation purposes and realisation of an RTD-based detector is based on an InGaAs/AlAs material system and was grown by molecular beam epitaxy (MBE) by IQE Ltd on a semi-insulating InP substrate.

The epitaxial layer structure consists of a 4.7 nm InGaAs quantum well (Eg = 0.75 eV) sandwiched between 2.5 nm thick AlAs barriers (Eg = 2.16 eV), forming a double barrier quantum well structure (DBQW). The structure is completed by three-step doping-graded spacer layers on either side of the DBQW (un-doped, 5E16 doping and 2E16 doping), a drift layer on the collector side and highly doped contact layers (2E18 and 3E19 doping) on both sides, as detailed in Table 3.1. The presented epitaxial layer structure was previously investigated within the research group for the purpose of realising high-power RTD sources [1], and was designed specifically to enhance the device *I-V* characteristics by maximising the peak-to-valley current and voltage differences, as proposed in [2]. In the context of the work described in this thesis, the structure was chosen and characterised due to the high non-linearity displayed around the peak current region, making it suitable for a square-law detector application.

The distinct characteristic of this structure is the introduction of a relatively large depletion region (120 nm). Although this feature will highly reduce the device self-capacitance [3] and facilitates the sharp transition between the positive and negative differential resistance regions, as discussed in Chapter 2, it however negatively impacts the RTD peak-current density. The value for the peak-current density was estimated at approximately 18 kA/cm^2 and was determined based on the measured DC characteristics acquired from various fabricated device sizes on this structure, further presented in Chapter 5 and 6.

Table 3.1 RTD Epitaxial layer structure

Layer	*Thickness (Å)*	*Composition*	*Doping (cm^{-3})*	*Description*
1	400	$In_{0.53}Ga_{0.47}As$	3E19 : Si	Collector
2	800	$In_{0.53}Ga_{0.47}As$	2E18 : Si	Sub-Collector
3	1200	$In_{0.53}Ga_{0.47}As$	5E16 : Si	Drift Region
4	100	$In_{0.53}Ga_{0.47}As$	2E16 : Si	Spacer
5	20	$In_{0.53}Ga_{0.47}As$	Un-doped	Spacer
6	25	AlAs	Un-doped	Barrier
7	47	$In_{0.53}Ga_{0.47}As$	Un-doped	Well
8	25	AlAs	Un-doped	Barrier
9	20	$In_{0.53}Ga_{0.47}As$	Un-doped	Spacer
10	100	$In_{0.53}Ga_{0.47}As$	2E16 : Si	Spacer
11	100	$In_{0.53}Ga_{0.47}As$	5E16 : Si	Spacer
12	800	$In_{0.53}Ga_{0.47}As$	2E18 : Si	Sub-Emitter
13	4000	$In_{0.53}Ga_{0.47}As$	3E19 : Si	Emitter
14	2000	InP	Un-doped	Buffer
		SI : InP		Substrate

Starting from the presented grown material structure, the process to realise a functional RTD device can be illustrated using the diagrams in Fig. 3.1. The initial fabrication step is represented by the deposition of the top contact metal layers (i.e. emitter or collector contact depending on the chosen polarity), as shown in Fig. 3.1 (a). For this purpose, a Ti/Pd/Au (20/30/150 nm [4]) metal scheme was chosen, due to the reported low specific contact resistance that can be achieved with this material combination (0.73 Ωμm^2 [5]).

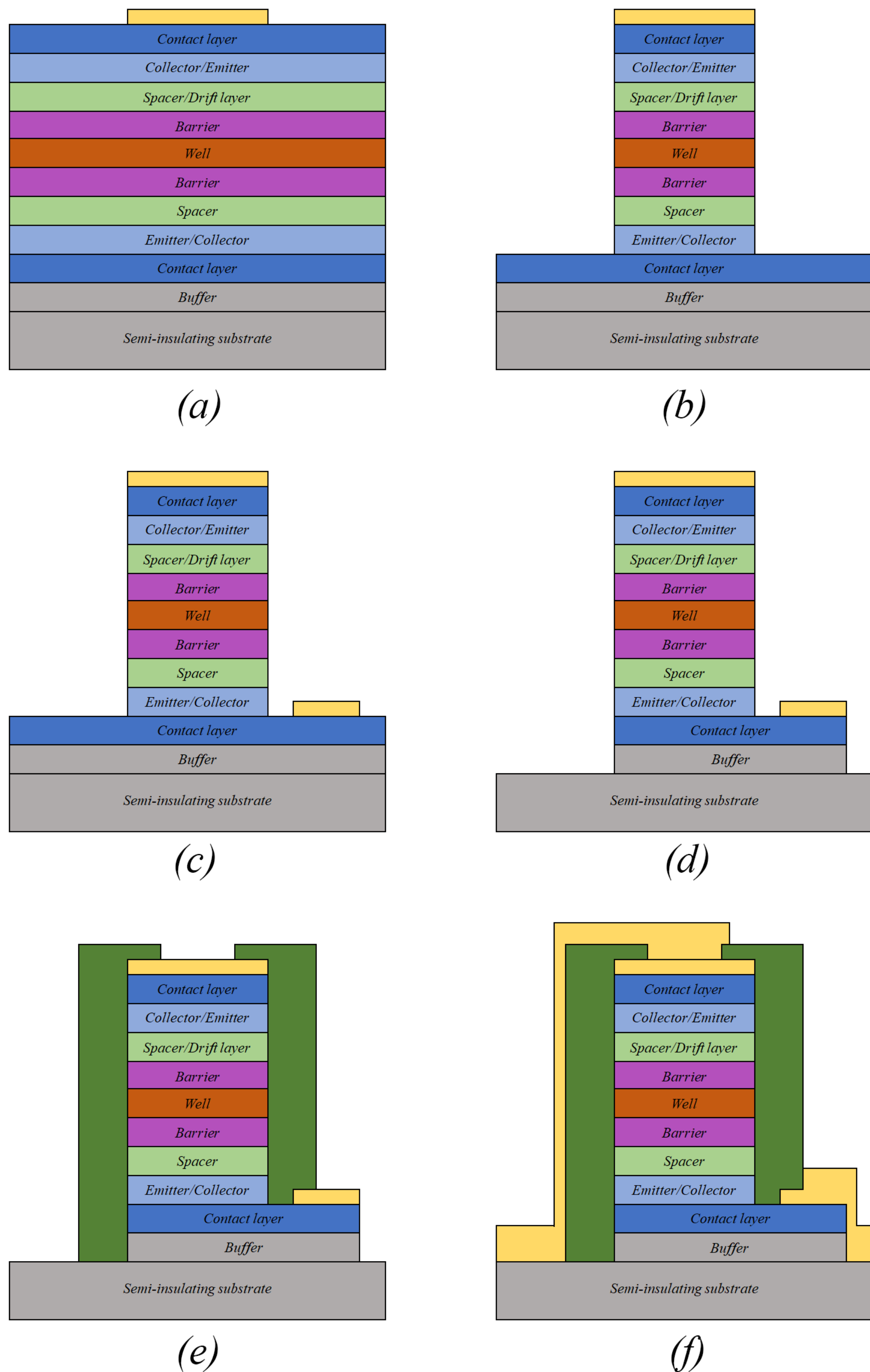

Figure 3.1 Diagram of RTD fabrication process: (a) Top contact metal deposition. (b) Etch to bottom contact layer. (c) Bottom contact metal deposition. (d) Etch to substrate. (e) Passivation layer deposition and via opening. (f). Bond-pad metal deposition.

Following the initial metallisation step, which predominantly determines the device active area, the top mesa can be defined by a wet etching process down to the bottom emitter/collector layer (Fig. 3.1 (b)), with the use of an orthophosphoric acid (H_3PO_4) together with hydrogen peroxide (H_2O_2) solvent diluted with water (i.e. H_3PO_4:H_2O_2:H_2O in the ratio 1:1:38). The presented two steps are repeated in order to create the bottom contact and define a single RTD structure (Fig. 3.1 (c) and Fig. 3.1 (d)). The buffer layer is etched using a different solvent (i.e. HCl:H_2O_2 with ratio of 1:4) exposing thus, the semi-insulating InP substrate. Further, a polyimide (i.e. PI-2545) layer is deposited, for the purpose of passivating the semiconductor surface and isolating the created mesa, and a via is opened for the top contact (Fig. 3.1 (e)), using a dry etch process (i.e. combination of CF_4/O_2 gases with flow rates of 5/20 sccm). Finally, the device metallic bond-pads are deposited, using a Ti/Au metal scheme, with a relatively large thickness (20/380 nm), in order to ensure their integrity during probing/bonding. Fig. 3.1 (f) illustrates a vertical cross-section of a fabricated RTD device, for which the complete fabrication process is detailed in Appendix A. A micrograph image of the fabricated RTD device is shown in Fig. 3.2.

Additional steps, typically before the bond-pad metal deposition, may be employed in order to realise passive components (i.e. thin film resistors or metal-insulator-metal (MIM) capacitors), required for RTD based monolithic integrated circuits. The design and realisation of such components will be further discussed in Chapter 4.

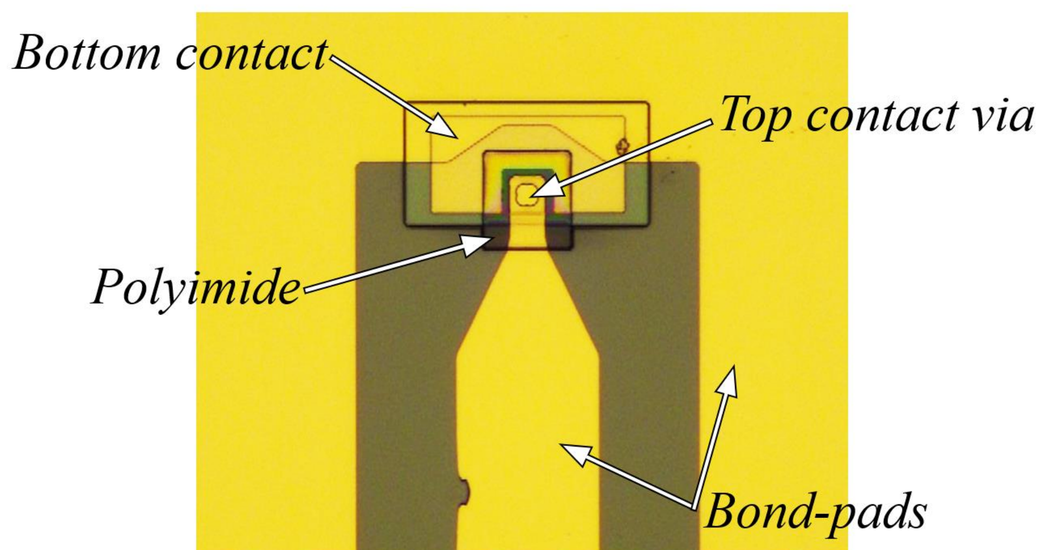

Figure 3.2 Micrograph of realised RTD device.

3.3 Fabrication processes

3.3.1 Sample preparation and cleaning

The discussed fabrication process requires as an initial step the preparation of individual samples from the grown 3-inch material wafer, in order to accommodate multiple fabrication runs. In this project, square samples with a side length between 10 – 12 mm were manually cleaved using a precision diamond scriber (Wafer Scribe ATV RV-129). Furthermore, as the originally outsourced wafer is coated with a layer of photoresist, in order to protect the polished sides during transportation from unwanted abrasion, a three-step cleaning stage is required. The choice of solvents for this purpose involve acetone ($(CH_3)_2CO$), methanol (CH_3OH) and isopropyl alcohol (IPA - C_3H_8O), with the sample placed in an ultrasonic bath, which also ensures the physical removal of any contaminant particles. As acetone is the primary organic compound involved in the removal of the resist coating, its high evaporation rate leads to associated residue on the sample surface, which can be further cleaned with methanol, followed by IPA. The same sample cleaning scheme is adopted between the individual fabrication steps in order to ensure uniform etching or good metal adhesion for deposition processes. The last step in sample preparation is represented by the identification of the correct side on which the fabrication is carried out. As previously discussed, due to the fact that both sides of the original wafer are polished, correct identification of the epi-side is important. A DC/impedance measurement obtained via probing of the wafer would reveal a higher impedance, typically in the MΩ range on the InP substrate side, in comparison to a tens of Ohms range on the side with the epitaxially grown device layers.

3.3.2 Lithography

Patterning is one of the main fabrication processes involved in semiconductor manufacturing technology, in which various features and structures are transferred from a mask onto the sample, via a radiation sensitive compound called resist [6]. The commonly employed lithography techniques include photolithography [7], in which the shape transfer from a template mask is achieved via exposure from an ultra-violet (UV) source, and electron-beam lithography (EBL) [8], which uses a highly focused beam of electrons to scan the sample surface. EBL is characterised by a superior

resolution in comparison with standard optical lithography, being typically adopted for patterning of sub-micron features, however its high associated costs and process times make it an unattractive solution for the RTD device fabrication involved in this work.

As the designed RTD mesa sizes described in this thesis range from 5×5 μm^2 up to 25×25 μm^2, photolithography was chosen as the primary patterning technique, which satisfies the imposed resolution constraints (achievable resolution of 0.5 μm). In addition, the high throughput of this optical lithography process constitutes an important advantage in terms of lowering the fabrication time for a complete RTD fabrication run, which requires a total of 9 patterning steps (including the realisation of passive components for RTD-based circuits). Another important benefit of the chosen patterning technique in terms of overall cost is represented by the reusability of the fabricated template mask in processing multiple samples with the same design (i.e. for different epitaxial structures), or even in the case of repeated fabrication runs.

The photolithography process was carried out using a Karl SuSS MA6 mask aligner, which using a UV source (with a corresponding wavelength $\lambda = 365$ nm) can transfer the designed layer pattern onto the sample, by exposing the coated resist through the optical windows, defined by a chromium metal layer on a physical mask. The hard mask, which incorporates the multi-layer RTD device and circuit layouts, was designed using the Tanner L-Edit software tool from Mentor Graphics [9], and realised using EBL, for increased feature accuracy, by Compugraphics International Ltd. Specific alignment markers are also included in the mask (along the boundaries), so that a subsequent fabrication step can be aligned with the preceding one.

Furthermore, the designed mask polarity needs to be made in line with the choice of light sensitive coating material, which is typically composed of a polymer, sensitiser and solvent [10] combination. Depending on the nature of the used polymer, which changes its chemical structure under UV radiation, photoresists can be classified as positive-tone, which becomes more soluble to developer agents, and negative-tone, for which in contrast, the exposure triggers a polymerisation reaction, making it difficult to dissolve. Negative-tone photoresist is known to have better adhesion capabilities to semiconductor wafers, without pre-treatment, and can attain a higher feature height-to-width ratio [11], but it is also characterised by lower resolution and inferior thermal stability in comparison to its counterpart. In this work, the patterning processes were

carried out using different positive-tone photoresists, from the S1800 series provided by MicroChem, in combination with a positive optical mask.

The uniform coating of the sample with a thin layer of the specific photoresist is achieved through a standard spin coating process. For this purpose, the compound dissolved into liquid form with the addition of the solvent, is deposited in the centre of the semiconductor material, which in turn is spun at a very high speed (typically around 4000 rpm), in order to achieve the desired film. Various parameters, such as spin time, speed and ramp speed, play key roles in the defined distribution and thickness of the applied photoresist. The generic three step (i.e. deposition, spread and thickness control) spin coating cycle can be illustrated using the timing diagram in Fig. 3.3, in which the compound is dispensed onto the stationary wafer.

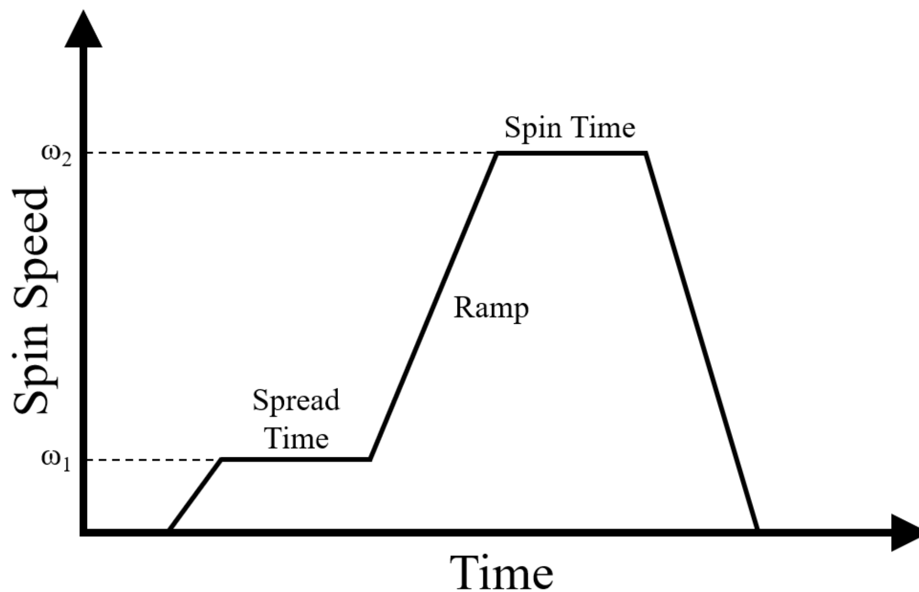

Figure 3.3 Typical photoresist spin coating cycle. Adapted from:[12].

Two photoresists (S1805 and S1818) were used in the fabrication of RTD devices described in this thesis. Based on the variation in compound viscosity, they can achieve different layer thicknesses under the same coating cycle conditions. The measured film thickness for the S1805 and S1818 photoresists (around 0.5 µm and 2 µm respectively, at 4000 rpm) are shown in Fig. 3.4, with a corresponding variation of approximately one over the square root of the spin speed. This feature plays a crucial role, particularly in the case of desired metal deposition thickness, for which the choice of photoresist needs to be made accordingly.

After the coating process, the excess solvent in the photoresist film is removed by a soft bake treatment, also called prebake (approximately 1 min at 115° C), which stabilises the compound at room temperature, improving the adhesion, and also making it less prone to contamination factors.

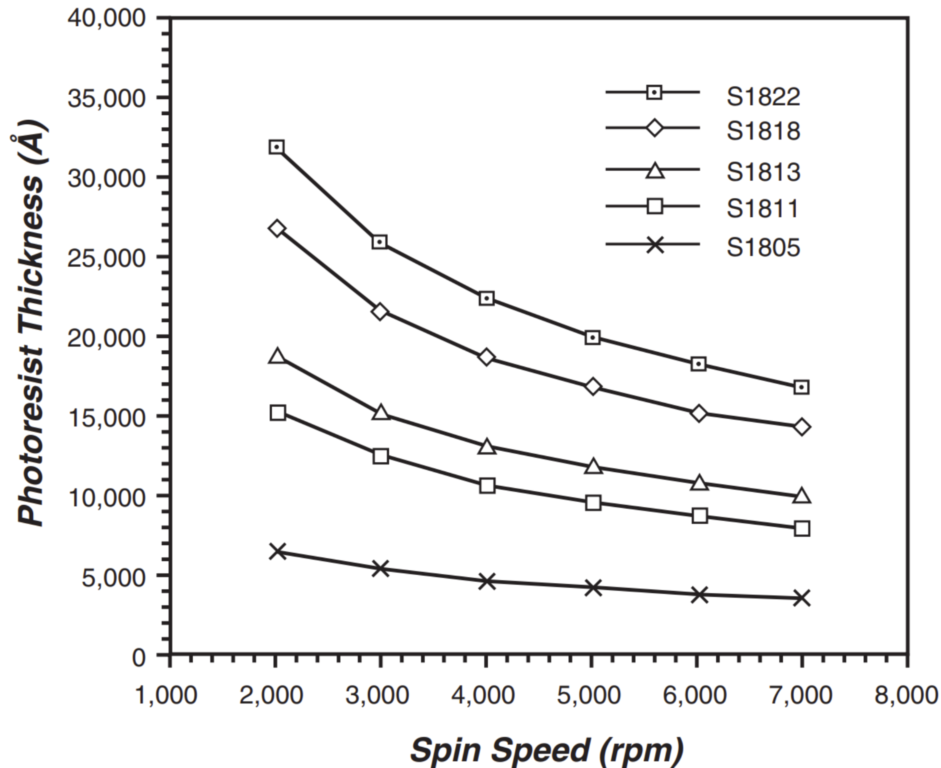

Figure 3.4 Characteristic spin speed curves for S1800 series photoresist. Source:[13].

Various other techniques can be adopted to improve the patterning process, such as removing waste resist from the back side of the sample, or excess resist near the sample edges.

By ensuring uniformity, the contact between the optical mask and the sample is thus improved, minimising the light diffraction effect during exposure. Following exposure (typically between 2 and 3 seconds required for the S1800 series resist) a developer is used to dissolve the exposed photoresist, revealing the design pattern.

Finally, a low temperature plasma ashing process is used to remove any residual resist (120 W RF power for 2 min.), which was not dissolved during the development phase, yielding the sample ready for the required metallisation or etching stage. The complete

photolithography process, adopted for a positive-tone photoresist, is presented with the aid of the diagrams in Fig. 3.5.

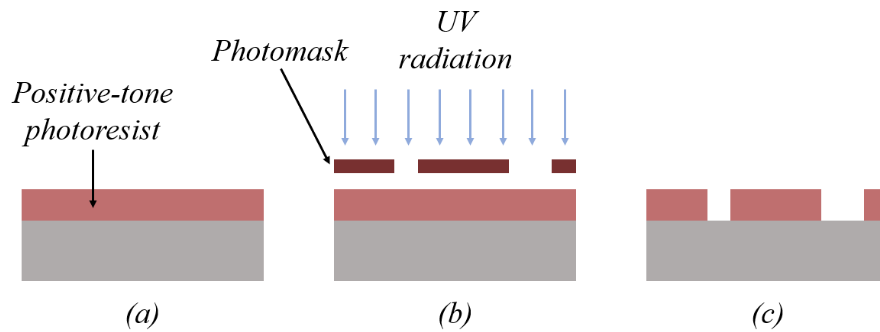

Figure 3.5 Photolithography process flow: (a) photoresist spin coating, (b) exposure using designed photomask under UV radiation, and (c) resist development

3.3.3 Metal deposition and lift-off process

Metal deposition in semiconductor devices and monolithic integrated circuits fabrication can be achieved through various methods, such as vacuum metallisation, also called physical vapour deposition (PVD), flame and/arc spraying, sputtering and plating processes [14]. The chosen technique for the metallisation processes involved in the fabrication of the device contacts and bond-pads in this project is electron-beam physical vapour deposition (EBPVD). In this process, the deposition is carried out under high-vacuum conditions in which an electron beam from a charged source (typically a tungsten filament) is focussed onto a target crucible, containing the desired metal, releasing metal atoms, which precipitate onto the sample. An important advantage of this processing technique is represented by the low pattern side wall coverage, which facilitates an optimal lift-off application.

The metal deposition process was carried out using the Plassys MEB550S (Plassys II and Plassys IV) equipment, capable of multi-layer coating, with up to 8 metals and alloys, including gold (Au), aluminium (Al), germanium (Ge), molybdenum (Mo), nickel (Ni), nickel-chromium (NiCr), palladium (Pd) and titanium (Ti).

A key aspect which was considered in the deposition of the metal contacts is the use of the available argon gun feature in the Plassys IV metallisation equipment, which uses plasma activated atoms to bombard the surface of the sample, and thus vaporise

any organic contaminants and natural oxides which form when the sample is exposed to air. This surface treatment technique, together with the discussed choice of metal scheme, should provide an optimal metal-semiconductor contact resistance, which was assessed through characteristic transmission line model (TLM) (details in Appendix B) and high-frequency measurement, and will be further discussed in Chapter 5.

Following the successful deposition of metal onto the entire surface of the sample, the next step of the metallisation process is the lift-off of the excess metal film (described below), in order to obtain the required design. For this purpose, a positive photoresist stripper formulation (SVC-14) is used, which removes the coating without damaging the thin metallic film. As previously discussed, the choice of photoresist thickness for patterning (i.e. present underneath the unwanted metal film regions) plays a critical role in maintaining the integrity of the features during the lift-off process. Generally, a higher resist thickness in comparison to the chosen film deposition thickness needs to be employed, (typically a ratio of resist to feature thickness > 2) in order to ensure metal discontinuity. In the case of the contact metal deposition, which has a total chosen thickness of 200 nm [4], a single layer of the S1805 photoresist coating would provide a sufficient height difference (approximately 300 nm) to meet the imposed specification. The complete process steps associated with the fabrication of the device metal contacts is illustrated in Fig. 3.6.

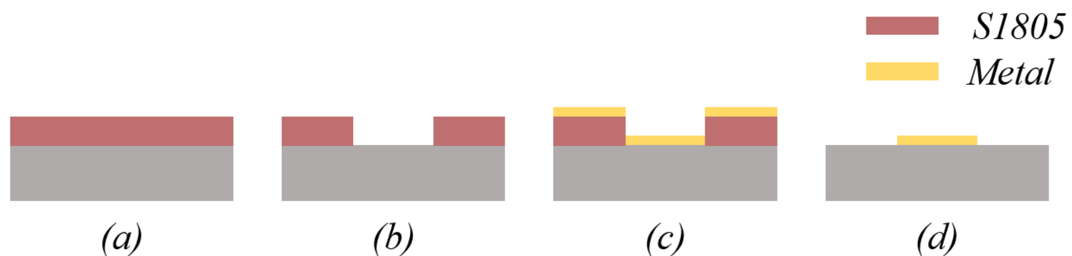

Figure 3.6 RTD metal contact fabrication steps: (a) spin coating S1805, (b) exposure and pattern development, (c) metal deposition, and (d) lift-off.

Other techniques to further optimise this process include the use of a photoresist treatment with organic compounds, such as chlorobenzene (C_6H_5Cl) or toluene (C_7H_8), prior to exposure, in order to create a specific undercut, by varying the solubility of the top part of the coating. However, the use of such compounds has been recently stopped within the JWNC facility, due to associated health risks. Instead, a slow lift-

off process has been employed using an SVC-14 photoresist stripper, with the sample placed in hot bath (50° C) for several hours.

A variation of the described process, however, was adopted for the fabrication of the RTD bond-pads, for which a Ti/Au metal scheme was chosen, with a total combined thickness of 400 nm (20/380 nm). Due to the increased deposition thickness, a lift-off resist (LOR-10A) coating was used in addition to the S1805 photoresist, in order to achieve a bi-layer lift-off process. During the two-step spin-coating process, a thin layer of LOR-10A was first applied to the sample, which by having a different dissolution rate in comparison to the S1805 photoresist, in the presence of the specific developer, creates a large undercut profile (Fig. 3.7 (b)). This feature guarantees a robust lift-off process, by ensuring no metal deposition along the resist sidewalls, as seen in the diagram illustration in Fig. 3.7.

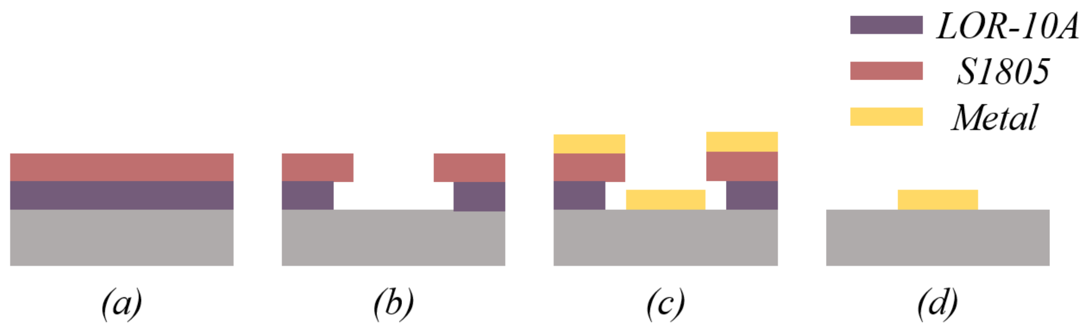

Figure 3.7 RTD bond-pad fabrication steps: (a) spin coating LOR-10A followed by S1805, (b) exposure and pattern development, showing the characteristic obtained undercut, (c) metal deposition, and (d) bi-layer lift-off process.

Poor metal lift-off, in the case of low photoresist thickness, without a well-defined undercut, could result in film peeling during subsequent fabrication steps, which could in turn lead to potential overall circuit failure.

3.3.4 Dielectric deposition

Deposition of dielectric materials, such as silicon dioxide (SiO_2), or silicon nitride (Si_3N_4) for fabrication of metal-insulator-metal (MIM) capacitors, or device passivation layers can be achieved by chemical vapour deposition (CVD). During this process, the sample is exposed under vacuum conditions to gas or vapor precursors,

for which a thermally induced chemical reaction triggers the formation of a solid coating at the heated interface [15].

The realisation of MIM capacitors for RTD based detectors, in this project, was accomplished using silicon nitride (Si_3N_4) as the insulator layer, which was deposited by inductively coupled plasma chemical vapour deposition (ICP-CVD) using the System 100 ICP-CVD from Oxford Instruments. The primary advantage of this deposition technique consists in the low achievable process temperature with the aid of the high plasma density (typically $>10^{11}$ cm^{-3}) present at the sample interface [16], making it thus suitable with the use of the S1800 series photoresist (i.e. it can be patterned using a lift-off process). Although the deposition directivity is low (i.e. deposition on the resist sidewalls is possible), the relatively low dielectric layer thickness of 75nm that was used, makes it possible to pattern Si_3N_4 film with the bi-layer lift-off process. The design and characterisation of the passive component will be further discussed in Chapter 4.

3.3.5 Etching and via opening process

The RTD mesa can be realised by either a wet or dry etching process, which selectively removes semiconductor material layers around the predefined contact, following the successful metal deposition and lift-off stages. Wet etching, which has been the primary methodology adopted in this work for device fabrication, involves the use of a liquid reactant (typically a diluted acid compound), which dissolves the specific material. This technique is generally preferred due to its low associated cost, process time and minimal surface impact, without the need for complex fabrication equipment, which requires operation by specialised personnel [17].

Although wet etching is characterised by a high degree of selectivity (i.e. solvents can be specific to the targeted material), the process also suffers from high isotropy [18] (but also dependent on the crystal orientation), which is defined as the ratio of lateral-to-vertical etching rate. This effect will result in an undercut profile of the device mesa (i.e. semiconductor is etched underneath the mask structure), which is exacerbated in the case of a high feature aspect ratio (i.e. mesa area to thickness ratio). This in turn leads to a degradation of the RTD effective area. An illustration of the wet etching

process used in the realisation of the RTD mesa, using the top metal contact as a mask is shown in Fig. 3.8.

The wet etching process of the InGaAs and AlAs layers was performed using a highly diluted solution composed of hydrogen peroxide, which acts as an oxidizing agent, and orthophosphoric acid (H_3PO_4:H_2O_2:H_2O = 1:1:38), with an etch rate of approximately 100 nm/min.

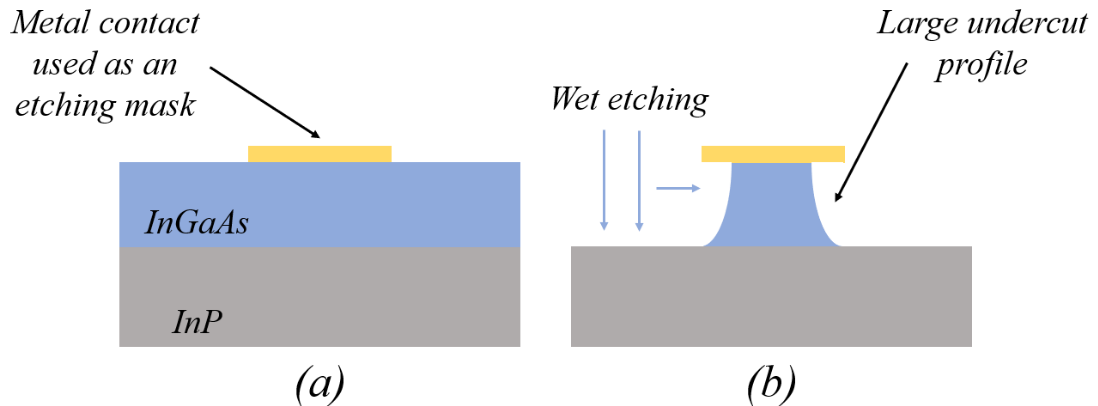

Figure 3.8 Illustration of the wet etching process used to define the InGaAs RTD mesa, using the metal contact as an etching mask (a). The isotropic nature of the process causes a large undercut profile of the mesa (b).

Due to the high selectivity of the described etchant, which does not react with the InP substrate, a different solution of hydrochloric acid and hydrogen peroxide (HCl:H_2O_2 = 1:4) was used to remove the InP buffer layer, with a characteristic etch rate of around 600 nm/min. An SEM image of a fabricated RTD top mesa is presented in Fig. 3.9.

In order to avoid the large undercut profile created by the wet etching process, particularly in the case of sub-micron device active areas, the RTD mesa can be defined by a dry etch technique. A dry etch process for InP-based materials has been developed by the JWNC at University of Glasgow, and has been proven to produce well-defined structures, with vertical feature side-walls [19], based on reactive ion etching (RIE), with the aid of a methane/hydrogen/oxygen gas combination (CH_4/H_2/O_2), with corresponding flow rates of 6, 54 and 0.16 sccm, respectively. This processing technique was not adopted in this work, due to the high designed RTD active areas (> 5 × 5 μm^2).

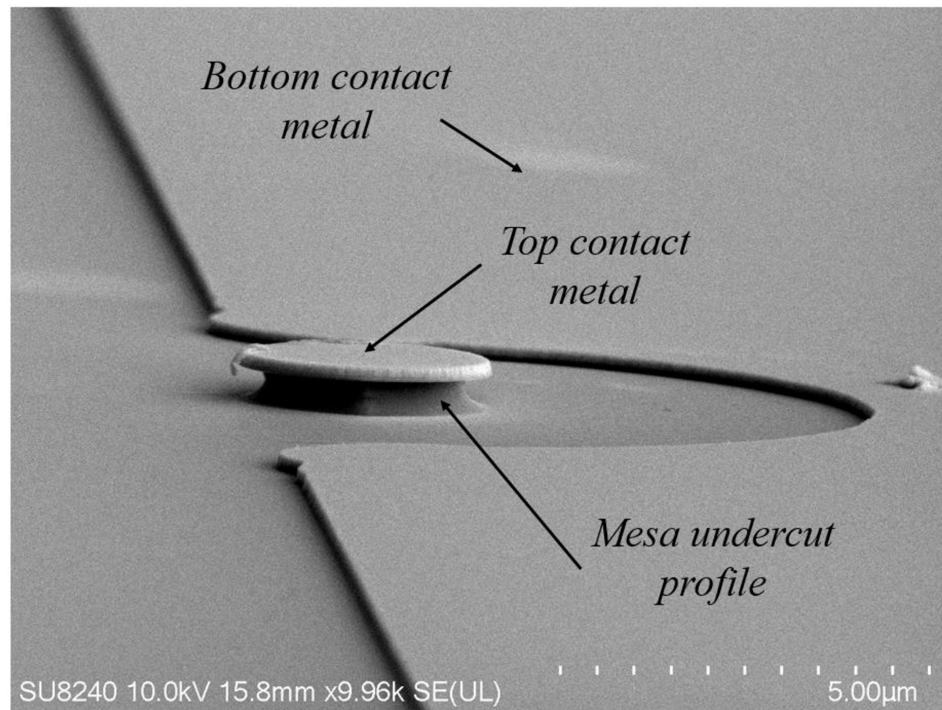

Figure 3.9 SEM image of a realised RTD top a mesa displaying the undercut profile due to the isotropic nature of the wet etching process.

A dry etch method, however, was used to open a via in the passivation layer, in order to facilitate the physical connection between the top metal contact and the deposited bond-pad. The dry etching process relies on material removal by exposing the sample to a bombardment of high energy gas ions, which react with the exposed surface, and has been preferred for this particular purpose due to its high uniformity and anisotropic characteristic (i.e. directional etching). As previously discussed, the device passivation was accomplished using the PI-2545 polyimide from HD Microsystems, with a coating thickness of approximately 1.2 μm, in order to meet the required RTD mesa height (approximately 1.16 μm distance from the top contact layer to the InP substrate). The PI-2545 was applied to the sample using a spin coating process, with a spin speed of 8000 rpm, in order to achieve the desired thickness [20] and thermally cured at 180° C for 6 hours. The specific dry etching process of the PI-2545 layer was adapted from [17], and has been carried out in this work using the RIE80+ equipment from Oxford Instruments. For this purpose, a combination of tetrafluoromethane (CF_4) and oxygen (O_2) gases was used, with corresponding flow rates of 5 sccm and 20 sccm, respectively, which resulted in a measured etch rate of approximately 215 nm/min for the polyimide. Due to the fact that this process also etches the S1805 coating, used to

define the via feature at a measured rate of 150 nm/min, a higher thickness of photoresist layer was chosen, and achieved using spin coating at 1500 rpm, with a resulting thickness of around 0.9 μm (based on Fig. 3.4).

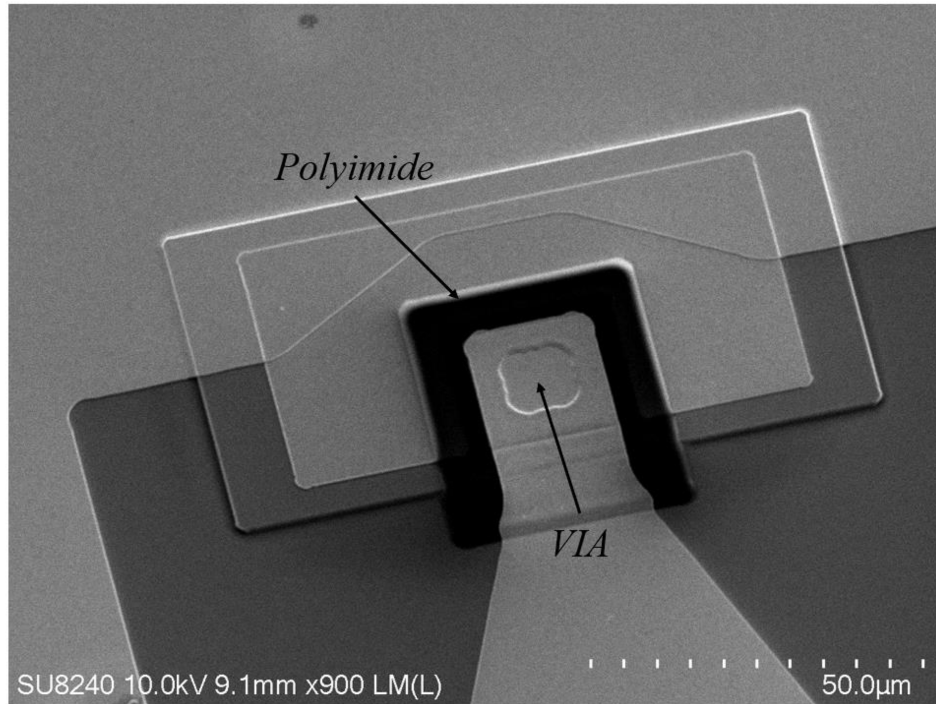

Figure 3.10 SEM image of the realised via in the polyimide passivation layer, which surrounds the RTD mesa and aid the connection between the top metal contact and bond-pads.

To further ensure the integrity of the designed via pattern, the precise process timing (i.e. time required for the removal of the exposed polyimide layer) was controlled using a laser interferometry end-point detector LEM from Horiba Scientific [21]. In this in situ technique, a monochromatic light beam from a laser source is directed at the partially transparent, exposed polyimide film (i.e. patterned by the photoresist layer) on the sample. The detected intensity of the total reflected radiation is altered by the constructive and destructive interference, generated between the reflected radiation from the vacuum-polyimide interface and the polyimide-substrate interface. The continuous variation in optical path length between the reflected light beams, as a result of the change in polyimide thickness during the etching process, translates to an oscillating behaviour of the overall detected radiation intensity (i.e. due to the phase difference of the two light components) [22]. Upon the entire removal of the polyimide layer, the signal intensity will remain constant signalling the process completion.

Given the relatively small sample size (12 mm × 12 mm), the process timing was monitored continuously using a single point measurement, with the light beam directed at the center of the sample. The typical process time using this technique is approximately 6 min (350 seconds) and can vary slightly due to potential uneven distribution of the PI-2545 during the spin coating process.

3.4 Summary and discussion

In this chapter, the main processes associated with the realisation of RTD devices and monolithic integrated circuits have been described. The complete device fabrication flow has been presented starting from the epitaxial heterostructure of the device.

Photolithography was the preferred patterning technique due to the low process cost and design repeatability. This process satisfied the imposed feature constraints determined by the choice of device active area sizes (ranging between 5 × 5 μm^2 and 25 × 25 μm^2), which were investigated in relation to device stability and also maximising the device non-linear characteristics for the detector application, further described in Chapter 5 and 6 respectively. Two different lift-off techniques, based on the thickness of the deposited metal, in the case of device contacts and bond-pads, or dielectric material for MIM capacitor realisation were employed (single layer and bi-layer). Furthermore, a wet etching process for the purpose of defining the RTD mesa structure, by selective removal of the InGaAs/AlAs layers was adopted, while a dry etch process, based on reactive-ion etching was used to open a via in the RTD passivation layer. The complete RTD fabrication process is detailed in Appendix A, while the characterisation of various circuit components and RTD devices is further discussed in Chapter 4 and 5, respectively.

3.5 References

[1] A. C. Cornescu, R. Morariu, A. Ofiare, A. Al-Khalidi, J. Wang, J. M. L. Figueiredo, and E. Wasige, "High-efficiency bias stabilization for resonant tunneling diode oscillators," *IEEE Transactions on Microwave Theory and Techniques,* vol. 67, no. 8, pp. 3449-3454, 2019.

[2] S. Javalagi, V. Reddy, K. Gullapalli, and D. Neikirk, "High efficiency microwave diode oscillators," *Electronics Letters,* vol. 28, no. 18, pp. 1699-1701, 1992.

[3] P. Roblin and H. Rohdin, *High-speed heterostructure devices: from device concepts to circuit modeling*. Cambridge university press, 2002.

[4] A. C. Cornescu, "High efficiency and high frequency resonant tunneling diode sources," PhD Thesis, University of Glasgow, 2019.

[5] A. M. Crook, E. Lind, Z. Griffith, M. J. W. Rodwell, J. D. Zimmerman, A. C. Gossard, and S. R. Bank, "Low resistance, nonalloyed Ohmic contacts to InGaAs," *Applied Physics Letters,* vol. 91, no. 19, p. 192114, 2007.

[6] R. F. Pease and S. Y. Chou, "Lithography and other patterning techniques for future electronics," *Proceedings of the IEEE,* vol. 96, no. 2, pp. 248-270, 2008.

[7] R. C. Jaeger, *Introduction to microelectronic fabrication*. Prentice Hall Upper Saddle River, NJ, 2002.

[8] M. Altissimo, "E-beam lithography for micro-/nanofabrication," *Biomicrofluidics,* vol. 4, no. 2, p. 026503, 2010.

[9] Menthor. "Tanner EDA - L-Edit." https://www.mentor.com/tannereda/multimedia/tanner-16-3-pycell-ipdk-support-webinar (accessed 30.12.2020).

[10] J. M. Quero, F. Perdigones, and C. Aracil, "Microfabrication technologies used for creating smart devices for industrial applications," in *Smart Sensors and Mems*: Elsevier, pp. 291-311, 2018.

[11] J. M. Shaw, J. D. Gelorme, N. C. LaBianca, W. E. Conley, and S. J. Holmes, "Negative photoresists for optical lithography," *IBM journal of Research and Development,* vol. 41, no. 1.2, pp. 81-94, 1997.

[12] C. A. Mack, *Field guide to optical lithography*. SPIE Press Bellingham, WA, 2006.

[13] Shipley. "Microposit S1800 series photo resists " https://kayakuam.com/wp-content/uploads/2019/09/S1800.pdf (accessed 02.12.2020).

[14] K. Seshan, *Handbook of thin film deposition processes and techniques*. William Andrew, 2001.

[15] H. O. Pierson, *Handbook of chemical vapor deposition: principles, technology and applications*. William Andrew, 1999.

[16] J. Lee, K. Mackenzie, D. Johnson, S. Pearton, F. Ren, and J. Sasserath, "Development of low-temperature silicon nitride and silicon dioxide films by inductively coupled plasma chemical vapor deposition," in *Materials Research Society Symposium Proceedings*, vol. 573: Materials Research Society, pp. 69-80, 1999.

[17] J. Wang, "Monolithic microwave/millimetrewave integrated circuit resonant tunnelling diode dources with around a milliwatt output power," University of Glasgow, 2014.

[18] S. J. Moss and A. Ledwith, *Chemistry of the Semiconductor Industry*. Springer Science & Business Media, 1989.

[19] L. Wang, "Reliable design of tunnel diode and resonant tunnelling diode based microwave sources," PhD Thesis, University of Glasgow, 2012.

[20] T. Walewyns, N. Reckinger, S. Ryelandt, T. Pardoen, J.-P. Raskin, and L. A. Francis, "Polyimide as a versatile enabling material for microsystems

fabrication: Surface micromachining and electrodeposited nanowires integration," *Journal of Micromechanics and Microengineering,* vol. 23, p. 095021, 2013.

[21] HoribaScientific. "Laser Interferometric Camera and Endpoint Detector." https://www.horiba.com/uk/scientific/products/process-equipment/endpoint-detection/details/lem-502/ (accessed 30.12.2020).

[22] W. Wei, L. Zhongwen, W. Wu, and G. Yungui, "Optical interferometry endpoint detection for plasma etching," in *2007 8th International Conference on Electronic Measurement and Instruments*, pp. 4-252-4-255, 16-18 Aug. 2007, 2007.

Chapter 4. Components for RTD circuits

4.1 Introduction

As briefly discussed in Chapter 3, additionally to the realisation of the RTD device, various other components need to be considered for the successful implementation of monolithic integrated circuits. In relation to the targeted application in this project, which consists of an RTD based detector, the design requirements include passive components such as thin film resistor networks, for device stabilisation purposes, transmission lines, realised in coplanar waveguide (CPW) configurations, metal-insulator-metal (MIM) capacitors for RF decoupling, and inductive elements, designed as shorted CPWs. In this chapter, the design concepts of the above-mentioned components are described, and their assessed performance is presented as a comparison between theoretical determined values and experimental data. Furthermore, an InP based PIN junction diode suitable for hetero-epitaxial integration with the presented RTD structure is proposed and characterised, in order to investigate its performance for high-speed applications.

4.2 Design of passive components

4.2.1 Coplanar waveguide (CPW)

The coplanar waveguide (CPW), which was first demonstrated in [1], is a type of planar transmission line, consisting of a central conductor with adjacent, equally spaced ground planes on either side, as shown in Fig. 4.1. In comparison with the more popular microstrip transmission line design, the CPW has a superior advantage in terms of fabrication simplicity, which arises from the fact that all conductive elements are situated in the same plane, eliminating thus the need for via connections to a backside ground plane. In addition, the CPW is characterised by a superior performance at millimetre-wave (mmWave) frequencies (i.e. above 30 GHz) in particular due to its suppression of higher spurious wave propagation modes, lower radiation loss and minimal dispersion properties [2]. The main disadvantages of this structure are its relatively low power handling capability and the requirement for potential airbridge connections between the ground planes at discontinuities or at

quarter wavelength intervals ($\lambda/4$). This technique is implemented in order to suppress the parasitic mode (coupled slotline mode) while equalising the potential of the two ground planes [3]. Fortunately, both disadvantages are not applicable to the inherently low power (mW levels) and compact (longest CPW dimension is less than $\lambda/4$) RTD circuits.

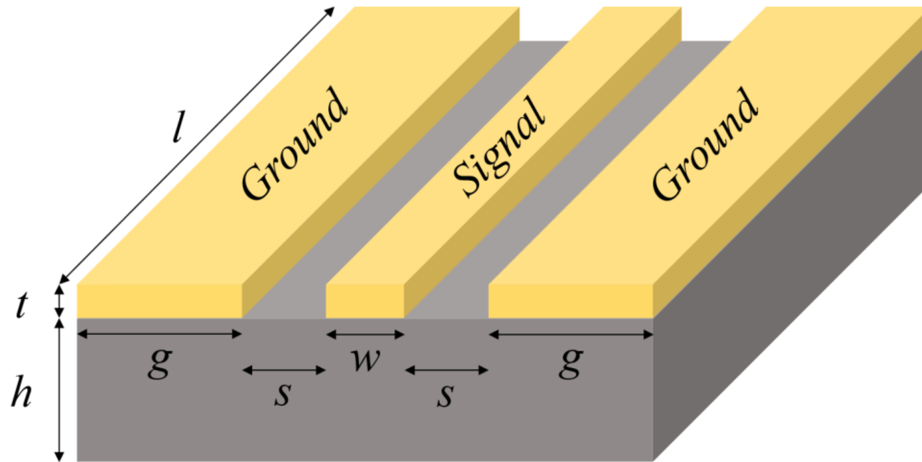

Figure 4.1 Diagram of a standard coplanar waveguide (CPW) transmission line structure. The key design parameters include the thicknesses of the substrate (h) and conductor (t), the conductor length (l), the conductor spacings (s) and the widths of the ground planes (g) and signal line (w).

In this work, the CPW has been used to connect to RTD devices for on-wafer probing. The characteristic impedance (Z_0) of the CPW is defined in terms of the width of the central conductor line (w), the spacing between the adjacent conductors (s) and the substrate dielectric constant (ε_r) by [4]:

$$Z_0 = \frac{30\pi}{\sqrt{\varepsilon_{eff}}} \frac{K(k')}{K(k)} \tag{4.1}$$

where ε_{eff} is the effective dielectric constant, and can be approximated as [5]:

$$\varepsilon_{eff} = \frac{\varepsilon_r + 1}{2} \tag{4.2}$$

and $K(k)$ and $K(k')$ represent a complete elliptic integral of the first kind and its complement, for which k and k' are given by:

$$k = \frac{w}{w + 2s} \tag{4.3}$$

$$k' = \sqrt{1 - k^2} \tag{4.4}$$

Finally, the ratio of the two integrals can be approximated by:

$$\frac{K(k')}{K(k)} = \frac{1}{\pi}\log\left(2\frac{1 + \sqrt{k'}}{1 - \sqrt{k'}}\right), for\ k \leq 0.7 \tag{4.5}$$

The designed CPW characteristic impedance, used in this work has been chosen at Z_0 = 50 Ω, in order to satisfy the impedance matching requirement imposed by the measurement equipment. The structural parameters (i.e. w, and s) required to obtain the targeted impedance have been computed with the aid of the LineCalc tool, available within the Advanced Design System (ADS) software from Agilent Technologies [6]. Based on the InP substrate used in the design of the RTD epi-structure, detailed in Table 3.1, with a corresponding thickness of h = 630 μm and a dielectric constant ε_r = 12.5 [7], the calculated parameters for the width of the central conductor and the conductor spacings are 60 μm and 40 μm, respectively. In addition, in order to ensure minimal signal attenuation within the CPW structure, the conductor thickness should typically be chosen to be at least 3 times the skin depth (δ) [8], which defines the relative depth of the current flow in the conductor. The skin depth is given by:

$$\delta = \sqrt{\frac{\rho}{\mu_0 \mu_r f \pi}} \tag{4.6}$$

where ρ is the metal resistivity (ρ_{gold} = 2.44 × 10^{-8} Ωm), μ_0 is the permeability of vacuum (μ_0 = 4π × 10^{-7} H/m), μ_r is the relative permeability (μ_r = 1), and f is the targeted design frequency. For example, for a targeted frequency of f = 110 GHz (i.e. maximum frequency for device RF characterisation) the corresponding skin depth, based on Eqn. 4.6 is approximately δ = 237 nm, and will vary proportional to the square root of f^{-1}.

In RTD-based circuits, the CPW is used to convey DC and RF signals between the device and various passive components, and in a shorted configuration (i.e. CPW stub,

it is used to realise an inductive element) [9]. Fig. 4.2 shows an inductor designed as a shorted CPW stub.

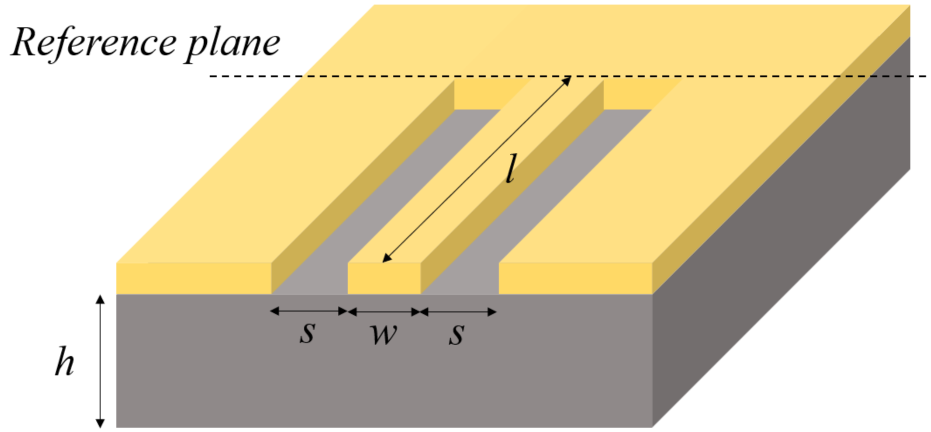

Figure 4.2 Inductor realised as a CPW in shorted configuration. Adapted from: [9].

The input impedance (Z_{in}) of a standard CPW structure looking into the line (assuming a lossless line model) can be defined in terms of its effective length (l) for an arbitrary load (Z_L) as [8]:

$$Z_{in} = Z_0 \frac{Z_L + jZ_0 tan(\beta l)}{Z_0 + jZ_L tan(\beta l)} \tag{4.7}$$

where β is the phase constant computed as:

$$\beta = \frac{2\pi f \sqrt{\varepsilon_{eff}}}{c_0} \tag{4.8}$$

Considering the special case shown in Fig. 4.2, for which the CPW is terminated in a short, the load impedance can be approximated as $Z_L \approx 0$ (i.e. neglecting the inductive component, which appears beyond the indicated reference plane, due to the stored magnetic energy resulting from the RF current flow though the termination [9]). Eqn. 4.7 can thus be simplified to:

$$Z_{in} = jZ_0 tan(\beta l) \tag{4.9}$$

where Z_{in} considered purely imaginary, irrespective of length l. Furthermore, for a given CPW with a designed electrical length less than $\pi/2$, the input impedance can be considered as an inductive reactance:

$$Z_{in} = j\omega L = jZ_0 tan(\beta l) \quad (4.10)$$

where L is the equivalent inductance of the CPW line, and ω is the angular frequency defined as:

$$\omega = 2\pi f \quad (4.11)$$

From a design perspective, Eqn. 4.10 can be rearranged to obtain the desired CPW length l in terms of the targeted operating frequency and designed characteristic impedance:

$$l = \frac{1}{\beta}\tan^{-1}\left(\frac{\omega L}{Z_0}\right) \quad (4.12)$$

This concept of the shorted CPW stub as inductor, for the design of RTD based integrated circuits, however, suffers from a major drawback, due to the fact that it does not facilitate different potentials between the signal line and ground conductors. This limitation can be overcome by loading the transmission line short by a MIM capacitance [5]. The realised capacitor, between the central signal conductor and ground plane appears in series with the line inductance and can be designed to act as an RF low impedance path at the design frequency. The design concept of MIM capacitors will be further detailed in the following section.

4.2.2 Metal-insulator-metal (MIM) capacitor

Metal-insulator-metal (MIM) and interdigital are the two approaches to realise planar capacitors for MMICs. The implementation choice is typically based on the size constraints imposed by the design and the required capacitor value. Generally, MIM capacitors are preferred due to their low associated parasitics and high quality factor (*Q*), used particularly for highly compact circuit designs, which require capacitance values in the pF range [10].

In this project, MIM capacitors were mainly used in the design of RTD-based detectors. The design details of the detector circuit, together with its operation principle will be further discussed in Chapter 6. The basic design layout of the designed MIM capacitor consists of two metal layers separated by a dielectric layer,

as shown in Fig. 4.3, with the geometry of the component designed to load the shorted CPW between the signal and ground lines.

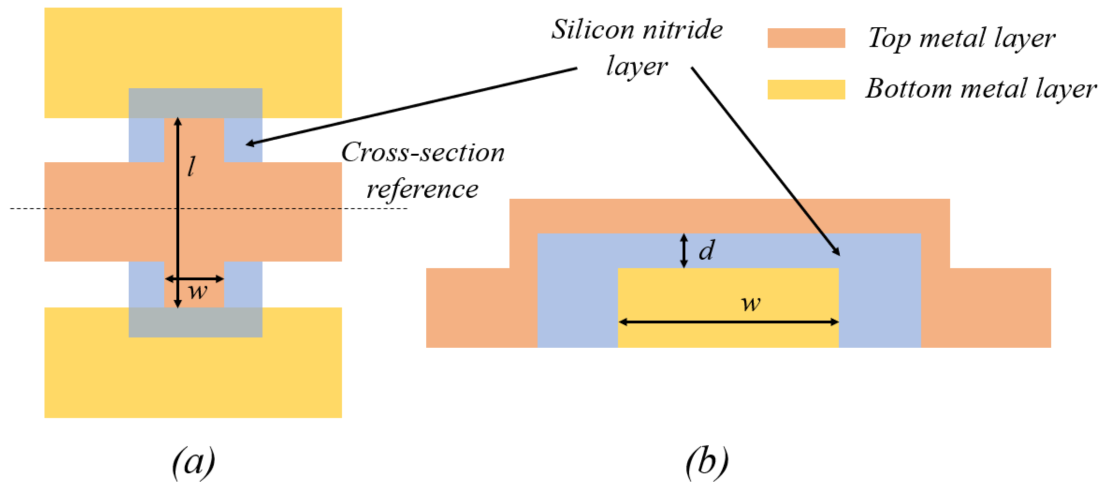

Figure 4.3 Top (a) and cross-sectional (b) view of a standard MIM capacitor layout used to load the shorted CPW, with an effective area defined by w and l, and a dielectric thickness d.

The designed capacitance value can be computed as:

$$C = \varepsilon_0 \varepsilon_r \frac{wl}{d} \tag{4.13}$$

where ε_0 is vacuum permittivity (ε_0 = 8.854 × 10^{12} F/m), ε_r is the material dielectric constant, w and l are the component width and length, and d is the thickness of the dielectric layer.

In this work, silicon nitride (Si_3N_4) with a thickness of d = 75 nm was the choice dielectric material (ε_r = 6.8). Considering the insulator layer structural and physical parameters, the computed capacitance, based on Eqn. 4.13 is approximately 0.8 fF/µm^2. The parasitic components formed formed between the (lateral) top and bottom conductor was neglected in this estimation as it was estimated to ~ 0.6 fF, lower by four orders of magnitude compared to the designed capacitance. Capacitors, in parallel configuration, with a fixed width of w = 140 µm (determined by the ground-to-ground spacing of the designed 50 Ω CPW structure) and various lengths l, ranging from 10 µm up to 20 µm have been designed and fabricated in this work. The characterisation of such passive component will be further described in section 4.3.

4.2.3 Thin-film resistors

Thin-film resistors were employed for device stabilisation purposes, particularly in order to suppress the low-frequency bias parasitic oscillations of the RTD within the NDR region during characterisation. Typically, metal thin-film resistors are used in MMIC (monolithic microwave integrated circuit) designs as they offer a higher temperature stability and precision, with a lower temperature coefficient of resistance (TCR) in comparison to semiconductor mesa resistors [11][12]. For this purpose, a nickel-chromium (NiCr) alloy (60:40) was chosen for the realisation of the stabilising resistors, deposited by EBPVD directly on the InP substrate. Even though NiCr resistors are commonly characterised by good power density handling capability, low TCR (77 ppm/°C [13]), and high resistance to oxidation [14], they generally tend to suffer from low fabrication repeatability due to high variation in Ni:Cr percentage as a result of the difference in vapour pressure between the two constituent metals [15], which could result resistivity variations between sequential runs.

The layout design of the shunt resistor network (i.e. two parallel thin-film resistors between the signal line and the ground plane of the CPW structure), is shown in Fig. 4.4 (top and side view).

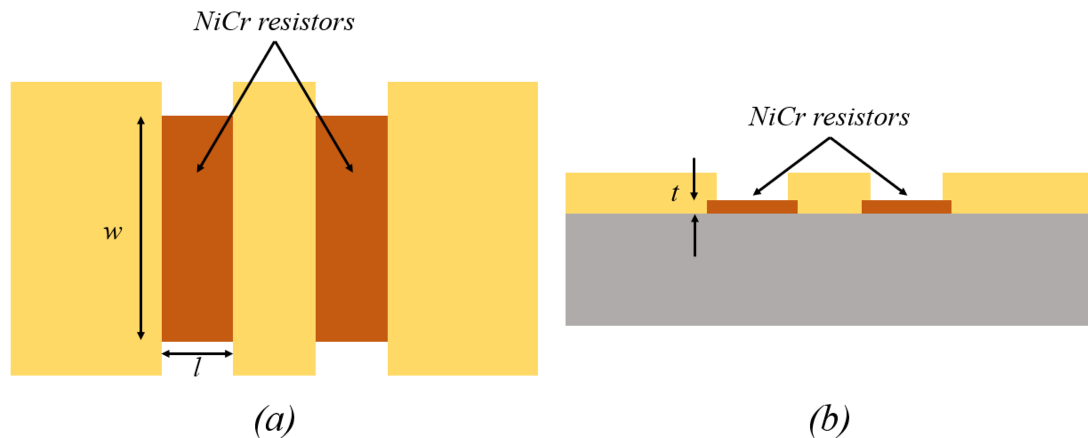

Figure 4.4 Top (a) and side view (b) of the thin-film NiCr shunt resistor network, for which w, l, and t are the width, length and thickness of the NiCr layer, respectively.

The designed resistor value can be computed by:

$$R = \rho \frac{l}{wt} = R_{sh} \frac{l}{w} \tag{4.14}$$

where l, w, and t are the length (in the direction of the current flow), width and thickness of the NiCr thin-film resistor respectively, and ρ is the material bulk resistivity ($\rho = 1.65 \times 10^{-6}$ Ωm). A more common expression for the resistor value, in the case of constant thickness designs, can be given in terms of the sheet resistance R_{sh}, defined as $R_{sh} = \frac{\rho}{t}$ (Ω/□). The defined sheet resistance value of NiCr for a thin-film thickness of 33 nm has been determined experimentally at approximately 50 Ω/□ in [16], and was adopted as a design guideline for the realisation of the shunt resistor network in this work.

4.3 Characterisation of passive components

The accuracy of the designed passive components described in section 4.2, including CPW transmission lines, MIM capacitors and thin-film NiCr resistors, used in the characterisation of RTD devices and the realisation of RTD-based detector circuits, was assessed using 2-port scattering parameter (S-parameter) measurements up 110 GHz. For this purpose, the vector network analyser (VNA) Keysight E8361A was used in order to measure the transmission and reflection coefficients (S_{12}, S_{21}, S_{11} and S_{22}) of the structure under test, as a function of applied signal frequency. Standard calibration of the VNA was performed to eliminate systematic errors and to move the measurement reference plane close to the tips of the probes. In this project, the Short-Open-Load-Thru calibration technique was performed, using the reference loads provided on the impedance standard substrate (ISS) from Cascade Microtech.

By measuring the provided short, open, load (50 Ω) structures, for each individual port, and further connecting the two ports using the thru structure, the VNA software can compute, and further compensate for [17]:

- Directivity, due to generated signal leakage through the transmission path directly towards the receive path, thus bypassing the structure under test.
- Transmission/reflection tracking, due to potential frequency variations between the reference and transmitted/reflected waves.
- Port match errors, due to source/load mis-matches, resulting in multiple reflections between the ports and the structure under test.
- Signal leakage or crosstalk between probes.

4.3.1 Coplanar waveguide

The characterisation of the Finite Ground CPW transmission line was performed using a fabricated structure on the semi-insulating InP substrate of the RTD wafer. As previously discussed, the targeted design characteristic impedance was chosen as Z_0 = 50 Ω and was realised using a signal line width w = 60 μm, and a spacing s = 40 μm to each ground plane. The width of the ground plane was designed with g = 150 μm, 2.5 times larger than the signal line width, in order to ensure minimal radiation losses [18]. An SEM image of the fabricated test structure (l = 500 μm) is shown in Fig. 4.5.

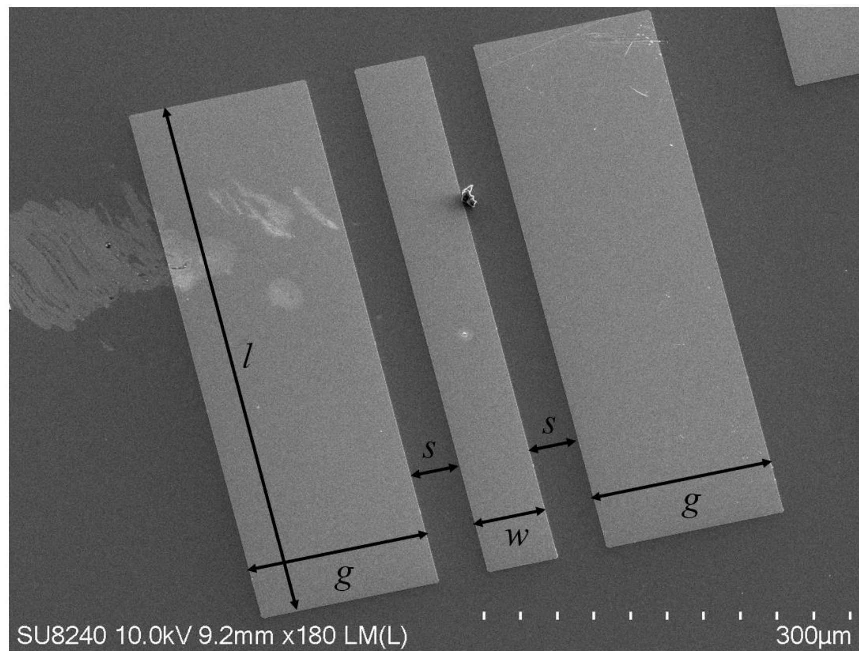

Figure 4.5 SEM image of a Finite Ground CPW transmission line test structure designed with a characteristic impedance Z_0 = 50 Ω.

The computed inductance per unit length of the presented transmission line is approximately 0.42 fH/nm, while the calculated insertion loss is approximately 0.53 dB/mm at 110 GHz [19].

The test structure was characterised using a 2-port S-parameter measurement up to 110 GHz. The corresponding port-1 and port-2 reflection coefficients (S_{11} and S_{22}) are shown on the plotted Smith chart in Fig. 4.6. As expected, the experimentally determined characteristic impedance Z_0 of the CPW is in good agreement with the designed value of 50 Ω. In addition, the measured transmission coefficients (S_{12} and S_{21}), plotted in Fig.4.7, indicate an average insertion loss of approximately 0.2 dB,

ensuring minimal signal attenuation when transmitted through the structure. Noise was observed for frequencies above 60 GHz, which is believed to be introduced by the measurement equipment extenders, which provide a transition between the coaxial and rectangular waveguide, in order to facilitate the frequency range up to 110 GHz.

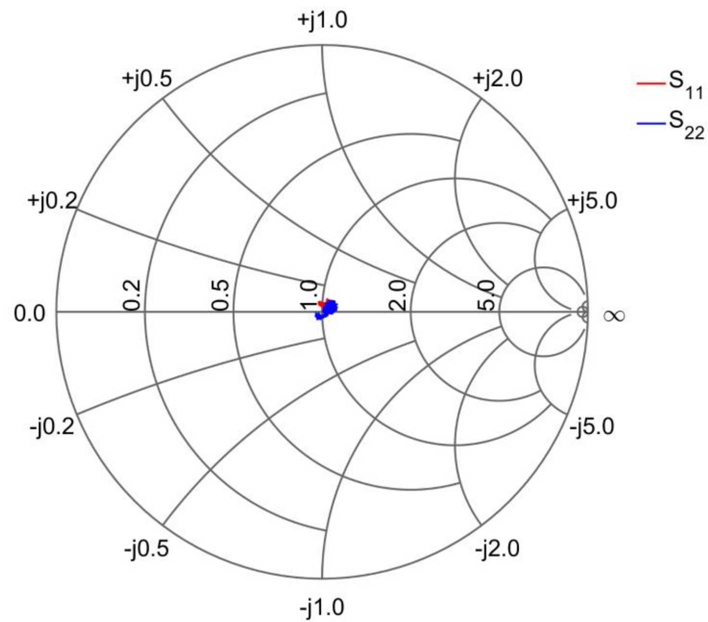

Figure 4.6 Measured Port-1 and Port-2 reflection coefficients (S_{11} and S_{22}) of the CPW test structure presented on a Smith chart.

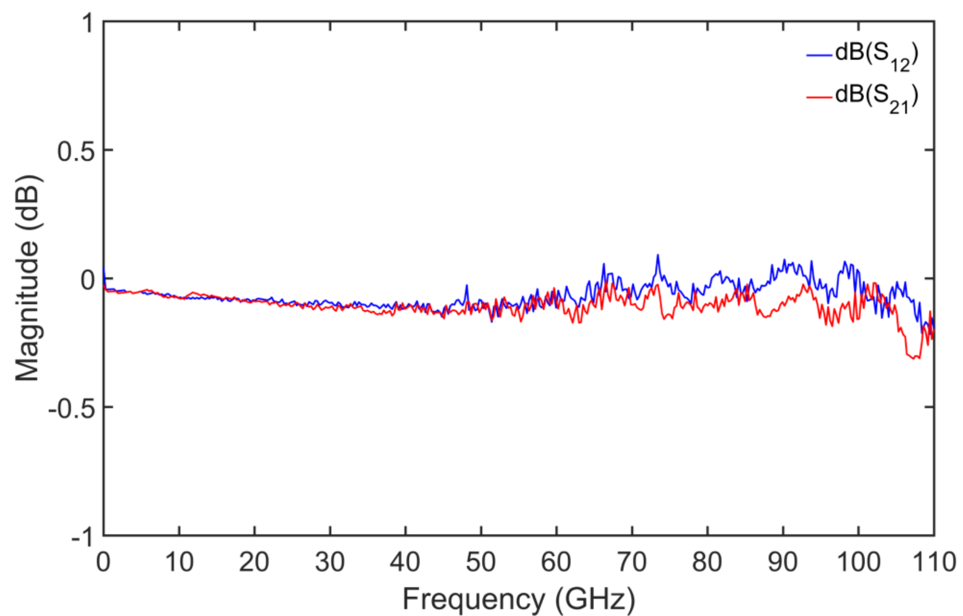

Figure 4.7 Measured transmission coefficients (S_{12} and S_{21}) of the CPW test structure.

4.3.2 MIM capacitors

In the design of RTD-based detector circuits, MIM capacitors were designed in a parallel configuration, in order to realise shorted CPW inductors, while also providing a low impedance path for specific signal frequencies. An SEM image of a realised test structure, for characterisation purposes of parallel MIM capacitors is shown in Fig. 4.8.

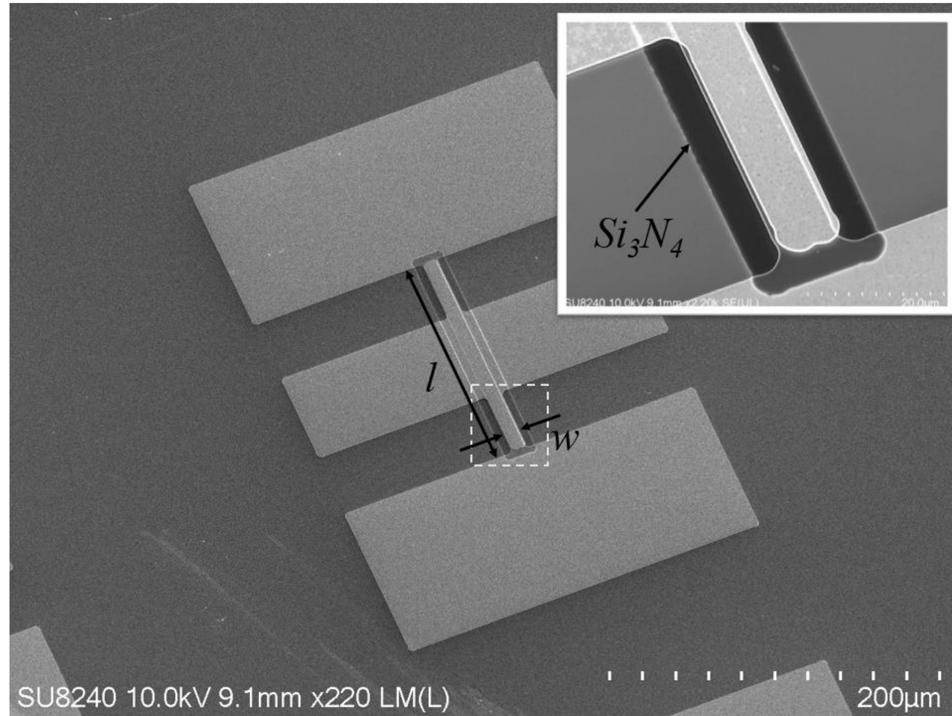

Figure 4.8 SEM image of a fabricated CPW test structure, shorted by a parallel capacitor. The inset shows the Si_3N_4 dielectric layer sandwiched between two metal layers to realise the MIM capacitor.

The behaviour of the MIM capacitor can be modelled using the equivalent circuit shown in Fig. 4.9, where R_s is the series resistance introduced by the conductor, L is the equivalent inductance of the shorted CPW structure, and C represents the designed MIM capacitor. Similar to the case of the standard CPW transmission line, the MIM capacitor shorted structure, was characterised using S-parameter measurements, up to 110 GHz. The equivalent circuit parameters (i.e. R_s, L and C), were extracted by fitting the measured reflection coefficient of the structure, with the aid of the presented model in the entire frequency range, using a standard optimization process. Fig. 4.10 shows a comparison between the measured and modelled structure in the form of its reflection

and transmission coefficients S_{11} and S_{21} on a Smith chart, with the extracted parameter values of: R_s = 0.2 Ω, L= 40.6 pH and C = 1.8 pF. The obtained capacitance is close to the designed value of 1.68 pF, which was estimated using Eqn. 4.13, for an area of 140 μm × 15 μm and a Si_3N_4 dielectric thickness of 75 nm. Furthermore, the measured data indicates that the capacitor will act as a low impedance ($Z = 0.65 + j0.03$ Ω) path to ground, for frequencies above 18.5 GHz, and its performance will start degrading at very high frequencies, where the series parasitic inductance becomes dominant.

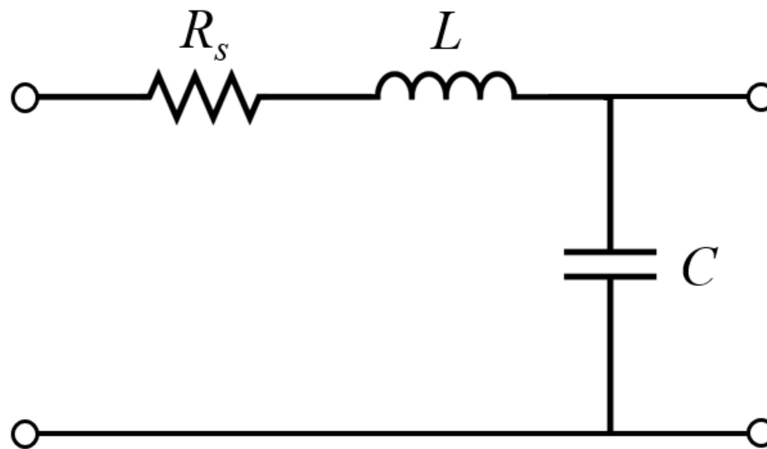

Figure 4.9 Equivalent circuit model of a shorted CPW by a MIM capacitor.

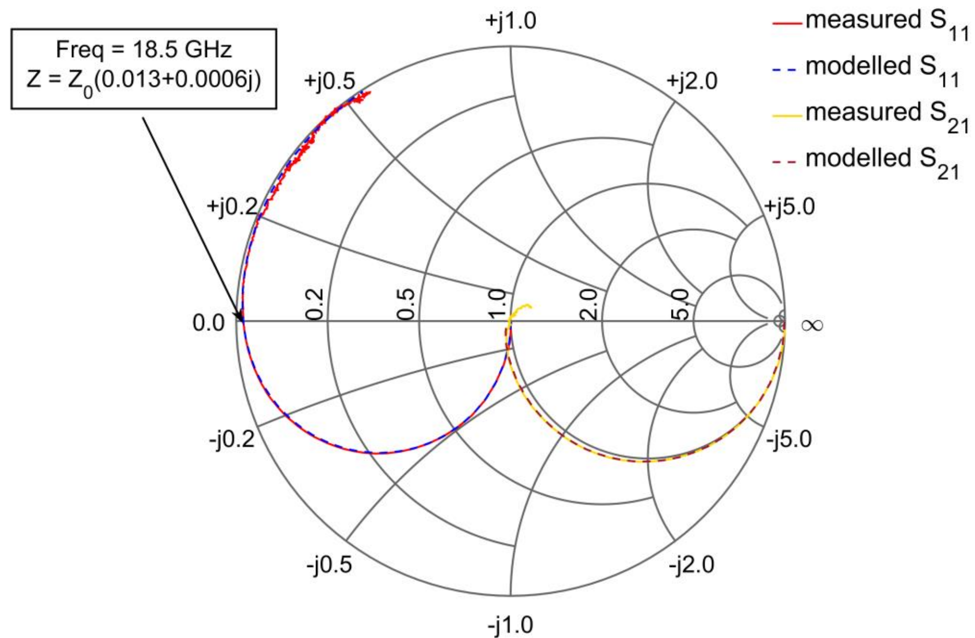

Figure 4.10 Measured and simulated reflection and transmission coefficients S_{11} and S_{21} of a shorted CPW by a MIM capacitor.

4.3.3 Thin-film resistors

NiCr thin-film resistors were used to suppress the bias parasitic oscillations of the RTD, when operated within the NDR region. The stabilising resistance was realised by a parallel combination of two shunt devices (across the CPW structure), in order to provide a symmetrical input port design. A micrograph of a fabricated shunt resistor network test structure is shown in Fig. 4.11.

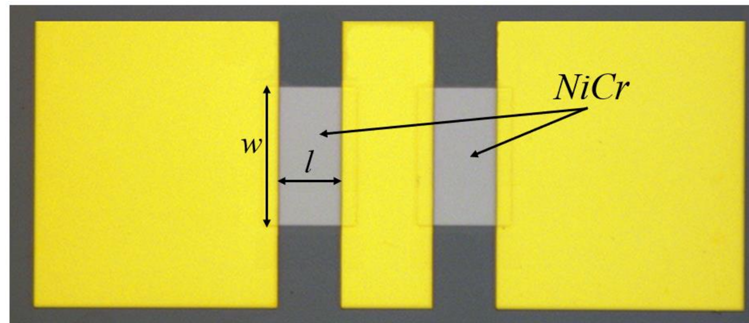

Figure 4.11 Micrograph of a fabricated resistor network test structure.

Due to the fact that typically the DC characteristics of such a biasing network show an accurate design procedure, the performance of a shunt resistor structure was also investigated using 2-port S-parameter measurements.

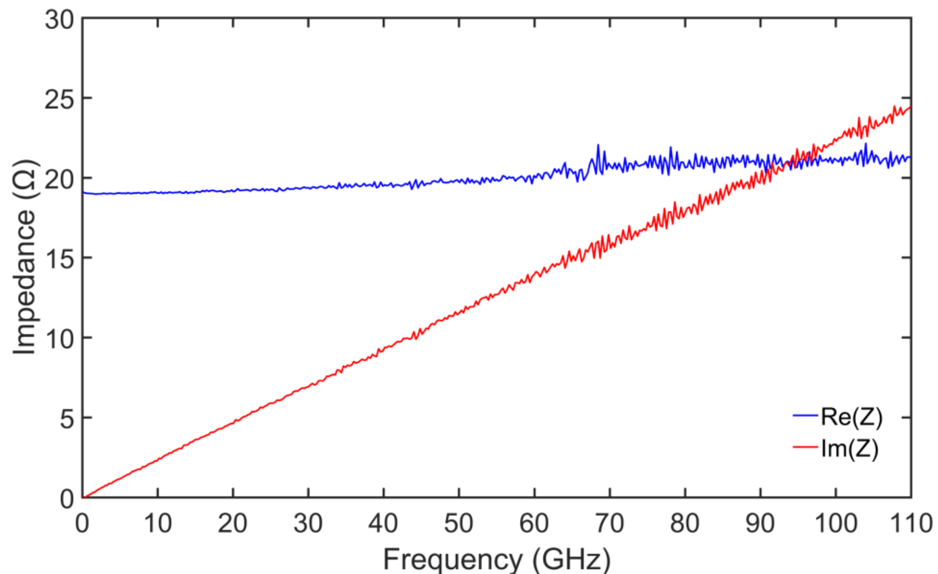

Figure 4.12 Measured Z_{11} parameter of a shunt resistor network test structure.

The acquired measurements from the presented test structure, were converted to equivalent Z-parameters, where the input parameter Z_{11} models the CPW pad parasitics

together with the shunt resistor and is presented in Fig. 4.12. The real part of the Z-parameter indicates an equivalent network resistance of 19 Ω close to DC, with a frequency variation of approximately 8% over 110 GHz. The determined resistance is in close agreement with the parallel equivalent designed 20 Ω value, for which, the individual component resistance (40 Ω) was computed using Eqn. 4.14 for the structural parameters w = 40 μm, l = 50 μm and t = 33 nm. The inductive behaviour displayed by the imaginary part of Z_{11} is attributed primarily to the series parasitic component introduced by the CPW structure, estimated at L_p = 35 pH.

4.4 PIN diodes for high-speed applications

The passive components described in section 4.2 constitute the key building blocks of fundamental RTD-based circuits, including sinusoidal oscillators and direct detectors. However, for high-speed applications, which require more complex circuitry, other components need to be considered [20] for purposes such as RF signal higher-order modulation [21][22], or routing of the signal through defined transmission paths in the case of high-frequency transceiver modules [23]. This section describes the performance of a proposed *p*-type intrinsic *n*-type (PIN) diode structure, suitable for monolithic integration with the RTD device for high-speed switching and modulation applications.

Figure 4.13 Illustration of a standard PIN diode.

The PIN diode is a semiconductor device, which comprises of a wide intrinsic region (drift region) sandwiched between highly doped *p*-type and *n*-type regions [24], as illustrated in Fig. 4.13. Due to the presence of the un-doped semiconductor material, the rectification capabilities of the PIN diode are inferior to the standard *p-n* junction diode, however its fast switching speeds, low package parasitic inductance and ability to control high-power RF signals make it a suitable solution for numerous applications operating at microwave and mmWave frequencies [25].

Based on the polarity of the applied bias, between the highly doped regions, PIN diodes can operate in two distinctive modes, which can be easily illustrated using the device equivalent circuits [26] presented in Fig. 4.14.

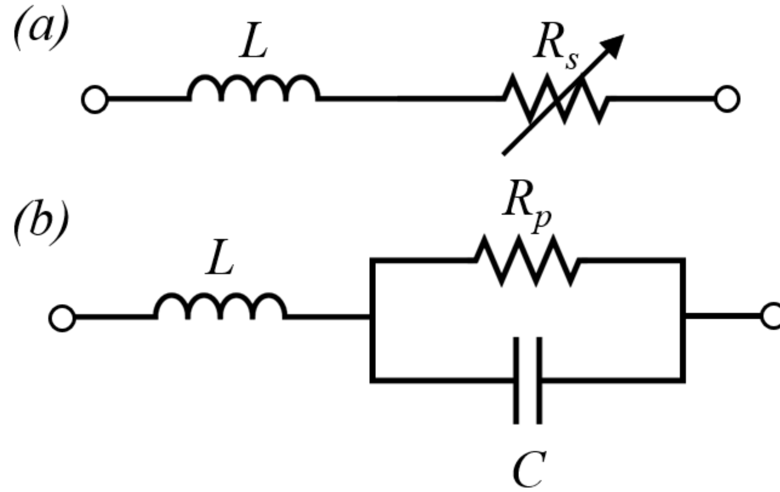

Figure 4.14 Equivalent circuit of a PIN diode in forward bias operation (a), where R_s denotes the series variable resistance, and in reverse bias operation (b), where R_p is the large parallel resistance and C is the device capacitance. L denotes in both states the series parasitic inductance, independent of biasing condition.

Under forward bias conditions (Fig. 4.14 (a)), the device acts as a variable RF resistance (R_s), dependent on the charge concentration in the i-layer (i.e. current controlled resistance), behaviour which can be exploited in the realisation of high-speed switches, attenuators and amplitude modulators [25]. The variable series resistance R_s can be defined as:

$$R_s = \frac{l^2}{(\mu_N + \mu_P)Q} \tag{4.15}$$

where l is the width of the i-layer, μ_n and μ_p are the mobility of electrons and holes in the material, respectively, and Q is the amount of stored charge in the un-doped layer (assuming same concentration of holes and electrons in the highly doped regions) given as:

$$Q = I_F \tau \tag{4.16}$$

where I_F is the forward bias current and τ is the carrier lifetime.

In reverse bias operation (Fig. 4.14 (b)), the PIN diode can be modelled as the parallel combination of a loss element (R_p) and device capacitance (C), in series with the parasitic inductance. The value of the parallel resistance R_p is considered infinite for an ideal device, given the absence of free charge in the i-layer. However, due to unwanted material impurities, a finite large resistance models the associated leakage current. The device capacitance, primarily determined by the thickness of the i-layer l, the effective area A and semiconductor dielectric constant ε_r, for an operating frequency above the dielectric relaxation constant [25], can be expressed as:

$$C = \frac{\varepsilon_0 \varepsilon_r A}{l} \tag{4.17}$$

In contrast to the standard p-n junction diode, for which the device capacitance displays a continuous variation with bias, up to the breakdown voltage, the PIN diode capacitance becomes constant beyond a small applied reverse bias, lowering the complexity of the associated circuit design impedance matching process.

The proposed InGaAs based PIN diode epi-layer design investigated in this work was adapted from [27] and is presented in Table 4.1. The relatively large i-layer region was chosen in order to reduce the device capacitance, thus improving the insertion loss, together with a higher doping of the p^+/n^+ layers, which will reduce the on-state resistance in order to improve isolation, when operated as a standard RF switch.

Table 4.1 PIN diode epitaxial layer structure

Material	*Thickness (µm)*	*Doping (cm^{-3})*
$In_{0.53}Ga_{0.47}As$ (p^+)	0.15	1E20 : Si
$In_{0.53}Ga_{0.47}As$ (n)	1	5E15 : Si
$In_{0.53}Ga_{0.47}As$ (n^+)	1	3E19 : Si
SI : InP	Substrate	-

For DC and RF characterisation purposes, PIN diodes with active areas of 10 × 10 µm^2 were fabricated using an optical mask and processing techniques described in Chapter 3. Compared to RTD fabrication, the single fabrication variation is represented by the

greater InGaAs etch depth during the mesa definition stage due to the larger layer thickness of the PIN structure. The forward bias operation of the PIN diode was investigated using the measured *I-V* characteristics, shown in Fig. 4.15, alongside the variation of the series resistance R_s. The measurements indicate a turn-on voltage of around 0.6 V and an on-state resistance R_{on} = 1.3 Ω at 0.8 V. The relatively low on-state resistance was achieved due to the designed high doping concentrations of the p^+/n^+ layers.

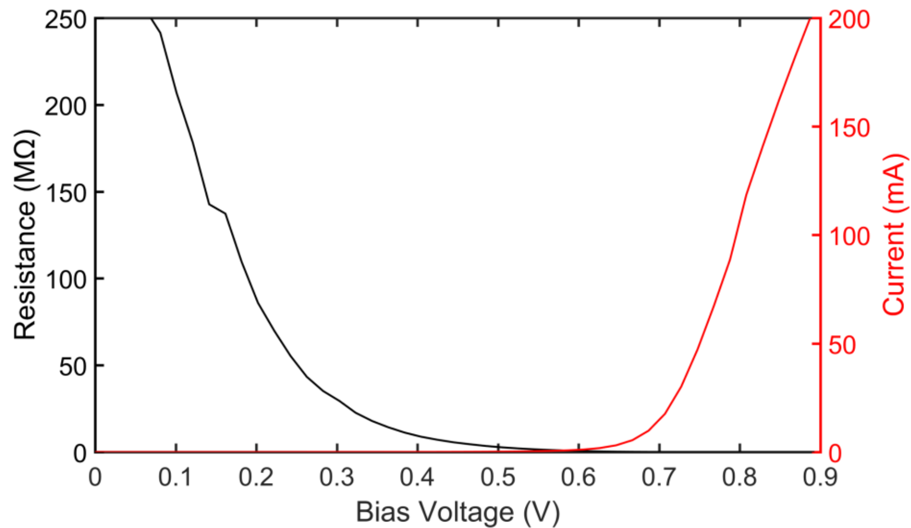

Figure 4.15 Measured I-V (red) and R-V (black) characteristics of a fabricated 10 × 10 μm² PIN diode.

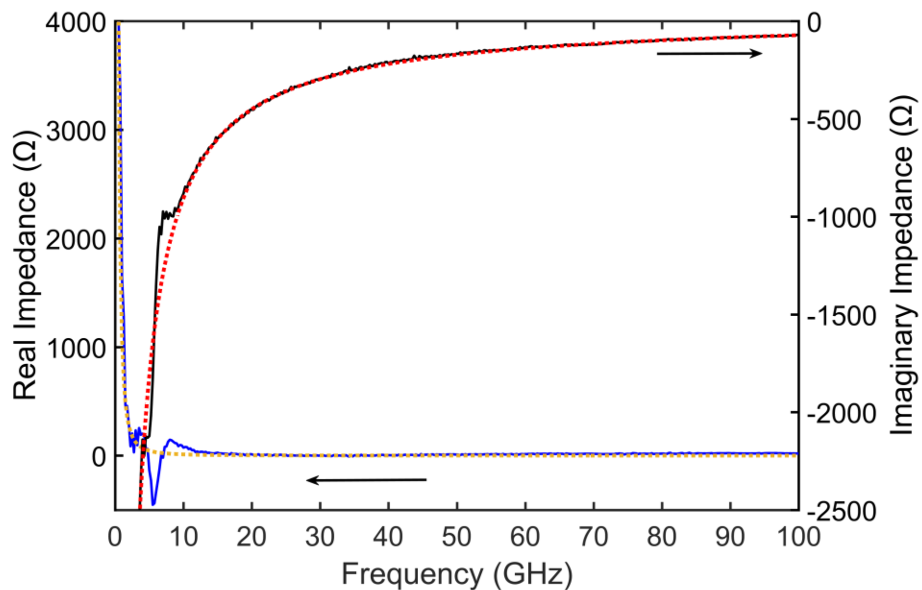

Figure 4.16 Measured (solid line) and simulated (dotted line) real and imaginary part of device input impedance in the off-state at 0 V.

The corresponding off-state device capacitance (i.e. zero-bias capacitance C_{off}) was determined at C_{off} = 18.2 fF, using high-frequency one-port S-parameter measurements, with the same methodology as described in section 4.3. This was achieved based on fitting the small-signal equivalent circuit of the PIN diode (Fig. 4.14 (b)) onto the converted imaginary impedance data, over the entire frequency range (up to 100 GHz), as shown in Fig. 4.16. Based on the acquired parameters, the maximum device cut-off frequency was estimated using $f_c = 1/(2\pi R_{on} C_{off})$ [28] at approximately 6.7 THz, which together with its wide resistance tuning range (between 1.3 Ω and 250 MΩ), confirms its suitability for integration in high-frequency applications, such as high-data rate communication systems, which will be explored in the future.

4.5 Summary and discussion

In this chapter, the design and fabrication of various integrated circuit (IC) components required for the realisation of device stabilising networks and RTD-based ICs have been presented. The basic passive components include coplanar waveguides (CPW), CPW shorted by a MIM capacitor, and thin film NiCr resistors. Corresponding test structures for each discussed component have been fabricated and characterised using S-parameter measurements up to 110 GHz. Good agreement between the experimentally acquired data and analytical/simulated behaviours has been observed, which validates the described design procedures and fabrication processes.

Furthermore, a PIN diode epitaxial structure, which will be shown to be suitable for monolithic epitaxial integration with the RTD was proposed and characterised. The PIN diode is expected to enable RTD-based high-speed switching or higher-order modulation schemes.

4.6 References

[1] C. P. Wen, "Coplanar waveguide: a surface strip transmission line suitable for nonreciprocal gyromagnetic device applications," *IEEE Transactions on Microwave Theory and Techniques,* vol. 17, no. 12, pp. 1087-1090, 1969.

[2] R. Garg, I. Bahl, and M. Bozzi, *Microstrip lines and slotlines*. Artech house, 2013.

[3] I. Roychoudhury and D. Bhattacharya, "Coplanar waveguide for microwave integrated circuits: a review," *IETE Technical Review,* vol. 10, no. 3, pp. 257-265, 1993.

[4] R. Masood and S. A. Mohsin, "Characterization of a coplanar waveguide open stub-based discontinuity for MMICs and filter applications," *International Journal of Antennas and Propagation,* vol. 2012, p. 423706, 2012.

[5] R. Simons and R. N. Simons, *Coplanar waveguide circuits, components, and systems*. Wiley Online Library, 2001.

[6] AgilentTechnologies. "Advanced Design System - Using LineCalc." http://literature.cdn.keysight.com/litweb/pdf/ads2008/linecalc/ads2008/Using_LineCalc.html (accessed 21.01.2021).

[7] K. Seeger, "Temperature dependence of the dielectric constants of semi-insulating III-V compounds," *Applied Physics Letters,* vol. 54, no. 13, pp. 1268-1269, 1989.

[8] D. M. Pozar, *Microwave engineering*. John Wiley & Sons, 2011.

[9] K. Beilenhoff, H. Klingbeil, W. Heinrich, and H. L. Hartnagel, "Open and short circuits in coplanar MMIC's," *IEEE Transactions on Microwave Theory and Techniques,* vol. 41, no. 9, pp. 1534-1537, 1993.

[10] P. J. Zampardi, K. Burger, and B. Moser, "Chapter 5 - Technology design interaction: System driven technology choices," in *Microwave Wireless*

Communications, A. Raffo and G. Crupi Eds.: Academic Press, pp. 209-259, 2016.

[11] R. Sharma, A. Kumar, and U. Ray, "Model MMIC nichrome resistors," *Microwaves & RF,* vol. 42, no. 2, pp. 76-87, 2003.

[12] K. Bansal, S. Chander, S. Gupta, and M. Gupta, "Design and analysis of thin film nichrome resistor for GaN MMICs," in *2016 3rd International Conference on Devices, Circuits and Systems (ICDCS)*, pp. 145-148, 3-5 March 2016, 2016.

[13] R. Driad, M. Krieg, N. Geldmacher, J. Rüster, and F. Benkhelifa, "Investigation of NiCr thin film resistors for InP-based monolithic microwave integrated circuits (MMICs)," *Journal of The Electrochemical Society,* vol. 158, no. 5, p. H561, 2011.

[14] Y. Kwon, N.-H. Kim, G.-P. Choi, W.-S. Lee, Y.-J. Seo, and J. Park, "Structural and surface properties of NiCr thin films prepared by DC magnetron sputtering under variation of annealing conditions," *Microelectronic Engineering,* vol. 82, no. 3, pp. 314-320, 2005.

[15] T. Lodhi, "InP based 77 GHz monolithic millimetre wave integrated circuits," PhD Thesis, University of Glasgow, 2001.

[16] C. Li, "Design and characterisation of millimetre wave planar Gunn diodes and integrated circuits," PhD Thesis, University of Glasgow, 2012.

[17] A. Rumiantsev and N. Ridler, "VNA calibration," *IEEE Microwave Magazine,* vol. 9, no. 3, pp. 86-99, 2008.

[18] G. E. Ponchak and E. M. Tentzeris, "Finite ground coplanar waveguide (FGC) low loss, low coupling 90-degree crossover junctions," *IEEE transactions on advanced packaging,* vol. 25, no. 3, pp. 385-392, 2002.

[19] T. Boutell. "CGIC-WCALC - Coplanar waveguide analysis/synthesis calculator." http://wcalc.sourceforge.net/cgi-bin/coplanar.cgi (accessed 15.12.2020).

[20] S. Lucyszyn and I. D. Robertson, "Analog reflection topology building blocks for adaptive microwave signal processing applications," *IEEE Transactions on Microwave Theory and Techniques,* vol. 43, no. 3, pp. 601-611, 1995.

[21] Y.-C. Jeong, "Design of a novel vector modulator," *Microwave Journal,* vol. 44, no. 10, pp. 156-156, 2001.

[22] M. J. Kobasa and E. Arvas, "A surface mount vector modulator for PCS," in *Symposium on Antenna Technology and Applied Electromagnetics (ANTEM)*: IEEE, pp. 117-120, 2000.

[23] V. Ziegler, M. Berg, H. Tobler, C. Wolk, R. Deufel, J. Dickmann, A. Trasser, H. Schumacher, E. Alekseev, and D. Pavlidis, "InP-based monolithic integrated PIN diode switches for mm-wave applications," 1998.

[24] S. M. Sze and K. K. Ng, *Physics of semiconductor devices*. John Wiley & Sons, 2006.

[25] J. W. E. Doherty and R. D. Joos, "The pin diode circuit designers' handbook," *Microsemi corporation, Santa-Ana: California,* 1992.

[26] B. Liu, G. Lin, Y. Cui, and R. Li, "An orbital angular momentum (OAM) mode reconfigurable antenna for channel capacity improvement and digital data encoding," *Scientific reports,* vol. 7, no. 1, pp. 1-9, 2017.

[27] E. Alekseev, D. Pavlidis, and D. Cui, "InGaAs PIN diodes for high-isolation W-band monolithic integrated switching applications," in *1997 Proceedings IEEE/Cornell Conference on Advanced Concepts in High Speed Semiconductor Devices and Circuits*, pp. 332-340, 4-6 Aug. 1997, 1997.

[28] E. Alekseev, D. Pavlidis, and D. Cui, "High-isolation W-band InP-based PIN diode monolithic integrated switches," 1997.

Chapter 5. RTD device modelling

5.1 Introduction

As resonant tunnelling diodes have been proven to be among the fastest solid-state electronic devices operating at room temperature [1], in recent years they have been considered key components for successful realization of THz oscillators, with fundamental frequencies of approximately 2 THz (1.98 THz) [2], high-sensitivity detectors in both wireless communication [3] and imaging systems [4], high-speed analogue-to-digital converters [5], digital logic gates [6] and memory [7]. However, in order for these applications to make the transition from the laboratory to the commercial and industrial markets, standard circuit design procedures need to be widely employed. The primary step in achieving the required methodologies is represented by the development of accurate device models, which can provide a foundation for their compact implementation into computer-aided design (CAD) software [8]. Such models would offer a new degree of circuit optimisation through simulation and functional verification, in comparison to the currently employed more generic theoretical and experimental approaches.

As previously discussed in section 2.4, modelling the high-frequency behaviour of RTDs has represented the main focus of numerous device characterisation studies in the past decades, resulting in the continuous evolution of the various proposed small-signal equivalent circuit representations. However, despite the establishment of a generic equivalent circuit model, that unifies the key RTD operational concepts evidenced experimentally (i.e. impedance measurements, or circuit performance analyses), the underlying physical mechanisms that determine the bias and frequency dependent circuit characteristics and their impact on the device performance are still highly disputed. In order to aid the combined efforts of validating the existing theoretical models, while also enabling their further development, a suitable extraction technique for small-signal equivalent circuit elements is needed.

This chapter presents the challenges associated with RTD accurate device modelling, particularly in the negative differential resistance (NDR) region which confers the RTD with its unique capabilities that, for instance, in enabling THz sources, but which

induces parasitic oscillations with the bias cables in standard characterisation setups, hindering its accurate characterisation. In this context, a novel proposed systematic methodology is described for reliable RTD high-frequency characterisation.

5.2 RTD DC characteristics and bias instabilities

RTD devices with relatively large active areas of 10 × 10 μm^2 were realised on the low-current density epi-structure described in Table 3.1, using the basic photolithography techniques discussed in Chapter 3. The DC characteristics of a fabricated device were acquired using a Keysight B1500A device parameter analyser and are presented in Fig. 5.1. The *I-V* curve is characterised by a peak-valley voltage difference (ΔV) of around 2 V and peak-valley current difference (ΔI) of around 16 mA.

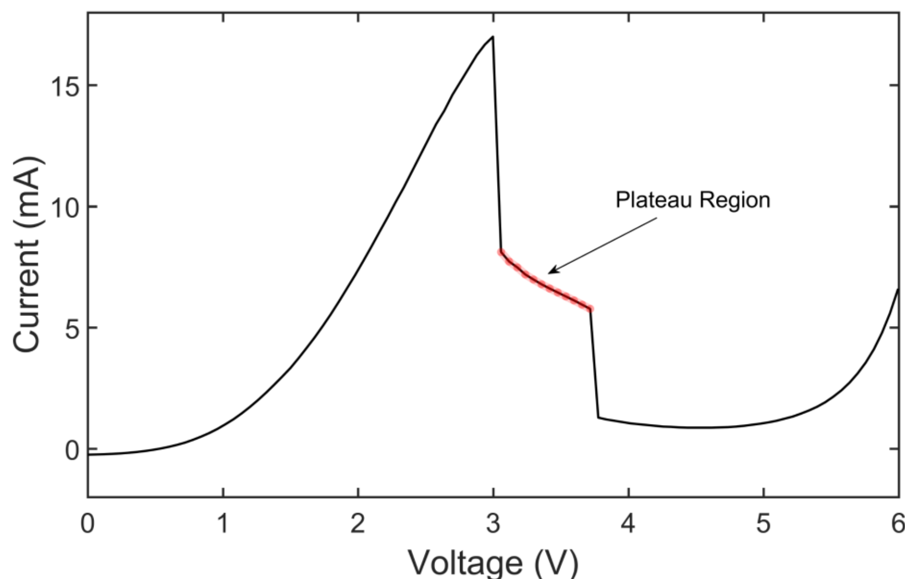

Figure 5.1 Measured I-V characteristics of a 10 × 10 μm^2 RTD device, exhibiting a plateau-like distortion within the NDR region, due to the presence of low-frequency parasitic oscillations.

One of the biggest challenges in accurate DC and high-frequency characterisation of the device NDR region is represented by the presence of low-frequency parasitic oscillations, which manifest in the *I-V* measurement in the form of a plateau-like distortion [9-12], as highlighted in Fig. 5.1 between 3 V and 3.7 V . Several intrinsic factors have been identified as potential causes for low-frequency oscillations (i.e. coupling mechanisms between adjacent energy levels in the emitter – quantum well

region [9]), however, in most cases, they are primarily attributed to the resonant circuit created between the biasing cable inductance and the device self-capacitance [13]. As device bias oscillations have also been proven to limit the performance of RTD based circuits, different suppression techniques are generally employed. The most common stabilizing approach consists of an external resistance connected in parallel with the RTD, chosen such that the combined circuit conductance is positive [14]. In order to analyse the DC stability criterion, the simple device RC model can be considered (Fig. 5.2), which consists of the device negative differential conductance (assuming operation within the NDR region) and self-capacitance.

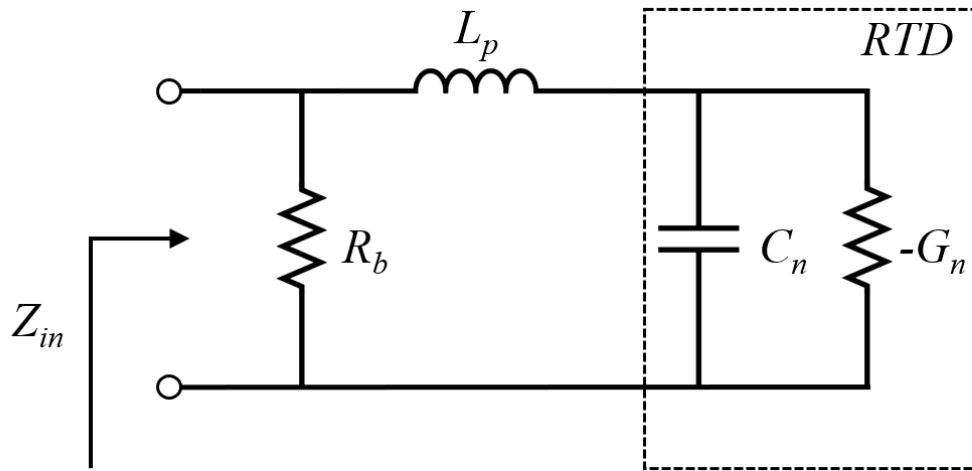

Figure 5.2 Stabilization circuit schematic of an RTD using a shunt-resistor (R_b), for low-frequency bias oscillation. A simplified RTD model consisting of the device negative differential conductance ($-G_n$) and self-capacitance (C_n) is considered, where L_p represents the parasitic inductance.

The admittance of the circuit presented in Fig. 5.2 is defined by:

$$Y_{in} = \frac{1}{Z_{in}} = \frac{1}{R_b} + \frac{1}{j\omega L_p + \frac{1}{-G_n + j\omega C_n}} \tag{5.1}$$

where L_p represents the parasitic inductive elements, R_b is the stabilizing resistor, $-G_n$ is the device negative differential conductance and C_n is the self-capacitance. Based on Eqn. 5.1, the real part of the circuit admittance is:

$$Re(Y_{in}) = \frac{1}{R_b} + \frac{-\frac{G_n}{G_n^2 + \omega^2 C_n^2}}{\left(\frac{G_n}{G_n^2 + \omega^2 C_n^2}\right)^2 + \left(\omega L_p - \frac{\omega C_n}{G_n^2 + \omega^2 C_n^2}\right)^2} = \frac{1}{R_b} - G_n \frac{1}{\left(1 - \omega^2 L_p C_n\right)^2 + \left(\omega L_p C_n\right)^2} \tag{5.2}$$

In order to satisfy the stability condition at DC (assuming $\omega = 0$), the real part of the admittance (Eqn. 5.2) needs to be positive [15][16]:

$$Re(Y_{in)} = \frac{1}{R_b} - G_n > 0 \tag{5.3}$$

Thus, from Eqn. 5.3, the value of the biasing resistor, based on the absolute value of G_n, given by Eqn. 2.10, can be chosen such that:

$$R_b < \frac{1}{G_n} = \frac{2\Delta V}{3\Delta I} \tag{5.4}$$

As a consequence, the considered resistance value needs to be small in order to suppress the bias oscillations. However, the value of the real part of the admittance will significantly decrease for $\omega \approx 1/\sqrt{L_p C_n}$, and thus at very high frequencies $Re(Y_{in})$ < 0, potentially making the circuit unstable. In this case, high-frequency oscillations may occur when the device is biased in NDR region. The criterion for high-frequency device stability is derived in [14], based on a Van der Pol analysis approach and is given as:

$$\frac{L_p G_n}{C_n} < R_b \tag{5.5}$$

Furthermore, for large current density RTD structures, a low stabilising resistor value will lead to high bias current associated power losses, in turn degrading the DC-to-RF conversion efficiency, when implemented in an oscillator circuit, or reducing the overall detection sensitivity in the case of RTD based receivers. Therefore, various other stabilization techniques have been proposed based on non-linear devices (i.e. Schottky diodes) [17] or RC networks [18]. However, for the device characterisation study discussed in this work, the simple shunt-resistor network was considered, primarily due to the reduced design and fabrication complexity. RTDs with similar

active areas were fabricated on the same sample, with an included thin film NiCr stabilizing resistor network (Fig. 5.3), in order to investigate and characterise the device NDR region. The stabilizing resistor value was chosen to be 20 Ω, in order to satisfy Eqn. 5.4, where $1/G_n$ = 83.3 Ω for this particular device.

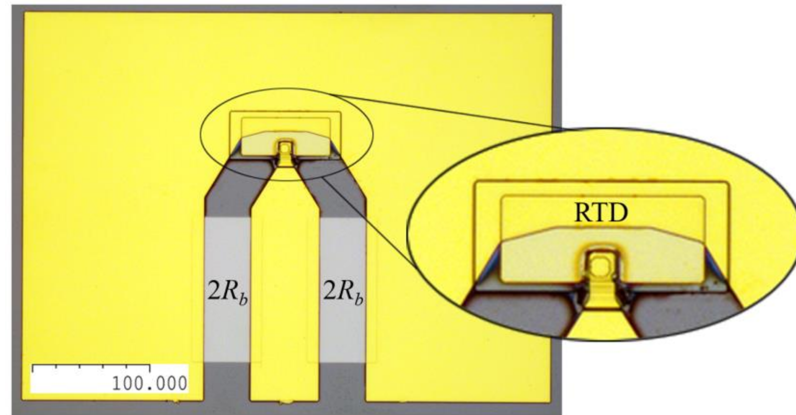

Figure 5.3 Micrograph of realised RTD with a 20 Ω stabilizing resistor network.

The device *I-V* characteristics were determined indirectly, by first de-embedding the current through the resistor and the measurements and are shown alongside the un-stabilised curve in Fig. 5.4.

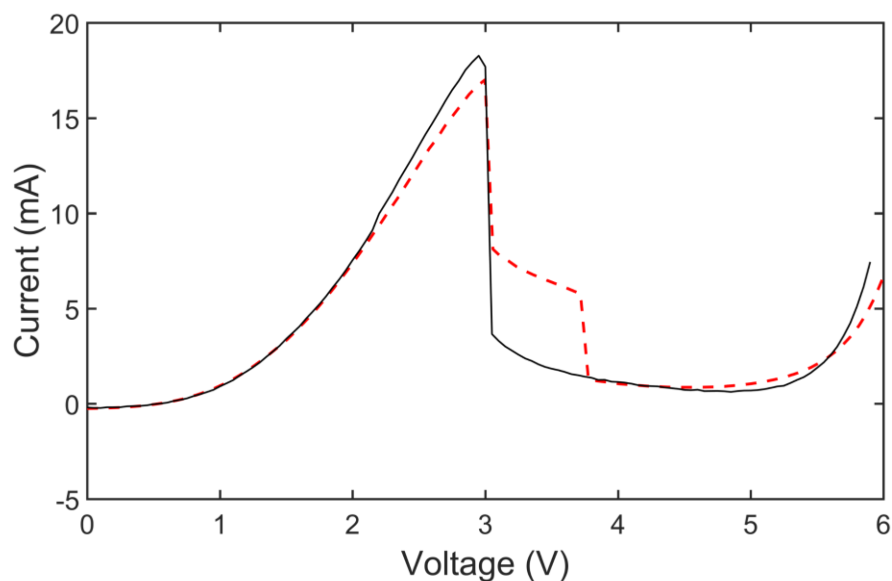

Figure 5.4 Comparison between the measured I-V characteristics of an un-stabilised (red) and stabilised (black) 10 × 10 μm² RTD device.

The effect of stabilising resistor network on the low-frequency bias oscillations can be directly observed from the de-embedded measurement, as the characteristic plateau-

like feature is absent in NDR region. The relatively small differences between the two separate sets of measurements, in terms of peak-current, can be attributed to the fabrication process not yielding two perfectly identical devices (i.e. uneven metal deposition, or anisotropic mesa etching). The sharp transition between the peak-current region and the NDR, as discussed in Chapter 2, is attributed to the narrow resonance that arises between the discrete energy levels in the quantum-well and the enhanced pseudo-triangular well (2D-2D tunnelling), as a result of the un-doped/lightly doped graded spacer layer, present in the epi-structure design [19]. Furthermore, the relatively large voltage drop across the wide depletion region, in the case of this particular epitaxial structure, leads to a shift in peak-voltage to a relatively high observed value (2.95 V), due to the increased bias requirement to achieve the resonance condition.

The impact of the presented stabilisation method on the low-frequency bias oscillations was further investigated using a Keysight E4448A spectrum analyser, connected to the measurement setup through a bias tee, as shown in Fig. 5.5, while the device was biased in the NDR region (3.1 V).

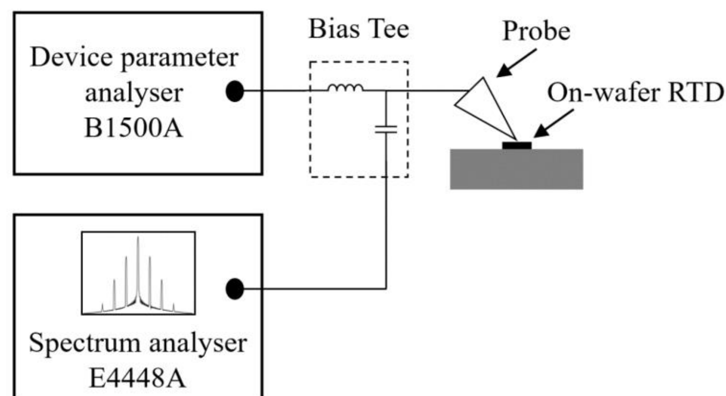

Figure 5.5 Diagram of on-wafer RTD measurement setup. The B1500A provides the device bias voltage and also acquires the current measurement, while the spectrum analyser is used to measure the parasitic oscillations.

Fig. 5.6 shows the measured low-frequency oscillations present in the case of the unstabilised device (red curve) that lie in the 1-2 MHz range for fundamental oscillations. The same measurement was taken from the device with an integrated stabilising shunt resistor (black curve), under the same bias conditions. No significant oscillations could be observed in the spectrum when biased within the NDR region.

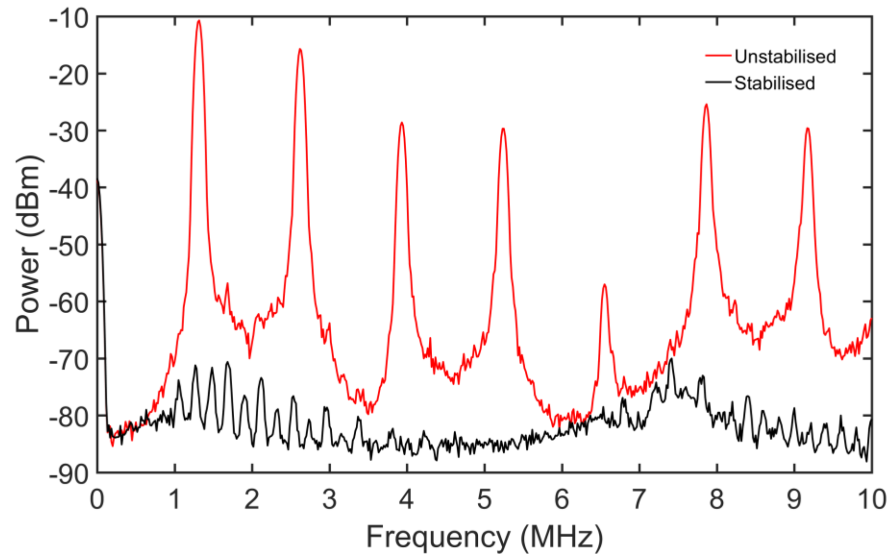

Figure 5.6 Measured low-frequency bias oscillations spectrum, in the NDR region for a stabilised (black) and un-stabilised (red) RTD.

The final performed DC analysis of the device was done using a double voltage sweep measurement (between 0 V and 6 V) for the stabilised RTD, which revealed no distinctive plateau-like regions or particular current discontinuities in both forward and reverse direction bias variation, that could potentially hinder the device high-frequency characterisation. However, a hysteresis behaviour was observed in the NDR region, when the reverse voltage sweep occurred after the positive increase in bias, as shown in Fig. 5.7.

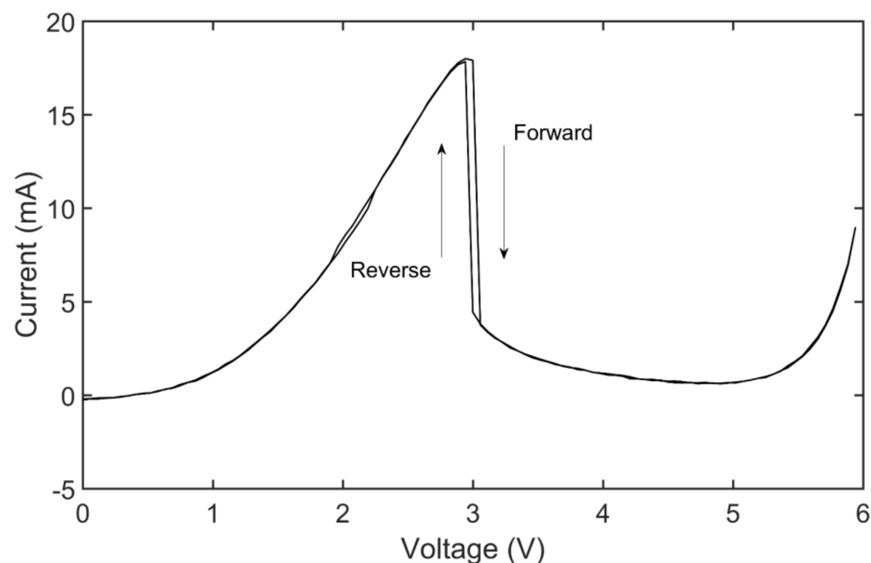

Figure 5.7 Measured stabilised device I-V characteristics using a forward and reverse voltage sweep.

Previous studies have related this behaviour to an extrinsic induced bistability operation regime by external series resistance [20-22] introduced in the metal-semiconductor contact regions or by the biasing equipment. In the case of this particular device, the relatively small voltage span of the hysteresis (approx. 50 mV) was observed unaffected by the variation in contact resistance (i.e. devices with different active areas) or different measurement setups (voltage source, cables, etc.). An alternative cause of this behaviour can be attributed to an intrinsic phenomenon, modelled by the dynamic charge build-up in the quantum well [23-25], which arises from the feedback-like dependence between the electron sheet concentration and the tunnelling current. This interaction leads to a change in the potential profile of the device, altering the energy level of the resonant state, and therefore reducing the effect of the applied bias, which results in two stable operational regimes [26][27]. Such behaviour has been demonstrated experimentally for specific layer structures in relation to the introduction of a large asymmetric spacer layer [28-30], similar to the one presented in this project, with a proven dependence of the hysteresis voltage span on the width of the un-doped/lightly doped region [31]. However, the observed hysteresis behaviour does not impose any restrictions on the device high-frequency characterisation of the device (i.e. no variation in current is observed at any set bias point during high-frequency measurements), and so it was not investigated further as part of this study.

5.3 RTD high-frequency characterisation

As previously mentioned, device bias circuit instabilities present in the NDR region have represented a major challenge in accurate characterisation of RTD devices at relevant operating frequencies. Typically, RTD studies of this nature within the NDR region, rely on the use of devices with small physical active area dimensions (usually $< 1\ \mu m^2$) [11][32], for which their proportionally small negative differential conductance can be compensated by the impedance of the measurement equipment (i.e. when characterised by a vector network analyser with a typical 50 Ω system impedance) to achieve a stable operating regime. This approach is, however, only applicable to low peak current density RTDs (typically < 100 kA/cm^2) [33]. In the case of high current density epitaxial designs (i.e. exceeding 300 kA/cm^2), however, a stabilising method needs to be adopted [34], making the characterisation of the NDR region usually impossible. RF characterisation of the NDR region of a stabilised device

using the common shunt resistor approach has been reported once in the literature [35], however no details about the passive component de-embedding were given, which puts in question the accuracy of the extracted data.

Currently, high-frequency modelling of RTDs is conducted in the positive differential resistance (PDR) regions of the device, and then the results are used to estimate the RF behaviour within its NDR region, based on theoretical and analytical predictions [36][37]. Furthermore, key equivalent circuit elements, such as the device self-capacitance, are generally extracted in narrow frequency range [36], and as such, there is limited scope to validate the accuracy of this approach.

5.3.1 Bond-pad and shunt resistor de-embedding

For the required high-frequency measurements for RTD characterisation, typically done using S-parameter measurements, the impact of the surrounding extrinsic circuit elements comprising the stabilisation resistor and bonding pads will be substantial. Therefore, modelling these extrinsic circuits as fixed value lumped elements, as presented in [38], is in most cases not adequate. For this purpose, a robust on-wafer bond-pad de-embedding technique is generally preferred. Two main methods are commonly described in the literature: the cascade method [39], which treats the device together with the extrinsic network as a series of unknown linear networks; and the short and open (SO) dummy pad test structure method [40], which models the two-port network as a standard transmission-line. The biggest known drawback of the cascade method is that its accuracy is based on the assumptions that the series of extrinsic networks represented by pads and interconnects are identical and their connection is a perfect short, which in practice is not accurate at very high frequencies.

The SO de-embedding technique has been primarily employed for RTD characterisation. It generally accommodates the pad geometry and uses short and open dummy pad test structures as illustrated in Fig. 5.8, in order to recreate a simplified model of the bond-pads. The open dummy pad test structure is used to characterise the parallel parasitic capacitive component (C_p), whereas the short dummy pad test structure is used to characterise the series inductive component (L_p).

The two-step SO de-embedding procedure can be summarised as follows: The RTD circuit Z-parameters are obtained from the measured one-port S-parameters:

$$Z = Z_0 \frac{1 + \Gamma_{in}}{1 - \Gamma_{in}} \tag{5.6}$$

where Γ_{in} or S_{11} is the input reflection coefficient of the RTD and bond-pad combination and Z_0 is the characteristic impedance of the measurement setup (typically 50 Ω).

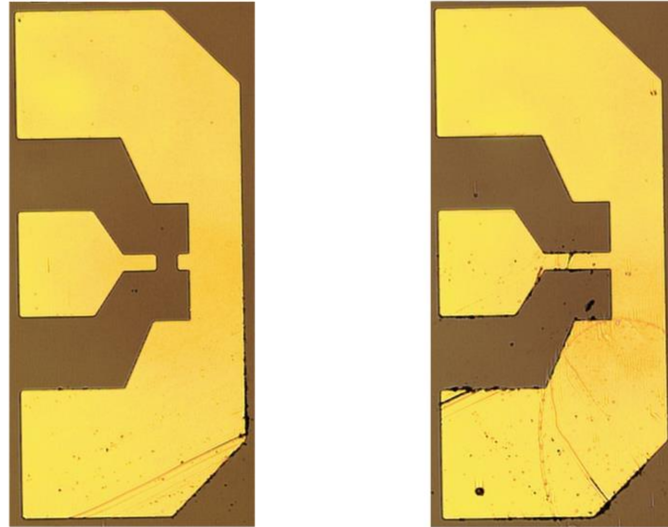

Figure 5.8 Micrographs of an open (left) and short (right) RTD dummy pad test structures. Source:[41].

The impact of the parallel capacitive component (C_p) can be first eliminated by subtracting the measured Y-parameters of the open dummy pad structure (Y_{open}) from the measured RTD admittance (Y_{meas}):

$$Y_{parallel} = Y_{meas} - Y_{open} \tag{5.7}$$

The impedance of the series inductive component (Z_{series}) can be isolated from the measured admittance of the short dummy-pad structure (Y_{short}) by again removing the parallel component:

$$Z_{series} = (Y_{short} - Y_{open})^{-1} \tag{5.8}$$

Finally, the Z-parameters of the RTD can be obtained as:

$$Z_{RTD} = \left(\left(Y_{parallel} \right)^{-1} - Z_{series} \right) \tag{5.9}$$

The accuracy of this method has been shown to produce reliable results for low peak current density devices, as attempted in [42], however, as previously stated, for high current density designs and even large active area RTD designs, an external stabilising circuit across the bond-pad structure is required in order to suppress existing oscillations. This configuration, with the additional extrinsic components, deviates from the standard transmission-line model and thus, the increased complexity cannot be fully accommodated by the SO method, which would also neglect additional parallel parasitic components introduced in the case of a shunt thin film resistor.

In this thesis, a new approach is proposed in order to accurately characterise the NDR regions of (stabilised) RTDs without limitations to device sizing or frequency [43]. This is based on a universal on-wafer bond-pad and shunt resistor de-embedding technique for reliable high-frequency device characterisation. The basis of the proposed method relies on the fact that the stabilising resistor including the extrinsic elements can be considered as a standard 2-port network connected to a load (RTD).

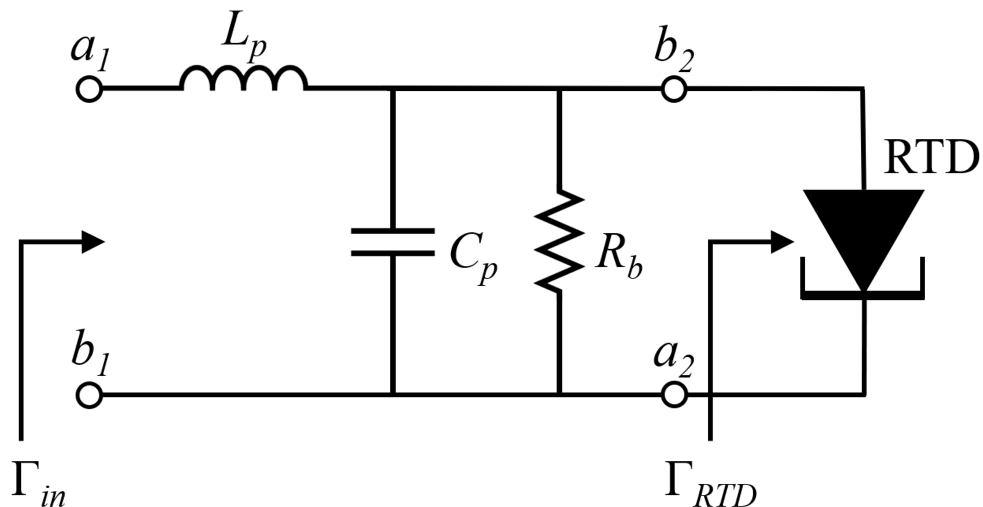

Figure 5.9 RTD biased through a shunt resistor R_b, which is modelled as a 2-port network together with the bond-pad parasitic elements (L_p and C_p).

Fig. 5.9 shows an RTD device with a shunt resistor for bias stabilisation connected across it, together with the parasitics elements (L_p and C_p) introduced by the metallic bond-pads. The bond pads and stabilisation resistor can be considered as a 2-port network, which can be represented by the S-parameter matrix in terms of the incident (a_i) and reflected (b_i) 'power waves' [44]:

$$\begin{pmatrix} b_1 \\ b_2 \end{pmatrix} = \begin{pmatrix} S_{11} & S_{12} \\ S_{21} & S_{22} \end{pmatrix} \begin{pmatrix} a_1 \\ a_2 \end{pmatrix} \tag{5.10}$$

By expanding the matrix identity in Eqn. 5.10, the reflected waves are given by:

$$b_1 = S_{11}a_1 + S_{12}a_2 \tag{5.11}$$

$$b_2 = S_{21}a_1 + S_{22}a_2 \tag{5.12}$$

If the RTD has a reflection coefficient, Γ_{RTD}, then using the standard above expansion, the circuit input reflection coefficient Γ_{in} will be given by [45]:

$$\Gamma_{in} = \frac{b_1}{a_1} = S_{11} + \frac{S_{12}S_{21}\Gamma_{RTD}}{1 - S_{22}\Gamma_{RTD}} \tag{5.13}$$

Finally, rearranging Eqn. 5.13, the reflection coefficient of the RTD can be obtained:

$$\Gamma_{RTD} = \frac{\Gamma_{in} - S_{11}}{\Gamma_{in}S_{22} - S_{11}S_{22} + S_{12}S_{21}} \tag{5.14}$$

The S-parameters (i.e. S_{11}, S_{12}, S_{21}, S_{22}) that define the 2-port network presented in the circuit (Fig. 5.9), can be determined by a two-port measurement of a fabricated auxiliary dummy-pad and resistor structure, identical to the one employed for the stabilised RTD, but without the device under test (DUT), as shown in Fig. 5.10.

The main advantage of the proposed procedure is represented by the fact that it ensures the stabilising network, together with the additional parasitic components are de-embedded from the intrinsic RTD data, thus greatly simplifying the device modelling process (i.e. making a clear distinction between the external shunt resistance and the device conductance together with the contact resistance). Furthermore, the reduced complexity of this de-embedding method, by requiring only one additional set of measurements (in comparison with the SO method), together with the use of measured data provides a significant improvement in accuracy, since no initial assumptions are required. The main disadvantage of this approach is however the requirement for a 2-port measurement of the auxiliary test structure, with the associated calibration stages of the measurement setup. Additionally, specific care must be taken in relation to the second port probe positioning in order to accurately reproduce the extent of the metallic pads.

For the experimental demonstration of the proposed method, S-parameter measurements of a stabilised RTD and the auxiliary test structures were done using the Keysight E8361A vector network analyser (VNA). The measurement setup was similar to the one presented in Fig. 5.5 (spectrum analyser replaced by the VNA), with both the bias voltage and VNA signal fed to the DUT using a 100 µm pitch ground-signal-ground (GSG) probe. An initial on-wafer calibration was initially performed, using the short-open-load-through (SOLT) technique described in Chapter 4.

The measurements were carried out in a 10 MHz – 110 GHz frequency span, with the port power set at -17 dBm to ensure that a maximum peak-to-peak voltage seen by the device was of less than 0.1 V. This is particularly important for the accurate characterisation of key device bias regions, such as the peak-current region, where the device differential conductance may vary between a positive and a negative value. For the auxiliary test structure, the probe for port 2 was positioned as indicated in Fig. 5.10.

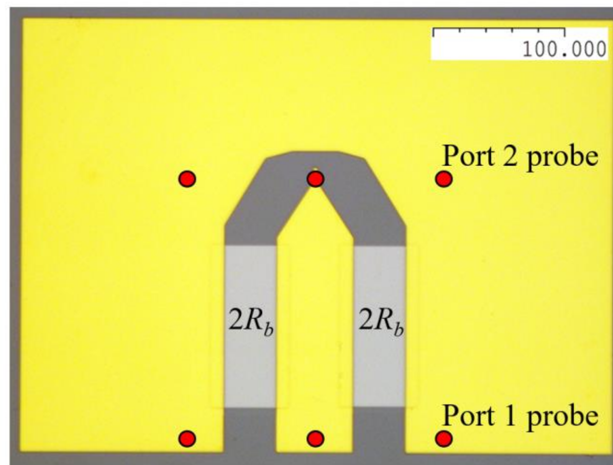

Figure 5.10 Micrograph of the auxiliary test structure – bond-pad and shunt resistor network. The red circles indicate the placement of standard ground-signal-ground (GSG) high-frequency probes for the 2-port measurement.

In order to assess the applicability of the proposed de-embedding method, initial measurements were acquired in the PDR region in the case of both the stabilised and unstabilised RTD device under the same bias conditions. The measured S_{11} parameters of the two devices, at a bias of 2.9V (close to the peak region) are shown in Fig. 5.11. The presence of the shunt resistor network in the case of the stabilised device (black curve) can be directly observed from magnitude and phase differences between the two sets of measurements, in the chosen frequency range.

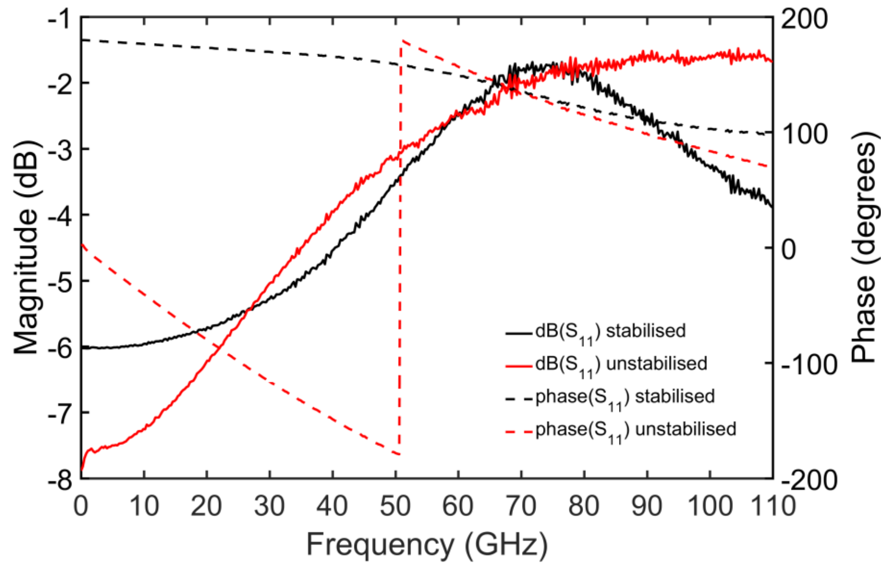

Figure 5.11 S-parameters stabilised (black trace) and unstabilised (red trace) RTD device biased at 2.9 V in the positive differential resistance (PDR) region – around the peak-current, showing magnitude (solid line) and phase (dashed line).

The presence of the shunt resistor network in the case of the stabilised device (black curve) can be directly observed from magnitude and phase differences between the two sets of measurements, in the chosen frequency range. The de-embedding procedure was carried out in both cases using the measured 2-port S-parameter data from their corresponding test structures (i.e. metal pads and shunt resistor in the case of the stabilised device, and only metal pads in the case of the un-stabilised device). An example of the measured S-parameters (magnitude and phase) from the pad and resistor test structure is shown in Fig. 5.12, where a clear variation in the behaviour of the input (S_{11}) and output port (S_{22}) reflection coefficients can be observed at higher frequencies. This response is attributed to the physical design differences between the transmission line geometries at port-1 and port-2 (i.e. tapered configuration at port-2).

A comparison between the resulting de-embedded signals from the two RTDs are shown in Fig. 5.13 (black trace – originally stabilised device and red trace originally unstabilised device). Good agreement can be observed between the two measurements under the same bias conditions, which validates the applicability of this procedure. The observed minor discrepancies at lower frequencies can be attributed to the fabrication factors. Overall, this result shows that the proposed de-embedding method is not limited by a specific device external circuitry, and so is suitable to accommodate different bond-pad and stabilizing network configurations.

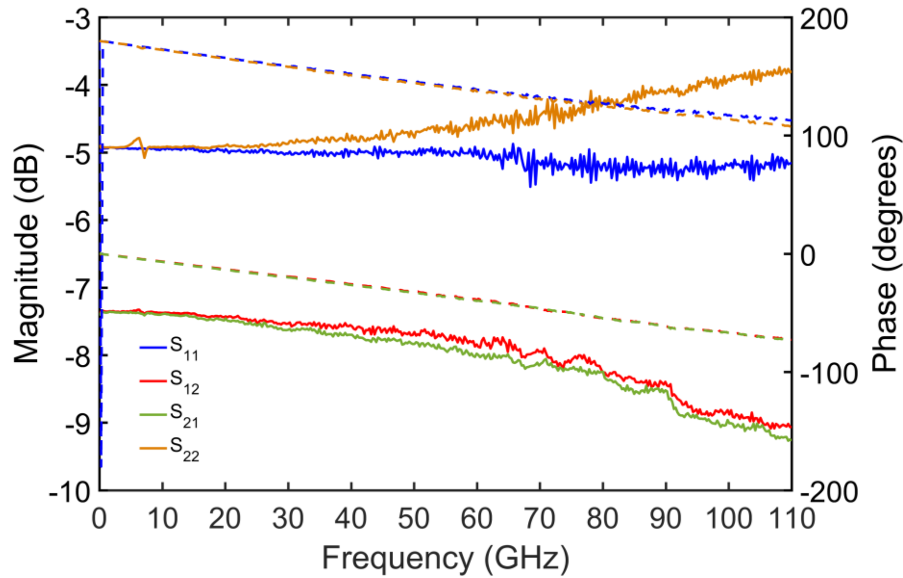

Figure 5.12 S-parameters of the pads and shunt resistor test structure used for de-embedding the stabilised device.

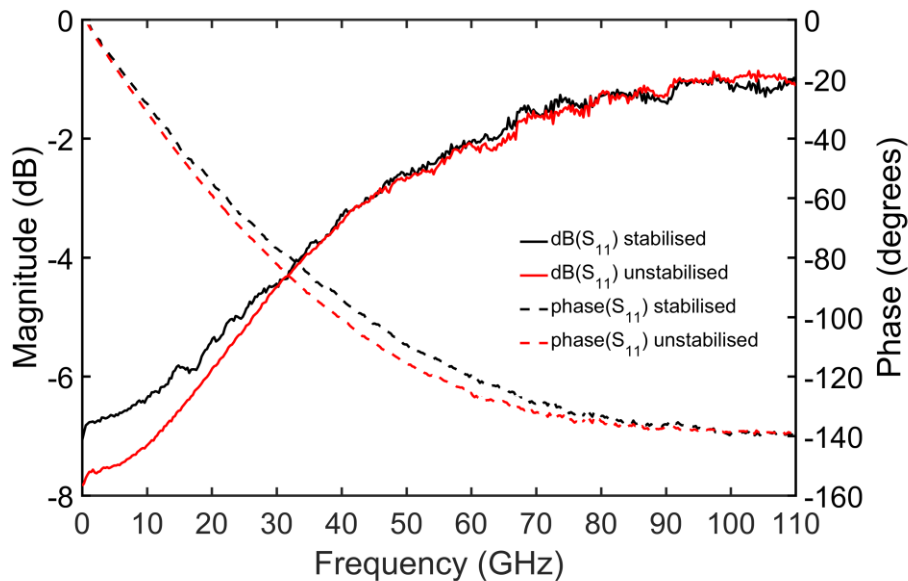

Figure 5.13 S-parameters stabilised (black trace) and unstabilised (red trace) RTD device biased at 2.9 V in the positive differential resistance (PDR) region, showing magnitude (solid line) and phase (dashed line) after the de-embedding procedure.

5.3.2 Small-signal equivalent circuit parameter extraction procedure

For the purpose of RTD high-frequency characterisation, based on the proposed de-embedding procedure, the generic parallel inductance RTD model shown in Fig. 5.14 which was previously discussed in section 2.4 was investigated.

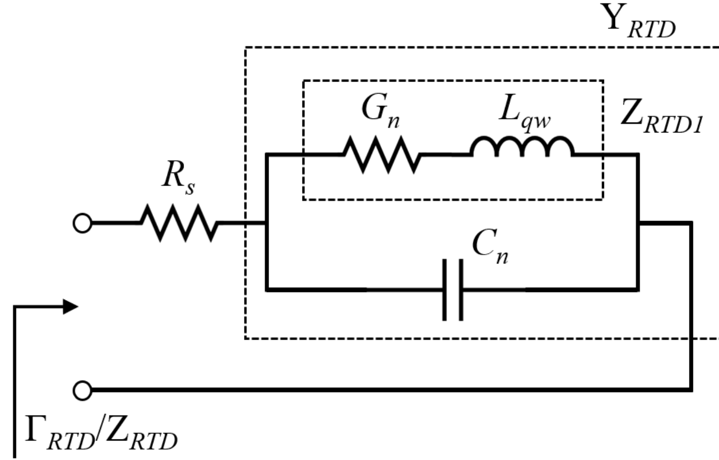

Figure 5.14 RTD parallel inductance model used in the device high-frequency characterisation. R_s is the contact and access resistance, G_n the device conductance, C_n the device self-capacitance and L_{qw} the quantum-well inductance.

The input impedance of the small-signal equivalent circuit can be described as:

$$Z_{RTD} = R_s + \frac{1}{j\omega C_n + \frac{1}{R_n + j\omega L_{qw}}} \tag{5.15}$$

or in terms of its real and imaginary input impedance as:

$$Re(Z_{RTD}) = R_s + \frac{R_n}{\left(1 - \omega^3 L_{qw} C_n\right)^3 - (\omega R_n C_n)^2} \tag{5.16}$$

$$Im(Z_{RTD}) = \frac{-\omega^3 L_{qw}^2 C_n - \omega R_n^2 C_n + \omega L_{qw}}{\left(1 - \omega^3 L_{qw} C_n\right)^3 - (\omega R_n C_n)^2} \tag{5.17}$$

where the resistance $R_n = G_n^{-1}$.

The increased model complexity does not allow for a purely analytical extraction of the RTD parameters, however an inspection of the circuit presented in Fig. 5.14 reveals a few key aspects in relation to the equivalent circuit elements and their influence at different frequencies. Firstly, based on Eqn. 5.16, it is clear that at the higher end of the measurement spectrum, the contact resistance R_s dominates the real part of the device impedance, since G_n is typically a few milli-Siemens, C_n is tens of femto-Farads or larger, L_{qw} is considered in the pico-Henry range, and therefore their contribution to the intrinsic device resistance can be negligible at millimetre-waves. Furthermore, at

high enough frequencies, the capacitance C_n would provide a short-circuit path, which would effectively mask any contributions to the input impedance from the series combination of G_n and L_{qw}. Based on these observations the following extraction procedure is proposed:

a) The de-embedded RTD S-parameter data (Γ_{RTD}) is first converted into Z-parameters, which provides the real and imaginary device impedance (Z_{RTD}). As previously explained, the real part of the impedance at high frequencies provides an estimate of R_s as:

$$R_s \approx Re(Z_{RTD})_{\omega \to \infty} \tag{5.18}$$

Fig. 5.15. provides such plots for one bias point in the PDR and another in the NDR, respectively. As expected, the real parts of the device input impedance become frequency independent at high frequencies (typically > 80 GHz), with $R_s \approx 2.5\ \Omega$ at $V_{bias} = 1$ V and $R_s \approx 3.5\ \Omega$ at $V_{bias} = 3.1$ V. These values of R_s are initial estimates at the respective bias voltages. The final value of R_s at each bias point is determined in conjunction with the simultaneous determination of the other intrinsic parameters, namely C_n, R_n and L_{qw}. Here, the basis of the parameter extraction is that each of these lumped elements is independent of frequency.

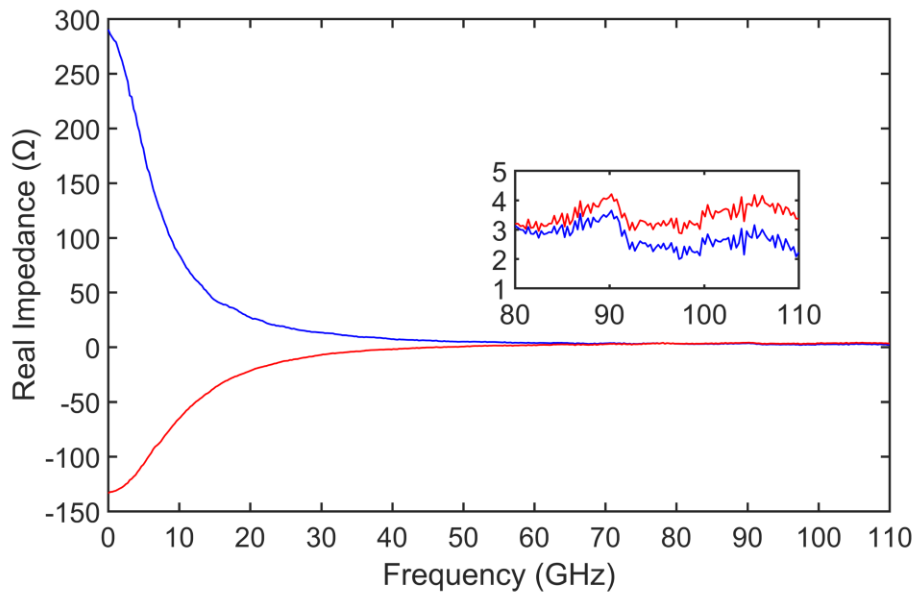

Figure 5.15 Real part of Z-parameters in the PDR region at 1V (blue curve) and in the NDR region at 3.1V (red curve). The high frequency regions used for Rs estimation are presented in the inset graph.

b) The initial R_s estimation is de-embedded from Z_{RTD}. The resulting data represents C_n in parallel with G_n and L_{qw} and thus, it can be expressed using its admittance:

$$Y_{RTD} = j\omega C_n + \frac{1}{R_n + j\omega L_{qw}} = \frac{R_n}{R_n^2 + \omega^2 L_{qw}^2} + j\omega \left(C_n - \frac{L_{qw}}{R_n^2 + \omega^2 L_{qw}^2} \right) \quad (5.19)$$

The circuit admittance with the de-embedded contact resistance value for the chosen two bias points defined in (a) is shown in Fig. 5.16.

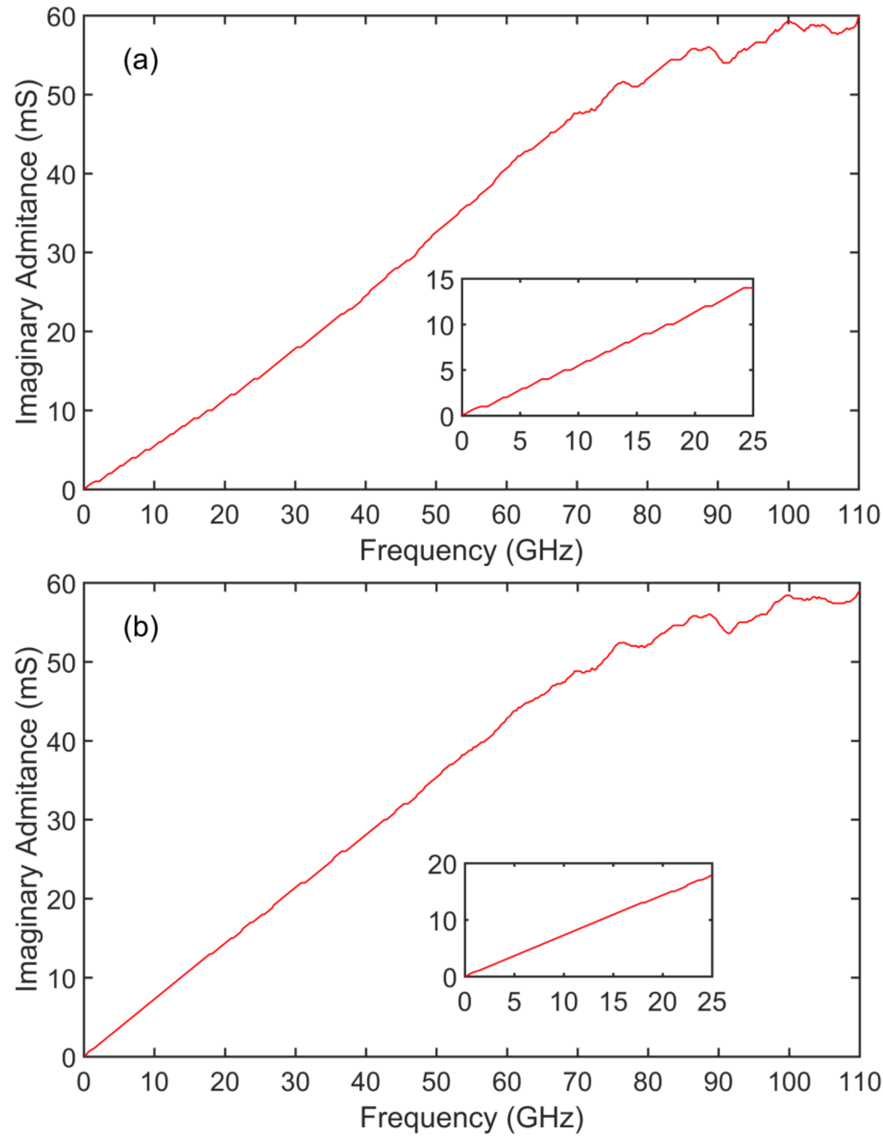

Figure 5.16 Imaginary part of Y-parameters with de-embedded R_s – linear region shown in inset used to estimate C_n: in the PDR region C_n= 93 fF (a) and in the NDR region C_n= 110 fF (b).

c) From (5.19), it should be clear that a correct value of R_s would provide an imaginary part which varies linearly with frequency (at low frequencies). The

value of R_s may be further adjusted to achieve this targeted linearity. At this stage C_n can be assumed dominant at lower frequency and estimated as:

$$\omega C_n \approx Im(Y_{RTD}) \tag{5.20}$$

Similarly to R_s, the estimated value of C_n can be de-embedded from the data in order to obtain the equivalent series circuit comprised of G_n and L_{qw}, which after converting to impedance can be expressed as:

$$Z_{RTD1} = R_n + j\omega L_{qw} \tag{5.21}$$

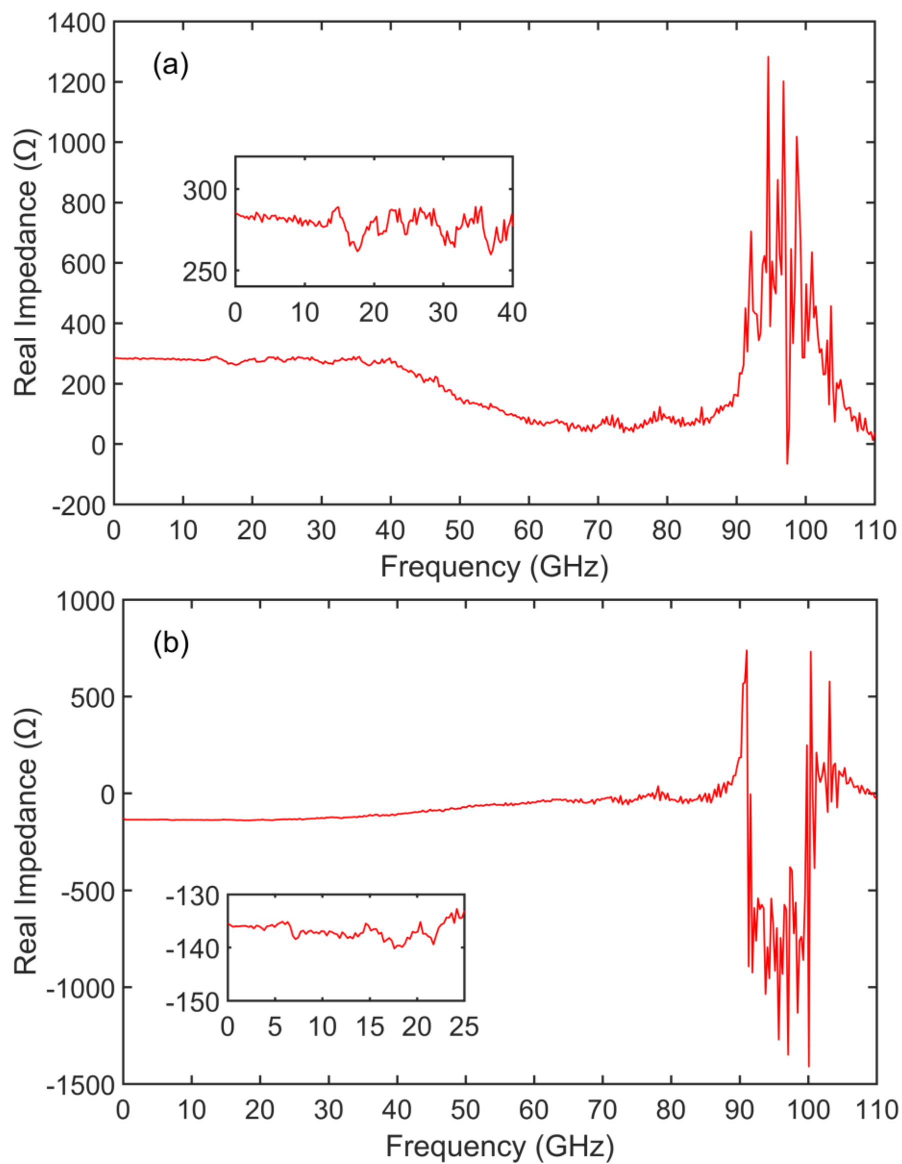

Figure 5.17 Real part of Z-parameters with de-embedded R_s and C_n – linear region shown in inset used to estimate R_n: in the PDR region R_n= 284 Ω (a) and in the NDR region R_n= 136 Ω (b).

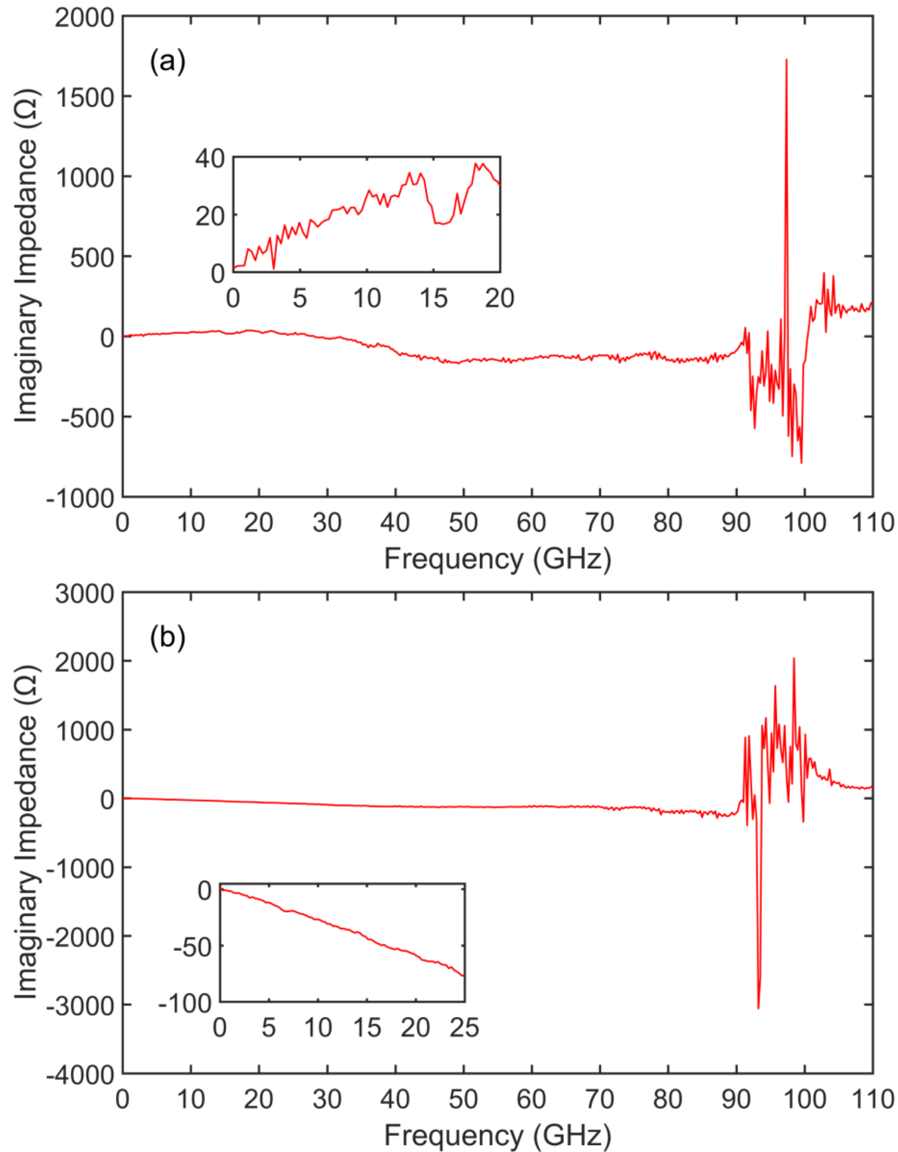

Figure 5.18 Imaginary part of Z-parameters with de-embedded R_s and C_n – linear region shown in inset used to estimate L_{qw}: in the PDR L_{qw} = 0.37 nH (a) and in the NDR region L_{qw} = -0.48 nH, where C_n is further adjusted to 94 fF to achieve linearity (b).

d) By using Eqn. 5.21 the correct value of R_s (and C_n) should provide the frequency independent values for R_n and L_{qw}. Thus, R_s and C_n can be again adjusted to achieve this. The real part of Z_{RTD1}, (Fig. 5.17), can be used to directly determine R_n, while the imaginary part (Fig. 5.18) yields L_{qw}. As expected, the magnitudes of both R_n and L_{qw} become negative when the device is biased in the NDR region.

In specific cases, for which the magnitude of L_{qw} is large (i.e. in the NDR region), its effects can be observed more dominant at lower frequencies in the susceptance

of the circuit ($Im(Y_{RTD})$). Using the estimation presented in (c) would provide an overcompensated value of C_n, which needs further adjustment in order to achieve linearity in the real and imaginary part of Z_{RTD1}.

In summary, the described extraction procedure starting with an estimate value of R_s would determine the intrisic RTD elements, through sequential de-embedding of the fixed component between stages. Due to the implied estimations, a few iterations might be required in specific bias ranges, in which the values for R_s and C_n are typically varied within ± 10% in order to account for potential under-/overcompensation. Futhermore, the somewhat random behaviour at higher frequencies, as shown in Fig. 5.17 and 5.18, might be attributed to reduced measurement accuracy at these frequencies.

The proposed extraction procedure was carried out for several key points thoughout the entire device bias range and the obtained parameters were used to compute simulated device input impedance and reflection coefficient. The results are compared with the measured impedance data as illustrated in the following figures (i.e. Fig. 5.19, Fig. 5.20 and Fig. 5.21, respectively), for the device input impedance in all three regions of interest.

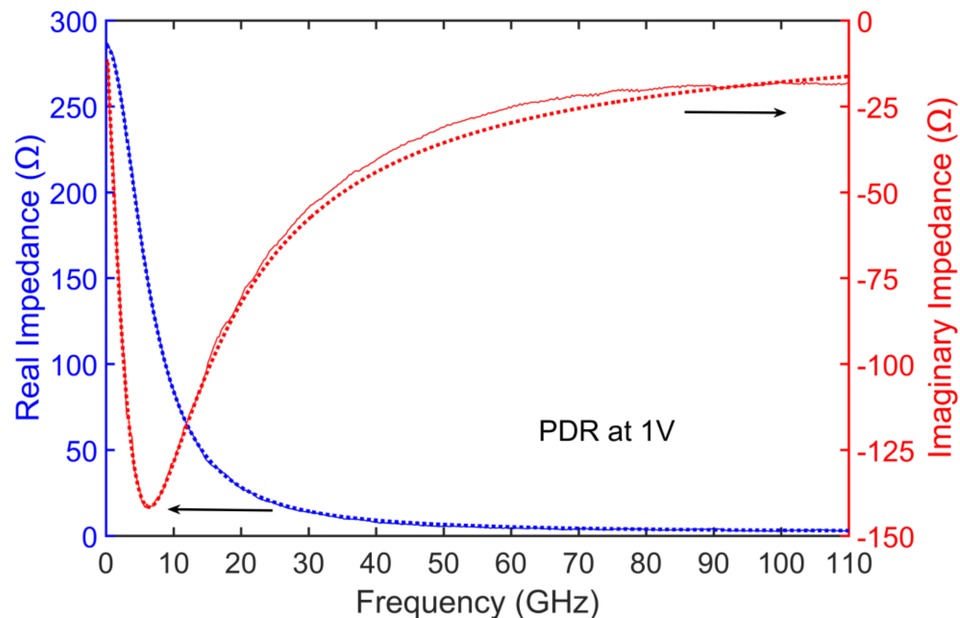

Figure 5.19 De-embedded real and imaginary measured (line) and fitted (circles) Z-parameters of a stabilised RTD at 1V in the first PDR region.

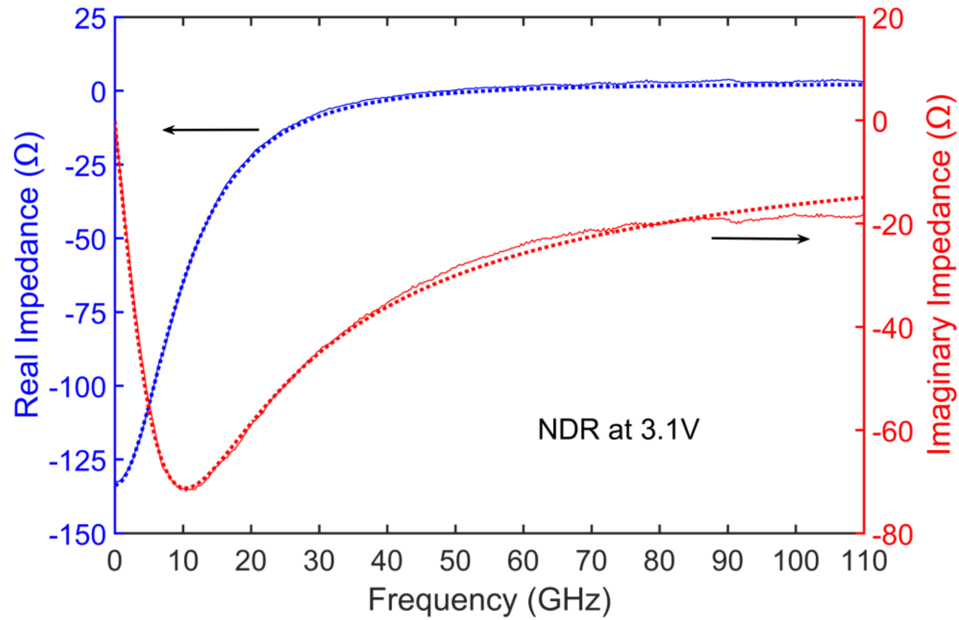

Figure 5.20 De-embedded real and imaginary measured (line) and fitted (circles) Z-parameters of a stabilised RTD at 3.1V in the NDR region.

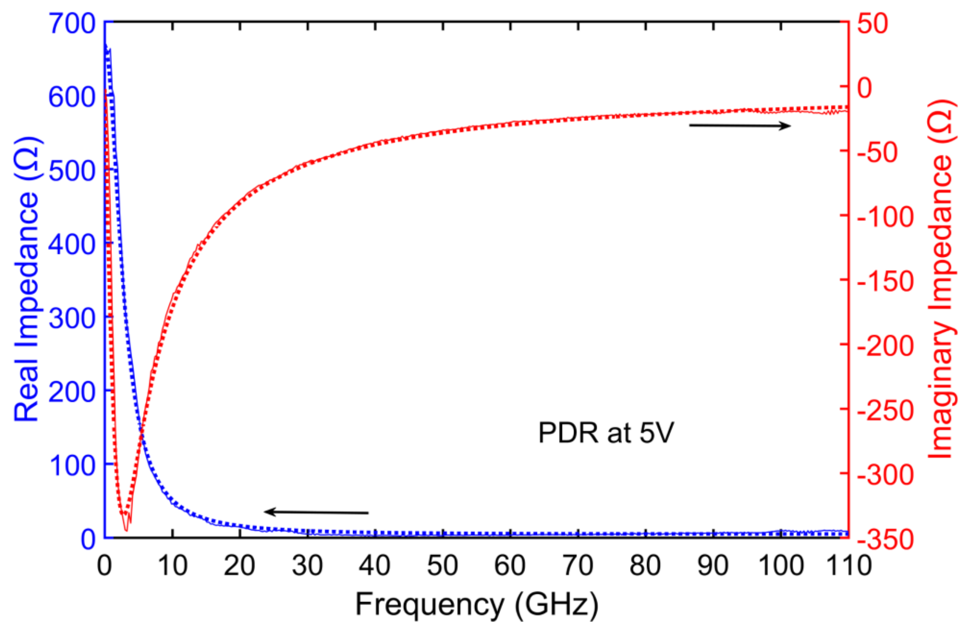

Figure 5.21 De-embedded real and imaginary measured (line) and fitted (circles) Z-parameters of a stabilised RTD at 5V in the second PDR region.

Excellent agreement between measurement and simulated RTD data, based on the above described extraction methodology, can be observed over the complete measurement frequency range (i.e. 10 MHz to 110 GHz), demonstrating the accuracy of the proposed procedure.

In order to further validate the accuracy of the extracted parameters, a standard optimisation process was used with the aid of the extracted data as starting parameters in order to obtain an error margin for each coefficient with 95% confidence bounds. A summary of the extracted small-signal equivalent circuit elements at various bias points, throughout the entire bias range, is presented in Table 5.1, alongside the computed variation range (tabulated in brackets), following the optimisation stage.

Table 5.1 Summary of extracted parameters

Bias Voltage (V)	R_s *(Ω)*	G_n *(mS)*	C_n *(fF)*	L_{qw} *(nH)*
1	2.5 (2.87)	3.52 (3.48 : 3.55)	93 (91 : 94)	0.37 (0.32 : 0.35)
2	3.18 (3.3)	11.11 (10.86 : 11.36)	86 (86 : 89)	0.11 (0.08 : 0.13)
2.9	3.5 (3)	7.57 (7.46 : 7.75)	85 (84 : 89)	0.17 (0.15 : 0.2)
3.1	3.6 (3.9)	-7.35 (-7.46 : -7.35)	94 (91 : 95)	-0.478 (-0.54 : -0.45)
3.4	3.73 (3.9)	-3.83 (-3.83 : -3.76)	92 (92 : 93)	-0.63 (-0.62 : -0.6)
3.6	3.8 (4)	-2.52 (-2.56 : -2.51)	91 (88 : 91)	-0.80 (-0.88 : -0.79)
4.8	4.3 (4.23)	0.52 (0.5 : 0.53)	90 (87 : 91)	8 (8.12 : 8.5)
5	4.42 (4)	1.49 (1.49 : 1.51)	90 (86 : 90)	1.8 (1.78 : 1.89)
5.2	5.12 (5.12)	3.09 (3.07 : 3.09)	89 (87 : 90)	0.54 (0.54 : 0.56)
5.4	5.23 (4.87)	5.2 (5.15 : 5.23)	88 (86 : 91.5)	0.28 (0.27 : 0.29)

A comparison between the computed goodness-of-fit based on the initially extracted parameter values and the improved fit obtained through an optimisation process using the initial values as the procedure start values is given in Table 5.2 in the form of R-squared value [46].

Table 5.2 Computed goodness-of-fit between measurement and simulation

Bias Voltage (V)	*R-squared extracted values*	*R-squared improved by optimization*
1	0.9985	0.9995
2	0.9988	0.9998
2.9	0.9679	0.9857
3.1	0.9939	0.9947
3.4	0.9965	0.9974
3.6	0.9988	0.9994
4.8	0.9696	0.9890
5	0.9876	0.9907
5.2	0.9919	0.9934
5.4	0.9897	0.9938

An R-squared value above 97% was obtained across the entire RTD operating range based solely on the initial extracted data. Overall, a further improvement of approximately 2% was observed after the optimisation stage which shows that good extraction accuracy can be achieved using the proposed procedure.

5.3.3 Modelling of RTD intrinsic parameters

The behaviour of the determined RTD equivalent circuit parameters has been further investigated, particularly in relation to their bias dependence, through alternative proposed theoretical and experimental estimation methods.

Firstly, the metal-semiconductor contact resistance was determined experimentally by using standard the transmission line model (TLM) measurements, which are detailed in Appendix B. The total R_s value (i.e. considering the contribution of the top and bottom contacts) for the 10 × 10 μm^2 devices investigated in this characterisation study is estimated at approximately 2.6 Ω. The results of the complete extraction procedure indicate a relatively small linear bias dependence of the contact and access resistance (1.3 Ω over a range of 4V), as shown in Fig. 5.22.

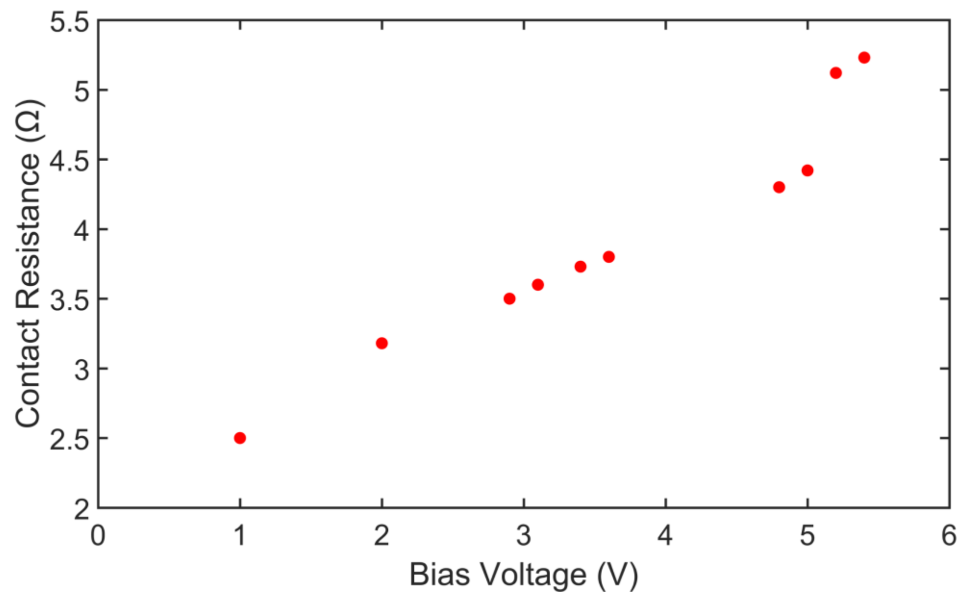

Figure 5.22 Extracted RTD contact resistance R_s showing a variation of approximately 1.3 Ω over a bias range of 4V.

The presented variation in contact resistance with bias was possible to observe at high frequencies, between 80 – 110 GHz. Even though this phenomenon has never been previously reported in the context of RTD characterisation studies, i.e. R_s is usually assumed to be bias independent, it could be attributed to the electric field dependence of the carrier mobility [47][48].

Furthermore, the estimated contact resistance has been de-embedded from the measured stabilised RTD *I-V* characteristics (Fig. 5.4) in order to yield the intrinsic device *I-V* curve. Based on the "true" current-voltage data, the device differential conductance G_n was computed directly as the first derivative of the de-embedded curve. Good agreement can be seen in Fig. 5.23, between the variation of G_n with bias and the extracted G_n values from S-parameter data.

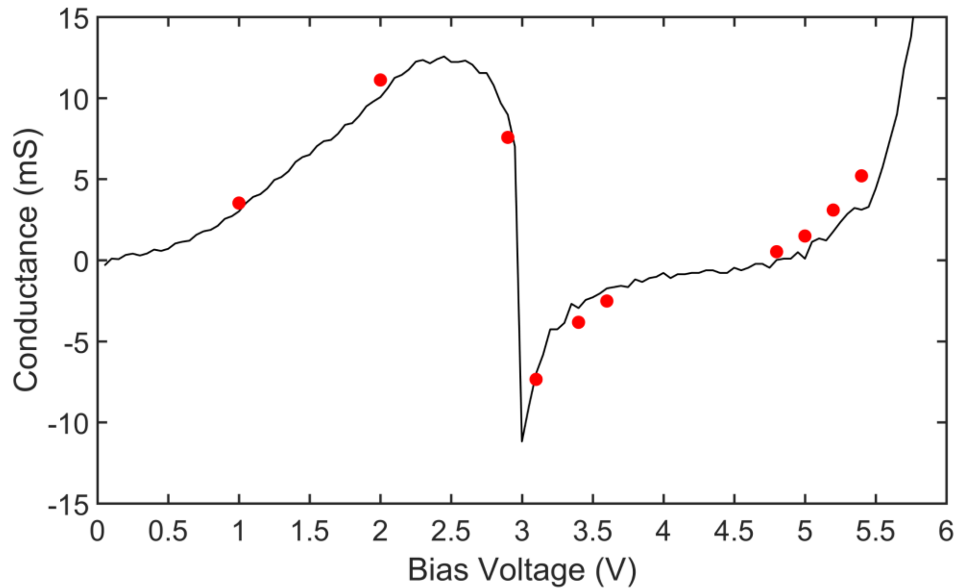

Figure 5.23 Differential device conductance Gn computed from the intrinsic I-V characteristics (black trace) and extracted (red dots).

The RTD self-capacitance, C_n can be computed throughout the entire bias range as the combination of geometric capacitance, C_0 together with the quantum-well capacitance, C_{qw}, which arises from the electron density change in the quantum well as a function of applied bias, as derived in [35]:

$$C_n = C_0 + C_{qw} = C_0 - \frac{G_n}{\nu_c} \tag{5.22}$$

Based on the approximation of the DBQW structure as a standard parallel-plate capacitor (i.e. an undoped region confined between a highly doped collector and emitter), C_0 was estimated as described in section 2.4 (Eqn. 2.14) at 88 fF, using the widths of the particular layer structure and their corresponding material dielectric constants summarised in Table 5.3.

Table 5.3 Summary of material parameters

Layer	*Width (L)*	*Dielectric constant (ε_r)*
Quantum-well	4.7 nm	13.1 [49]
Barrier	2.5 nm	13.1 [49]
Depletion region	120 nm	10.1 [50]

Assuming the width of the depletion region to be bias independent, the extracted device capacitance from S-parameters, which corresponds to C_n, indicates that the static capacitance C_0 is slightly higher (~90 fF). Furthermore, using this parameter (C_0), together with the measured device differential conductance, the magnitude of the quantum-well – collector electron escape rate (assumed bias independent), which defines C_{qw}, was determined using Eqn. 5.22 to be $1/\nu_c \approx 0.55$ ps. The total calculated RTD capacitance variation is presented in Fig. 5.24, alongside the extracted device capacitance from S-parameter data. The small observed discrepancies at lower bias voltages (approximately 4 fF) can be correlated to the assumption regarding the bias independency of the electron escape rate, which was not computed theoretically.

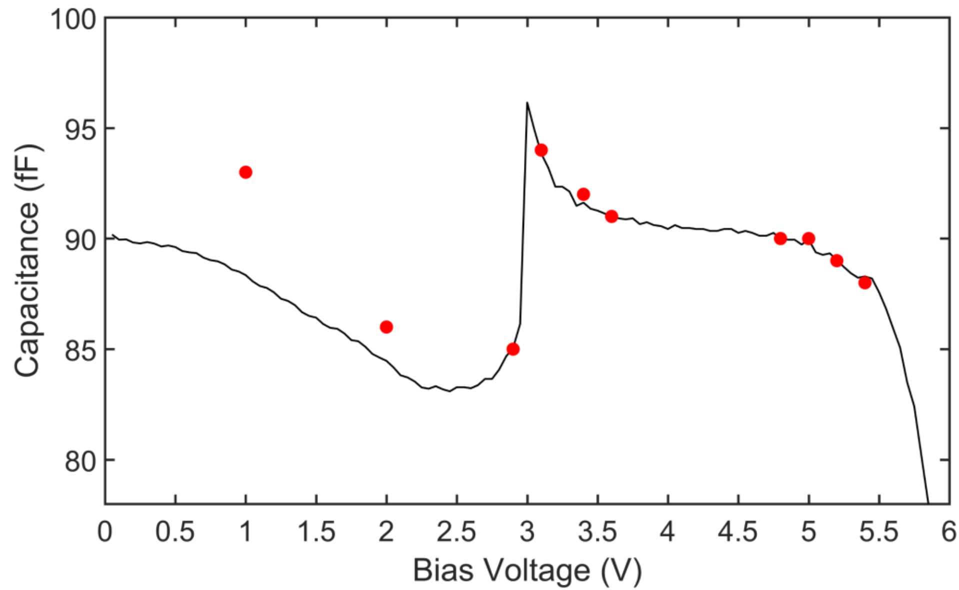

Figure 5.24 RTD Device capacitance C_n simulated (black trace) and extracted (red dots).

For modelling the behaviour of the quantum-well inductance, the initial derivation proposed in [51] was used, where, as previously stated, L_{qw} is determined by the electron dwell time (τ_{dwell}). In order to compute this quantity based on Eqn. 2.15, the energy full-width of the transmission probability function through the resonant state (ΔE_n) was estimated by the Wentzel–Kramers–Brillouin (WKB) approximation method as follows [52]:

$$\Delta E_n = E_n \exp\left[-2L_b\sqrt{\frac{2m_b(U_0 - E_n)}{\hbar^2}}\right] \quad (5.23)$$

where E_n is the nth resonance level, L_b is the width of the barrier (2.5 nm), U_0 is the barrier energy level (1.322 eV) and m_b is the effective electron mass in the barrier.

Fig. 5.25 shows the transmission probability through the RTDs DBQW structure, computed using the nonequilibrium Green function based 1D quantum transport simulator WinGreen software [53]. The estimation for the carrier lifetime is generally calculated for the first resonance energy level (E_0 = 0.17 eV for this structure), however, the transmission probability plot suggests that the primary resonant current occurs at a higher energy level (E_1 = 0.73 eV). Thus, the computed value for τ_{dwell} was found to be approximately 1.86 ps.

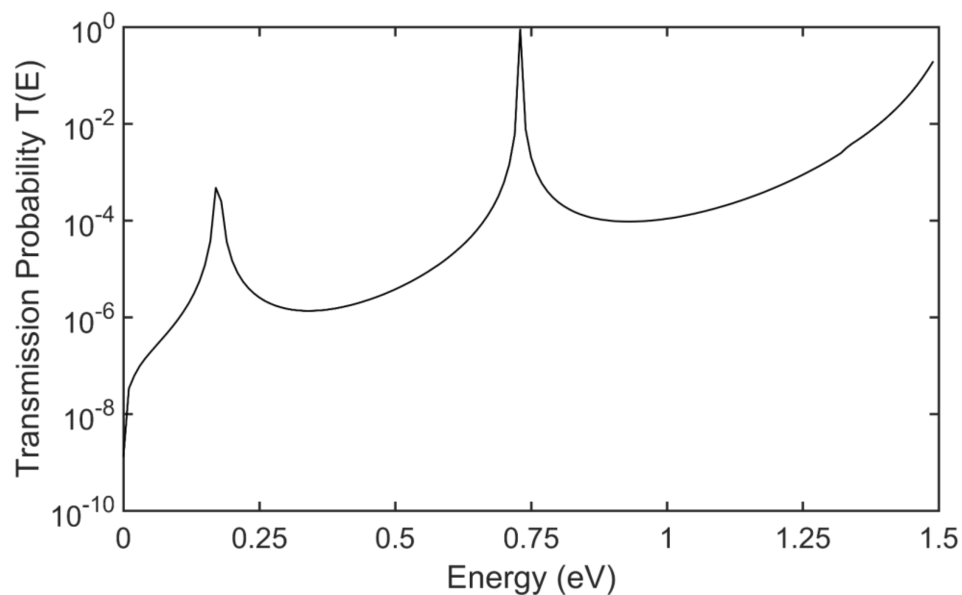

Figure 5.25 Simulated transmission probability for the measured RTD layer structure.

Based on the estimated value for the electron quasibound-state lifetime in the quantum-well and the experimentally determined RTD differential conductance, the variation of L_{qw} with bias was computed and is shown in Fig. 5.26, together with the extracted values from the S-parameter measurements. As expected, the computed inductance becomes negative in the NDR region following the nature of the differential conductance. However, a discrepancy can be observed between the measured and simulated data within this region, which can be better illustrated in Fig. 5.27, as a comparison between the computed (based on Eqn. 2.15) and extracted τ_{dwell}. This behaviour is consistent with the phenomenon described in [54], and relates the extracted time constant to the charge-relaxation process (τ_{rel}) of the RTD. A large

variation with bias of the associated time constant can be observed between the positive and negative differential resistance regions of the device.

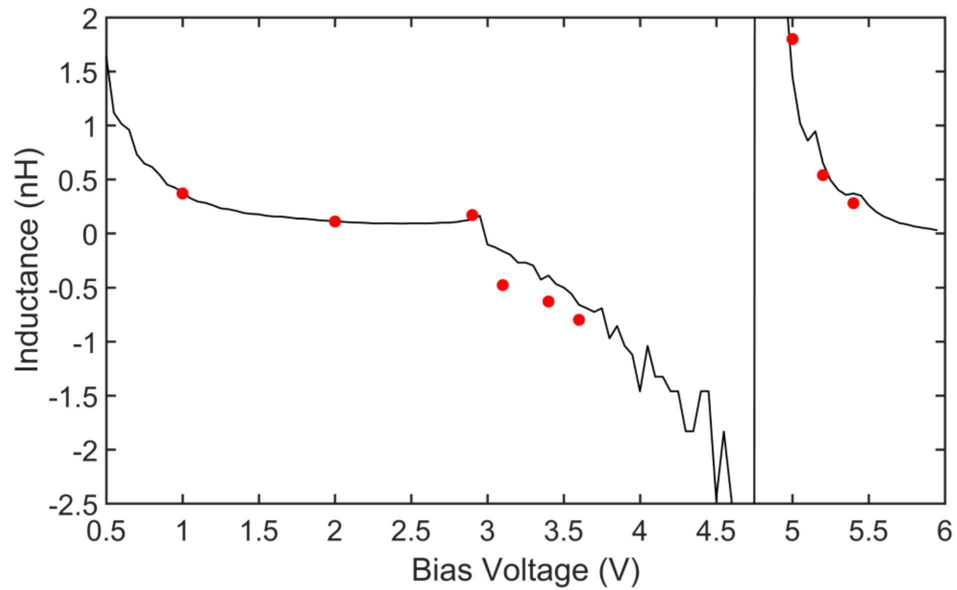

Figure 5.26 Quantum-well inductance Lqw simulated (black trace) and extracted (red dots).

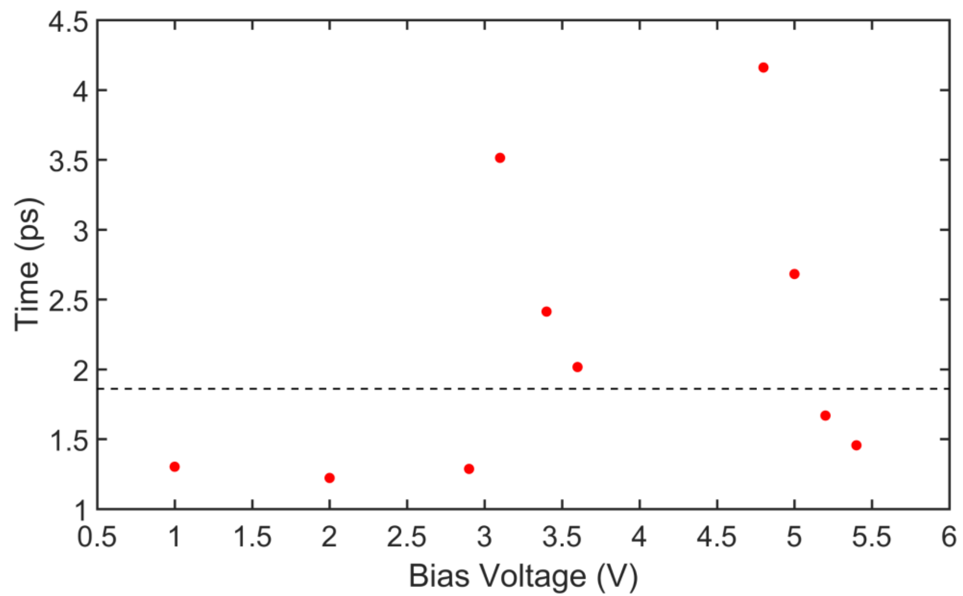

Figure 5.27 Electron dwell time τ_{dwell} computed (black dashed line) and extracted (red dots).

5.4 Summary and discussion

In this chapter the characterisation of an RTD device was described, particularly in relation to its high-frequency behaviour. The challenges associated with accurate modelling of the negative differential resistance (NDR) region due to the presence of low-frequency parasitic oscillations have been discussed. For this purpose, a standard stabilisation method, based on a shunt-resistor bias network was adopted, and its effectiveness to suppress bias oscillations was assessed experimentally in the MHz frequency range.

Due to the requirement for the external stabilisation network in the context of high-frequency RTD modelling, a novel on-wafer bond-pad and shunt-resistor de-embedding technique was developed. The accuracy of the proposed method, which relies principally on measured data from one auxiliary test structure, was demonstrated experimentally in the case of a stabilised RTD using S-parameter measurements up to 110 GHz across the entire device bias range.

Furthermore, using the obtained de-embedded data, a robust quasi-analytical small-signal equivalent circuit extraction procedure was described, based on a sequential approach, and validated by a standard optimisation process. The proposed procedure, aided by the high-frequency nature of the measurements, enabled an accurate extraction of the parameter values of the small signal equivalent circuit, resulting in a clear distinction between key RTD elements such as the differential conductance and contact resistance. Finally, the physical relevance of the acquired device bias-dependent parameters was determined based on alternative experimental and previously proposed theoretical approaches.

The presented complete experimental approach for high-frequency RTD characterisation is expected to provide a strong foundation for the ongoing development of compact CAD device models, thus accelerating the advancement of RTD technology for THz applications. The scalability of such models is further investigated in Chapter 6 in the context of realisation of an RTD based detector application.

5.5 References

[1] E. Ozbay, D. M. Bloom, D. Chow, and J. Schulman, "1.7-ps, microwave, integrated-circuit-compatible InAs/AlSb resonant tunneling diodes," *IEEE Electron Device Letters,* vol. 14, no. 8, pp. 400-402, 1993.

[2] R. Izumi, S. Suzuki, and M. Asada, "1.98 THz resonant-tunneling-diode oscillator with reduced conduction loss by thick antenna electrode," in *2017 42nd International Conference on Infrared, Millimeter, and Terahertz Waves (IRMMW-THz)*, pp. 1-2, 27 Aug.-1 Sept. 2017, 2017.

[3] S. Diebold, K. Nishio, Y. Nishida, J.-Y. Kim, K. Tsuruda, T. Mukai, M. Fujita, and T. Nagatsuma, "High-speed error-free wireless data transmission using a terahertz resonant tunnelling diode transmitter and receiver," *Electronics Letters,* vol. 52, no. 24, pp. 1999-2001, 2016.

[4] T. Miyamoto, A. Yamaguchi, and T. Mukai, "Terahertz imaging system with resonant tunneling diodes," *Japanese Journal of Applied Physics,* vol. 55, no. 3, p. 032201, 2016.

[5] T. P. Broekaert, B. Brar, J. P. A. van der Wagt, A. C. Seabaugh, F. J. Morris, T. S. Moise, E. A. Beam, and G. A. Frazier, "A monolithic 4-bit 2-Gsps resonant tunneling analog-to-digital converter," *IEEE Journal of Solid-State Circuits,* vol. 33, no. 9, pp. 1342-1349, 1998.

[6] T. Kim, Y. Jeong, and K. Yang, "New RTD-based SET/RESET latch IC for high-speed MOBILE D-flip flops," in *International Conference on Indium Phosphide and Related Materials, 2005*: IEEE, pp. 311-314, 2005.

[7] A. C. Seabaugh, Y.-C. Kao, and H.-T. Yuan, "Nine-state resonant tunneling diode memory," *IEEE Electron Device Letters,* vol. 13, no. 9, pp. 479-481, 1992.

[8] M. A. Bawiec, "Resonant tunnelling diode-based circuits: simulation and synthesis," in *Computer Aided Systems Theory - EUROCAST 2009*, Berlin, Heidelberg: Springer Berlin Heidelberg, pp. 873-880, 2009.

[9] Z. Qiu, Y. Gui, S. Guo, N. Dai, J. Chu, X. Zhang, and Y. Zeng, "Experimental verification on the origin of plateau-like current–voltage characteristics of resonant tunneling diodes," *Applied Physics Letters,* vol. 84, no. 11, pp. 1961-1963, 2004.

[10] P. Zhao, H. Cui, D. Woolard, K. Jensen, and F. Buot, "Simulation of resonant tunneling structures: Origin of the I–V hysteresis and plateau-like structure," *Journal of Applied Physics,* vol. 87, no. 3, pp. 1337-1349, 2000.

[11] C. Kidner, I. Mehdi, J. East, and G. Haddad, "Power and stability limitations of resonant tunneling diodes," *IEEE Transactions on Microwave Theory and Techniques,* vol. 38, no. 7, pp. 864-872, 1990.

[12] C. Kidner, I. Mehdi, J. R. East, and G. I. Haddad, "Bias circuit instabilities and their effect on the dc current-voltage characteristics of double-barrier resonant tunneling diodes," *Solid-State Electronics,* vol. 34, no. 2, pp. 149-156, 1991.

[13] W. F. Chow, "Principles of tunnel diode circuits," 1964.

[14] L. Wang, "Reliable design of tunnel diode and resonant tunnelling diode based microwave sources," Phd Thesis PhD Thesis, University of Glasgow, 2012.

[15] M. Bao and K. L. Wang, "Accurately measuring current-voltage characteristics of tunnel diodes," *IEEE Transactions on Electron Devices,* vol. 53, no. 10, pp. 2564-2568, 2006.

[16] M. Reddy, R. Yu, H. Kroemer, M. Rodwell, S. Martin, R. Muller, and R. Smith, "Bias stabilization for resonant tunnel diode oscillators," *IEEE Microwave and Guided Wave Letters,* vol. 5, no. 7, pp. 219-221, 1995.

[17] M. Reddy, M. J. Mondry, M. Rodwell, S. Martin, R. Muller, R. Smith, D. Chow, and J. Schulman, "Fabrication and dc, microwave characteristics of submicron Schottky-collector AlAs/In0. 53Ga0. 47As/InP resonant tunneling diodes," *Journal of Applied Physics,* vol. 77, no. 9, pp. 4819-4821, 1995.

[18] A. C. Cornescu, R. Morariu, A. Ofiare, A. Al-Khalidi, J. Wang, J. M. Figueiredo, and E. Wasige, "High-efficiency bias stabilization for resonant tunneling diode oscillators," *IEEE Transactions on Microwave Theory and Techniques,* vol. 67, no. 8, pp. 3449-3454, 2019.

[19] C. Goodings, H. Mizuta, J. Cleaver, and H. Ahmed, "Variable-area resonant tunneling diodes using implanted in-plane gates," *Journal of Applied Physics,* vol. 76, no. 2, pp. 1276-1286, 1994.

[20] B. Jogai and E. Koenig, "A parametric study of extrinsic bistability in the current-voltage curves of resonant-tunneling diodes," *Journal of Applied Physics,* vol. 69, no. 5, pp. 3381-3383, 1991.

[21] T. Foster, M. Leadbeater, L. Eaves, M. Henini, O. Hughes, C. Payling, F. Sheard, P. Simmonds, G. Toombs, and G. Hill, "Current bistability in double-barrier resonant-tunneling devices," *Physical Review B,* vol. 39, no. 9, p. 6205, 1989.

[22] T. J. Slight, C. Ironside, C. Stanley, M. Hopkinson, and C. Farmer, "Integration of a resonant tunneling diode and an optical communications laser," *IEEE Photonics Technology Letters,* vol. 18, no. 14, pp. 1518-1520, 2006.

[23] H. Berkowitz and R. Lux, "Hysteresis predicted in I–V curve of heterojunction resonant tunneling diodes simulated by a self-consistent quantum method," *Journal of Vacuum Science & Technology B: Microelectronics Processing and Phenomena,* vol. 5, no. 4, pp. 967-970, 1987.

[24] R. Mains, J. Sun, and G. Haddad, "Observation of intrinsic bistability in resonant tunneling diode modeling," *Applied Physics Letters,* vol. 55, no. 4, pp. 371-373, 1989.

[25] F. Sheard and G. Toombs, "Space-charge buildup and bistability in resonant-tunneling double-barrier structures," *Applied Physics Letters,* vol. 52, no. 15, pp. 1228-1230, 1988.

[26] H. Mizuta and T. Tanoue, *The physics and applications of resonant tunnelling diodes*. Cambridge university press, 2006.

[27] M. Rahman and J. Davies, "Theory of intrinsic bistability in a resonant tunnelling diode," *Semiconductor Science and Technology,* vol. 5, no. 2, p. 168, 1990.

[28] E. Alves, L. Eaves, M. Henini, O. Hughes, and M. Leadbeater, "Observation of intrinsic bistability in resonant tunnelling devices," *ElL,* vol. 24, p. 1190, 1988.

[29] M. Leadbeater, E. Alves, L. Eaves, M. Henini, O. Hughes, F. Sheard, and G. Toombs, "Charge build-up and intrinsic bistability in an asymmetric resonant-tunnelling structure," *Semiconductor Science and Technology,* vol. 3, no. 10, p. 1060, 1988.

[30] A. Zaslavsky, V. Goldman, D. Tsui, and J. Cunningham, "Resonant tunneling and intrinsic bistability in asymmetric double-barrier heterostructures," *Applied Physics Letters,* vol. 53, no. 15, pp. 1408-1410, 1988.

[31] C. Goodings, H. Mizuta, and J. Cleaver, "Electrical studies of charge build-up and phonon-assisted tunneling in double-barrier materials with very thick spacer layers," *Journal of Applied Physics,* vol. 75, no. 4, pp. 2291-2293, 1994.

[32] P. Fay, J. Lu, Y. Xu, N. Dame, D. H. Chow, and J. N. Schulman, "Microwave performance and modeling of InAs/AlSb/GaSb resonant interband tunneling diodes," *IEEE Transactions on Electron Devices,* vol. 49, no. 1, pp. 19-24, 2002.

[33] T. Wei, S. Stapleton, and O. Berolo, "Scattering parameter measurements of resonant tunneling diodes up to 40 GHz," *IEEE Transactions on Electron Devices,* vol. 42, no. 7, pp. 1378-1380, 1995.

[34] A. Teranishi, K. Shizuno, S. Suzuki, M. Asada, H. Sugiyama, and H. Yokoyama, "Fundamental oscillation up to 1.08 THz in resonant tunneling diodes with high-indium-composition transit layers for reduction of transit delay," *IEICE Electronics Express,* vol. 9, no. 5, pp. 385-390, 2012.

[35] Q. Liu, A. Seabaugh, P. Chahal, and F. J. Morris, "Unified AC model for the resonant tunneling diode," *IEEE Transactions on Electron Devices,* vol. 51, no. 5, pp. 653-657, 2004.

[36] S. G. Muttlak, O. S. Abdulwahid, J. Sexton, M. J. Kelly, and M. Missous, "InGaAs/AlAs resonant tunneling diodes for THz applications: an experimental investigation," *IEEE Journal of the Electron Devices Society,* vol. 6, pp. 254-262, 2018.

[37] S. Diebold, S. Nakai, K. Nishio, J. Kim, K. Tsuruda, T. Mukai, M. Fujita, and T. Nagatsuma, "Modeling and simulation of terahertz resonant tunneling diode-based circuits," *IEEE Transactions on Terahertz Science and Technology,* vol. 6, no. 5, pp. 716-723, 2016.

[38] M. Long, H. Ying-Long, Z. Yang, W. Liang-Chen, Y. Fu-Hua, and Z. Yi-Ping, "A small signal equivalent circuit model for resonant tunnelling diode," *Chinese Physics Letters,* vol. 23, no. 8, p. 2292, 2006.

[39] C.-I. Lee, W.-C. Lin, and Y.-T. Lin, "An improved cascade-based noise deembedding method for on-wafer noise parameter measurements," *IEEE Electron Device Letters,* vol. 36, no. 4, pp. 291-293, 2015.

[40] M. Koolen, J. Geelen, and M. Versleijen, "An improved de-embedding technique for on-wafer high-frequency characterization," in *Proc. Bipolar Circuits Technol. Meeting*: Minneapolis, MN, pp. 188-191, 1991.

[41] A. Ofiare, "Components and circuits for tunneling diode based high frequency sources," University of Glasgow, 2016.

[42] M. Feiginov and D. R. Chowdhury, "Experimental demonstration of resonant-tunneling-diode operation beyond quasibound-state-lifetime limit," in *Journal of Physics: Conference Series*, vol. 193, no. 1: IOP Publishing, p. 012016, 2009.

[43] R. Morariu, J. Wang, A. C. Cornescu, A. Al-Khalidi, A. Ofiare, J. M. L. Figueiredo, and E. Wasige, "Accurate small-signal equivalent circuit modeling

of resonant tunneling diodes to 110 GHz," *IEEE Transactions on Microwave Theory and Techniques,* vol. 67, no. 11, pp. 4332-4340, 2019.

[44] K. Kurokawa, "Power waves and the scattering matrix," *IEEE Transactions on Microwave Theory and Techniques,* vol. 13, no. 2, pp. 194-202, 1965.

[45] G. Gonzalez, *Microwave transistor amplifiers analysis and design*. Prentice-Hall, Inc., 1996.

[46] C. Heumann and M. Schomaker, *Introduction to statistics and data analysis*. Springer, 2016.

[47] C. Nasser, D. Ritter, and M. Rudolph, "Bias dependence of the access resistance in GaN HEMTs," in *2018 22nd International Microwave and Radar Conference (MIKON)*, pp. 271-273, 14-17 May 2018, 2018.

[48] S. Ghosh, S. A. Ahsan, Y. S. Chauhan, and S. Khandelwal, "Modeling of source/drain access resistances and their temperature dependence in GaN HEMTs," in *2016 IEEE International Conference on Electron Devices and Solid-State Circuits (EDSSC)*: IEEE, pp. 247-250, 2016.

[49] P. Bhattacharya, *Properties of lattice matched and strained indium gallium arsenide*. Stevenage: INSPEC, the Institution of Electrical Engineers, 1993.

[50] S. Tiwari, *Compound semiconductor device physics*. Academic press, 2013.

[51] E. R. Brown, C. D. Parker, and T. C. L. G. Sollner, "Effect of quasibound-state lifetime on the oscillation power of resonant tunneling diodes," *Applied Physics Letters,* vol. 54, no. 10, pp. 934-936, 1989.

[52] C. Cohen-Tannoudji, B. Diu, and F. Laloe, *Quantum Mechanics, volume 1.* (Inc., Paris). Hermann and John Wiley & Sons, 1977.

[53] K. M. Indlekofer and J. Malindretos. "WinGreen software." https://www.hs-rm.de/en/rheinmain-university/people/indlekofer-klaus-michael/research-and-development/wingreen/ (accessed 30.12.2020).

[54] M. N. Feiginov, "Does the quasibound-state lifetime restrict the high-frequency operation of resonant-tunnelling diodes?," *Nanotechnology,* vol. 11, no. 4, p. 359, 2000.

Chapter 6. RTD-based detector

6.1 Introduction

As discussed in the introductory chapter of this thesis, the terahertz (THz) frequency range has become an important target for research fields involving high data rate wireless communications and high-resolution sensing due to its extremely large available bandwidth, which is yet to be allocated for specific applications [1]. As a semiconductor electronic device based THz source, the RTD has been proven to be one of the primary contenders in the race for integration into consumer based applications due to its high oscillation frequency [2], relatively high output power (~1 mW in the 220 GHz– 325 GHz frequency range) [3][4], low manufacturing cost and compact implementation, in comparison to other candidate technologies.

Additionally to the proven implementation as a THz transmitter, the RTD's performance in a square-law detection scheme is also currently researched due to its strong non-linearity in the *I-V* characteristics. Furthermore, the fact that the RTD detector can be designed in a similar fashion as an RTD source raises the important advantage of having the capability of integrating the transmitter/receiver (Tx/Rx) system on one chip, or operating the same device in either configuration by altering the biasing conditions [5], thus considerably reducing design fabrication costs.

The work presented in this chapter focuses on demonstrating the operation and performance of an RTD-based detector operating as a square-law demodulator. This was done primarily from the perspective of an accurate circuit simulation methodology enabled by the device modelling procedure described in Chapter 5. Results of a data transmission experiment using the detector in the W-band (75 – 110 GHz) frequency range are also described.

6.2 RTD detector basics

The standard double-barrier RTD *I-V* characteristics display two high non-linearity regions as shown in Fig. 6.1. The first region (a) is exhibited by the initial tunnelling-current flow through the device, proportional to the thermal component expressed as:

$$J_{RTD} \approx exp\left(\frac{\alpha eV_{bias}}{kT}\right) \tag{6.1}$$

where V_{bias} is the bias point of the device, k is Boltzmann's constant, e is the electron charge, T is the temperature, and α is a device factor describing the voltage drop between the emitter and the quantum well. This initial region, which is also present in the more commonly used Schottky diode detectors, has a comparable non-linearity, generated by the same thermal mechanism, but weaker by a factor of α, which is dependent on the device layer structure characteristics (i.e. thicknesses of the emitter-well and of the well-collector regions).

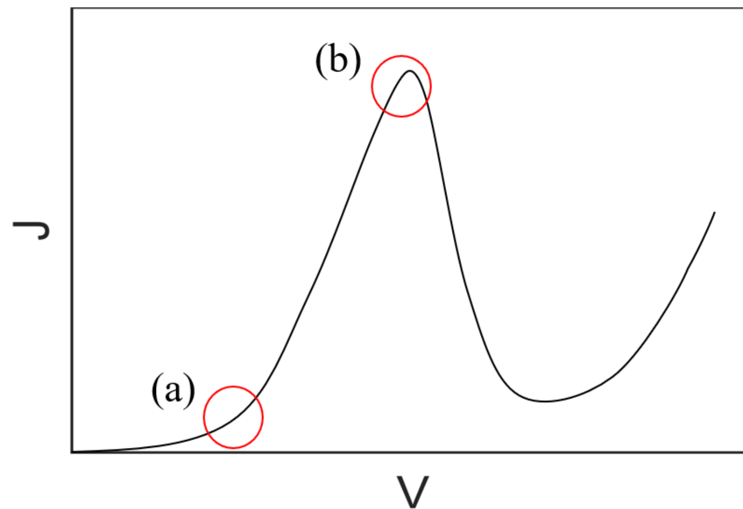

Figure 6.1 Typical RTD I-V characteristics showing the two high non-linearity regions.

The second region of interest (b) can be observed near the current peak, at the start of resonant-current switch-off. At this point, the non-linearity will be significantly higher due to the fact that it is predominantly determined by the broadening of the quantum-well resonant sub-band, rather than thermal exponent, as in the case of Schottky diodes [6]. This has been experimentally shown in [7], where the sensitivity of an RTD based detector was shown to be around 12 dB higher than that of commercially available Schottky diode.

The initial investigation into the operation of RTDs as THz detectors was originally presented in [8], where the device was proven to have a frequency response up to 2.5 THz. The non-linearity was investigated by measuring the changes in the DC *I-V*

characteristics when high power, pulsed, far-infrared radiation was applied from a free-electron laser, as shown in Fig. 6.2. The shifts in the bias point of the device produced by the oscillating field were captured in the form of a rectified response using a tungsten probe tip. In a similar fashion, the highest reported frequency response measured for such devices was 3.9 THz [9]. Currently, RTD based detectors with integrated antennas have been reported in imaging systems [10], wireless data links [11], and spectrometer applications [12].

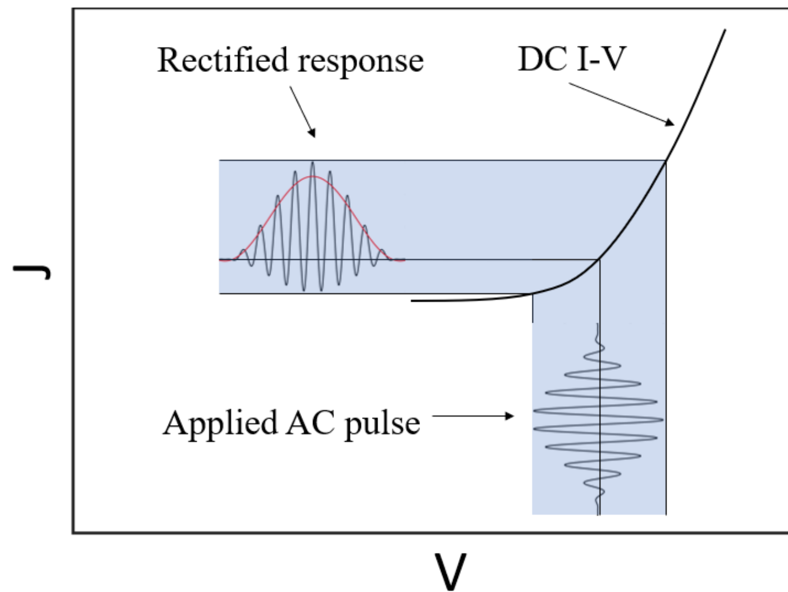

Figure 6.2 Rectified response of an applied THz pulse by the device non-linear I-V characteristics (Fig. 6.1) for region (a). Adapted from [9].

Recent work suggests that triple-barrier (TB) RTDs could have improved performance compared to devices explored in this thesis (double-barrier RTDs), when employed as detectors, since they have a stronger non-linearity in both regions (a) and (b). This is because of the fact that the resonant current is not predominantly determined by thermal effects, but rather due to the alignment of the 2D sub-bands in the adjacent quantum-wells [6]. Furthermore, triple barrier RTDs exhibit region (a) at zero bias, as shown in Fig. 6.3. [13], providing a superior curvature component due to the additional tunnelling current contribution in forward direction that is quantum mechanically blocked in reverse bias. The shift in the high non-linearity region would thus provide an important advantage in terms of the required operating voltage, enabling TB-RTDs to be designed as zero bias detectors. The rectification capabilities of such devices have been investigated in [14] for a device integrated into an on-chip slot antenna,

providing a relatively high responsivity of 66 kV/W for an applied 280 GHz signal. However, the main disadvantage of these devices is their low current density and relatively high impedance, when compared to double-barrier RTDs, which results in difficulty to design an optimal matching network between the detector and antenna [15].

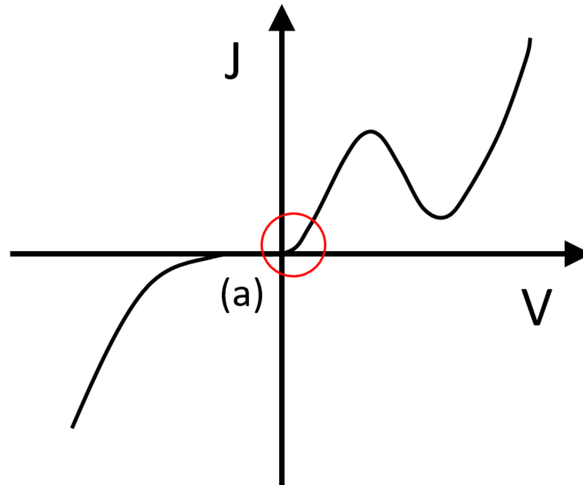

Figure 6.3 Typical TB-RTD I-V characteristics.

6.2.1 Square-law demodulation

The theory of operation of a non-linear device as a square-law demodulator can be easily illustrated in the context of electronic communication systems that employ a standard amplitude modulation (AM) scheme. Fig. 6.4 shows the generalised frequency spectrum of an amplitude modulated signal.

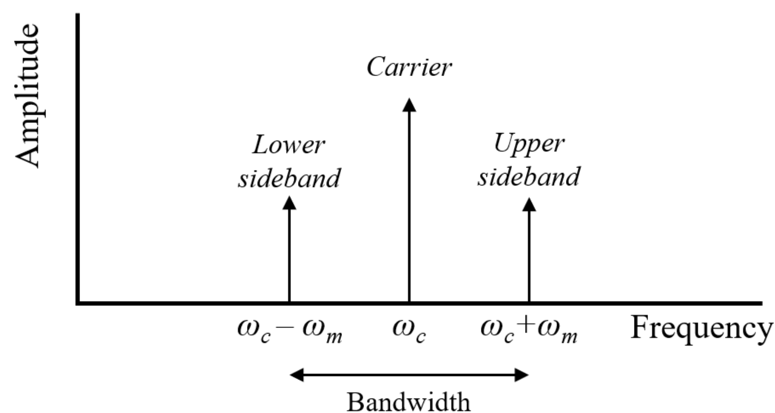

Figure 6.4 Frequency spectrum of a standard AM signal, showing the centre carrier frequency ω_c and the sidebands of the baseband signal of frequency ω_m.

The non-linear regions exhibited by the device *I-V* characteristics presented in Fig. 6.1 can be approximated by a quadratic function in the form:

$$i(t) = k_1 v(t) + k_2 v^2(t) \tag{6.2}$$

where k_1 and k_2 are constants associated with the particular device. If the applied time varying voltage $v(t)$ is an AM wave expressed as:

$$v(t) = A_c\big(1 + mx(t)\big)\cos(\omega_c t) \tag{6.3}$$

where A_c is the carrier amplitude, m is the modulation index (defined as the ratio of the modulation signal amplitude to the carrier amplitude), $x(t)$ is the original baseband signal and ω_c is the angular frequency of the carrier [16]; the output of the system can be expressed as:

$$i(t) = k_1 A_c\big(1 + mx(t)\big)\cos(\omega_c t) + k_2 A_c^2\big(1 + mx(t)\big)^2 cos^2(\omega_c t) \tag{6.4}$$

By expanding Eqn. 6.4 and using the identity $cos^2(x) = \frac{1+\cos(2x)}{2}$, we get:

$$\begin{aligned} i(t) = {} & k_1 A_c \cos(\omega_c t) + k_1 A_c m x(t)\cos(\omega_c t) + \frac{1}{2}k_2 A_c + k_2 A_c^2 m x(t) \\ & + \frac{1}{2}k_2 A_c^2 m^2 x^2(t) + \frac{1}{2}k_2 A_c^2 \cos(2\omega_c t) \\ & + k_2 A_c^2 m x(t)\cos(2\omega_c t) + \frac{1}{2}k_2 A_c^2 m^2 x^2(t)\cos(2\omega_c t) \end{aligned} \tag{6.5}$$

The terms containing high-frequency carrier components ($\cos(\omega_c t)$ and $\cos(2\omega_c t)$) are filtered out using a low-pass filter at the output stage, for which the cut-off frequency is determined by the baseband signal. The remaining components represent:

- $\boldsymbol{\frac{1}{2}k_2 A_c}$ – DC component.
- $\boldsymbol{k_2 A_c^2 m x(t)}$ – scaled version of the original baseband signal, which can be recovered with the aid of a low-pass filter stage.
- $\boldsymbol{\frac{1}{2}k_2 A_c^2 m^2 x^2(t)}$ – distortion component.

If however, the RTD *I-V* characteristics around the operating region of the detector cannot be represented as a quadratic function, as shown in Fig. 6.5 for an experimental

device, a more accurate approximation can be obtained using a higher order Taylor series expansion at the peak-current point [17], as shown by the red trace in the inset figure. The form of the expansion is represented as:

$$I(V) = I(V_0) + \left(\frac{dI}{dV}\right)_{V=V_0} dV + \frac{1}{2!}\left(\frac{d^2I}{dV^2}\right)_{V=V_0} dV^2 + \frac{1}{3!}\left(\frac{d^3I}{dV^3}\right)_{V=V_0} dV^3 + \cdots \tag{6.6}$$

By inspecting this equation from the perspective of the output current, it can be determined that the cubic and higher order terms can be ignored for a given relatively small input signal (i.e. $dV = V - V_0$ is small). Since the first term is a DC component and the net response of the second term will be effectively zero, the non-linearity will be predominantly proportional to the second derivative of the device *I-V* characteristics. Furthermore, as also illustrated by the simplified approximation, the main advantage of this demodulation technique is therefore represented by the fact that the output current is proportional to the square of the amplitude of the incoming voltage signal. Thus, the overall response of the system will produce a linear output with respect to the input power, proportional to the *I-V* curvature component [18]:

$$Curvature\ component = \left(\frac{d^2I}{dV^2}\right)/\left(\frac{dI}{dV}\right) \tag{6.7}$$

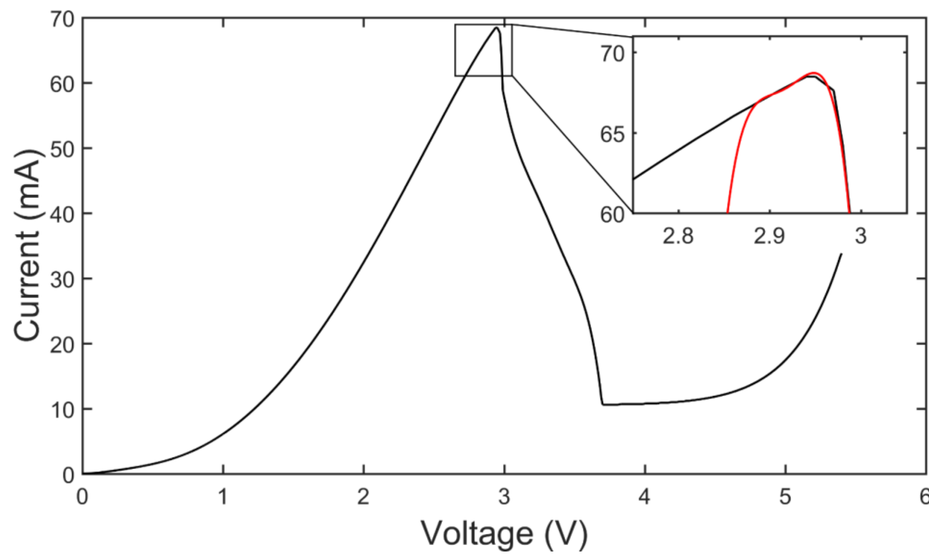

Figure 6.5 Measured I-V characteristics of a fabricated device. Inset graph shows the non-linearity region approximated by a 5th order Taylor series expansion.

The major limitation of this detector, however, is related to the signal distortion introduced by the scaled noise component, as shown from Eqn. 6.5. The spurious free dynamic range level is proportional to the ratio of desired output to the undesired one, and is equal to:

$$Dynamic\ range\ level \propto \frac{k_2 A_c^2 m x(t)}{\frac{1}{2} k_2 A_c^2 m^2 x^2(t)} = \frac{2}{m x(t)} \tag{6.8}$$

The performance of this demodulation method will thus be decreased if the input AM wave has a high percentage modulation (m is close to unity). A comparison between AM modulated waves for different index m is exemplified in Fig. 6.6.

Furthermore, as the operating region is chosen close to the start of the resonant-current switch-off, the precise bias voltage needs to be adjusted according to the amplitude of the input signal. This is essential in order to ensure that the RTD is not forced into the NDR region, where it tends to induce strong parasitic oscillations. Thus, the main constraint of using an RTD as a detector is related to the responsivity degradation with increased input signal power due to the necessity to lower the bias point in order to maintain the integrity of the recovered baseband signal.

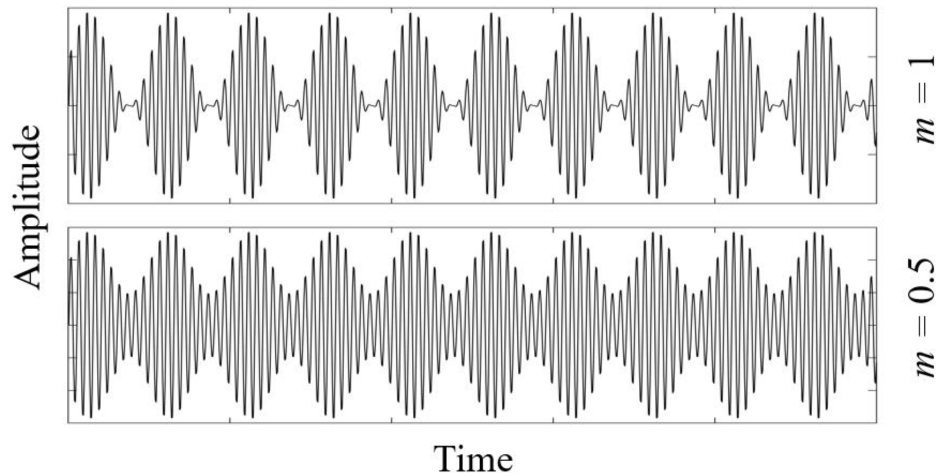

Figure 6.6 Amplitude modulated signals with different modulating index m.

Such detectors that employ an RTD operating in the square-law region have been demonstrated with data rates up to 13 Gbps [19] with an RTD based transmitter in a wireless-link experiment (7.5 cm at 345 GHz) and 9 Gbps [11], as part of a wireless uncompressed 4 k video signal transmission experiment (10 cm at around 286 GHz).

6.2.2 Synchronous demodulation

In square law detection, detector sensitivity is the major bottleneck in terms of maximum achievable data rate, and so coherent RTD detectors have recently been proposed as an alternative. In contrast to the square-law detector operation, coherent detection relies on multiplying (mixing) the incoming signal by the original carrier. i.e. same frequency and phase, as shown in the diagram in Fig. 6.7.

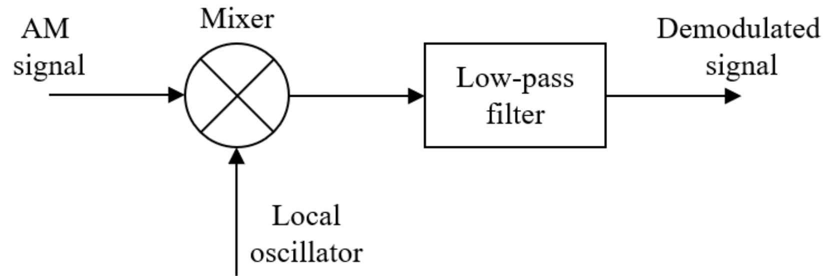

Figure 6.7 Block diagram of standard coherent detector circuit.

By using the standard form for an AM signal described by Eqn. 6.3, the output of the mixer can be expressed as:

$$v_{out}(t) = A_c\big(1 + mx(t)\big)\cos(\omega_c t) \times A_c\cos(\omega_{LO} t + \phi) \qquad (6.9)$$

where it is considered that the local oscillator is synchronised with the AM transmitter with a frequency $\omega_{LO} = \omega_c$ and a phase difference $\phi = 0$. Using the same trigonometric identity $cos^2(x) = \frac{1+\cos(2x)}{2}$ the above equation can be expanded as:

$$v_{out}(t) = \frac{1}{2}{A_c}^2 + \frac{1}{2}{A_c}^2\cos(2\omega_c t) + \frac{1}{2}{A_c}^2 mx(t) + \frac{1}{2}{A_c}^2 mx(t)\cos(2\omega_c t) \qquad (6.10)$$

Eqn. 6.10 is similar to the expansion of the square-law detector output and so the output can be evaluated from the perspective of its frequency components. Thus, after the low-pass filter stage where the high-frequency carrier components (terms containing $\cos(2\omega_c t)$) are eliminated, the demodulated signal will contain a DC component and a scaled version of the original baseband signal. In addition to the fact that signal recovery in direct demodulation is not dependent directly on the *I-V* characteristics of the non-linear device (Eqn. 6.7), the SNR is greatly improved by the

absence of any distortion component within the desired spectrum [20]. However, mismatches between the transmitter and local oscillator carrier signals, as seen from Eqn. 6.9. would lead to distortion in the detected signals (i.e. additional components in the form of $\cos(\omega_{LO} + \phi)$). Thus, the main disadvantage of this demodulation scheme is related to the increased design complexity, usually in the form of phase-locked loop (PLL) circuits required to achieve synchronization between the Tx and Rx elements [21].

A different approach to match the carrier signal at the receiver side is proposed in [22], in which the coherency is achieved by using an injection-locking mechanism at the RTD based local oscillator, as exemplified in Fig. 6.8. This phenomenon is exploited by setting the received signal carrier frequency in close vicinity of the fundamental oscillating frequency of the RTD LO [23]. The locking range in which the synchronization of the signals occurs is given by [24]:

$$Locking\ range = \frac{f_0}{Q}\frac{\Delta V}{V_0}\sqrt{\frac{1}{1-\left(\frac{\Delta V}{V_0}\right)^2}} \tag{6.11}$$

where f_0 and V_0 are the frequency and voltage amplitude of the LO, Q is the LCR resonator figure of merit and ΔV denotes the voltage variation induced by the injection.

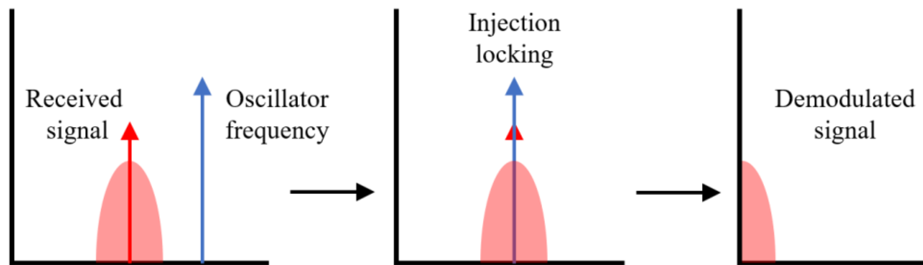

Figure 6.8 Coherent detection by injection locking mechanism. Adapted from:[22].

The highest data rate achieved by this homodyne detection scheme is 27 Gbps with a bit error rate (BER) below 10^{-10} (i.e. error free transmission) [25], using a uni-travelling-carrier photodiode (UTC-PD) at the transmitter side, and 30 Gbps [26] in an RTD based Tx/Rx wireless link. However, the record error-free data rate reported with an RTD detector is 32 Gbps [27], in a square-law demodulation scheme together with a photonic based transmitter (3 cm at around 350 GHz).

6.3 RTD detector realisation and simulation

6.3.1 Detector design and modelling

The device epitaxial layer structure design chosen for the detector application is identical to the one presented in Chapter 3 and characterised for the RTD small-signal parameter extraction and modelling in Chapter 5. With the aid of the fabricated 10 × 10 μm^2 device, the material parameters (independent of mesa area) were determined around the region of interest (current-peak) and are summarised in Table 6.1.

Table 6.1 Summary of material parameters.

Operating Point	R_s	C_0	$\frac{1}{\nu_c}$	τ_{dwell}
Peak current region	360 Ωμm^2	0.9 fF/μm^2	0.55 ps	1.15ps

where R_s is the contact resistance, C_0 is the geometric capacitance, ν_c is the quantum-well – collector electron escape rate, and τ_{dwell} is the electron life time in the well.

A relatively large device active area of 20 × 20 μm^2 was investigated for this application, in an attempt to maximise the targeted non-linearity of the device *I-V* characteristics. The increased peak-current value exhibited in the same bias voltage span, would translate to a superior second order derivative component (d^2I/dV^2), resulting in a net increase in detector responsivity.

The measured *I-V* characteristics have been previously presented in Fig. 6.5 and exhibits a plateau-like feature in the NDR region (between 2.94V and 3.7V) due to the presence of parasitic oscillations during DC measurements. Using these characteristics as the starting point, together with the extracted parameters shown in Table 6.1, the small-signal behaviour of the RTD can be accurately computed over the entire bias range. In order to accurately determine the differential device conductance (G_n), the *I-V* characteristics of the large area RTD (20 × 20 μm^2) were modelled based on the stable *I-V* behaviour of the devices characterised in Chapter 5 (10 × 10 μm^2). Fig. 6.9 shows the modelled device *I-V* characteristics, alongside the extracted G_n, calculated using Eqn. 2.13.

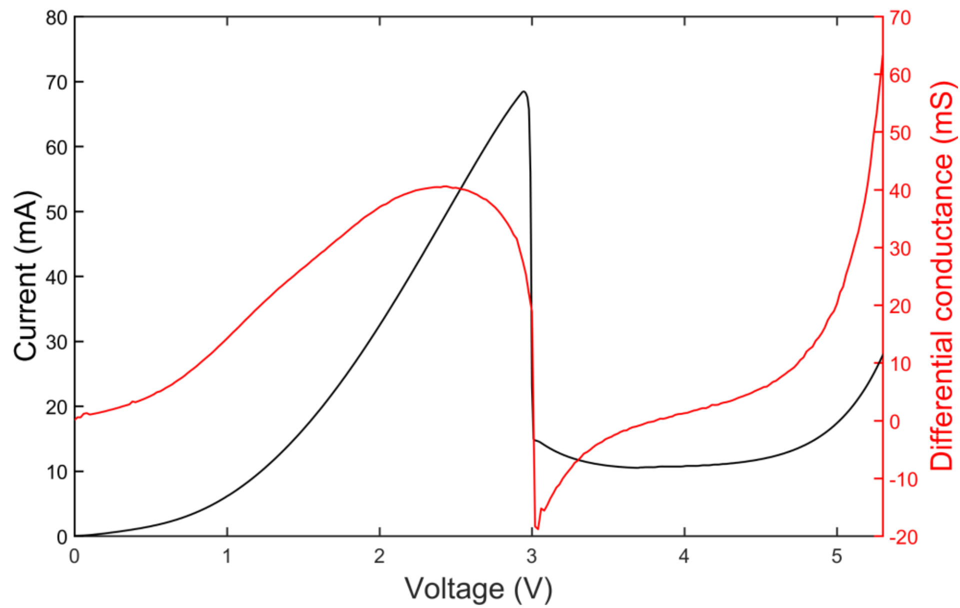

Figure 6.9 Modelled I-V characteristics under stable operating regime (black). Computed differential conductance G_n (red).

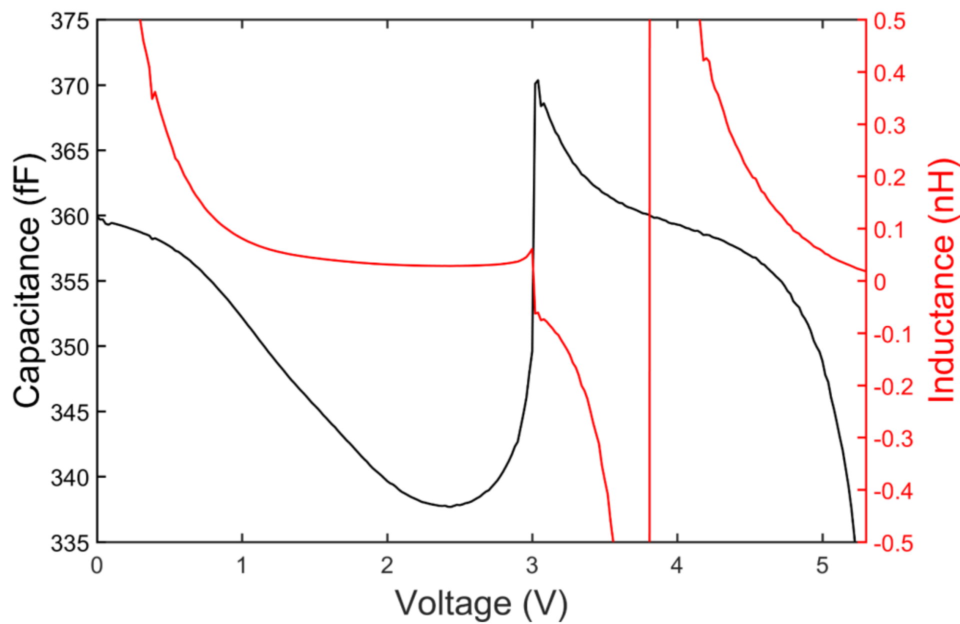

Figure 6.10 Modelled device capacitance C_n (black) and quantum-well inductance L_{qw} (red).

The contact resistance (R_s), assumed bias independent for this application, was calculated using the device area as a simple scaling factor. The last two parameters of the small-signal equivalent circuit model, the device capacitance (C_n) and the quantum-well inductance (L_{qw}) are obtained from the computed G_n and the extracted parameters by Eqn. 2.22 and Eqn. 2.16, respectively, and are shown in Fig. 6.10.

The modelled device parameters together with the *I-V* characteristics were used in creating a non-linear model of the device [28][29] in order to simulate and analyse the performance of the RTD in a square-law detector circuit. Although the small-signal parameters C_n and L_{qw} are bias dependent, the values used are considered (fixed) around the peak current region, where the operating point of the circuit lies.

The circuit topology chosen for the detector design is similar to the one described in [11], with the RTD acting as the square-law device in a shunt-diode configuration [30] as shown in Fig. 6.11.

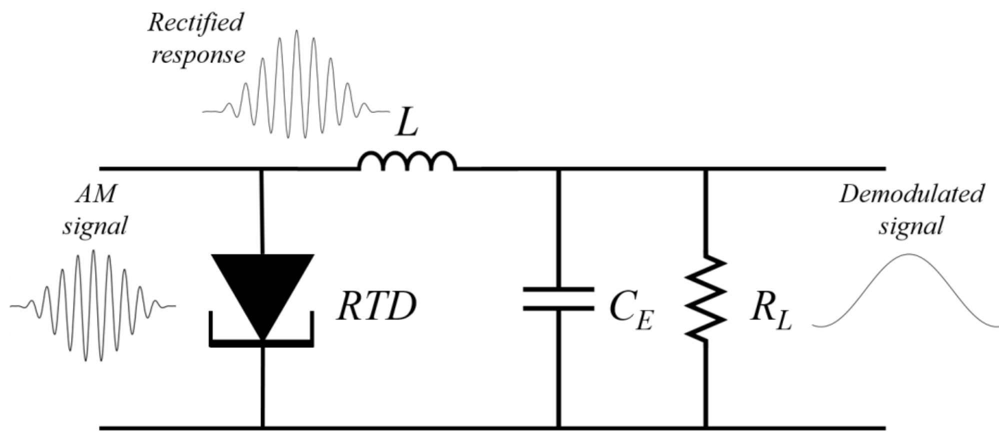

Figure 6.11 Shunt-diode detector circuit.

The presence of an RF modulated signal applied at the input of the detector circuit will cause a variation of the operation point of the RTD. When the device is biased in the highly non-linear region, as shown in Fig. 6.5, the RTD will produce an asymmetric response (i.e. rectified response) between the negative and positive cycles of the incoming AM signal, proportional to the degree of non-linearity of the *I-V* characteristics. The two components L and C_E form a low-pass filter for the rectified signal, which rejects the high-frequency carrier component. Following the low-pass pass filter, the demodulated signal is measured across the load resistance R_L, which is typically 50 Ohms (determined by the measurement equipment). The operation principle of the detector circuit will be further illustrated in section 6.3.2.

In terms of the specific circuit design, the value for the capacitor was chosen at C_E = 1.35 pF, while the inductor was realised using tapered CPW line (200 μm length) with a designed inductance of L = 130 pH, creating thus a low-pass filter stage with a cut-

off frequency f_c = 12 GHz ($f_c = 1/2\pi\sqrt{LC}$). This initial detector circuit was developed for operation in the W-band frequency range (75 – 110 GHz), in order to be compatible for pairing with an existing high-power RTD-based source in a wireless-link system experiment. The modulation and transmission capabilities of this oscillator have already been demonstrated within the research group for data rates up to 10 Gbps (OOK modulation) over a distance of 50 cm. [31].

Since it is ensured that the RTD will never operate within the NDR region, no stabilizing network was included in this design, leading to an increase in overall sensitivity. A micrograph of a fabricated detector circuit is shown in Fig. 6.12.

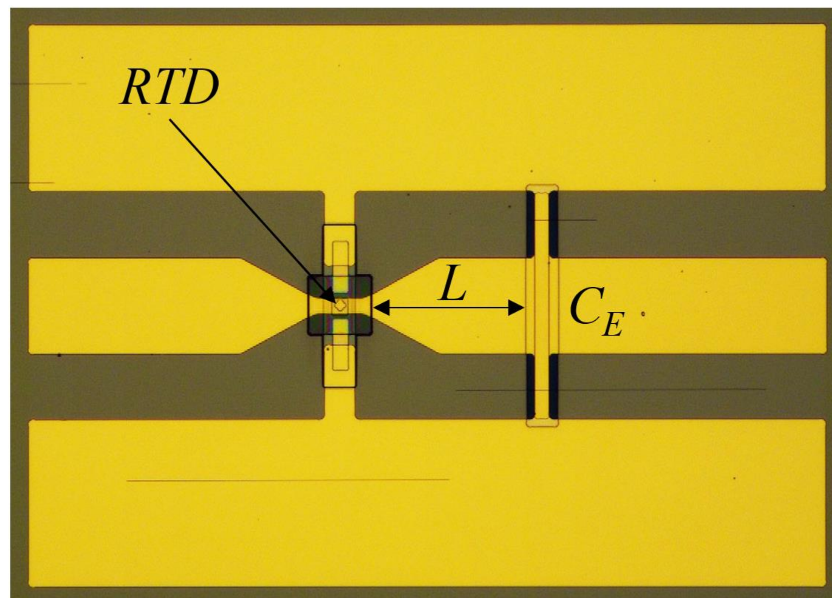

Figure 6.12 Micrograph of fabricated RTD detector.

The complete equivalent circuit model of the detector circuit is represented in Fig. 6.13, where C_p and L_p denote the parasitic capacitance and inductance, introduced by the metal pads and were estimated based on the designed CPW structure using the software tool described in Chapter 4 [32].

The designed circuit elements together with the predicted equivalent device parameter values were used to simulate the entire modelled circuit behaviour up to 100 GHz and compared to the realised detector for validation. The experimental data was acquired using a 2-port S-parameter measurement from the fabricated circuit shown in Fig. 6.12, using the same setup conditions described in section 4.3 (frequency range between 10 MHz and 100 GHz), with the RTD biased in the current peak region (around 2.95 V).

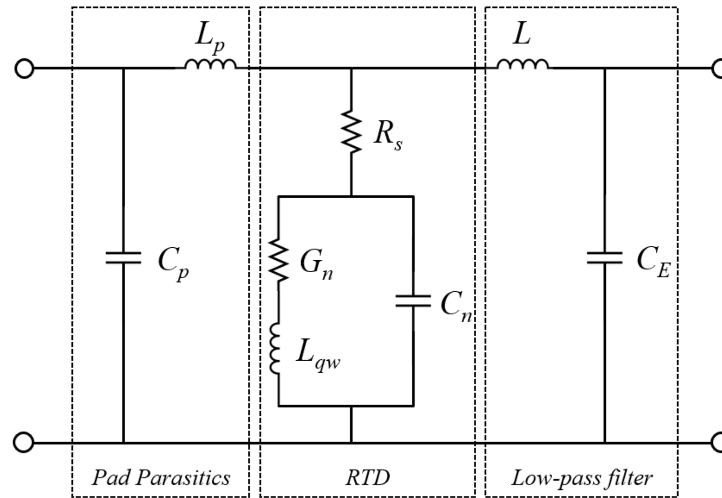

Figure 6.13 Equivalent circuit model of the RTD detector.

Fig. 6.14 shows the comparison between the measured (black trace) and simulated (blue trace) equivalent input Z-parameters (Z_{11}) of the detector circuit. A final optimisation process using the predicted circuit components as starting values was performed in order to further improve the accuracy (red trace) of the developed detector software model, which will be further discussed in section 6.3.2. Based on the same analytic approach described in section 5.3.2, the goodness-of-fit (R-squared value) between the measured and simulated (optimised) behaviour was computed at 0.9398 (real(Z_{11})) and 0.9832 (imag(Z_{11})), respectively, for which the fitting inaccuracies could be attributed to the reduced measurement accuracies at higher frequencies, or to the simplified model of the surrounding parasitics.

A summary of the computed circuit parameters is presented in Table 6.2 alongside the obtained values as a result of the optimisation process. The observed discrepancies between measurement and simulation were determined predominantly as a result of an overestimation of the pad parasitic elements.

Table 6.2 Summary of extracted parameters.

	L_p (pH)	C_p (fF)	G_n (mS)	R_s (Ω)	C_n (fF)	L_{qw} (pH)	L (pH)	C_e (pF)
Modelled/ Designed	71	28	25.6	0.9	346	44.9	132	1.35
Optimised	54.5	18.6	27.7	1.2	360	25	122	1.3

Overall good agreement can be observed between the simulated and optimised values, particularly in relation to the predicted RTD intrinsic elements and estimated circuit components, which validates the accuracy of the modelling and design process.

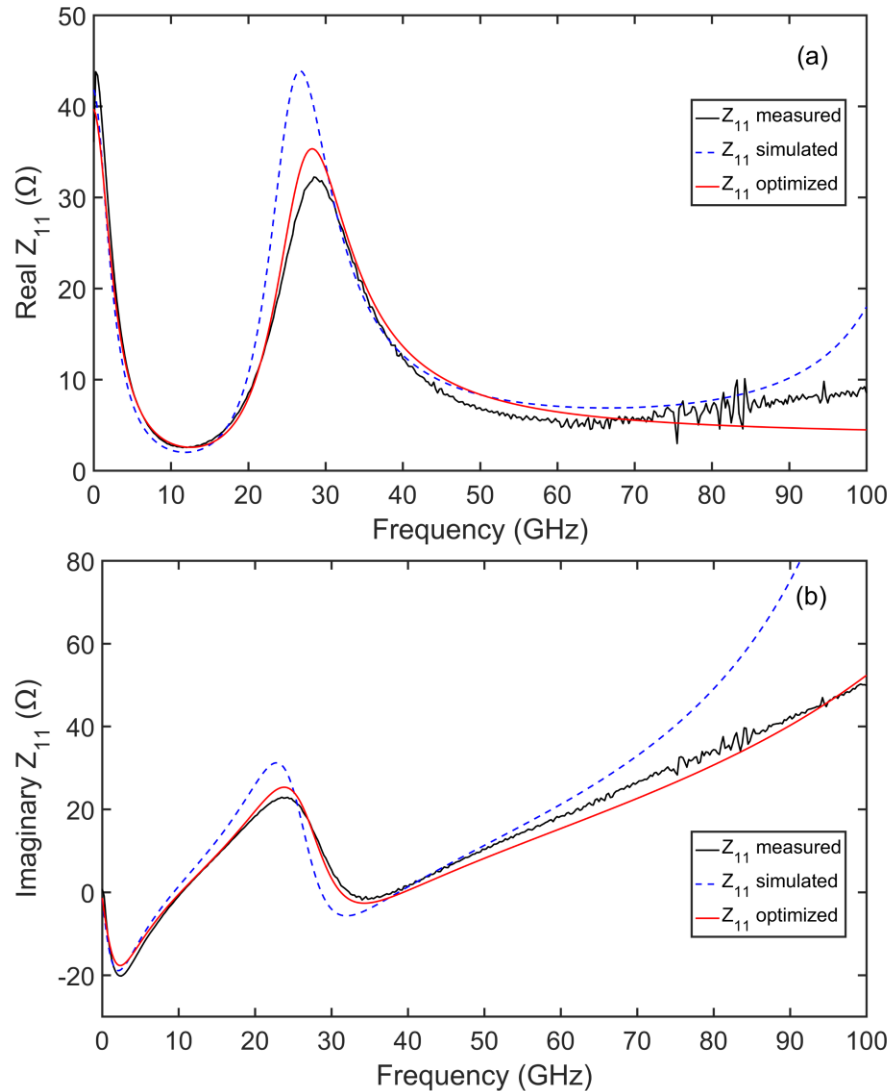

Figure 6.14 Comparison between measured (black trace) and simulated (blue trace) real (a) and imaginary (b) Z_{11} of the RTD detector circuit. The result of the final optimisation process is shown as the red trace.

6.3.2 Detector simulations

The optimised parameters were used in creating an accurate device and circuit model in Keysight's Advanced Design System (ADS) software in order to simulate the performance of the detector in the intended frequency band. The implemented RTD RF large-signal model is illustrated in Fig. 6.15, where the device *I-V* characteristics are represented as a voltage dependent current source [33][34]. As previously stated,

the remaining device parameters are considered bias independent for this particular application, with the fixed extracted values at the operational bias point (i.e. considerably small variation in values neglected for a low amplitude applied signal). The measured device *I-V* characteristics, shown in Fig. 6.5 have been reproduced using the Curve Fitting Toolbox in MATLAB software and described as a series of explicit equations in terms of voltage (detailed in Appendix C).

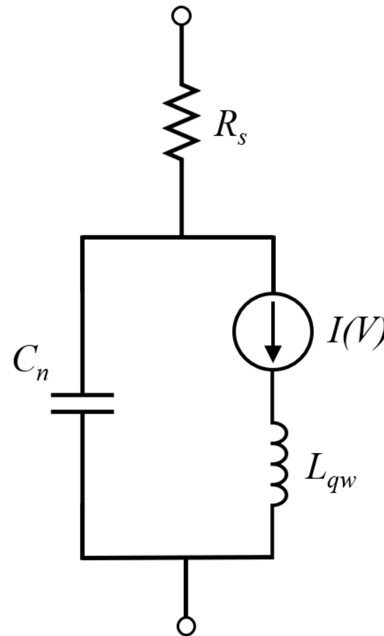

Figure 6.15 RTD large signal model used for software implementation, where the device I-V characteristics are represented as a voltage dependent current source.

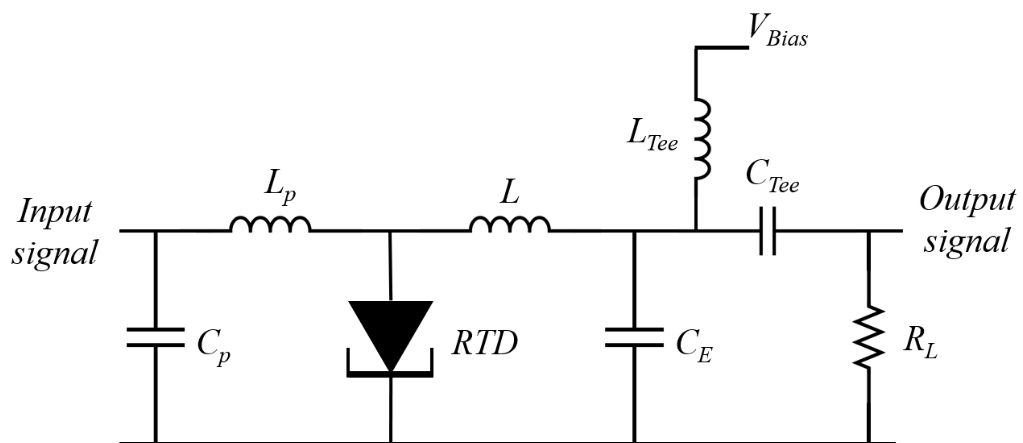

Figure 6.16 Schematic of complete RTD detector circuit.

The schematic representation of the simulated RTD detector is shown in Fig. 6.16. The device is biased in the highly non-linear region at the output of the circuit through the

DC port of a bias-tee network, while the demodulated signal is recovered through the AC port and measured across the load resistance R_L.

In order to further illustrate the circuit's operation, a standard AM signal with a modulation index m=0.5 was simulated and applied at the input of the detector circuit (Fig. 6.17 (a)). The chosen carrier frequency was $f_{carrier}$ = 90 GHz, while the modulating signal was set at f_{signal} = 1 GHz. Fig. 6.17 (b) shows the simulated rectified signal response at the input of the low-pass filter stage for the device biased close to the current peak region (2.944V). Finally, the demodulated signal is shown in Fig. 6.17 (c).

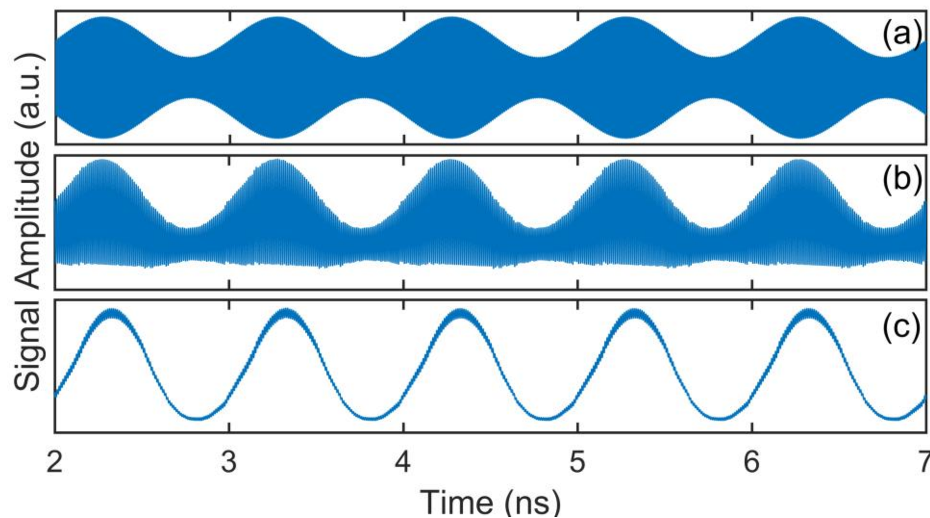

Figure 6.17 Simulated detector operation for a standard AM input signal (a), showing the rectified RTD response (b) and demodulated signal (c).

To evaluate the detector performance and suitability for integration with the high-power RTD source described in [31], similar data transmission conditions and modulation scheme were investigated. As such, the input signal was constructed based on an on-off keying (OOK) modulation scheme, generated using a pseudo-random bit sequence (PRBS) as the baseband signal (1 Gbps), and modulated by a high-frequency carrier (90 GHz), as illustrated in Fig. 6.18.

The input signal power was set relatively low at -26.5 dBm in order not to saturate the detector while the demodulated output was evaluated using eye-probe component with load impedance of 50 Ω. The complete simulation conditions and setup are given in Appendix C.

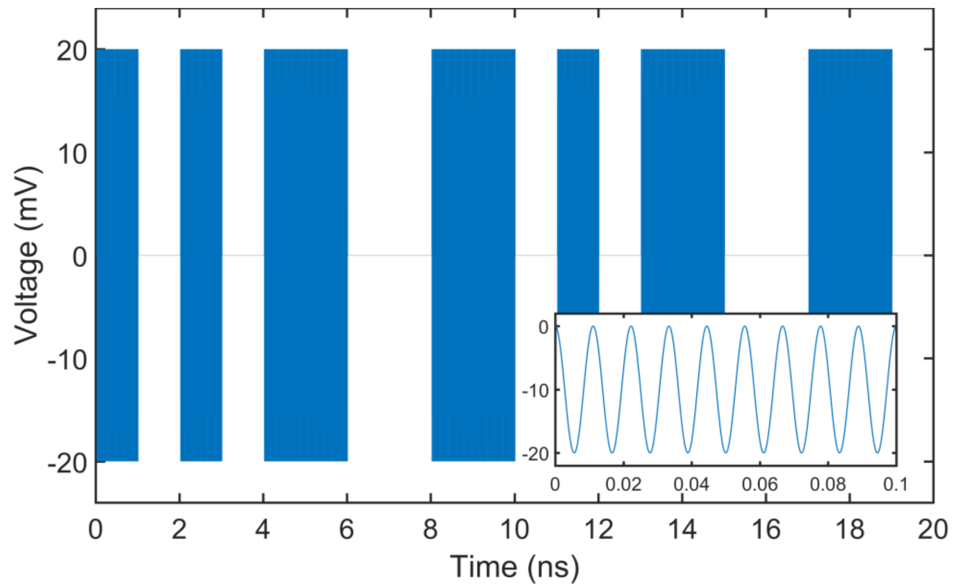

Figure 6.18 ADS generated OOK modulation of a 90 GHz carrier signal (shown in inset graph) by a 1 Gbps pseudo-random bit sequence.

The simulated 1 Gbps eye diagram at 90 GHz is presented in Fig. 6.19 in the form of a density plot for a simulation interval of 1 μs, 10000 points and an amplitude resolution of 1 μV.

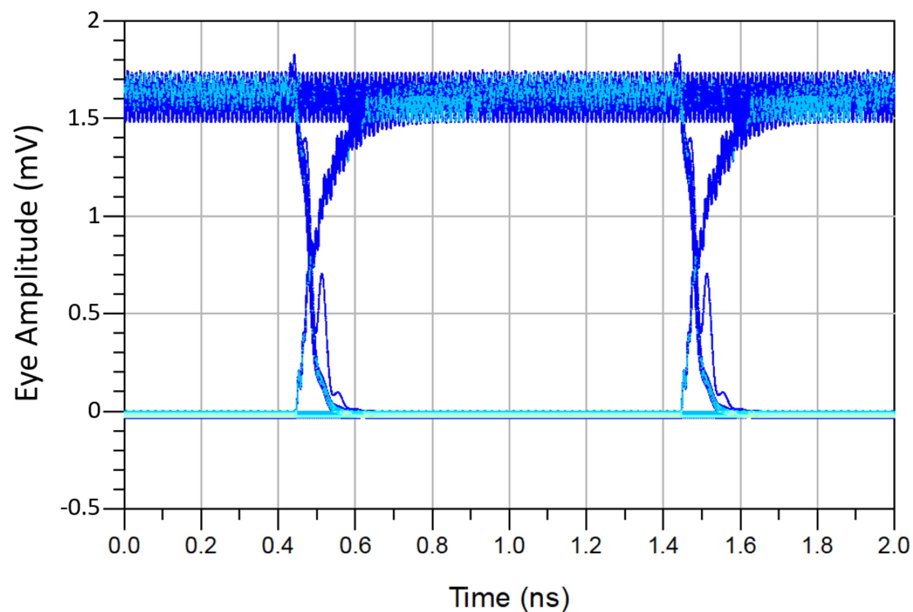

Figure 6.19 Simulated 1 Gbps eye diagram at 90 GHz. Eye amplitude of 1.62 mV and a SNR of 27.1 dB

The calculated eye amplitude using the default 40% and 60% lower and upper eye level boundaries is 1.62 mV for a generated bit pattern with an amplitude of 40 mV

peak-to-peak. The signal-to-noise ratio was calculated at 27 dB, based on the eye amplitude and the standard deviation (σ) for the logic level-0 and logic level-1, computed by the software [35] using Eqn. 6.12:

$$SNR = \frac{Amplitude}{\sigma_{level1} + \sigma_{level0}} \tag{6.12}$$

The maximum achievable data rate for this detector is defined by the low-pass filter stage (formed by L and C_E) with a cut-off frequency of 12.64 GHz, based on the optimised circuit values. A degradation in eye amplitude and signal-to-noise ratio can be observed at a data rate close to the cut-off frequency (12 Gbps), as seen in Fig. 6.20, due to the distortion (attenuation) of the higher frequency components of the PRBS data. However, an eye contour at a bit-error rate (BER) of 10^{-12} is identified by the system, which proves the data integrity is not altered.

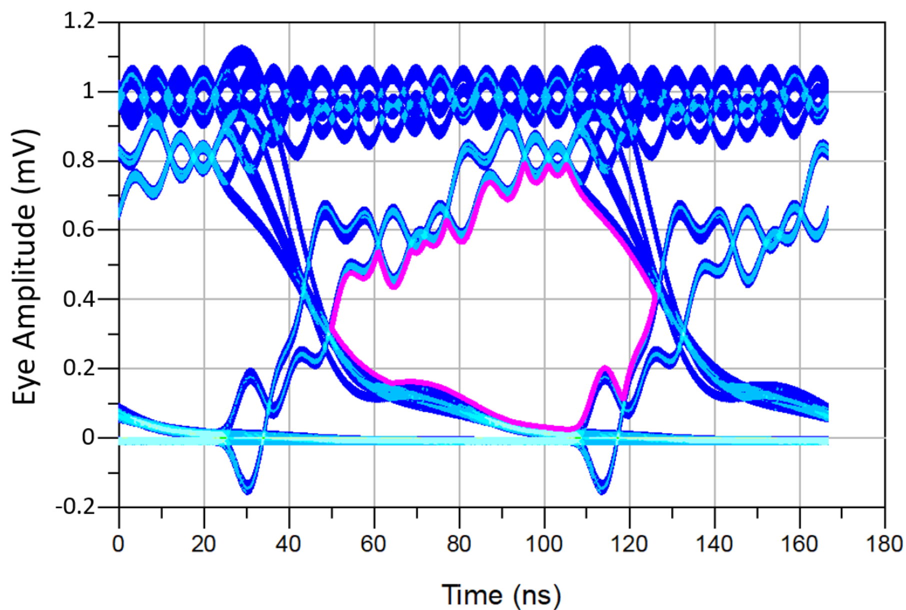

Figure 6.20 Simulated 12 Gbps eye diagram at 90 GHz. Eye amplitude of 0.87mV and a SNR of 16.1 dB. Eye contour at BER of 10^{-12} shown in purple outline.

6.4 W-band measurements

The demodulation capability of the fabricated RTD detector was assessed in the W-band frequency range as part of a data transmission experiment with an RTD based source similar to the one described in [31]. In order to minimise the complexity of the testing setup, which required on-wafer probing at the receiver end, a waveguide

packaged RTD source was used as the Tx sub-system. A picture of the prototype packaged RTD W-band oscillator is shown in Fig. 6.21. The rectangular WR-10 waveguide inner dimensions are 2.54 mm x 1.27 mm.

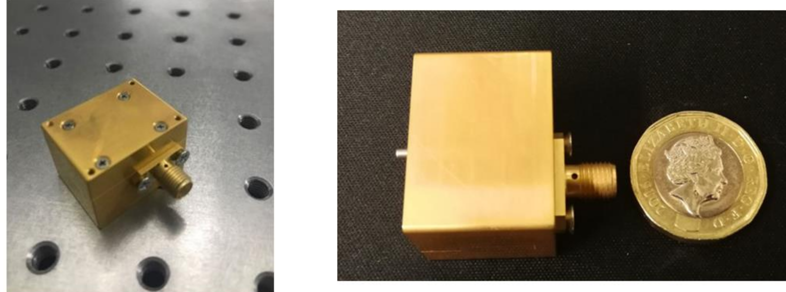

Figure 6.21 Pictures of the packaged RTD oscillator integrated in a WR-10 rectangular waveguide, used as a Tx sub-system in data transmission experiment.

The oscillation frequency of the source was found to be 84.5 GHz [36], when measured using an external W-band mixer (Keysight 11970W) in order to down-convert the high order frequencies to the measurement range of the Keysight E4448 spectrum analyser. The output power was measured at approximately -7 dBm, measured directly using an Erickson PM5 power meter.

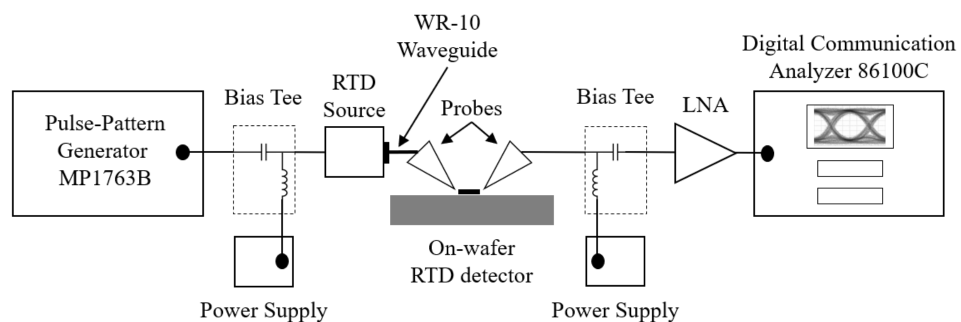

Figure 6.22 Block diagram of experimental setup, using a packaged RTD source.

The complete experimental setup is presented in the block-diagram schematic in Fig. 6.22. The output port of the packaged RTD source was connected directly to a matching rectangular waveguide WR-10 probe (Cascade Microtech infinity probe: i110-T-GSG-100-BT), which provided the input signal to the on-wafer detector circuit. The oscillator on the transmitter side was powered through the DC-port of a bias-tee network, while the baseband modulating signal was fed through the RF port

from an Anritsu pulse pattern generator MP1763B. The output of the detector was measured using a coplanar probe (ACP40-GSG-100), which also provided the operating bias point of the RTD. The recovered baseband signal at the AC port of the bias-tee network was amplified by an LNA (Mini-circuits ZX60-83LN12) with a typical gain of 22 dB and 8 GHz bandwidth and captured on an Agilent high-speed digital communication analyser (86100C Infiniium DCA-J).

The relatively high generated signal power present at the input of the detector was considered when setting the operating point of the RTD, as to not enter the NDR region. This, however, would translate into an overall decrease in system responsivity, due to the fact that the RTD operating point will be slightly shifted towards the lower linear region. The detector responsivity in relation to input signal power was simulated for the above described carrier frequency at 1 Gbps data rate and is illustrated in Fig. 6.23, without the amplifier stage.

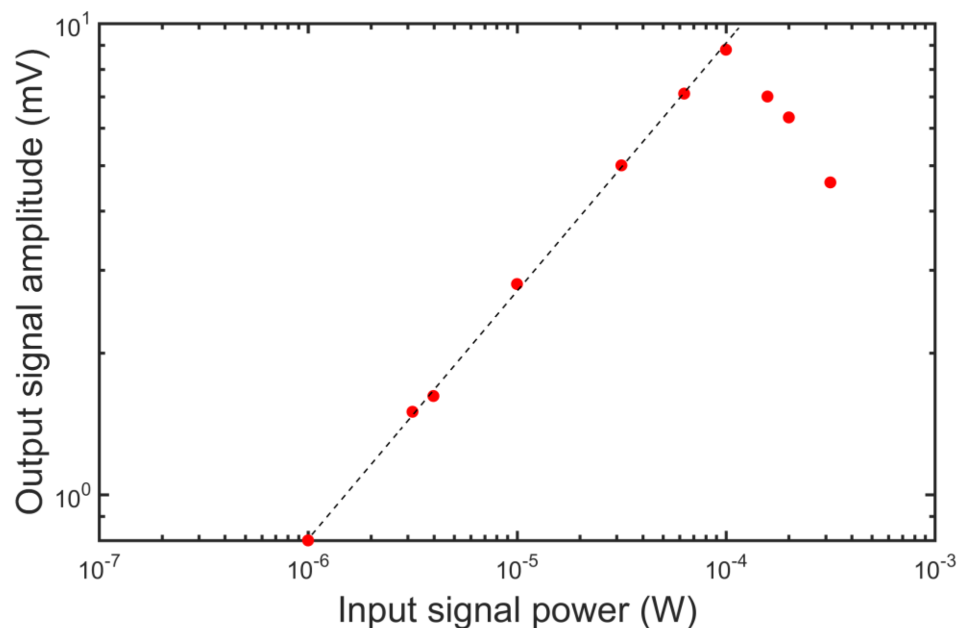

Figure 6.23 Simulated detector output signal amplitude for various input signal power at 84 GHz. Saturation behaviour observed above -10 dBm.

The maximum achievable responsivity was computed at 800 V/W at -30 dBm (1 μW) input power, with the device biased at V_{bias} = 2.945 V. A saturation behaviour of the RTD can be observed to highly impact the amplitude of the detected signal above -10 dBm (100 μW), for which the corresponding device bias voltage was decreased at V_{bias} = 2.93 V in simulation.

For the initial measurement, the original baseband signal was generated as an alternating '0-1' bit pattern with a data rate of 1.5 Gbps and an amplitude of 250 mV, used to switch the operating point of the source RTD between the NDR region ('on-state') to the first PDR region ('off-state') in order to reproduce an OOK modulation scheme. The simulated performance of the detector under the presented experimental conditions (i.e. input signal and modelled LNA characteristics) is shown as the generated density plot in Fig. 6.24, with an eye amplitude of 94.64 mV and a SNR of 25.35 dB.

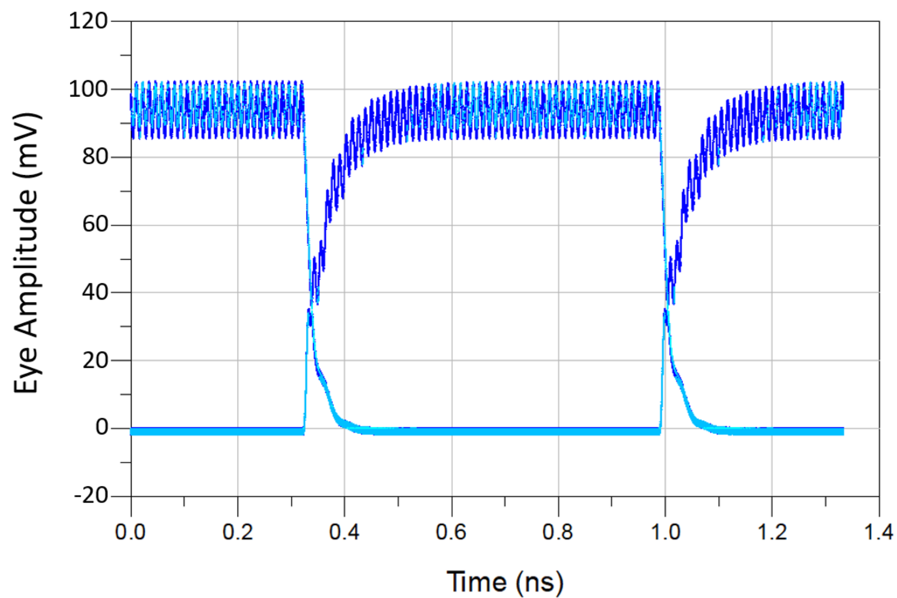

Figure 6.24 Simulated 1.5 Gbps eye diagram at 84 GHz. Eye amplitude of 94.64 mV and a SNR of 25.35 dB.

As a comparison, the recovered demodulated signal, captured by the digital communication analyser, is presented in the form of the measured eye-diagram in Fig. 6.25, with an eye amplitude of 83.94 mV and a SNR of 21.3 dB. Overall, good agreement between simulation and experimental data can thus be observed from the perspective of the demodulated baseband signal, which validates the design procedure. The minor difference in SNR can be primarily attributed to impedance mismatches between the detector circuit and measurement equipment (i.e. cables and connectors). This effectively could lead to undesired reflections of some harmonics, which appear as distortions in the square-wave output signal in the form of 'ringing' and 'shoulder' artefacts resulting in closure of the observed eye pattern [37]. Other potential causes that could lead to the observed variation could be related to the different measurement

setup used between the circuit characterisation procedure and data transmission experiment (i.e. variation in parasitics), as well as various noise factors (i.e. thermal noise component) that were not included in simulation.

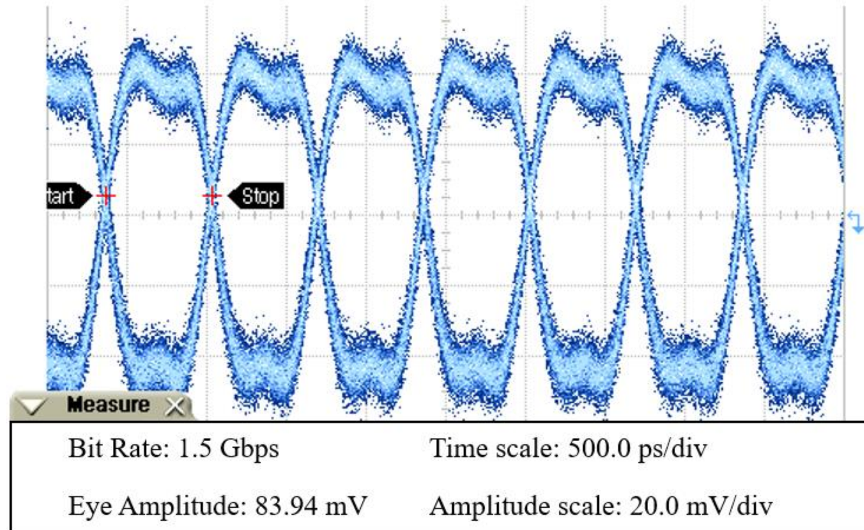

Figure 6.25 Measured eye-diagram of demodulated 1.5 Gbps signal. Eye amplitude of 83.94 mV and SNR of 21.3 dB.

The final acquired eye-diagram measurement is presented in Fig. 6.26 for a higher data rate of 4 Gbps under the same experimental conditions, with an eye amplitude of 72.63 mV and SNR of 14.16 dB. A degradation in the signal-to-noise ratio compared to the previous measurement can be observed.

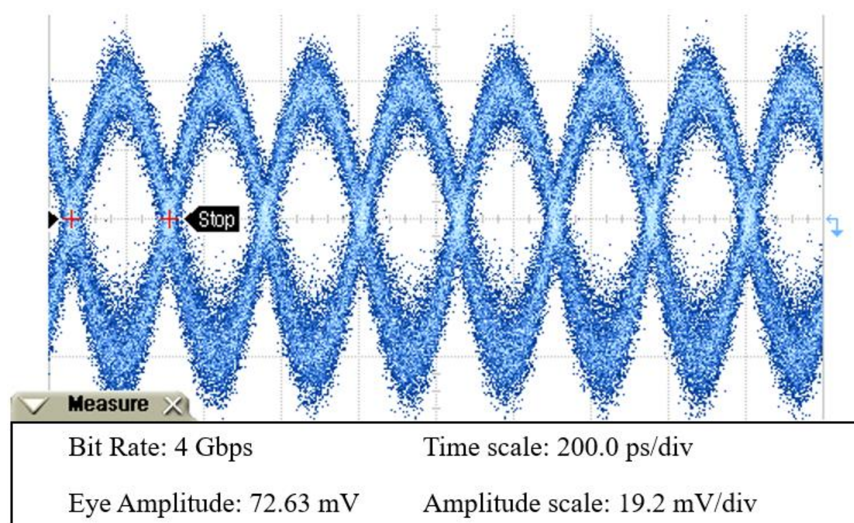

Figure 6.26 Measured eye-diagram of demodulated 4 Gbps signal. Eye amplitude of 72.63 mV and SNR of 14.16 dB.

6.5 Detector sensitivity measurements

The circuit's input reflection coefficient (S_{11}), acquired as part of the measured S-parameters from the fabricated detector (Fig. 6.27) indicates that the highest detector responsivity can potentially be achieved within the Ka frequency band (26.5 – 40 GHz). For this purpose, a detector sensitivity analysis [38] was conducted by experimentally assessing the frequency dependent responsivity in the specified frequency band, using a synthesised swept signal generator (Anritsu 68007B) in a wired configuration. The frequency of the continuously tunable wave was varied between 26.5 and 40 GHz, while modulated using a low frequency pulse generator, with a pulse width of 2.5 ms and a period of 5 ms.

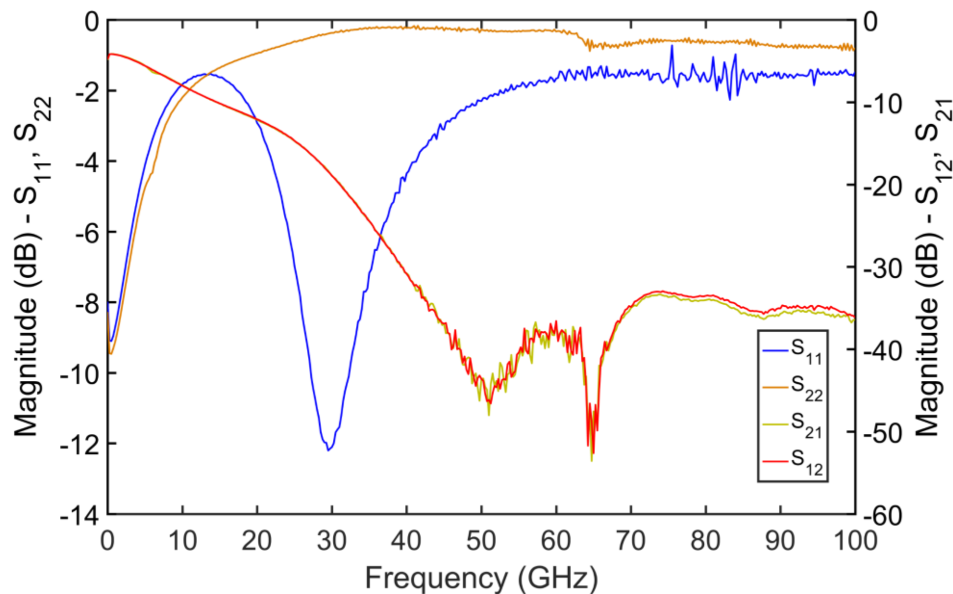

Figure 6.27 Measured S-parameters of fabricated detector circuit, with the RTD biased around the peak current region at 2.95V.

Due to the internal configuration of the source modulating circuit, the baseband signal was observed present in the RF spectrum, as exemplified in Fig. 6.28 (signal amplitude and frequency chosen for clear illustration of the spectrum).

In order to maintain the integrity of the detected data (i.e. original baseband signal propagating through the system and overlapping in frequency with the demodulated signal), a high-pass filter (Mini-Circuits ZHSS-8G+), with a cut-off frequency of 8 GHz, was introduced between the source and detector.

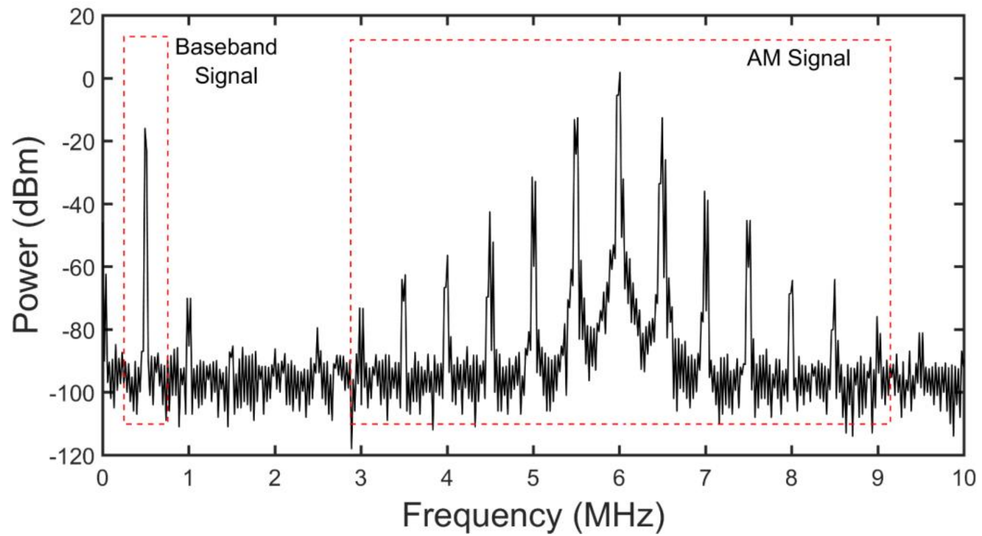

Figure 6.28 RF spectrum of a 6 MHz central frequency AM wave, showing the 0.5 MHz original baseband signal.

The input power was set at -25 dBm and was calibrated using the spectrum analyser for each independent reading to account for potential losses associated with cables and connectors up to the detector input probe. The demodulated signal amplitude was measured using a Keysight high-speed oscilloscope InfiniiVision MSOX6004A, with a 20 GS/s sampling rate, at the AC port of the required bias tee. The complete measurement setup is shown in the block diagram in Fig. 6.29.

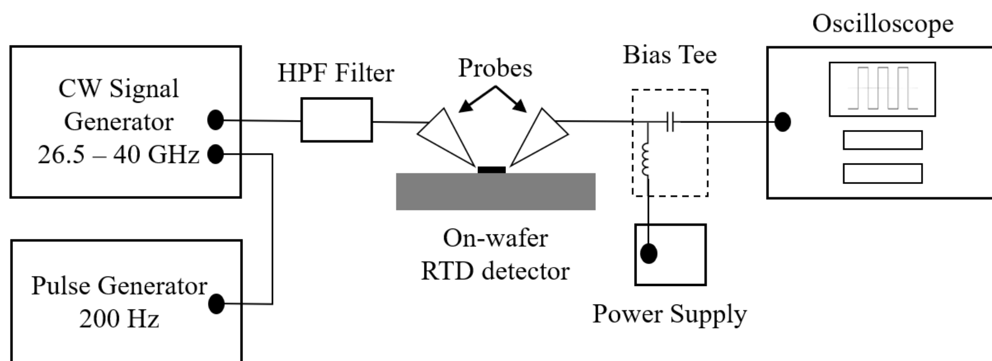

Figure 6.29 Block diagram of Ka-band sensitivity measurement setup, using a modulated continuous wave signal generator.

The measurements were acquired using a 50 Ω load, to ensure optimal impedance matching between the detector output and oscilloscope input. High load impedance measurements were not conducted using this setup due to the capacitive nature (14 pF)

of the 1 MΩ oscilloscope input impedance option, in order to avoid distortion in the form of 'ringing' artefacts in the detected signal.

The detector responsivity was computed using the calibrated signal input power and the measured detected pulse amplitude [38]. The impedance mismatch between the device and source was considered using Eqn. 6.13, in terms of the actual absorbed power by the detector [39], based on the measured S_{11} parameter.

$$Responsivity = \frac{V_{amp}}{P_{in}(1 - |S_{11}|^2)} \tag{6.13}$$

The probe insertion losses were also factored in, in the specified frequency range, as quoted by the manufacturer [40]. The detector responsivity as a function of frequency is plotted in Fig 6.30, with an observed maximum value of 4 kV/W at 38 GHz.

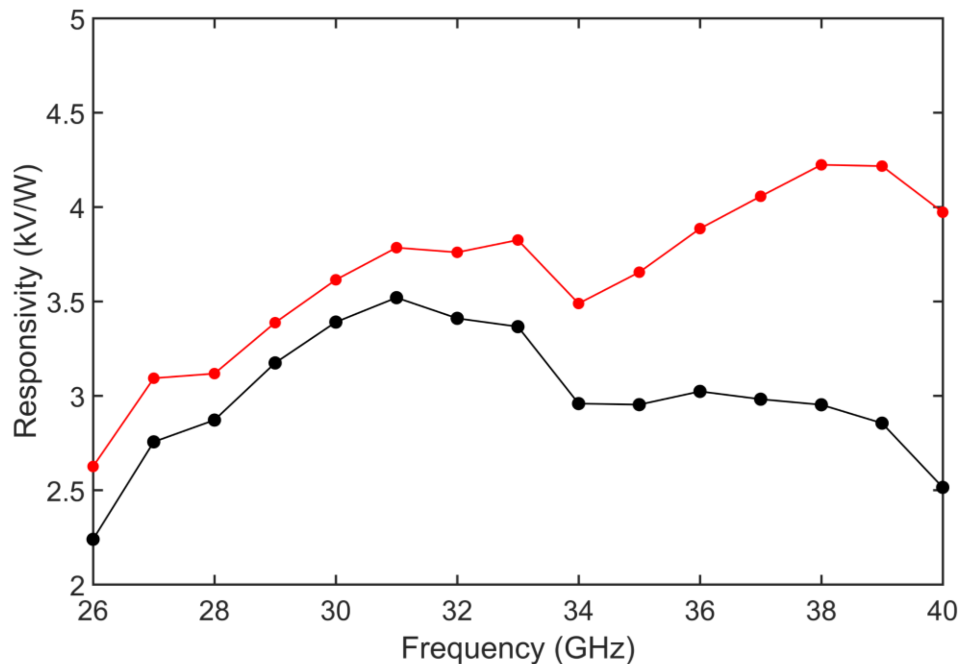

Figure 6.30 Measured (black) and corrected (red) detector responsivity as a function of carrier frequency for a 50 Ω load.

Another important figure of merit is the noise equivalent power (NEP), which is a measure of the noise level generated by the detector. This is primarily used to identify the minimum power that can be detected and is defined as the signal power that gives a signal-to-noise ratio of one in a one hertz bandwidth. This quantity was estimated using Eqn. 6.14, where NSD is the detector noise spectral density:

$$NEP = \frac{Responsivity}{NSD} \tag{6.14}$$

The NSD of the detector was measured using the band-noise function of the spectrum analyser, with a set noise integration bandwidth of 1 MHz, to be around -130 dBm/Hz. Using the above equation for the peak responsivity the computed minimum NEP of the detector was calculated at 16.74 pV/√Hz.

For comparison purposes with commercially available Schottky diode detectors (Table 6.3), the responsivity for a purely resistive load impedance of 1 MΩ was calculated with an estimated mismatch loss of 37 dB in detected power, using Eqn. 6.15.

$$Mismatch\ loss = -10\ \log\left(1 - \left(\frac{Z_0 - Z_L}{Z_0 + Z_L}\right)^2\right) \tag{6.15}$$

The high load impedance estimation indicates a detected signal amplitude increase of approximately 10 dB, which translates to a peak responsivity of around 13 kV/W.

Table 6.3. Summary of Ka-band detector performances.

Ref.	*Detector*	*Responsivity (kV/W)*
[41]	Fairview Microwave FMMT3005	1
[42]	Krytar 203AK	0.5
[43]	ELVA-1 ZBD-28	3.5
[44]	Keysight 8474E	0.4
[45]	Spacek-Labs DKa-2	2.8
[46]	Pacific Millimeter Products KaD	1
[47]	Millitech DET-28	1.6
[48]	Farran WDP-28	1
-	**This work**	**9.5 – 13.38**

The highest sensitivity, in the context of a square-law detector operating within the Ka frequency band, was reported in [13] for a triple-barrier RTD. The quoted (corrected) responsivity for the particular detector is 30 kV/W at 30 GHz (measured responsivity approx. 2 kV/W), for a set input power of -30 dBm. However, it is to be noted that the process of achieving this value is dependent upon successful impedance matching between the source and detector and has yet to be experimentally demonstrated in the specified frequency range.

Lastly, based on the displayed responsivity performance, the presented detector was also investigated as part of a Ka-band RTD Tx/Rx wireless data transmission link, reported in [49], over an antenna separation distance of 15 cm. The adopted modulation scheme was similar to the one described in section 6.4 for which an error free transmission was achieved up to 2.4 Gbps, limited by the RTD source, with a computed responsivity of approximately 2.2 kV/W. The complete experimental setup of the wireless data-link is given in Appendix D.

6.6 Summary and discussions

In this chapter, the detection capability of RTDs, operating as square-law devices was described. The model for the $20 \times 20\ \mu m^2$ RTD device used in the detector was derived from that extracted from S-parameter measurements of a $10 \times 10\ \mu m^2$ device. The model was further implemented in a commercial circuit simulator and was used in the design of an RTD-based detector.

Furthermore, the detector performance under various data transmission configurations (i.e. different modulation schemes and data rates) was also simulated. The simulations compared well with experimentally derived data using RTD based transmitters and the RTD detector in the W-band, in waveguide connection configuration and in the Ka-band, in a wireless configuration [49] where data rates of up to 4 Gbps and 2 Gbps, respectively, with good signal-to-noise ratios were achieved.

Finally, a sensitivity analysis of the RTD detector within the Ka frequency band was conducted and indicated a superior responsivity when compared to commercially available Schottky diode detectors, which proves their feasibility of this technology for next generation wireless transmission systems.

6.7 References

[1] M. Tonouchi, "Cutting-edge terahertz technology," *Nature Photonics,* vol. 1, no. 2, p. 97, 2007.

[2] S. Suzuki, M. Asada, A. Teranishi, H. Sugiyama, and H. Yokoyama, "Fundamental oscillation of resonant tunneling diodes above 1 THz at room temperature," *Applied Physics Letters,* vol. 97, no. 24, p. 242102, 2010.

[3] J. Wang, A. Al-Khalidi, K. Alharbi, A. Ofiare, H. Zhou, E. Wasige, and J. Figueiredo, "High performance resonant tunneling diode oscillators as terahertz sources," in *2016 46th European Microwave Conference (EuMC)*: IEEE, pp. 341-344, 2016.

[4] A. Al-Khalidi, K. H. Alharbi, J. Wang, R. Morariu, L. Wang, A. Khalid, J. Figueiredo, and E. Wasige, "Resonant tunnelling diode terahertz sources with up to 1 mW output power in the J-band," *IEEE Transactions on Terahertz Science and Technology,* 2019.

[5] K. Arzi, A. Rennings, D. Erni, N. Weimann, W. Prost, S. Suzuki, and M. Asada, "Millimeter-wave signal generation and detection via the same triple barrier RTD and on-chip antenna," in *2018 First International Workshop on Mobile Terahertz Systems (IWMTS)*: IEEE, pp. 1-4, 2018.

[6] M. Feiginov, "Frequency limitations of resonant-tunnelling diodes in sub-THz and THz oscillators and detectors," *Journal of Infrared, Millimeter, and Terahertz Waves,* vol. 40, no. 4, pp. 365-394, 2019.

[7] T. Shiode, T. Mukai, M. Kawamura, and T. Nagatsuma, "Giga-bit wireless communication at 300 GHz using resonant tunneling diode detector," in *Asia-Pacific Microwave Conference 2011*: IEEE, pp. 1122-1125, 2011.

[8] T. C. L. G. Sollner, W. D. Goodhue, P. E. Tannenwald, C. D. Parker, and D. D. Peck, "Resonant tunneling through quantum wells at frequencies up to 2.5 THz," *Applied Physics Letters,* vol. 43, no. 6, pp. 588-590, 1983.

[9] J. S. Scott, J. P. Kaminski, M. Wanke, S. J. Allen, D. H. Chow, M. Lui, and T. Y. Liu, "Terahertz frequency response of an $In_{0.53}Ga_{0.47}As/AlAs$ resonant-tunneling diode," *Applied Physics Letters,* vol. 64, no. 15, pp. 1995-1997, 1994.

[10] T. Miyamoto, A. Yamaguchi, and T. Mukai, "Terahertz imaging system with resonant tunneling diodes," *Japanese Journal of Applied Physics,* vol. 55, no. 3, p. 032201, 2016.

[11] S. Diebold, K. Nishio, Y. Nishida, J.-Y. Kim, K. Tsuruda, T. Mukai, M. Fujita, and T. Nagatsuma, "High-speed error-free wireless data transmission using a terahertz resonant tunnelling diode transmitter and receiver," *Electronics Letters,* vol. 52, no. 24, pp. 1999-2001, 2016.

[12] K. Okamoto, K. Tsuruda, S. Diebold, S. Hisatake, M. Fujita, and T. Nagatsuma, "Terahertz sensor using photonic crystal cavity and resonant tunneling diodes," *Journal of Infrared, Millimeter, and Terahertz Waves,* vol. 38, no. 9, pp. 1085-1097, 2017.

[13] G. Keller, A. Tchegho, B. Münstermann, W. Prost, F. Tegude, and M. Suhara, "Triple barrier resonant tunneling diodes for microwave signal generation and detection," in *2013 European Microwave Integrated Circuit Conference*, pp. 228-231, 6-8 Oct. 2013, 2013.

[14] K. Arzi, S. Clochiatti, S. Suzuki, A. Rennings, D. Erni, N. Weimann, M. Asada, and W. Prost, "Triple-barrier resonant-tunnelling diode THz detectors with on-chip antenna," in *2019 12th German Microwave Conference (GeMiC)*: IEEE, pp. 17-19, 2019.

[15] G. Keller, A. Tchegho, B. Münstermann, W. Prost, F. Tegude, and M. Suhara, "Characterization and modeling of zero bias rf-detection diodes based on triple barrier resonant tunneling structures," in *2013 International Conference on Indium Phosphide and Related Materials (IPRM)*, pp. 1-2, 19-23 May 2013, 2013.

[16] T. T. S. C. Sekhar, *Communication theory*. Tata McGraw-Hill Education, 2005.

[17] G. Rieke and R. George, *Detection of light: from the ultraviolet to the submillimeter*. Cambridge University Press, 2003.

[18] P. Fay, W. Li, S. Rahman, Z. Jiang, and L. Liu, "Tunneling-based heterostructure devices for millimeter-wave and THz sensing," in *2016 IEEE National Aerospace and Electronics Conference (NAECON) and Ohio Innovation Summit (OIS)*: IEEE, pp. 448-451, 2016.

[19] J. Webber, N. Nishigami, J. Kim, M. Fujita, and T. Nagatsuma, "Terahertz wireless CDMA communication using resonant tunneling diodes," in *2019 IEEE Globecom Workshops (GC Wkshps)*, pp. 1-6, 9-13 Dec. 2019, 2019.

[20] R. Smith, "The relative advantages of coherent and incoherent detectors: a study of their output noise spectra under various conditions," *Proceedings of the IEE-Part IV: Institution Monographs,* vol. 98, no. 1, pp. 43-54, 1951.

[21] A. Grami, "Chapter 8 - Synchronization," in *Introduction to Digital Communications*, A. Grami Ed. Boston: Academic Press, pp. 357-375, 2016.

[22] K. Nishio, S. Diebold, S. Nakai, K. Tsuruda, T. Mukai, J. Kim, M. Fujita, and T. Nagatsuma, "Resonant tunneling diode receivers for 300-GHz-band wireless communications," in *Proceedings of URSI-Japan Radio Science Meeting*, vol. 49, 2015.

[23] M. Asada, "Theoretical analysis of subharmonic injection locking in resonant-tunneling-diode terahertz oscillators," *Japanese Journal of Applied Physics,* vol. 59, no. 1, p. 018001, 2019.

[24] T. Hiraoka, T. Arikawa, H. Ito, and K. Tanaka, "Injection Locking of Resonant Tunneling Diode Oscillator with a Single-Frequency Terahertz Wave," in *2019 44th International Conference on Infrared, Millimeter, and Terahertz Waves (IRMMW-THz)*, pp. 1-2, 1-6 Sept. 2019, 2019.

[25] N. Nishigami, Y. Nishida, S. Diebold, J. Kim, M. Fujita, and T. Nagatsuma, "Resonant tunneling diode receiver for coherent terahertz wireless communication," in *2018 Asia-Pacific Microwave Conference (APMC)*: IEEE, pp. 726-728, 2018.

[26] Y. Nishida, N. Nishigami, S. Diebold, J. Kim, M. Fujita, and T. Nagatsuma, "Terahertz coherent receiver using a single resonant tunnelling diode," *Scientific Reports,* vol. 9, no. 1, pp. 1-9, 2019.

[27] Y. Xiongbin, K. Jae-Young, F. Masayuki, and N. Tadao, "Efficient mode converter to deep-subwavelength region with photonic-crystal waveguide platform for terahertz applications," *Opt. Express,* vol. 27, no. 20, pp. 28707-28721, 2019.

[28] S. F. Nafea and A. A. S. Dessouki, "An accurate large-signal SPICE model for resonant tunneling diode," in *2010 International Conference on Microelectronics*, pp. 507-510, 19-22 Dec. 2010, 2010.

[29] E. Brown, O. McMahon, L. Mahoney, and K. Molvar, "SPICE model of the resonant-tunnelling diode," *Electronics Letters,* vol. 32, no. 10, pp. 938-940, 1996.

[30] T. K. Ishii, *Components and Devices*. Elsevier, 2013.

[31] J. Wang, A. Al-Khalidi, L. Wang, R. Morariu, A. Ofiare, and E. Wasige, "15-Gb/s 50-cm wireless link using a high-power compact III–V 84-GHz transmitter," *IEEE Transactions on Microwave Theory and Techniques,* vol. 66, no. 11, pp. 4698-4705, 2018.

[32] T. Boutell. "CGIC-WCALC - Coplanar waveguide analysis/synthesis calculator." http://wcalc.sourceforge.net/cgi-bin/coplanar.cgi (accessed 15.12.2020).

[33] S. Nafea and A. Dessouki, *An accurate large-signal SPICE model for resonant tunneling diode*. 2010, pp. 507-510.

[34] R. M. Abdallah, A. A. S. Dessouki, and M. H. Aly, "The Resonant Tunneling Diode characterization for high frequency communication systems," *Microelectronics Journal,* vol. 75, pp. 1-14, 2018.

[35] Keysight. "Application note: performing eye diagram measurements." http://na.support.keysight.com/vna/help/WebHelp13_20/Applications/Enhanc

ed_Time_Domain_Analysis/Eye_Diagram_and_Mask_Test/Performing_Eye_Diagram_Measurements.htm (accessed 30.06.2020).

[36] J. Wang, A. Al-Khalidi, R. Morariu, I. A. Ofiare, L. Wang, and E. Wasige, "15 Gbps wireless link using W-band resonant tunnelling diode transmitter," in *2018 48th European Microwave Conference (EuMC)*: IEEE, pp. 1405-1408, 2018.

[37] K. J. Han, H. Takeuchi, and M. Swaminathan, "Eye-pattern design for high-speed differential links using extended passive equalization," *IEEE Transactions on Advanced Packaging,* vol. 31, no. 2, pp. 246-257, 2008.

[38] Y. Takida, S. Suzuki, M. Asada, and H. Minamide, "Sensitivity measurement of resonant-tunneling-diode terahertz detectors," in *2019 44th International Conference on Infrared, Millimeter, and Terahertz Waves (IRMMW-THz)*: IEEE, pp. 1-2, 2019.

[39] T. Takahashi, M. Sato, Y. Nakasha, and N. Hara, "Lattice-matched p+-GaAsSb/i-InAlAs/n-InGaAs zero-bias backward diodes for millimeter-wave detectors and mixers," in *2012 International Conference on Indium Phosphide and Related Materials*, pp. 95-98, 27-30 Aug. 2012, 2012.

[40] FormFactor. "Probe selection guide." https://www.formfactor.com/download/probe-selection-guide/?wpdmdl=2561&refresh=5f09d25e518391594479198 (accessed 11.07.2020).

[41] FairviewMicrowave. "Zero biased waveguide detector." https://www.fairviewmicrowave.com/zero-biased-waveguide-detector-wr-28-sma-female-negative-26.5-40-ghz-fmmt3005-p.aspx (accessed 15.07.2020).

[42] Krytar. "Zero bias schottky detectors." https://krytar.com/pdf/200zbs.pdf (accessed 15.07.2020).

[43] ELVA-1. "Millimeter wave systems and components." http://elva-1.com/data/files/docs/atalogue_ELVA_2013web.pdf (accessed 15.07.2020).

[44] Keysight. "RF & microwave test accessories." https://www.keysight.com/en/pd-1000001922%3Aepsg%3Apro-pn-8474E/planar-doped-barrier-diode-detector-001-50-ghz?cc=GB&lc=eng (accessed 17.05.2020).

[45] SpacekLabs. "Millimeter-wave and waveguide detectors." https://www.spaceklabs.com/product-details/dka-2 (accessed 15.07.2020).

[46] PacificMillimeter. "Broad band detectors." http://www.pacificmillimeter.com/Detectors.html (accessed 17.05.2020).

[47] Millitech. "General purpose detectors." https://www.amtechs.co.jp/product/IS000093-DET.pdf (accessed 15.07.2020).

[48] Farran. "Planar detectors." https://www.farran.com/contentFiles/productFiles/WDP-28.pdf (accessed 15.07.2020).

[49] A. C. Cornescu, "High efficiency and high frequency resonant tunneling diode sources," PhD Thesis, University of Glasgow, 2019.

Chapter 7. Conclusion and future work

7.1 Conclusion

The resonant tunnelling diode (RTD), which relies on the quantum mechanical tunnelling transport mechanism, is considered a promising solution for compact terahertz applications operating at room temperature, due to its large bandwidth, high-speed switching capabilities, simple circuitry and low power consumption [1]. The adaptability of this device has been demonstrated primarily in the context of high-frequency sources, i.e. oscillators with fundamental frequencies around 2 THz [2] by exploiting its large negative differential resistance region (NDR) and high sensitivity detectors [3] based on its highly non-linear current-voltage characteristics, in both wireless communication [4] and imaging systems [5].

Although intense on-going research has been devoted to the realisation of such applications in the THz frequency range, the specific circuit design methodologies and optimization procedures have yet to be fully established. This is primarily due to the lack of accurate models for the high-frequency behaviour of the devices. Various RTD small-signal equivalent circuit models have been extensively researched and proposed based on theoretical approaches, however their limited experimental demonstration, typically within narrow frequency ranges(up to 20-30 GHz), has most often put in question their validity. Furthermore, studies related to device high-frequency characterisation have often been hindered by the presence of bias parasitic oscillations within the NDR region, which is typically the key bias range exploited in the successful realisation of RTD-based circuits. The purpose of this PhD was to investigate an experimental approach to characterise RTD devices, especially the NDR region under a stable operating regime, to develop a procedure for accurate extraction of their small-signal equivalent circuit parameters and investigate their frequency dependence, with the ultimate goal of investigating the design procedures of RTD-based integrated circuits (ICs).

The key results achieved within this project can be summarised as follows:

1. A universal on-wafer bond-pad and shunt resistor de-embedding technique has been developed in order to accurately investigate the high-frequency behaviour of stabilised RTD devices. The novel method can be generically adapted to allow different pad geometries and stabilising networks, without limitation to device sizing and operating frequency, by relying on the use of measured data from a single auxiliary dummy-test structure. The proposed method has been demonstrated with the aid of S-parameter measurements up to 110 GHz and has been validated by comparative measurements between two identical devices, with different extrinsic circuitry (i.e. with and without the stabilising resistor network) for which the de-embedding procedure has been employed.

2. From the acquired de-embedded data of a stabilised RTD throughout the entire bias range, a novel quasi-analytical sequential small-signal equivalent parameter extraction procedure was developed. This approach, enabled by the high-frequency measurements, permitted the precise extraction and differentiation of key device parameters, within specific spectral ranges. The computed goodness-of-fit of the measured S-parameter data, based on the extracted values revealed an accuracy above 97% across the entire device bias range, which validates the accuracy of the proposed method. It is believed that the developed high-frequency modelling procedure will provide a strong foundation for further advancement and optimisation of RTD technology.

3. The scalability of the obtained equivalent circuit model parameters was demonstrated in the case of a larger active area RTD device, which together with the measured *I-V* characteristics, was used to develop an accurate non-linear device model. The model was implemented in a SPICE software package and enabled the design of an RTD square-law demodulator for high-speed data transfer systems. The detector performance was validated experimentally in the W-band and in the Ka-band in data-link experiments and achieved data rates of up to 4 Gbps. In addition, a sensitivity analysis of the detector within the Ka-band demonstrated a superior performance, in terms of determined responsivity (peak corrected responsivity 13.38 kV/W) when compared to traditional Schottky diode detectors.

The achieved results, in particular the characterisation and modelling of the active RTD, will enable the reliable design, simulation and optimisation of RTD based circuits for THz applications, and therefore facilitate their transition towards the industrial and consumer marketplace.

7.2 Future work

7.2.1 RTD-based detector

The performance of the realised RTD-based detector was analysed based mainly on a sensitivity analysis performed within the Ka-band and simulations at higher frequencies. However, the full extent of the simulated demodulation capabilities, in relation to maximum carrier frequency and data rate, have not been experimentally demonstrated due to various factors, such as imposed modulation limitation on the transmitter side (Ka-band) and unavailability of suitable high-frequency sources. There is therefore scope for more detailed and advanced work in the future.

The on-wafer demonstration of the detector circuit has placed numerous constraints regarding the successful establishment of a wireless testing environment, by requiring a total number of two probe stations (four probes required in total for both Tx and Rx on-wafer systems). This led to restrictions on component choices and the actual experimental setup due to space limitations. Waveguide packaging of the detector would afford more flexibility in the characterisation and should be considered in future experiments.

Further future work could include the design of advanced detector circuits for operation at higher carrier frequencies such as the J-band (220 – 325 GHz) where developments of wireless communications technologies is currently of great interest.

7.2.2 High data-rate wireless links

For the purpose of demonstrating the transmission and detection capability of RTDs in the presented wireless data link within this work, a simple modulation scheme, based on an on-off keying (OOK) method was adopted. This simple modulation scheme is however characterised by highly inefficient use of bandwidth in the case of ultra-high data-rate transmissions [6], while also imposing severe limitations on the

design of the RTD Tx circuit, e.g. in the case of the used Ka-band oscillator, the required biasing network restricts the circuit response time.

In order to meet the increasing demands for higher data-rates, upwards of tens of Gbps and match the requirements of the emerging 5G and future 6G infrastructures, high-order modulation schemes, such as quadrature amplitude modulation (16QAM, 64QAM and 256QAM formats used in standard 5G systems) need to be considered to efficiently increase the data throughput.

Currently, multi-Gbps data-rate systems, which employ such complex modulation schemes, have been commercially employed in the mm-wave bands, and more recently demonstrated up to 10 Gbps in the E-band, which offers a total combined bandwidth of 10 GHz (between 71 – 76 GHz and 81 – 86 GHz). In order to enable the future up-scale of high data-rate links, it is foreseen that the primary interest will target frequency ranges above 100 GHz, more precisely within the D-band (131 – 174.8 GHz), where 28 GHz of available bandwidth available within three sub-bands (141 – 148.5, 151.5 – 164 and 167–174.8 GHz) are currently being investigated for designation by international regulatory bodies [7].

As RTD-based sources have been demonstrated with state of the art output powers ranging from 1 mW in the J-band [8] to 2 mW in the W-band [9], it is believed that this technology is suitable to meet and overcome the imposed requirements of the upcoming high data-rate links, operating around 150 GHz. Furthermore, as previously stated, in order to achieve targeted data-rates upwards of 10 Gbps, the modulation of the sourced carrier signal needs to be accomplished on the RF side of the RTD oscillator, as required by the high-order QAM scheme. For the purpose of this direct carrier modulation scheme a vector modulator [10], based on directional couplers, with tuneable reflection terminations implementation can be adopted.

Such systems have been previously demonstrated at microwave frequencies with the use of transistor devices in cold configuration acting as the variable resistive elements (i.e. GaAs HBTs [11], MHEMTs [12] and MESFETs [13]). At mmWaves and terahertz frequencies, PIN diodes could represent a more appropriate solution, due to their high-speed switching capabilities, wide resistance tuning range and their processing and material suitability with the described RTD devices in this thesis [14].

A potential epitaxial layer structure, which integrates the two active components is shown in Fig. 7.1, where the PIN diode layers are grown on top of the RTD heterostructure. This capability would thus enable the monolithic integration of the modulator circuit with the transmitter, highly reducing chip size and associated fabrication costs.

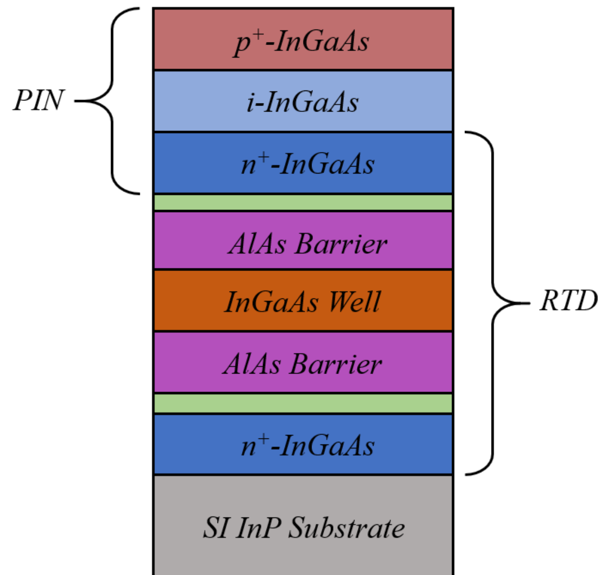

Figure 7.1 Epi-layer structure of RTD and PIN diode.

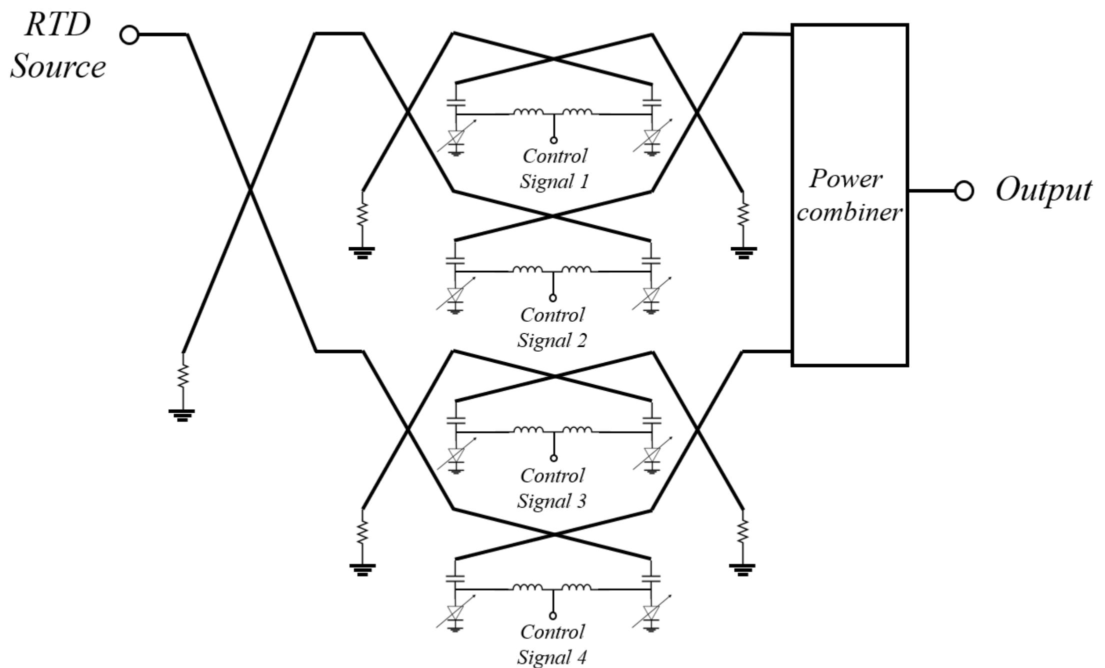

Figure 7.2 Circuit topology of a vector modulator using directional couplers enabled by PIN diode controls.

In terms of the specific realisation of the integrated direct carrier modulation system, a potential implementation is illustrated using the schematic diagram in Fig. 7.2, where the sourced signal from the RTD oscillator (present at the input port) is split between two orthogonal channels, using a quadrature coupler, with further biphase balanced amplitude modulators assigned to each individual signal line [15]. Based on this technique, the output signal is generated by an in-phase power combiner, with a specific amplitude and phase, determined by the biasing conditions of the individual pairs of control PIN diode elements. Considering the determined on (0.8 V) and off states (0 V) states of the PIN diodes described in section 4.4, the operation of the modulators can be summarised using Table 7.1.

Table 7.1 Summary of modulator operation

State	*Control Signal 1 (V)*	*Control Signal 1 (V)*	*Control Signal 1 (V)*	*Control Signal 1 (V)*	*Phase shift (degrees)*
On	0.8	0	0.8	0	0
On	0.8	0	0	0.8	90
On	0	0.8	0	0.8	180
On	0	0.8	0.8	0	270
Off	0	0	0	0	-
Off	0.8	0.8	0.8	0.8	-

7.3 References

[1] H.-J. Song and T. Nagatsuma, *Handbook of terahertz technologies: devices and applications*. CRC press, 2015.

[2] R. Izumi, S. Suzuki, and M. Asada, "1.98 THz resonant-tunneling-diode oscillator with reduced conduction loss by thick antenna electrode," in *2017 42nd International Conference on Infrared, Millimeter, and Terahertz Waves (IRMMW-THz)*, pp. 1-2, 27 Aug.-1 Sept. 2017, 2017.

[3] K. Okamoto, K. Tsuruda, S. Diebold, S. Hisatake, M. Fujita, and T. Nagatsuma, "Terahertz sensor using photonic crystal cavity and resonant tunneling diodes," *Journal of Infrared, Millimeter, and Terahertz Waves,* vol. 38, no. 9, pp. 1085-1097, 2017.

[4] T. Shiode, T. Mukai, M. Kawamura, and T. Nagatsuma, "Giga-bit wireless communication at 300 GHz using resonant tunneling diode detector," in *Asia-Pacific Microwave Conference 2011*: IEEE, pp. 1122-1125, 2011.

[5] T. Miyamoto, A. Yamaguchi, and T. Mukai, "Terahertz imaging system with resonant tunneling diodes," *Japanese Journal of Applied Physics,* vol. 55, no. 3, p. 032201, 2016.

[6] W. M. Richard, "Amplitude shift keying modulation, demodulation and performance," in *Digital Communications with Emphasis on Data Modems: Theory, Analysis, Design, Simulation, Testing, and Applications*: Wiley, pp. 227-250, 2017.

[7] R. Lombardi, "Microwave and millimetre-wave for 5G transport," *ETSI White Paper,* vol. 25, 2018.

[8] A. Al-Khalidi, K. H. Alharbi, J. Wang, R. Morariu, L. Wang, A. Khalid, J. M. Figueiredo, and E. Wasige, "Resonant tunneling diode terahertz sources with up to 1 mW output power in the J-band," *IEEE Transactions on Terahertz Science and Technology,* vol. 10, no. 2, pp. 150-157, 2019.

[9] J. Wang, A. Al-Khalidi, L. Wang, R. Morariu, A. Ofiare, and E. Wasige, "15-Gb/s 50-cm wireless link using a high-power compact III–V 84-GHz transmitter," *IEEE Transactions on Microwave Theory and Techniques,* vol. 66, no. 11, pp. 4698-4705, 2018.

[10] Y.-C. Jeong, "Design of a novel vector modulator," *Microwave Journal,* vol. 44, no. 10, pp. 156-156, 2001.

[11] H.-Y. Chang, T.-W. Huang, H. Wang, Y.-C. Wang, P.-C. Chao, and C.-H. Chen, "Broad-band HBT BPSK and IQ modulator MMICs and millimeter-wave vector signal characterization," *IEEE Transactions on Microwave Theory and Techniques,* vol. 52, no. 3, pp. 908-919, 2004.

[12] L. Lok, C.-J. Hwang, H. Chong, I. Thayne, and K. Elgaid, "A W-band MMIC vector modulator utilizing tandem couplers and 50nm MHEMTs," in *2009 European Microwave Conference (EuMC)*: IEEE, pp. 1251-1254, 2009.

[13] A. Boveda and J. Alonso, "A 0.7-3 GHz GaAs QPSK/QAM direct modulator," *IEEE Journal of Solid-State Circuits,* vol. 28, no. 12, pp. 1340-1349, 1993.

[14] C. Paoloni, R. Basu, L. R. Billa, J. M. Rao, R. Letizia, Q. Ni, E. Wasige, A. Al-Khalidi, J. Wang, and R. Morariu, "Long-range millimetre wave wireless links enabled by travelling wave tubes and resonant tunnelling diodes," *IET Microwaves, Antennas & Propagation,* vol. 14, no. 15, pp. 2110-2114, 2020.

[15] A. E. Ashtiani, S.-i. Nam, A. d'Espona, S. Lucyszyn, and I. D. Robertson, "Direct multilevel carrier modulation using millimeter-wave balanced vector modulators," *IEEE Transactions on Microwave Theory and Techniques,* vol. 46, no. 12, pp. 2611-2619, 1998.

Appendix A. Fabrication process

Sample cleaning

1. Ultrasonic bath in acetone 3 minutes
2. Ultrasonic bath in methanol 3 minutes
3. Ultrasonic bath in isopropyl alcohol 3 minutes
4. Rinse in de-ionised water
5. Dry sample using pressurised nitrogen (N_2)

Top contact metal

1. Spin-coating with S1805 at 4000 rpm for 30 seconds
2. Soft bake sample at 115° C for 60 seconds using a hotplate
3. UV exposure using MA6 for 2.4 seconds
4. Develop resist using a solution of Microposit developer concentrate and water (MDC:H_2O – 1:1) for 50 seconds.
5. Rinse in de-ionised water
6. Dry sample using pressurised N_2
7. Ash sample at 120 W for 2 minutes
8. Deposit ohmic contact (Ti/Pd/Au – 20/30/150 nm) using Plasys IV
9. Excess metal lift-off using SVC-14 resist stripper in hot bath (50° C) for several hours
10. Rinse in de-ionised water
11. Dry sample using pressurised N_2

Etch into InGaAs to define top mesa

1. Spin-coating with S1805 at 4000 rpm for 30 seconds
2. Soft bake sample at 115° C for 60 seconds using a hotplate
3. UV exposure using MA6 for 2.4 seconds
4. Develop resist using a solution of Microposit developer concentrate and water (MDC:H_2O – 1:1) for 50 seconds.
5. Rinse in de-ionised water
6. Dry sample using pressurised N_2

7. Etch InGaAs down to bottom contact layer using a solution of H_3PO_4:H_2O_2:H_2O – 1:1:38 , with an etch rate of approximately 100 nm/min
8. Rinse in de-ionised water
9. Measure obtained etch depth using the DektakXT stylus profiler
10. Remove resist coating using acetone for 30 seconds

Bottom contact metal

1. Same processing steps as for the top contact

Etch to the semi-insulating InP substrate

1. Spin-coating with S1805 at 4000 rpm for 30 seconds
2. Soft bake sample at 115° C for 60 seconds using a hotplate
3. UV exposure using MA6 for 2.4 seconds
4. Develop resist using a solution of Microposit developer concentrate and water (MDC:H_2O – 1:1) for 50 seconds.
5. Rinse in de-ionised water
6. Dry sample using pressurised N_2
7. Ash sample at 120 W for 2 minutes
8. Etch remaining InGaAs layers using a solution of H_3PO_4:H_2O_2:H_2O – 1:1:38, with an etch rate of approximately 100 nm/min
9. Etch InP buffer layer using a solution of HCl:H_3PO_4 – 1:4 for approximately 30 seconds
10. Rinse in de-ionised water
11. Measure obtained etch depth using the DektakXT stylus profiler, or check the exposed layer conductivity
12. Remove resist coating using acetone for 30 seconds

Passivation and via opening

1. Spin-coating with PI-2545 at 8000 rpm for 30 seconds
2. Soft bake sample at 115° C for 2 minutes using a hotplate
3. Bake sample for 6 hours in oven at 180° C
4. Spin-coating with S1805 at 1500 rpm for 30 seconds
5. Soft bake sample at 115° C for 2 minutes using a hotplate

6. UV exposure using MA6 for 2.8 seconds
7. Develop resist using a solution of Microposit developer concentrate and water ($MDC:H_2O$ – 1:1) for 75 seconds.
8. Soft bake sample at 90° C for 10 minutes using a hotplate
9. Dry etch polyamide using a combination of $CF_4:O_2$ gases with flow rates of 5 and 20 sccm, and a 200W RF power using interferometer end-point detection (process time is about 350 seconds)
13. Remove resist coating using acetone for 30 minutes

NiCr thin-film resistor

1. Spin-coating with S1805 at 4000 rpm for 30 seconds
2. Soft bake sample at 115° C for 60 seconds using a hotplate
3. UV exposure using MA6 for 2.4 seconds
4. Develop resist using a solution of Microposit developer concentrate and water ($MDC:H_2O$ – 1:1) for 50 seconds.
5. Rinse in de-ionised water
6. Dry sample using pressurised N_2
7. Ash sample at 120 W for 2 minutes
8. Etch into the InP substrate using a solution of $HCl:H_3PO_4$ – 1:4 for approximately 30 seconds
9. Deposit NiCr – 30 nm using Plasys IV
10. Remove resist coating using acetone for 30 seconds

First bond-pad

1. Spin-coating with LOR 10A at 6000 rpm for 30 seconds
2. Soft bake sample at 150° C for 3 minutes using a hotplate
3. Spin-coating with S1805 at 4000 rpm for 30 seconds
4. Soft bake sample at 115° C for 2 minutes using a hotplate
5. UV exposure using MA6 for 2.4 seconds
6. Develop resist using MF319 for 75 seconds.
7. Ash sample at 120 W for 2 minutes
8. Deposit Ti/Au – 20/380 nm using Plasys IV
9. Remove resist coating using acetone for 30 seconds

MIM capacitor

1. Spin-coating with LOR 3A at 3000 rpm for 30 seconds
2. Soft bake sample at 150° C for 3 minutes using a hotplate
3. Spin-coating with S1805 at 4000 rpm for 30 seconds
4. Soft bake sample at 115° C for 2 minutes using a hotplate
5. UV exposure using MA6 for 2.4 seconds
6. Develop resist using MF319 for 75 seconds.
7. Ash sample at 120 W for 2 minutes
8. Deposit Si_3N_4 – 75 nm using ICP-CVD
9. Remove resist coating using acetone for 30 seconds

Second bond-pad

1. Same processing steps as for the first bond-pad

Appendix B. TLM measurements

The metal-semiconductor contact resistance represents an important parameter which highly impacts the device performance, especially those operating at high frequencies [1]. The resistance would limit the maximum device cut-off frequency lead to large losses (I^2R or Joule heating), unwanted thermal effects and overall reduced sensitivity in the case of detector applications.

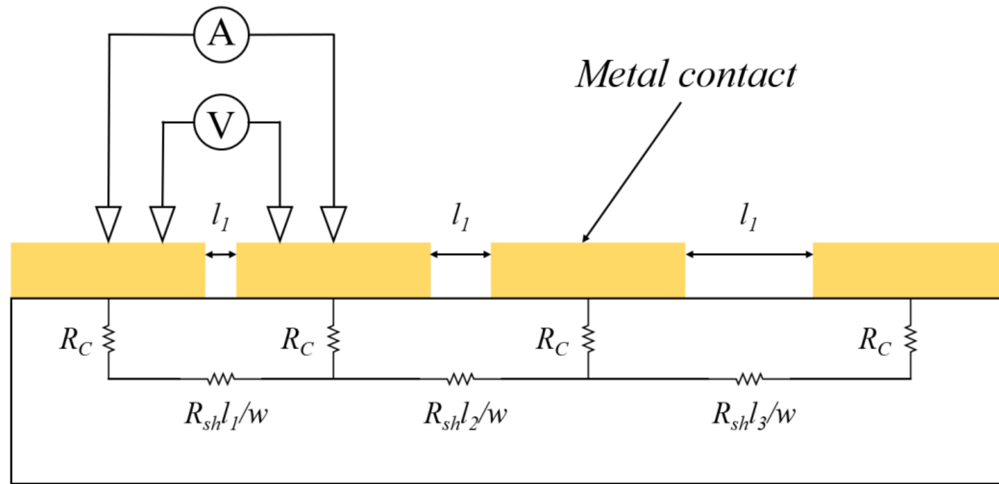

Figure B.1 Diagram of a standard TLM test structure (cross-section view) and the corresponding 4-probe resistance measurement setup. The metallic contacts are fabricated with various separation distances (l_1, l_2, l_3, etc.)

Ohmic contact resistances were extracted from standard by transmission lime model (TLM) measurements [2], of fabricated test structures [3], as illustrated in Fig. B.1. The TLM structure comprises a number of identical metal contact pads, deposited on the semiconductor interface, with distinct separation distances. The resistance characterisation method consists of 4-probe measurement [4][5], in which a constant current is applied between each pair of adjacent contacts (i.e. two probes used to supply the current through the structure with the remaining pair of probes used to measure the resulting voltage). Based on this measurement between each individual pair of neighbouring contacts, the total resistance (R_t) can be acquired, which represents the sum of the corresponding first and second contact resistance ($2 \times R_c$, assuming identical contact resistance) and the semiconductor sheet resistance (R_{sh}). R_t can thus be computed as:

$$R_t = 2R_c + R_{sh}\frac{l}{w} \tag{B.1}$$

where l is the corresponding separation distance and w is the width of the designed separation, defined by the contact size.

The acquired data, as a result of the complete structure measurement (i.e. total number of contact pairs) should indicate a linear variation of the obtained resistance as a function of contact separation distance, as shown in Fig. 4.18.

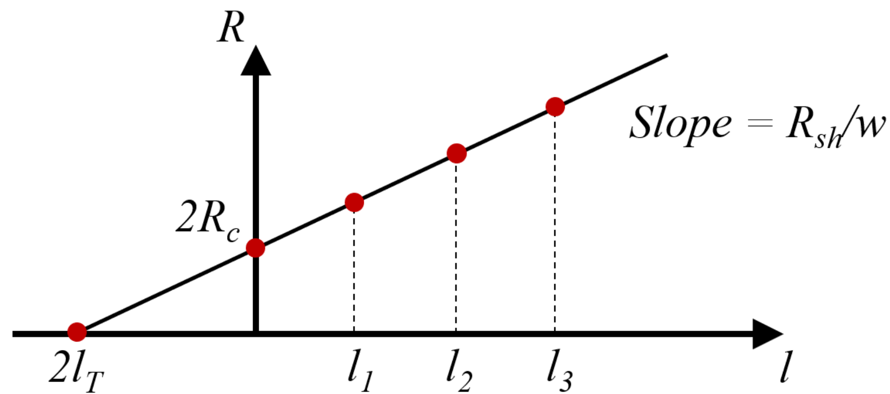

Figure B.2 Illustration of measured total resistance R_t as a function of contact separation distance. The equivalent total contact resistance ($2 \times R_c$) and transfer length ($2 \times l_T$) can be obtained at the intersection of y-axis and x-axis, respectively

Several key parameters can be obtained by analysing the obtained plot, including the value of the total contact resistance ($2 \times R_c$), which is obtained at the intersection of the plotted data with the y-axis (i.e. $l = 0$), and total transfer length ($2 \times l_T$), at the intersection of with the x-axis (i.e. $R_t = 0$). The transfer length l_T, represents the average path distance of the current flow from the metal contact into the semiconductor [1]. Furthermore, the slope of the plotted line, based on Eqn. B.1, represents the ratio of the semiconductor sheet resistance to the contact pad width (R_{sh}/w). Finally, the specific metal contact resistance can be computed as [1]:

$$\rho_c = l_T^2 R_{sh} \tag{B.2}$$

An SEM image of a fabricated TLM test structure is shown in Fig. 4.19, realised in order to individually characterise the corresponding top and bottom metallisation

layers, using the Ti/Pd/Au metal scheme. The contact spacings were l = 1 μm, 2 μm, 3 μm, 5 μm, 7 μm, 9 μm, 11 μm, 13 μm and 15 μm, respectively, which are known to provide easily and accurately measurable resistances.

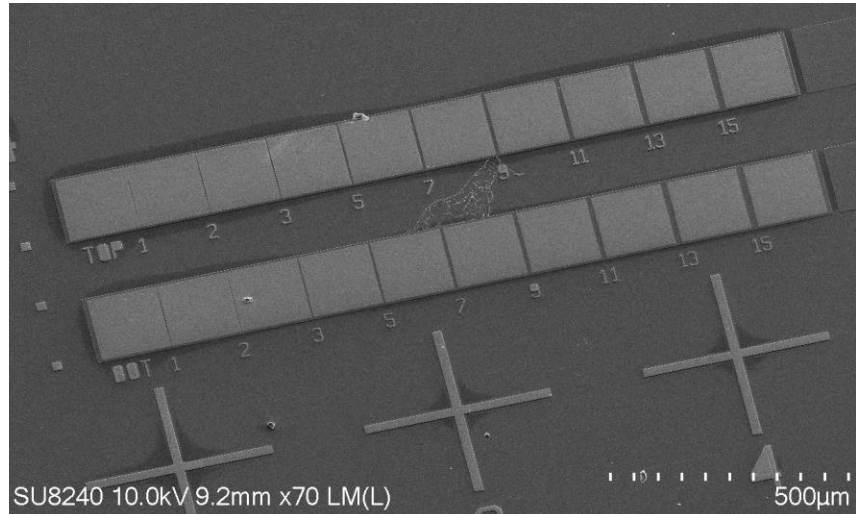

Figure B.3 SEM image of two fabricated TLM test structures, used to characterise the contact resistance of the RTD top and bottom metal contacts.

The measured total resistances R_T for each corresponding contact spacing distance are plotted in Fig. B.4, while the extracted contact resistance R_c, transfer length l_T, sheet resistance R_{sh} and the specific contact resistance ρ_c for the top and bottom metallisation layer are shown in Table B.1.

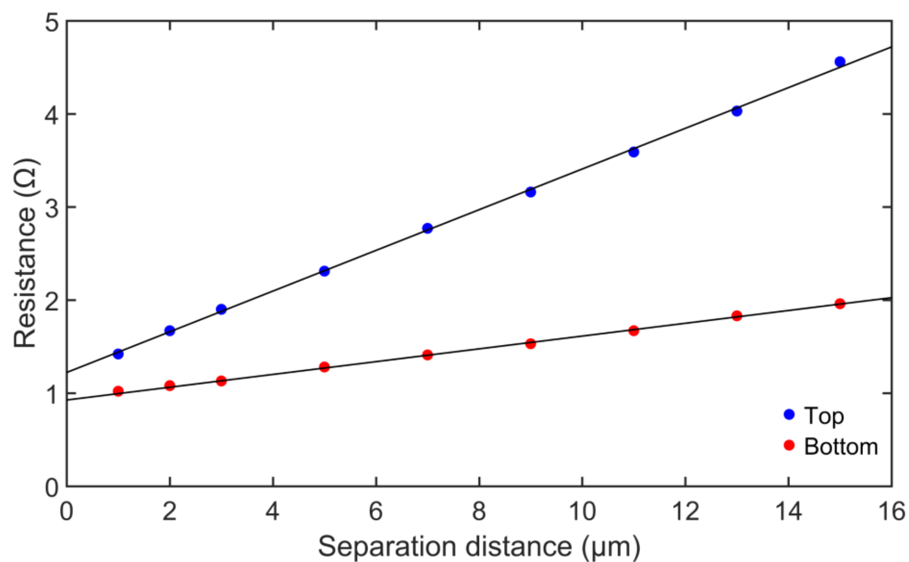

Figure B.4 Measured total resistance R_t as for the top and bottom metallisation layer as a function of contact separation distance.

Table B.1 Summary of extracted parameters from TLM measurements.

	R_c (Ω)	R_{sh} (Ω/□)	l_t (μm)	ρ_c (Ωμm^2)
Top contact	0.61	32.8	2.8	256
Bottom contact	0.46	10.3	6.7	468

The lowest obtained specific contact resistance ρ_c = 256 Ωμm^2 (top) is approximately two orders of magnitude worse than the 0.73 Ωμm^2 reported in [6] using the same metallisation scheme. The high obtained value can be attributed to the absence of a semiconductor de-oxidation process, prior to the metal deposition, due to the unavailability of the argon gun feature of the Plassys IV deposition tool at the time of the sample processing. However, this factor has been mitigated with the use of large active area RTD devices (i.e. > 100 μm^2) for which the highest total contact resistance of approximately 2.6 Ω was considered acceptable, from the perspective of the targeted application and characterisation study presented in this thesis.

References

[1] D. K. Schroder, *Semiconductor material and device characterization*. John Wiley & Sons, 2015.

[2] H. Murrmann and D. Widmann, "Current crowding on metal contacts to planar devices," *IEEE Transactions on Electron Devices,* vol. 16, no. 12, pp. 1022-1024, 1969.

[3] G. K. Reeves and H. B. Harrison, "Obtaining the specific contact resistance from transmission line model measurements," *IEEE Electron Device Letters,* vol. 3, no. 5, pp. 111-113, 1982.

[4] M. Brown and E. Jakeman, "Theory of the four-point probe technique as applied to the measurement of the conductivity of thin layers on conducting substrates," *British Journal of Applied Physics,* vol. 17, no. 9, p. 1143, 1966.

[5] L. B. Valdes, "Resistivity measurements on germanium for transistors," *Proceedings of the IRE,* vol. 42, no. 2, pp. 420-427, 1954.

[6] A. M. Crook, E. Lind, Z. Griffith, M. J. W. Rodwell, J. D. Zimmerman, A. C. Gossard, and S. R. Bank, "Low resistance, nonalloyed Ohmic contacts to InGaAs," *Applied Physics Letters,* vol. 91, no. 19, p. 192114, 2007.

Appendix C. RTD detector - simulation setup

RTD - SPICE model

The developed RTD SPICE model is shown in Fig. C.1, where the device *I-V* characteristics are represented by a voltage dependent current source, implemented in the ADS software as a symbolically-defined device (SDD). The complete RF large signal model also incorporates the device capacitance *Cn*, the quantum-well inductance L_{qw} and the series resistance R_s, assumed bias independent for the described simulations.

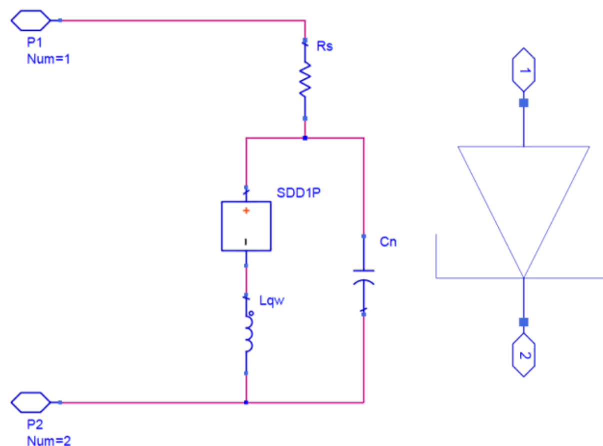

Figure C.1 ADS schematic of implemented RTD model (left) and component (right).

The current equations (in terms of applied voltage) which define the SDD component were empirically obtained from the measured device *I-V* characteristics (with the de-embedded series resistance R_s) using the Curve Fitting Toolbox (CFTOOL) in MATLAB software. Although the primary investigated operating bias range for the detector was represented by the non-linear region around the peak-current, the fitting procedure was carried in the entire bias range for completion.

The best fitting for the *I-V* characteristics shown in Fig. 6.5 was obtained based on a Gaussian representation within three operating regions (1st PDR, around the peak-current region and NDR together with the 2nd PDR region), which takes the form:

$$I(V) = \sum_{k=1}^{n} \left(a_k * \exp\left(-\left(\frac{V - b_k}{c_k} \right)^2 \right) \right) \quad (1)$$

The computed fitting coefficients are summarised in Table C.1.

Table C.1 Summary of fitting coefficients

Coefficient	*1st PDR region (V < 2.861)*	*Peak-current region (2.861 < V < 2.906)*	*NDR and 2nd PDR region (2.906 < V < 5.4)*
n	8	3	8
a_1	0.005408	0.06719	0.1772
a_2	0.007221	0.06378	0.03148
a_3	0.001821	0.005994	0
a_4	0.03451	-	0.09993
a_5	-0.0001167	-	0.01216
a_6	1.042e-05	-	0.006869
a_7	0	-	0
a_8	0.03127	-	0.01151
b_1	2.963	2.851	2.479
b_2	2.877	2.989	3.125
b_3	2.664	2.896	3.191
b_4	2.947	-	6.371
b_5	2.231	-	3.42
b_6	2.175	-	3.564
b_7	2.088	-	5.175
b_8	2.351	-	4.806
c_1	0.1023	0.08259	0.3462
c_2	0.1749	0.06849	0.272
c_3	0.1818	0.02141	0.0001902
c_4	0.7145	-	0.8276
c_5	0.1363	-	0.1622
c_6	0.04871	-	0.09077
c_7	3.193e-05	-	0.0002705
c_{18}	1.062	-	2.905

A comparison between the measured and fitted device *I-V* characteristics is shown in Fig. C.2.

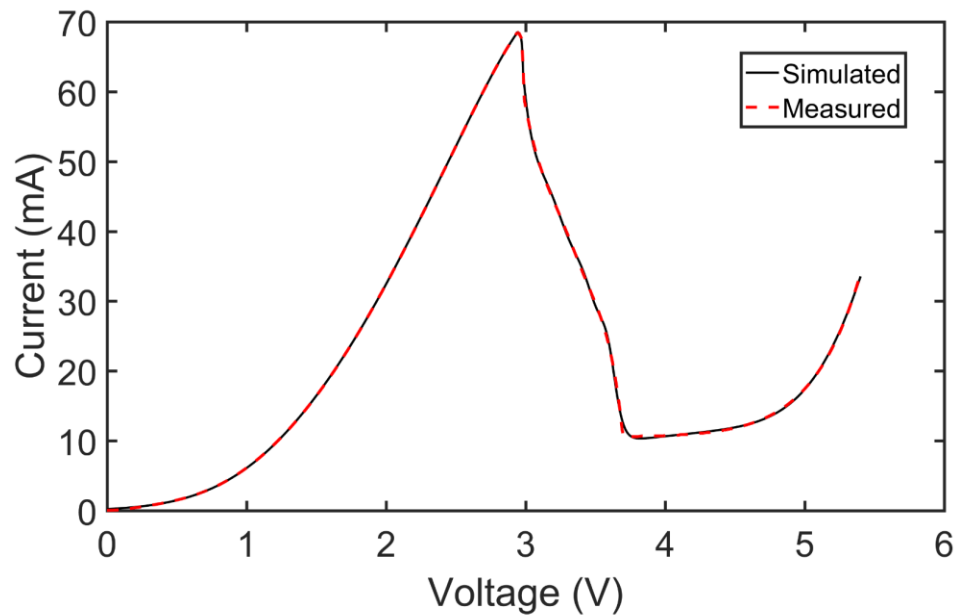

Figure C.2 Measured (black) and fitted (red) RTD device I-V characteristics.

Simulation setup – OOK modulation scheme

The described OOK modulation scheme (Fig. 6.19) used for the detector data transmission simulations was implemented using a *time-domain pseudo-random bit sequence source* (VtPRBS) and modulated onto a high-frequency carrier generated by an AC source component (VtSine). The complete simulation setup is shown in Fig. C.3 including the eye probe component used for the presented density plots.

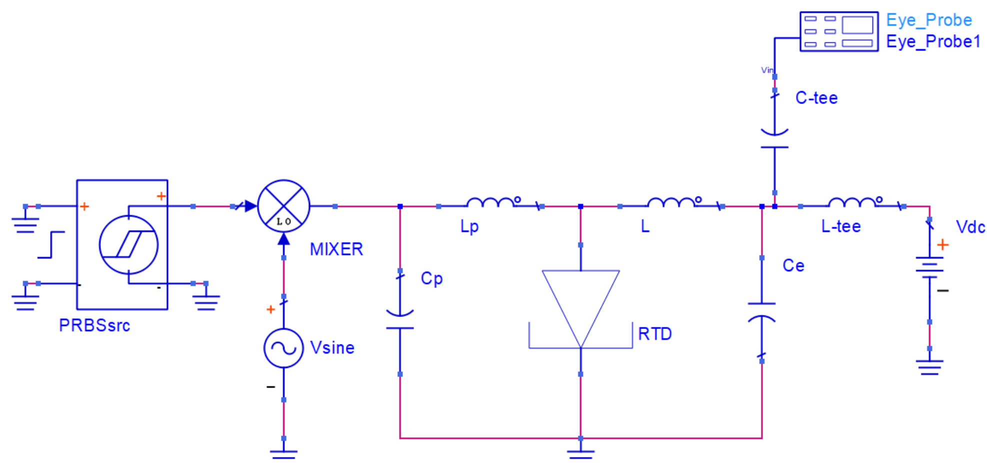

Figure C.3 ADS schematic of the detector setup.

Appendix D. RTD wireless transmission link

The high detector responsivity, as indicated in Chapter 6 was demonstrated in an RTD based Tx/Rx wireless data transmission link Ka frequency band (26.5 – 40 GHz). The experiment presented in this section was conducted jointly with Dr. Andrei Cornescu, responsible for the design and development of the high power RTD based source, as part of his PhD research project.

The complete experimental setup is presented in the block diagram schematic in Fig. D.1 and in Fig. D.2. The realised RTD circuits (Tx and Rx sub-systems) were operated in an on-wafer probing configuration, biased independently from two power supplies. The high-frequency AM signal, generated at the Tx side, was transmitted over a distance of 15 cm (limited by the available measurement setup space) using a pair of matching WR-28 horn antennas (15 dBi gain), connected to the RTD circuits using a CPW-to-waveguide transition. No amplification stage was introduced between the output of the detector and measurement equipment.

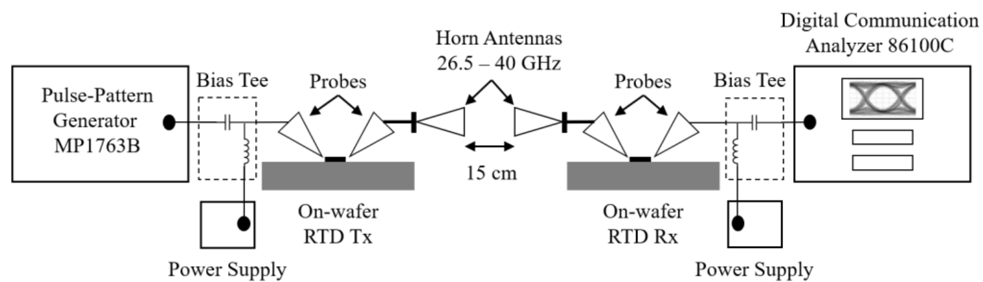

Figure D.1 Block diagram of wireless data transmission setup, using an on-wafer RTD source.

The oscillation frequency at the output of the RTD transmitter was measured at 30 GHz, with an output power of -8.1 dBm. An attenuation of 19.79 dB was observed in the received signal strength (RSS) at the output of the receiver antenna, measured at 27.89 dBm. The baseband signal was generated using the similar specifications as in the W-band experiment in section 6.4.1 (amplitude of 250 mV peak-to-peak), to create the OOK modulation scheme.

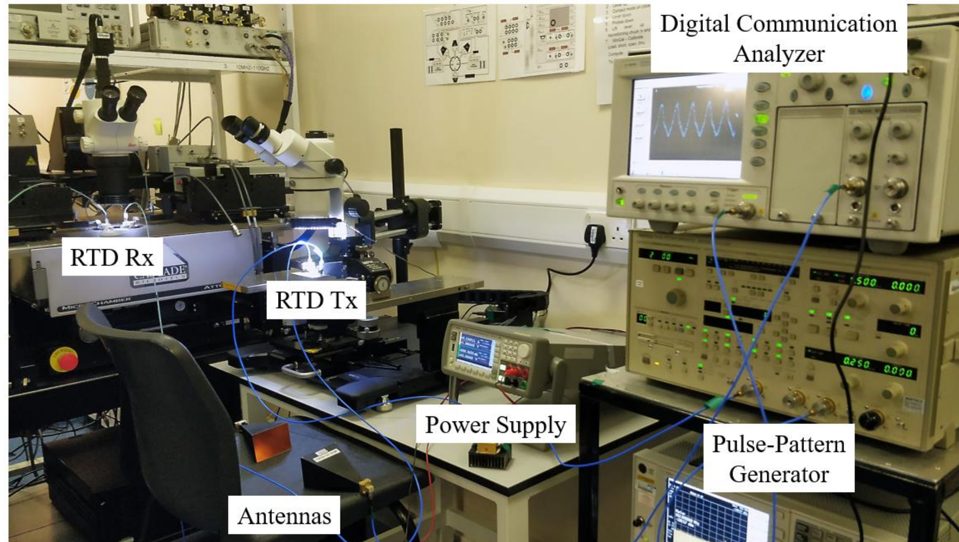

Figure D.2 Picture of wireless data transmission setup.

The maximum transmitted data rate with the current setup was estimated at 2.6 Gbps, primarily limited by the large *RC* time constant present at the input of the RTD oscillator circuit. Considering this major bottleneck, associated with the RTD transmitter, a detector with a reduced output low-pass filter cut-off frequency of 6.5 GHz, (L = 200 pH, C_e = 3 pF) was explored in order to improve the SNR.

The measured eye diagram of the recovered demodulated signal is presented in Fig. D.3, with an eye amplitude of 3.6 mV and a SNR of 19.22 dB, for a 2 Gbps data rate. The relatively low AM signal power, present at the input of the detector, enabled the device biasing in the highest non-linearity region (current peak), which lead to an increased detection sensitivity. The overall detector responsivity, at the specified frequency, was calculated at 2.21 kV/W. A bit pattern contour can be observed for a measured eye diagram at a data rate close to the cut-off frequency of the output low-pass filter (6 Gbps), presented in Fig. D.4, however no eye opening was identified by the measurement equipment.

In order to validate the date transmission accuracy, the BER was measured using an Anritsu MP1764c error detector. The measured BER as a function of transmitted signal data rate is plotted in Fig. D.5, which shows an error free transmission (BER < 10^{-10}) up to 2.4 Gbps. Alternative Ka-band RTD based sources and antenna pair selection should be investigated in the future, in order to experimentally determine the maximum achievable data rate, together with optimal transmission distance.

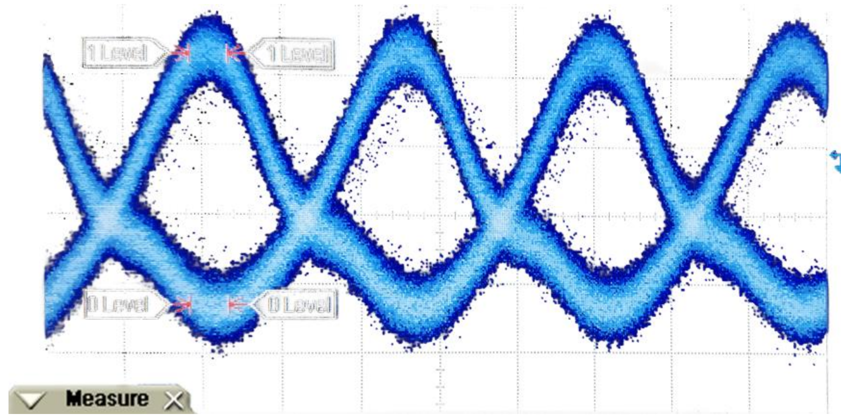

Figure D.3 Measured eye-diagram of demodulated 2 Gbps signal. Eye amplitude of 3.6 mV and SNR of 19.22 dB.

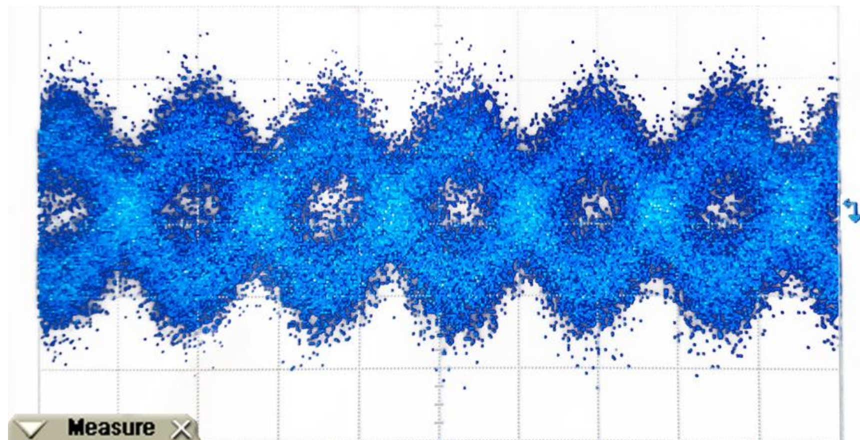

Figure D.4 Measured eye-diagram of demodulated 6 Gbps signal. No clear eye opening was identified.

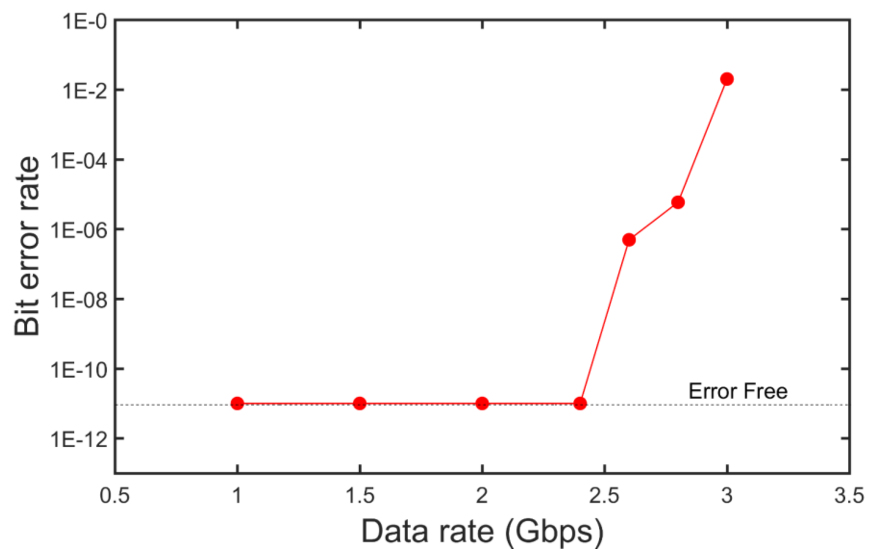

Figure D.5 Measured BER vs data rate. Error free transmission up to 2.4 GHz.